Spring 2019

Structural Health Monitoring and Non-Destructive Inspection of Composite and Metallic Structures

Asaad Qasim Migot

STRUCTURAL HEALTH MONITORING AND NON-DESTRUCTIVE INSPECTION OF COMPOSITE AND METALLIC STRUCTURES

BY

Asaad Qasim Migot

Bachelor of Science
University of Baghdad, 1993

Master of Science
University of Baghdad, 2007

Submitted in Partial Fulfillment of the Requirements

For the Degree of Doctor of Philosophy in

Mechanical Engineering

College of Engineering and Computing

University of South Carolina

2019

Accepted by:

Victor Giurgiutiu, Major Professor

Lingyu Yu, Committee Member

Jamil Khan, Committee Member

Juan Caicedo, Committee Member

Cheryl L. Addy, Vice Provost and Dean of the Graduate School

ACKNOWLEDGEMENTS

I would like to acknowledge and express my deep gratitude to my academic advisor, Dr. Victor Giurgiutiu, for his mentorship and kind support over the past few years. I am greatly appreciative of the time he has dedicated to guiding me throughout the journey of my Ph.D. His mentoring represents such a truly rewarding experience. I would like to thank the other members of my committee Dr. Lingyu Yu, Dr. Jamil Khan, Dr. Juan Caicedo for being part of my Committee and for their invaluable guidance. I want to thank my dear colleagues for their friendship and accompany throughout my laborious journey. Also, I would like to express my thankfulness to Iraqi ministry of higher education and scientific research for their financial support.

ABSTRACT

Structural Health Monitoring (SHM) and Nondestructive Testing (NDT) techniques are being used as effective tools for investigating variety of civil, mechanical, and aerospace applications. In recent years, these techniques become such incredible tools for continuously monitoring of various structures. The aim of the dissertation work is to develop SHM and NDT methodologies for acoustic emission sources localization, damage detection and quantification in metallic and composite structures using a network of sensors, guided wave and developed imaging methods. This work is implemented through preparing metallic and composite specimens, setting up experiments, designing efficient networks of sensors, modeling guided wave interaction with damages and developing imaging methods. A sparse array of sensors and guided waves in conjunction with imaging methods are powerful tools for quantifying the damage information in metallic and composite structures. The desertion work is organized in three major parts.

In part I, the impact points on metallic plate are localized using efficient a network of sensors, numerical method and developed imaging method. The hyperbola path-based developed imaging method precisely localizes the impact points inside and outside the network area. Two newly imaging methods are used successfully for localizing the impact points on composite plates. The first imaging method is used for localizing the impact points on composite plates with unknown material properties. The second imaging method is used for localizing the impact points on composite plates with known material properties.

In part II, estimation of crack size, shape, and orientation is investigated numerically and experimentally using Lamb wave. A hybrid global-local (HGL) approach is used in conjunction with the imaging methods for the numerical simulation. The HGL approach allowed fast and efficient prediction of scattering wave signals for Lamb wave interaction with crack from various incident directions. The simulation results show the directionality effect of the scattering wave signals and suggested an optimum transmitter-sensor configuration. Two imaging methods are used: one involves synthetic time reversal concept and the other involves Gaussian distribution function. Both imaging methods show very good agreement during simulations. Experiments are designed and conducted based on the simulated results. The directionality effect of incident Lamb waves on the imaging results is studied. The effect of summation, multiplication and combined algorithms for each imaging method is studied. It is found that both methods can successfully predict the crack size and orientation. Attempt is made to use these imaging methods for detecting and sizing smaller sized damage (1-mm to 3-mm diameter hole). The results confirm that these methods can successfully localize the hole.

In part III, four SHM and NDT techniques have been developed and used to localize and quantify the delamination in two composite plates. The effect of delamination size and depths are studied. For the NDT technique, appropriate setting of Rollerform and Omniscan devises is successfully used for localizing and sizing the delamination by extracting C-scan image, S-scan image and A-plot. For SHM technique, new methodologies and efficient networks of sensors (PWAS) are used successfully for accurately imaging the delamination in composite plates. Setting appropriate SLDV experiment helps to study the guided wave interaction with delamination and to study

generated trapped waves. A new structural vibration methodology is used for detecting and quantifying delamination in composite plates. This methodology is based on the local vibration under piezoelectric wafer active sensors (PWAS) excitation. The PWAS transducer is used for the high-frequency excitation with a linear sine wave chirp from 1 kHz to 500 kHz and the scanning laser Doppler vibrometer (SLDV) was employed to measure the local vibration response of the composite plates. The local defect resonance frequencies of delamination were determined from SLDV measurements and the operational vibration shapes were extracted and utilized to quantify the delamination. The dissertation finishes with conclusions, and suggestions for future work.

TABLE OF CONTENTS

LIST OF TABLES

LIST OF FIGURES

CHAPTER 1
INTRODUCTION

In recent years, the necessity of health monitoring a huge amount of aerospace, navel and vehicle structures spark a great revolution in the field of structural health monitoring (SHM) and non-destructive test (NDT) techniques. Many researches have been implemented and many technologies have been developed in these fields. The emerging revolution of SHM and NDT techniques help the engineering community to diagnose different kinds of structures in real time, keep safety structures, detect structural invisible damages in early steps and prevent the catastrophic accidents. The goal of this research is to develop and enhance reliable SHM and NDT methods for detecting and identifying the impact sources and damages on isotropic and composite structures. This chapter represents the introduction to the dissertation and contains the motivation of implementing this research, the discussing of research goals and objectives and the organization of the dissertation work.

1.1 MOTIVATION

Structure health monitoring (SHM) and non-destructive techniques (NDT) play a significant role in the field of investigating and maintaining the safety of structural systems. In recent years, the aerospace applications are increased and developed rapidly. Preventing the catastrophic accidents of aging structures and reducing the maintenance cost have been raised a clear need for reliable and cheaper damage monitoring techniques. The sufficient of SHM system requires an effective number of sensors, a good distribution on area of

interested and effective methodologies for interpretation the received signals to extract the best results of detection and identifying of certain types of damage. SHM can be used as a passive system or active system. Passive SHM uses passive sensors which receive the signals from inspected structure without interaction with the structure. This system do not provide direct measurement of the damage information. Active SHM system uses active sensors which interact with the structure and perform the process of the presence or absence of damage. The interaction of guided waves with damages represents the main parts of SHM methods of detection and identifying damages. Construction efficient structural data processing methods can achieve the successful SHM and NDT systems and can interpret these data in best effective output results. These results can be used to identify the location, shape and size of structural damages. The challenge of SHM techniques is to develop an effective method works in conjunction with a network of sensors and guided waves to interpret the sensing paths signals into damage identifying results.

1.2 RESEARCH GOAL, SCOPE, AND OBJECTIVES

The research goal of the PhD work presented in this dissertation is to develop and enhance the SHM and NDT methods for identifying the impact sources and damages on isotropic and composite plates. The scope of this research covers the experiments, and finite element simulation of using SHM techniques for identifying structural damage. The objectives of the work presented in this proposal work are as follows:

1. Research efficient methods for impact sources localization on metallic and composite structures.
2. Investigate and enhance several numerical methods to localize impact sources.
3. Developed imaging methods to localize impact sources.

4. Study the interaction of Lamb wave with a crack damage
5. Develop efficient methods with enhanced accuracy for identifying the minimum detectable damage size.
6. Develop and enhance efficient methods for identifying damages in composite plates using NDT, SHM, SLDV and vibration-based techniques.

1.3 ORGANIZATION OF THE DISSERTATION

The dissertation is organized in eight chapters. The focus and contents of each chapter is introduced in Chapter 1.

In Chapter 2, state of the art of damage identification in structures like plate using guided waves, sparse array of sensors and imaging methods. Also, the state of the art of acoustic emission sources localization in structures like plates.

In Chapter 3, the experiment of impact sources localization on isotropic plates is presented. The effect of increasing the number of used sensors on the accuracy of calculated results are studied. The imaging methods are developed and used for impact sources localization on isotropic plates.

In Chapter 4, the experiment of impact sources localization on composite plates is implemented. Numerical methods are used for processing the received signals of impact sources and detecting the location of these impact sources on the interested area. New two imaging methods are developed for detecting the location of impact sources on composite plates. The first imaging method is used for the composite plate with unknown its material properties. The second imaging method is used for the composite plate with known its material properties.

In Chapter 5, two experiments are presented for identifying damages in two isotropic plates using sparse array of sensors, guided waves and imaging methods.The first experiment is performed for identifying crack damage using received signals of pitch-catch mode and pulse-echo mode. The second experiment is performed for identifying through thickness-hole using pitch-catch mode. Two sensors are used successfully for damage localization using pulse-echo mode and imaging methods.

In Chapter 6, the multi-physics finite element technique is used to simulate the interaction between Lamb waves and a crack damage at different incident angles. The hybrid global-local (HGL) approach with imaging methods provide a fast and efficient simulation of crack size estimation.

In Chapter 7, four techniques are used for identifying the delamination in two composite specimens. The first specimen has three different sizes of simulated circular delamination inserted at the same thickness depth. The second specimen has three simulated circular delamination inserted at different thickness depths. First, the NDT technique is used to visualize the delamination areas using Omani scan device and Rollerform. The experimental setup and imaging results of NDT method are presented and discussed. Second, the SHM technique is used for imaging the structural damages in both specimens using sufficient networks, guided waves and imaging methods. The experimental setup of SHM techniques, the group velocities dispersion and tuning curves of Lamb wave modes, scattered waves and imaging results are discussed. The scanning laser Doppler vibrometer (SLDV) experiment is implemented for visualizing the interaction of Lamb waves with the delamination. The wavefield images, time-space domains and frequency-wavenumber domains of pristine and damaged areas are discussed.

The vibration-based technique is used to identify the delamination areas of both specimens. The resonance frequencies and mode shapes of pristine and damaged areas are determined and discussed.

The proposal work finishes in Chapter 8 with the conclusions, major contributions and future work.

CHAPTER 2
STATE OF THE ART IN STRUCTURAL HEALTH MONITORING (SHM) USING DAMAGE IMAGE

This chapter introduces most of the fundamental imaging diagnostic approaches which are used in conjunction with a network of sensors and guided waves for identifying a damage in a structure like plate. Also, explaining the methods of increasing the accuracy of resulting image. Many researches are studied for acoustic emission source localization in plates.

2.1 INTRODUCTION

In the last two decades The Structural health monitoring (SHM) techniques are widely used for assessing the health conditions of different kinds of structures. It can virtually promote the performance of structures. This technique include of choosing the type and distribution of sensors, transmitting and receiving signals, data processing and fusion [1]. SHM can be used as passive or active techniques. Passive SHM consists of monitoring some parameters (loading stress, environment action, performance indicators, acoustic emission from cracks, etc.) and indicates the state of structural health. The Active SHM accomplishes proactive examination of the structure, detects damage, and determines the state of structural health from the evaluation of damage extension and intensity. Both methods attempt for performing a diagnosis of the structural situation, to be followed by a prognosis of the remaining life. Passive SHM uses passive sensors to acquire the structural data without interaction with the structure. They cannot be used for measurement of the

damage presence and intensity. Active SHM uses a network of sensors which interacts with the structure to determine the presence or absence of damage. The methods used for active SHM like those of nondestructive test techniques (NDT), e.g., eddy currents, ultrasonic, etc., only that they are used with embedded sensors. Hence, active SHM can be seen as a method of embedded NDT. The active SHM method employs piezoelectric wafer active sensors, which send and receive Lamb waves and determine the presence of cracks, delamination, disbands, and corrosion. Due to its similarities with NDE ultrasonic, this approach is also known as embedded ultrasonic [2]. Continuous SHM would lead to considerable life-cycle cost reduction since the damaged part can be replaced in time, preventing the failure of the whole structure and the loss of human lives. Another critical feature of a SHM system is its ability to detect the initiation and propagation of structural damage at an early stage. The early step of detection would bring a great safety enhancement. Equation Chapter (Next) Section 1

2.2 IDENTIFYING DAMAGES USING LAMB WAVES

The SHM techniques are developed for damages identification in metallic and composite structures. The idea of these methods is to distribute some sensors on the inspection area for acquiring signals. These signals are analyzed using various signal processing method to extract its features. These analyzed signals are used as input data with different algorithms to quantify the structural defects. In SHM, the damage can be defined as a new case of structural state (unhealthy state) which is different from the old case (healthy state). This damage can be seen if we make comparison between the unhealthy and healthy states. Based on this idea, we can use Lamb waves or impedance methods to detect damages in a structure like plate. In the case of damage identification

using Lamb waves, two modes are used for actuator sensor configuration [3]. These modes are pitch-catch and pulse-echo modes as shown in Figure 2.1.

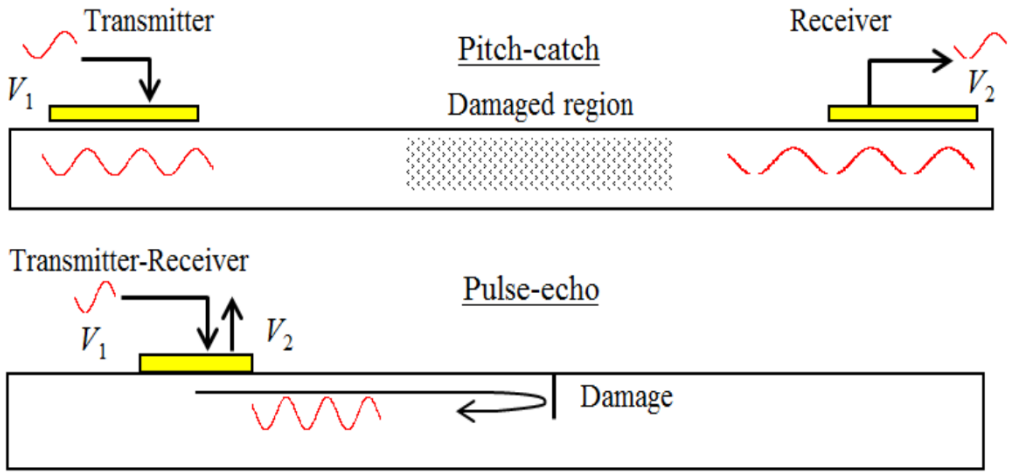

Figure 2.1: The configuration of pitch-catch and pulse-echo modes [3].

In pitch-catch mode, the elastic waves (i.e., Lamb waves) travel from the transmitter sensor across the inspection area. A receiver sensor captures these waves at the other end of signal path. In pulse-echo mode, the transmitter and receiver sensors are located in closed to each other. After traveling the elastic wave across the inspection area, the receiver sensor catches the scattered waveform emanated from the damage.

The simplest damage identification algorithm is the 'damage metric' a.k.a. 'damage index', 'damage indicator', 'DI', which is used to measure of the amount of damage present in the structure. In spectrum based SHM, the damage metric results from the comparative processing of 'pristine' and 'damage' cases. The damage metric can identify the difference between the two cases due to damage presence. The best damage metric can only capture the features that are directly modified by the damage presence and can neglect the changes due to normal operation conditions (i.e., statistical difference within a population of

specimens, and expected changes in temperature, pressure, ambient vibrations, etc.). Ideally, the damage metric should be able to evaluate the vibration or E/M impedance spectra and indicate damage presence, location, and severity. Development of suitable damage metrics and damage identification algorithms remains an open question in the practical application of structural health monitoring methods.

The DI represents extracted features from the captured signal that can be linked with damage at different states. An efficient DI can serve as an indicator to depict the damage. The features of a Lamb wave signal include time of flight (TOF), magnitude, attenuation, frequency, phase, spectrum and others. These parameters can change to different degrees in signals captured before and after the presence of damage in structures. Though application-specific, the basic principle in selecting signal features for damage identification is to extract those that are most sensitive to changes in damage parameters

To date, several damage metrics have been proposed and tried; among them, the most popular are the root mean square deviation (RMSD), the mean absolute percentage deviation (MAPD), the covariance (Cov) and the correlation coefficient deviation (CCD). The mathematical expressions for these metrics are as follows

$$RMSD = \sqrt{\frac{\sum_{N}\left(S_i - S_i^0\right)^2}{\sum_{N}\left(S_i^0\right)^2}} \tag{2.1}$$

$$MAPD = \sum_{N}\left|\frac{S_i - S_i^0}{S_i^0}\right| \tag{2.2}$$

$$Cov = \frac{1}{N-1}\sum_{N}\left(S_i - \bar{S}\right)\left(S_i^0 - \bar{S}^0\right) \tag{2.3}$$

$$CCD = 1 - \frac{\sum_{N}\left(S_i - \bar{S}\right)\left(S_i^0 - \bar{S}^0\right)}{\sqrt{\sum_{N}\left(S_i - \bar{S}\right)^2 \sum_{N}\left(S_i^0 - \bar{S}^0\right)^2}} \tag{2.4}$$

where N is the number of frequencies in the spectrum, S_i are the elements of the spectrum, and the superscript 0 signifies the pristine state of the structure. The symbols $\bar{S}$, $\bar{S}^0$ signify mean values. The above equations yield a scalar number, the damage index (DI), which represents the relationship between the compared spectra. Thus, we expect that the resonant frequency shifts, the peaks splitting, and the appearance of new resonances that appear in the spectrum will alter the DI value and thus indicate the presence of damage. The advantage of using above equations is that the spectrum does not need any pre-processing, i.e., the data obtained from the measurement equipment can be directly used to calculate the DI [4].

The ultrasonic guided waves were used as a tool for monitoring the health of strands, which are widely used in applications of civil structures, the damage index values are function of a notch cut depths in a strand. The results show the sensitivity of damage index to notch depth [5]. Piezoelectric based built-in diagnostic technique monitored the fatigue crack growth in metallic structures. The damage index measured from piezo ceramics which installed on the coupons shows a good correlation with the actual fatigue crack growth obtained from visual inspection. Also, the results show that damage index values for the paths B and C which are closed to the crack are higher than paths A and D which are not closed the crack as shown in the Figure 2.2 [6]. A methodology based on Lamb waves was used to detect and localize damages on aluminum plate. In this work a two-ring-shaped arrangement of piezo transducers to reduce the area of isolated region and to

increase the resolution of monitoring system. This methodology is based on the propagation of Lamb waves using the pitch-catch configuration and fusion of the parameters extracted from signals processed by discrete wavelet transform (DWT) and Hilbert transform (HT). The results show that this methodology is effective to detect and localize damages in established regions of monitored area [7].

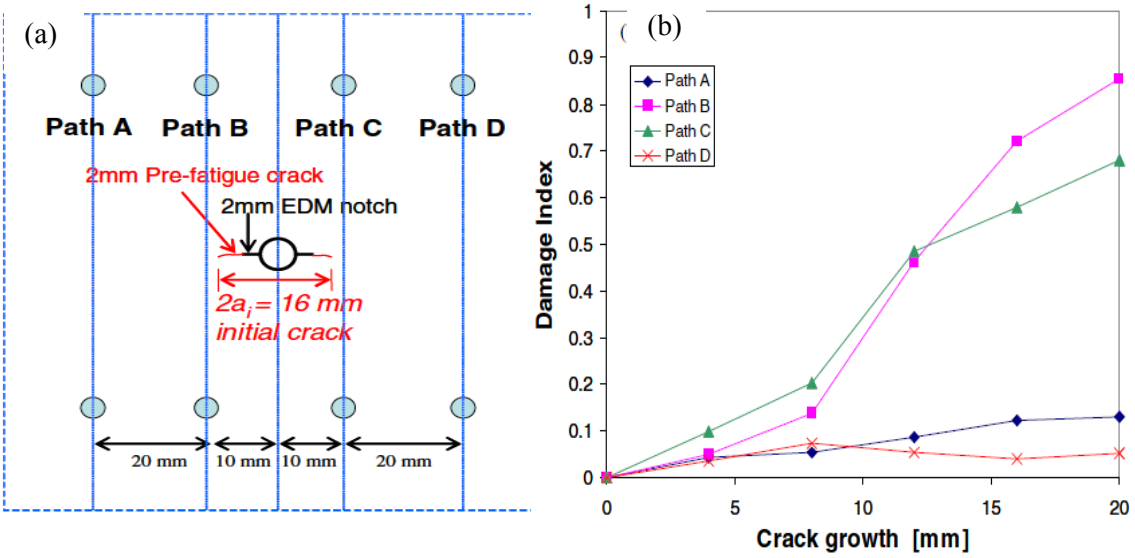

Figure 2.2: (a) Specimen with paths sensors; (b) damage index as a function with crack growth [6].

Different crack events were monitored by NDT methods (ultrasonic and eddy current) and damage index method to quantify the method of damage index. The results demonstrated that the damage index correlated well with the conventional NDT methods [8]. The time domain of Lamb waves received signals in an inspection area were used in many researches for damage identification. The difference in time of flight between the incident wave and the scattered wave can be used for determining the distance between the damage point and the location of received sensor as shown the Figure 2.3. In this case the damage is localized as a function of difference in time of flight and the group velocity of propagating wave

$$L = \frac{v_g \times \Delta t}{2} \tag{2.5}$$

where L is the distance between the damage and the reviser sensor; v_g is the group velocity of propagating wave.

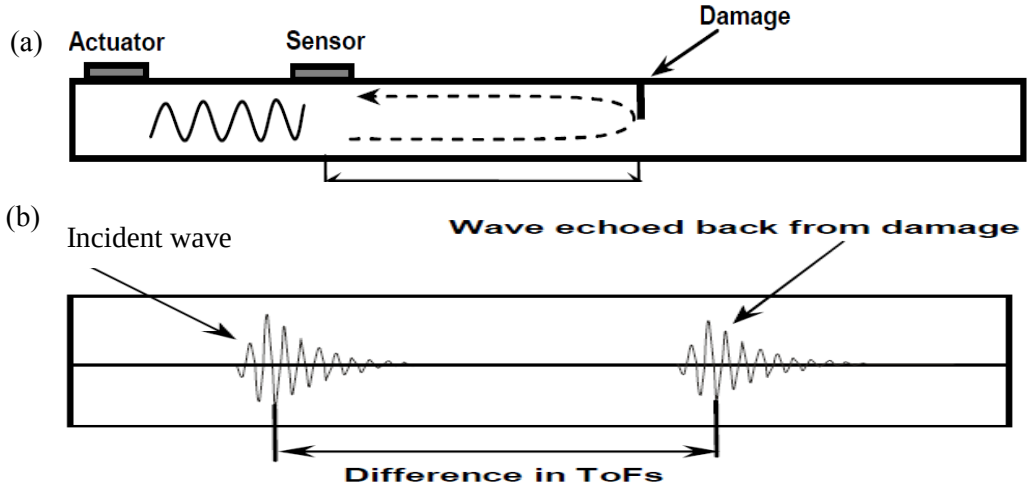

Figure 2.3: (a) Damage detection in a beam; (b) signal captured by sensor [9].

In two dimension inspection area, the distances among actuator, sensors and damage (as shown in the Figure 2.4) can be determined as follow [9]

$$\begin{aligned} L_{A-D} &= \sqrt{\left((x_D - x_A)^2 + (y_D - y_A)^2\right)} \\ L_{D-S} &= \sqrt{\left((x_D - x_S)^2 + (y_D - y_S)^2\right)} \\ L_{A-S} &= \sqrt{\left((x_A - x_S)^2 + (y_A - y_S)^2\right)} \\ \Delta t = t_{A-D-S} - t_{A-S} &= \frac{L_{A-D}}{v_g} + \frac{L_{D-S}}{v_g} - \frac{L_{A-S}}{v_g} \end{aligned} \tag{2.6}$$

where Δt is the difference in TOF between the incident wave and scattered wave, L_{A-D} is the distance between the actuator and the damage point (x_A, y_A), L_{D-S} is the distance between the damage point and the sensor, L_{A-S} is the distance between the actuator and sensor.

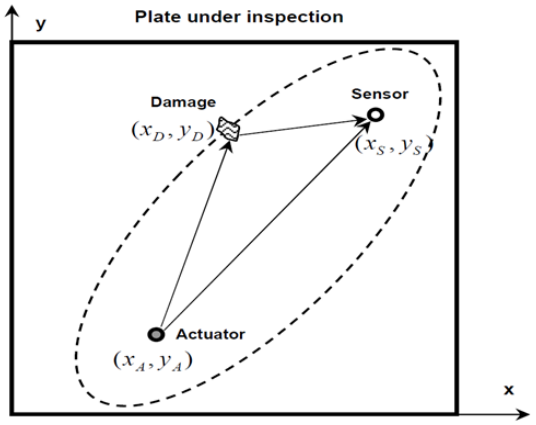

Figure 2.4: The orbit of a sensing path [9].

The ellipse orbit represents the damage orbit. All the points on this orbit have the same distances from ellipse foci (actuator and sensor points). In triangulation approach, three sensors are required for damage localization [10]. These three sensors generate three paths which intersect at damage point as shown in the Figure 2.5. To get accurate results for localization a damage using this approach, the TOF of scattered wave should be accurately determined, more sensors needed and good distribution of sensors in an inspection area. To catch the scattered damage wave from the measured signal of actuator sensor path, we should study the baseline signal (healthy signal) between them or study the position actuator and sensor relative to the boundaries.

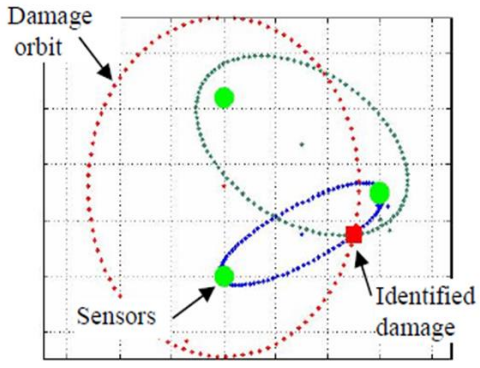

Figure 2.5: Triangulation principle for damage identification [10].

2.3 IMAGING TECHNIQUE FOR DAMAGE DETECTION IN ISOTROPIC PLATES

In recent years, many researchers deal with visualizing the structural damages on an inspection area. Many approaches have been extracted in the field of using Lamb waves, networks of sensors and imaging methods for visualizing the defects. These imaging algorithms have been sufficiently used to localize and size different kinds of defects in aerospace structures. These imaging approaches are known in most of researchers as a probability-based diagnostic imaging which use color map to describe and signalize the probability of existence the defects on the inspection area. Also, we can set a certain threshold for the color map to indicate the shape and the size of a defect. Using or fusing more signals of actuator sensors paths makes the results of imaging the damage more accurate. So, the basic idea of imaging algorithm for damage detection is to divide the inspection area into pixel points and to find the total field value (probability image) for every pixel point from all the actuators- sensors paths. The pixel point with highest field value represent the damage point. A digital imaging method for appropriate sparse actuator/sensor networks has been developed [11] based on the principle of time reversal concept. The results show the effectiveness of new imaging method for locating and sizing the structural damages. This imaging method was investigated with a network of piezoelectric actuator/sensor for characterizing the damage an aluminum plate. The results showed the effectiveness of diagnostic imaging method for visualization scattering location and estimation the location and size different kinds of damages [8]. Image fusion refers to the combining, or fusing, of the multiple images with the overall goal of obtaining an

improved image; i.e., a better signal-to-noise ratio and more accurate localization of damage [12].

Different imaging approaches have been developed to determine the field value of pixel based on the Lamb wave captured signal of actuator-sensor path as follow:

2.3.1 TIME OF FLIGHT OF SCATTERED SIGNAL

This method of construction imaging is based on determination the time of flight of scattered signal for every induvial actuation sensor path. Based on Eq.(2.6), an ellipse damage orbit is obtained for an actuator sensor path. The hyperbola path can be created using three sensors (one actuator and two sensors). The difference in time of flight of scattered waves of sensor number one and number two can be used to find the hyperbola damage orbit. The field value of pixel points can be determined using Gaussian distribution function as follow:

$$f(z_i) = \frac{1}{\sigma_i \sqrt{2\pi}} \exp\left[\frac{-z_i^{\,2}}{2\sigma_i^{\,2}}\right] \tag{2.7}$$

where $f(z_i)$ is Gaussian distribution function, representing density of damage presence at mesh node [13]. The pixel points fall on the damage orbit have the highest field value (degree of probability is 100%). The field values of pixels decrease with increasing the distance between the pixel points and the orbit points. The damage presents after fusion all the images from different paths. Figure 2.6 shows an ellipse orbit construct based on the TOF of actuator sensor path and the Gaussian distribution function for finding the field value of pixels. The TOF-based field value was sufficiently use for visualize structural damage [13]. They used this method with a network of sensors in pulse-echo mode to predict L-shape crack and triangular through thickness-hole cracks in aluminum plates.

The results demonstrated the effeteness of this probability images approach for damage prediction visually and quantitatively. Figure 2.7 shows the setup of aluminum specimen with L-shape crack and its probability image.

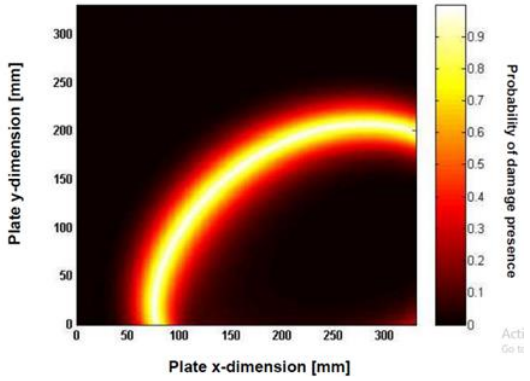

Figure 2.6: Ellipse orbit for an actuator sensor path [13].

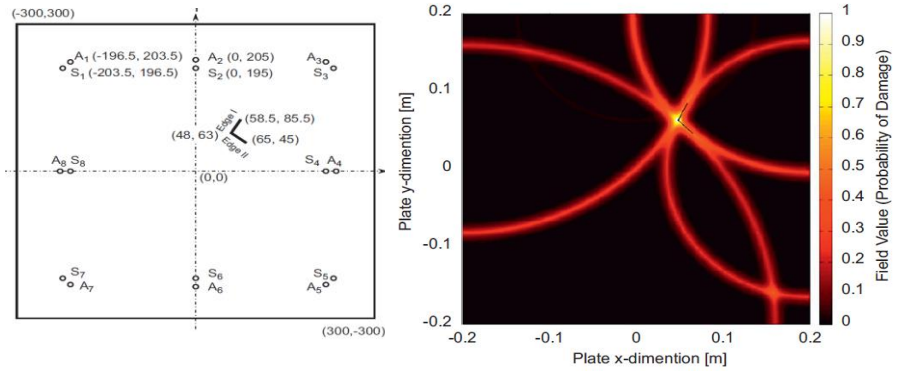

Figure 2.7: TOF-based diagnostic image; (a) setup of network sensors; (b) the probability image [13].

2.3.2 THE MAGNITUDE OF SCATTERED WAVE

The field value can be determined as a function of the magnitude of scattered wave which exist from the damage after guided waves hit it. If, we have an actuator-sensor path, the scattered signal can be defined after subtraction two signals (baseline and measured signals) captured by this path in two different situations (the healthy and damaged situations)

$$s(t) = f(t) - f^0(t) \tag{2.8}$$

where $s(t)$, $f(t)$, $f^0(t)$ are the scattered, measured and baseline signals respectively. If we have a network of sensors on an inspection area with a damage at (x, y), the time t for the incident wave to travel from the actuator at position (x_i, y_i) to the damage point and then received the sensor at (x_j, y_j) can be determined using the following equation

$$t(x,y) = \frac{1}{c_g}.\left(\sqrt{\left((x-x_i)^2 + (y-y_i)^2\right)} + \sqrt{\left((x-x_j)^2 + (y-y_j)^2\right)}\right) \tag{2.9}$$
$$(i, j = 1, 2, ..., N)$$

where c_g is the group velocity for both incident and scattered waves. For creating an image using scattered wave magnitude approach, the field value of pixel (x, y) after finding the magnitude of a time value $t(x, y)$. To find the total field value for all sensing paths to assemble the final image, the following equation is adopted [9]

$$\begin{aligned} I(x,y) &= \frac{1}{N_P}\sum_{k=1}^{N_p} r_k(t,x,y) \\ N_P &= N(N-1) \\ k &= 1, 2, ..., N_p \end{aligned} \tag{2.10}$$

In the above equation, $r_k(t, x, y)$ is the scattered signal captured by k^{th} actuator sensor path, N is number of used sensors, N_P is the total number of paths. This method is used in the ref. [12] to indicate the hole plate. To overcome the complexity of the signals such as the dispersive effect, they used digital bandpass filtering. The differential signals filtered at multiple frequencies were determined using timeshift averaging algorithms. This approach is constructed many images for the same state and these images are fused to get better results of damage localization. Focusing array imaging algorithm for quantitative

crack damage detection in isotropic plates was investigated [14]. In this work, the field values of pixel points are determine base on signal magnitude. For certain locations/ orientations of the crack relative to the sensor network, the crack is shown as two highlighted spots in the resulting image, representing the two tips of the crack; thus, the size and the orientation of the crack can be estimated. The signal magnitude and the imaging result of identifying the crack are shown in Figure 2.8.

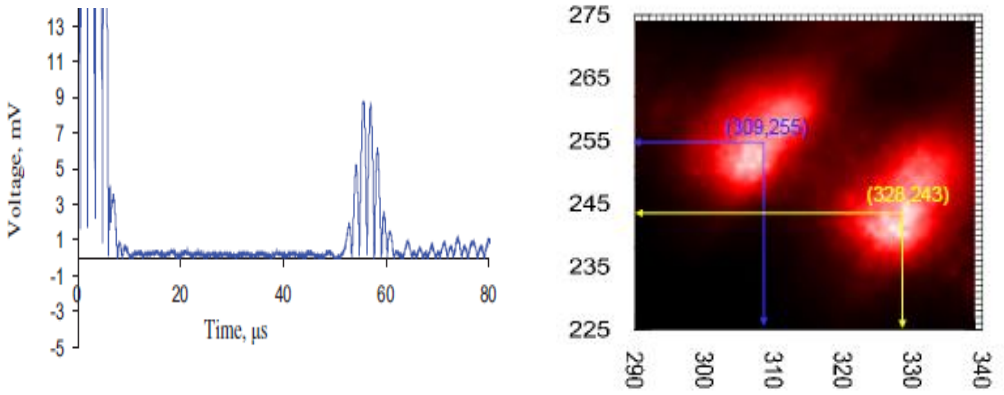

Figure 2.8: (a) Scattered signal magnitude; (b) crack image quantification [14].

A probability-based diagnostic imaging as a function of signal magnitude was used in conjunction with sparse array of sensors to quantify through thickness-hole (6- mm diameter) in an aluminum plate. The image results show that the accuracy of diagnostic image increase with increasing the number of paths or used sensors. Figure 2.9 shows four images with different number of used sensors, The image (c) with highest number of sensors has the accurate image result [15]. As shown in Figure 2.8, the scattered signal of sensing path has multiple peaks which lead to multiple orbits like ellipse. So, the diagnostic image becomes unclear. Also, the reflected waves from bounders may affect the scattered wave which decrease the resolution of imaging results. Many researchers use the signal processing to overcome this issue and get more accurate imaging result.

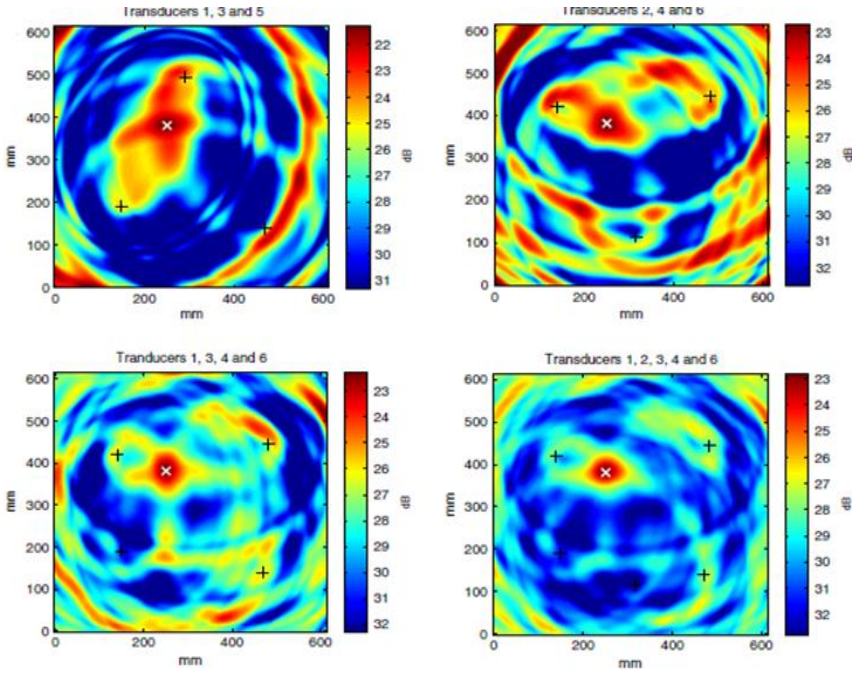

Figure 2.9: Imaging results of through-thickness hole using different number of sensors; (a) 3 sensors; (b) 3 sensors with different configuration; (c) 4 sensors; (d) 5 sensors [15].

The Hilbert transform and short Fourier transform (STFT) are two good tools to create envelope of signal magnitude. This step improves the resolution and the accuracy of imaging results. The STFT is used to convert the measurement signals from different sensing paths to interpret the signals easily and effectively and get better imaging results for visualization the damage extent in a composite plate [16].The total field value of pixel points for fusion all the images from different path can be written as a function of STFT or Hilbert transform as follow [9]

$$I(x,y)=\frac{1}{N_P}\sum_{k=1}^{N_p}\mathrm{H}_k(t,x,y)$$

or

$$I(x,y)=\frac{1}{N_P}\sum_{k=1}^{N_p}S_k(\omega_0,\tau,x,y) \qquad (2.11)$$

$$N_P=N(N-1)$$

$$k=1,2,...,N_p$$

where $H_k(t,x,y)$ is the Hilbert transform of $r_k(t,x,y)$ and $S_k(\omega_0,\tau,\mathrm{x},\mathrm{y})$ is the STFT of $r_k(t,x,y)$ In the above equations ω_0,τ are the angular frequency and time of propagated wave.

2.3.3 ENERGY OF SCATTERED SIGNAL

The Lamb waves have energy during their propagation in an inspection area. The field value of pixel points can be introduced as a function of the energy of scattered wave. If we say there is a damage at point (x,y) in an inspection area, the energy, $t(x,y)$ of scattered signals of sensing path k^{th} The total field value of pixel points regarding energy can be determined as follow[9]

$$
\begin{aligned}
&I(x,y)=\frac{1}{N_P}\sum_{k=1}^{N_p}E_k(x,y)\\
&E_k(x,y)=\int_{T_1}^{T_2}\left[r_k(t,x,y)\right]^2.dt\\
&N_P=N(N-1)\\
&k=1,2,...,N_p
\end{aligned}
\tag{2.12}
$$

where $E_k(x,y)$ is the energy of scattered signal of sensing path k^{th}, T_1,T_2 are the starting and ending points of the range.

The image approaches based on the energy of scattered signal were successfully used for localization a damage in plate [17]. The images of simulated damage in plate of non-constant thickness with a sparse array of sensors show the ability of this method for damage localization on inhomogeneous plate as shown the Figure 2.10.

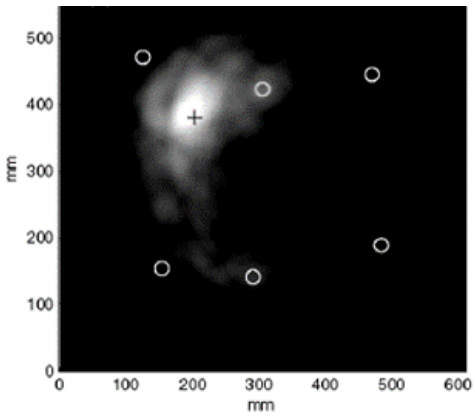

Figure 2.10: Energy-based image for damage localization [17].

2.3.4 SIGNAL CORRELATION BASED IMAGE

The correlation coefficient is estimated between baseline and measured signals for a particular sensing path. When the coefficient is equal to one that means no defect in the area of sensing path. The value of correlation coefficient is dependent on the position of defect relative to the sensing path area. The correlation coefficient of the path which is closer to the damage is lower than the path which is further from the damage. Based on that, the probability diagnostic image of certain path can be estimated as a function of correlation coefficient between baseline and measured signal. The total field value $\mathrm{I}(x,y)$ at pixel points (x,y) can be determined from all the sensing paths

$$I(x,y)=\sum_{k=1}^{N_P}(1-\rho_k)\left(\frac{-1}{\beta-1}.R(x,y)+\frac{\beta}{\beta-1}\right)$$

where

$$R(x,y)=\begin{cases}\dfrac{\left(\sqrt{\left((x-x_i)^2+(y-y_i)^2\right)}+\sqrt{\left((x-x_j)^2+(y-y_j)^2\right)}\right)}{\sqrt{\left((x_i-x_j)^2+(y_i-y_j)^2\right)}}, R(x,y)<\beta \\ \beta, R(x,y)\geq\beta\end{cases} \quad (2.13)$$

$(k=1,2,...,N_P)$

In the above equation, ρ_k is the correlation coefficient between baseline and measured signals of path k^{th}, β is a scaling parameter controlling the area influenced by actuator-sensor paths (its value around 1.05). This correlation analysis based technique called RAPID (reconstruction algorithm for probabilistic inspection of defects) was used to inspect a wing skin with a corrosion square area (200 mm length) [18]. The results showed good performance for damage detection, localization and sizing in complex aircraft wing structure as shown in Figure 2.11.

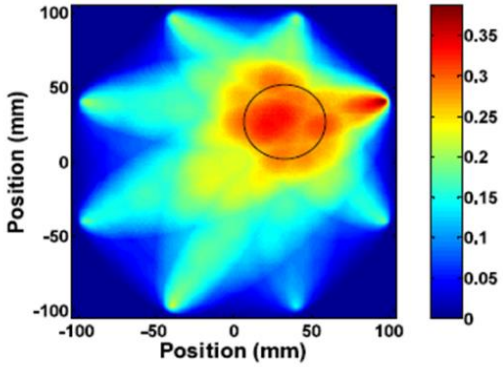

Figure 2.11: Imaging based correlation coefficient result of corrosion in wing skin [18].

2.4 DAMAGE DETECTION IN COMPOSITE PLATES

Composite materials have been used in many fields of industry. The problems of damage detection such as delamination that can initiate and grow in composite have been studied by many researchers [19]. Delamination damage may happen within the composite plate due to impact loading or cyclic loadings. Because of the embedded nature of delamination damage, visual inspection is not able to easily detect it and, therefore, nondestructive evaluation (NDE) techniques are used and extensively investigated for this type of diagnosis problems in composites [20]. Many non-destructive techniques can be used for damage detection in composite materials such as thermography, ultrasonic, eddy

currents, etc. Many researches show the efficiency and the effectiveness of ultrasonic guided waves method for SHM, due to their ability to cover large areas and to sense small defects. Advances in guided wave based SHM technologies over the last decade have demonstrated the feasibility of detecting and locating damage in composite structural components [21]

The active and passive methods were used for impact damage detection in composite aircraft wing-box structure [22]. For the active method, the Lamb wave and 3D laser vibrometer were used to spate the in-plane and out-plane Lamb wave components. The change in the amplitude of Lamb wave interaction with delamination were recorded using simple laser scan. The impact position was localized using passive approach and modified triangulation algorithm. Three composite structures made of glass fiber reinforced plastic, hybrid composite carbon fiber-reinforced plastic. These structures, which extracted from the vertical stabilizer of a military aircraft with barely visible impact damage and delamination, were inspected using various NDT techniques to investigate the application of these techniques [23]. The results show the effectiveness of this method for damage quantification in composite materials.

The Delamination in composite plate was evaluated experimentally using symmetric Lamb wave mode [24]. The results show that the amplitude of guided wave decreases over the delamination area. The research determined the delamination size by observing the change in signal amplitude of a cycle in the waveform. The results showed that the accuracy in measuring the length of a delamination depends on the size of the used probe. Smaller probes are more sensitive to changes in signal amplitude, and therefore can measure the length of a delamination more accurately, than a bigger probe.

A comprehensive review contains studying the advancing and performances of Lamb wave-based damage identification techniques for composite structures was implemented [25]. Most of this review was placed on study the characteristics of Lamb waves in laminated composites, wave mode selection, modeling and simulation methods, signal processing and identification approaches. A case study was implemented experimentally to support and validate the study. A system of smart devices was developed to permanently attach on the surface of the composite structure. This system can be used for monitoring the interaction of Lamb waves with defects as shown in the Figure 2.12. This system contains an array of transmitters to generate uniform asymmetric Lamb mode for inspection large area with small number of sensors. In this work the effect of damage size on Lamb waves was studied. So, this system could be used for damage detection at first step and location the damage with combination with a more sensitive technique such as ultrasonic C-Scan [26]. The induced delamination due to an impact was detected and quantified experimentally using guided wavefield data and special wavenumber imaging [22].

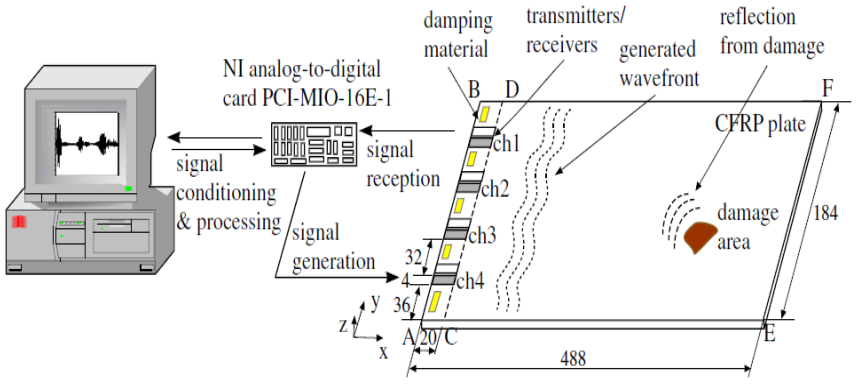

Figure 2.12: System configuration of monitoring the composite structure [26].

For a proved the concept the authors firstly investigated a specimen with simulated delamination (Teflon material insertion) and secondly a specimen with impact deli mention damage. In this experiment the guided waves are excited by a piezoelectric actuator and measured by a scanning laser Doppler vibrometer. The measured data which represents the wave propagation in the composite plate were analyzed using the spatial wavenumber imaging approach. The results show the ability of special wavenumber imaging for localization and quantification the delamination. The results were compared with ultrasonic C-scan image as shown in the Figure 2.13.

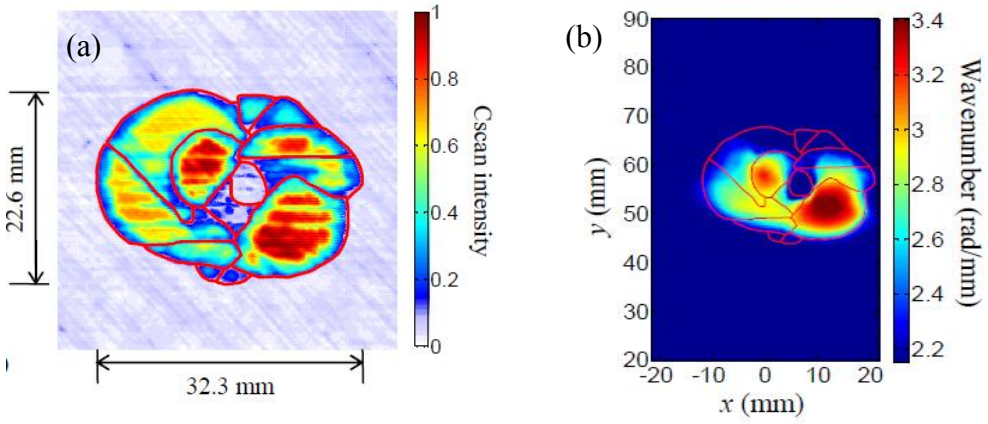

Figure 2.13: Delamination quantification images: (a) C-scan image; (b) special wavenumber image [21].

The probability-based diagnostic imaging approach using Lamb waves was developed to quantify multiple delamination in composite plate [27]. The authors investigated three woven fabric laminates (T650/F584). One of these specimens was used as a baseline specimen. The other specimens have different size of circular simulated delamination. Network of sensors were embedded in these specimen as shown in the Figure 2.14. The time of flight (TOF) extracted from the Lamb waves scattered signals of different sensing paths. The time of flight- based diagnostic imaging algorithms was used to

visualize the delamination. The results showed in Figure 2.14 demonstrated the effectiveness of such a probability-based imaging approach.

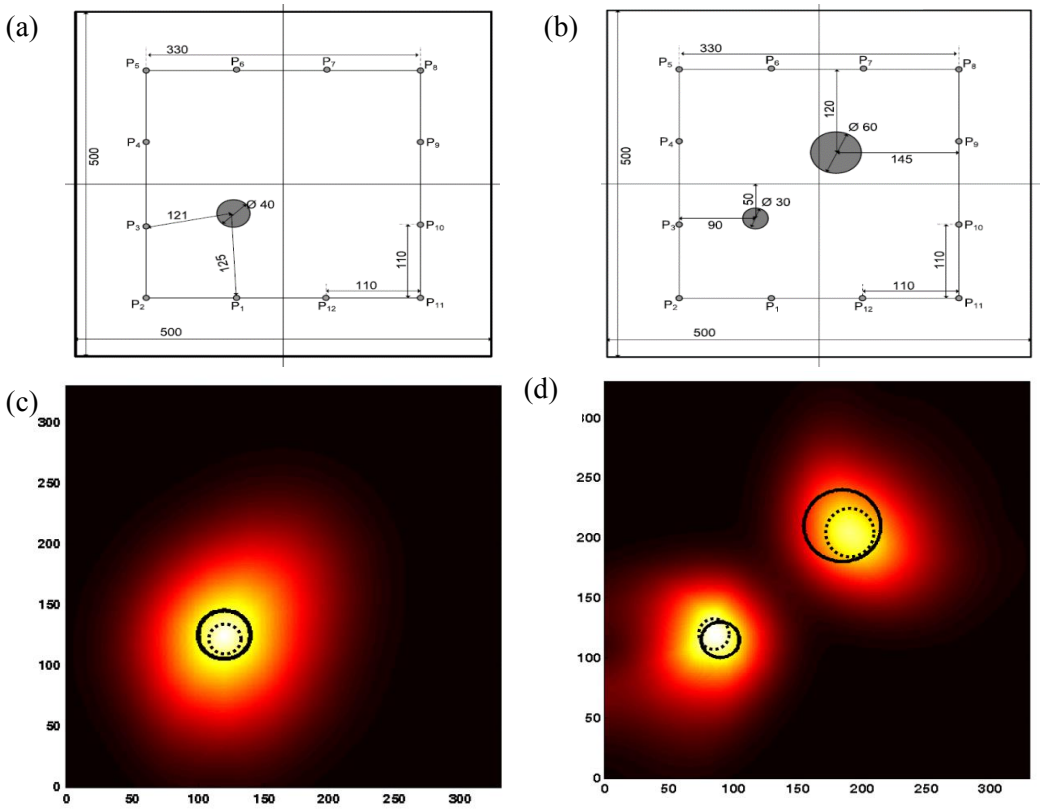

Figure 2.14: (a) Specimen with single delamination; (b) specimen with dual delamination; (c) image of single delamination; (d) image of dual delamination [27].

A stiffened composite panel with an artificial damage in the form of a through-thickness hole was visualized using correlation coefficient-based damage diagnostic method [28]. The network of active sensors which distributed in three rows to cover the monitoring area and the position of the artificial damage is shown in the Figure 2.15a. Different networks of sensing paths were investigated to estimate the probability of the presence of damage. The imaging results of this experiment as shown in Figure 2.15b reflected the effeteness of estimated probability of damage visualization in complex structures.

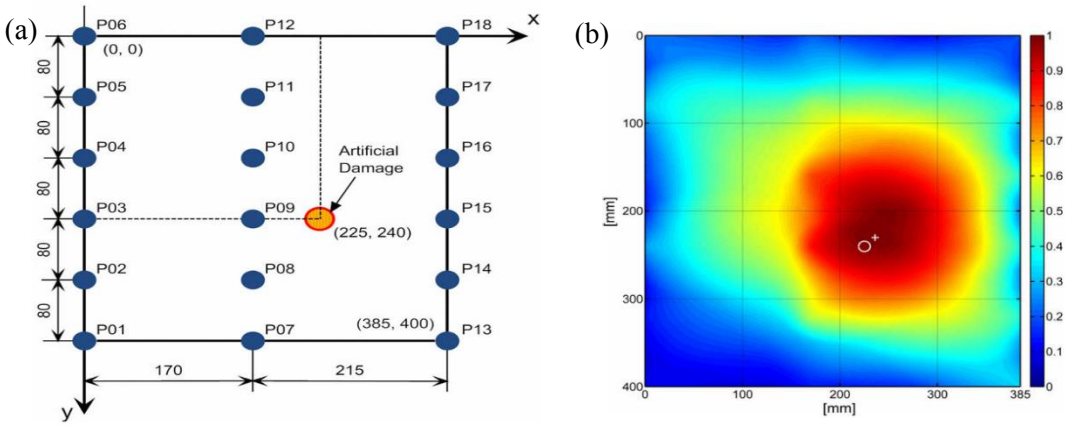

Figure 2.15: (a) Sensors distribution; (b) imaging result of damage quantification [28].

2.5 ACOUSTIC EMISSION SOURCE LOCALIZATION

Acoustic emission (AE) is the generation of transient elastic waves due to sudden redistribution of stress in material. Acoustic emission (AE) technique includes the listening and recording of generated acoustic emission waves using passive sensors. These sensors are fixed at different locations on the surface of the interesting structure. The AE technique analyze the recorded data for information about the source [29]. The Acoustic emission technique, as a non-destructive technique (NDT), can be used for detection and localization of structural defects. This technique is used to monitor aerospace structures, bridges, pressure containers, and pipelines, etc. [30]. The basic setup of flaw localization as shown in Figure 2.16. It can be localized using the following equation

$$d = 0.5(D - \Delta T \times v) \tag{2.14}$$

In the above equation, d is the distance from first hit sensor, D represents the distance between sensors, v represents the wave velocity. A new system in situ Structural Health Monitoring (SHM) was developed to localize the acoustic emission (AE) sources in anisotropic structures [31]. In this system, six piezoelectric sensors were used to measure the difference of stress waves.

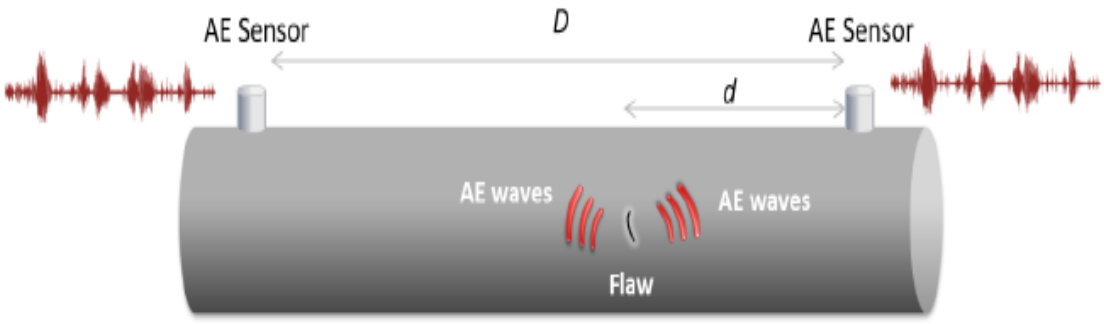

Figure 2.16: The basic idea of AE source localization [30].

The Continuous Wavelet Transform (CWT) with squared modulus was used in this to determine the time of arrivals (TOF) for every sensor. A set of nonlinear equations were solved by Newton's iterative method to find the impact location and flexural wave velocity. This new algorithms showed appropriate results. Two algorithms were used to localize random impact points on the wing structure using 2D and 1D array FBG sensors [32]. These algorithms are RMS and correlation. The results showed that both algorithms performed well. However, the results of RMS algorithm are better than correlation results. Also, the 2D and 1D array FBG sensors have the same results. So, the author proposed to use 1D array to reduce the number of sensors required to monitor impacts. The theories of wavelet transform and cross-time frequency spectrum (CTFS) were used with MATLAB code to obtain AE source with frequency-varying wave velocity in rectangular plate with four sensors. Two algorithms obtain the acoustic emission source points, the first one is CTFS based method and the second one is cross-correlation based method. The results show that the first algorithm is more accurate than second algorithm because the CTFT algorithm uses frequency-dependent wave velocity instead of constant speed [33]. A new method of an acoustic emission source localization was developed to localize impact points on anisotropic carbon fiber reinforced plastic (CFRP) plates. The Lamb waves produced

by pencil-lead and steel ball impact were monitored by using four resonant type transducers. These transducers were mounted on 300 mm square corner within 500 mm plate. A wavelet transform is used to determine of 65 kHz A0 Lamb wave. This new method determines the time of flight and the coordinates of impact points automatically. The results demonstrated that this algorithm is used for the source location of quasi-isotropic materials [34]. A novel methodology was investigated for impact localization and prediction of loading as a function of time. Fiber Bragg grating (FBG) sensors were used to measure the strain amplitude during impact on composite wing and aluminum plate. The wave velocity is not required in this method. It was found that the result of impact location are very accurate along wingspan and larger error along chord length due to the curvature of the wing along the chord [35].

A new approach was used to localize the acoustic source in an anisotropic plate without knowing the material properties or needing wave propagation along straight line. It was assumed that a non-circular wavefront is generated in anisotropic plate which has four clusters. Every cluster has three sensors which are used to determine the time difference of arrivals (TDOA). Based on (TDOA), there are four direction vectors are obtained for four cluster which are used with geometric vector analysis to obtain the acoustic source location [36]. An Iterative algorithm was used to localize the acoustic emission (AE) source in 3D non- dispersive material with six sensors. The propagation wave velocity is assumed constant in all direction, this velocity is determined by time of arrival before experimentation. A program based on iterative algorithm was developed to calculate the coordinates of AE source and the propagation velocity in the medium with a set of linear equations. After that the program performs a comparison between the velocity

measured and calculated, if the difference between both is greater than the tolerance, the program will increase the threshold until the result converges [37].

The most common techniques were explained for localization acoustic emission sources in plates. Some of these techniques are used only for isotropic materials like triangulation techniques and some of these are used for both isotropic and anisotropic materials. Also, the advantages and disadvantages of described techniques are discussed [38]. A new full automatic delta T technique was developed and demonstrated to localize the source of acoustic emission of damage in complex structure like plate with holes. This new approach was improved the running time delta T technique from 7 hours to 11 second. The results shows a good accuracy in damage locations [39].

A new formulation was used to localize the acoustic emission source in a large anisotropic plate. Six acoustic emission sensors were used to indicate the AE source in a structure like anisotropic plate without needing the information of material properties and wave velocity as shown in Figure 2.17. Also, the formulation was used for isotropic material with 4 sensors. The results demonstrated the effeteness of this method for monitoring the composite plate [40].

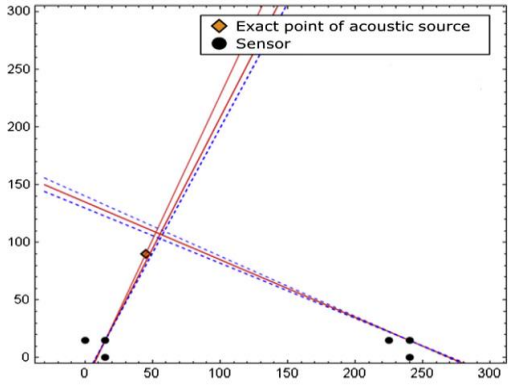

Figure 2.17: Predicted acoustic source location in composite plate [40].

A multi-agent system (MAS) monitors large-scale engineering structures using structural health monitoring (SHM) technology. The MAS consist of three kinds of agent which are sensing agent (SA), Signal processing agent (SPA), and damage evaluation agent. The MAS divide a large-scale structure into some subsystems to analyze it with three kinds of sensors. These sensors are piezoelectric ceramic sensor, Fiber Bragg grating (FBG) and strain gage. The result shows the efficiency of multi-agent system for large structural health monitoring [41].

2.6 SHM AND NDT

The structural health monitoring (SHM) has been used to monitor and diagnose the structural systems during life work. The SHM system will notice us by extracting time-dimension data when the structure becomes out of design domain. Many works have been achieved in the field of using SHM techniques for detecting, localizing and identifying structural damages. The Lamb waves which are generated by PWAS were used successfully for detecting damages in aluminum plate [42]. The non-destructive testing (NDT) techniques have been used in many applications such as aerospace and nuclear industry. The NDT can successfully identify various kinds of structural defects. The experimental results of investigating two welded plates using ultrasonic testing are presented [43]. A new method of ultrasonic time of flight diffraction was used to identify welded structure defects [44].

There are some differences between SHM and NDT techniques. The NDT equipment and probes are much expensive than SHM systems and sensors [45]. The size of SHM sensors are too small compared with NDT probes [46]. The SHM system can be used to monitor in-service structures. The NDT technique can be used to investigate out-

service structures. The NDT can identify the structural damages better than SHM. The frequency range of NDT probes is higher than the frequency range of SHM sensors. The SHM is more sensitive for damage detection than NDT. The NDT and SHM transducers have some differences. The NDT transduces are weakly connected with inspected structures through water or jell. The SHM sensors are strongly connected with inspected structures using adhesive bond.

PART I: IMPACT SOURCE LOCALIZATION ON METALLIC AND COMPOSITE PLATES

CHAPTER 3
IMPACT LOCALIZATION ON METALLIC PLATES

In this chapter, an experiment for localization impact points on metallic plate was implemented. In this experiment, we use the triangulation algorithm (existed method) and imaging method (developed method) in conjunction with sensing paths signals to localize the impact points. In the triangulation algorithm the group velocities of propagated waves are assumed to be unknown. The effect of increasing the number of used sensors on the accuracy of calculated location of impact points are investigated. In imaging method, the group velocities of propagated waves are assumed to be known. The idea of this method is to identify the intersection point of hyperbolae paths. This intersection point represents the impact source point. The image technique is used to find the individual images for every sensing path. After fusion all the images from different sensing paths using summation and or multiplication algorithms (finding the total field value for every pixel point), the pixel with highest field value represents the impact source point. Three sensors at least are needed in this imaging method to localize the impact point.

3.1 INTRODUCTION

The structural health monitoring (SHM) is a process implemented in the inspected structure to identify and assist the damage [47]. In recent years, the SHM systems of aerospace vehicles are developed to investigate and localize any impact events on their structures. These events caused a visible or invisible damage [32]. The acoustic emission (AE) waves, due to stress waves, are acquired by acoustic emission sensors which are fixed

at different locations on the surface of the strcuture. Based on these received signals the acoustic emission technique is used to localize the source of AE waves [29]. The AE caused by the growth of the fatigue crack is studied extensively using the physics-based approach [48]. The most common techniques are explained for localization acoustic emission sources in plates. Some of these techniques are used only for isotropic materials, like the triangulation technique, and some of these have been used for both isotropic and anisotropic materials. Also, the advantages and disadvantages of described methods are discussed [38]. The source of AE is localized in two-dimension plate by determining the difference in arrival time for an array of three sensors fixed on the interested structure [49]. For in situ SHM, a new system is used to localize the acoustic emission (AE) sources in an anisotropic structure by using six piezoelectric sensors and Continuous Wavelet Transform (CWT) to determine the time of flight (TOF) for every received signal. The impact location is determined by solving a set of nonlinear equations [31].

In recent years, many techniques have been developed for visualizing structural damage events in conjunction with a network of sensors distributed across the interested structure area. The simple idea of these methods is to present quantification results of damage identification regarding the probability of the existence of the defect. This probability-based image is implemented by fusion all the individual images of actuator-sensor paths [1]. In brief, the probability-based imaging techniques are based on finding the field values for every pixel from the signals of actuator-sensor or sensor-sensor paths. The hyperbola path which represents the locus of the damage or the acoustic emission source can be obtained by determining the difference in time of flight (TOF) of two scattered signals of two actuator-sensors paths or two signals received by two sensors.

In this work, an impact experiment on metallic plate was implemented to localize the impact points using triangulation method and developed visual method. Based on the determining of the time of flight, two methods are examined comparatively. The effect of increasing the number of sensors on the percentage errors of calculated results are studied.

3.2 EXPERIMENTAL SETUP

The following experiment was implemented to predict the location of impact points by small ball at different points on the plate. In this experiment, an aluminum plate has dimensions 914 mm in length, 503 mm in width and 1mm in thickness. This specimen was instrumented with a network of nine PWAS transducers as shown in the Figure 3.1. A small steel ball (0.33 g) is dropped from a height of 50 mm through a small plastic pipe on the plate at different locations. The impact signals are received by PWAS transducers and recorded by three Oscilloscopes. The sensors locations are listed in Table 3.1. Three impact points are investigated in this experiment with known their locations which are listed in the Table 3.2. In this work, two different methods were used to predict the location of impact points. The first method is the triangulation algorithm which is based on solving a set of nonlinear equations to find the coordinates of an impact point. The second method is the visual method.

Table 3.1: Sensors coordinates.

Sensors	S #1	S #2	S #3	S #4	S #5	S #6	S #7	S #8	S #9
x (mm)	100	100	100	450	450	450	800	800	800
y (mm)	100	250	400	100	250	400	100	250	400

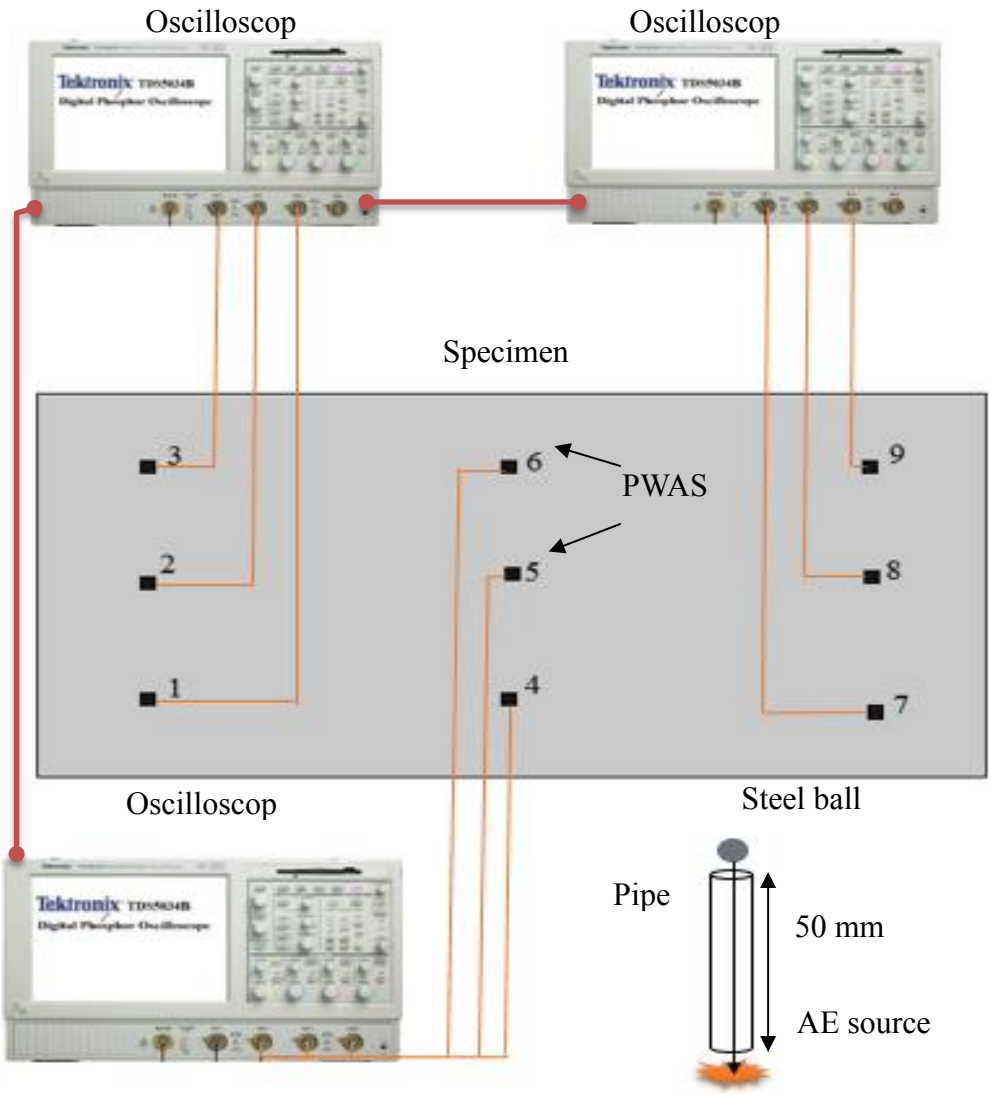

Figure 3.1: The configuration of impact experiment.

Table 3.2: Impact points coordinates.

Impact point	Point #1	Point #2	Point #3
X(mm)	275	600	700
Y(mm)	287.5	300	150

This new method is based on using imaging method to map hyperbole paths for every pair of two sensors. The intersection point of these hyperbolae paths represents the impact source point.

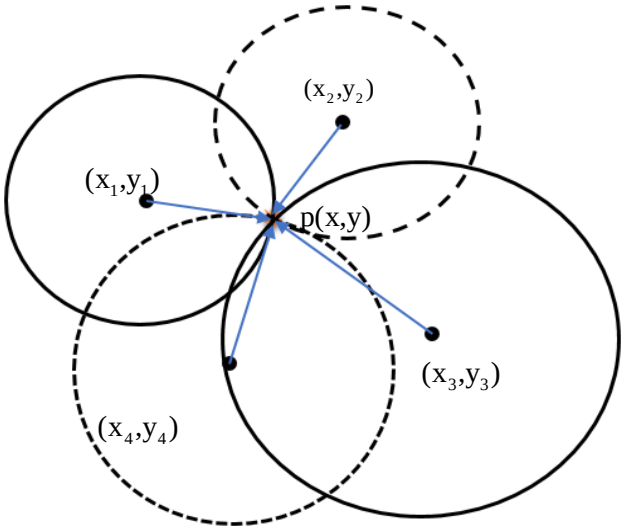

Figure 3.2: Triangulation algorithm with four sensors is used to localize an impact point.

3.3 TRIANGULATION ALGORITHM

The triangulation technique is used to localize the impact source point on isotropic plate. The surface coordinates of the impact source point can be determined using the circular equation [4], i.e.

$$\begin{aligned} &\left(x_i - x\right)^2 + \left(y_i - y\right)^2 = \left[c\left(t_i + t_0\right)\right]^2 \\ &i = 1, 2, \ldots, N \end{aligned} \tag{3.1}$$

If the wave speed, c is unknown (unknown material properties), the above equation represents a set of four nonlinear equations with four unknowns, x, y, c, t_0. The unknown variables are the impact point coordinates (x, y), the wave speed, c, and the trigger delay t_0. The known terms are the sensor's coordinates, (x_i, y_i) and the time of flight (TOF) of

the received signals t_i . Figure 3.2 shows the triangulation technique with four sensors to indicate the coordinates of impact point. Based on the Eq.(3.1), four PWAS sensors at least are used to detect the location of impact point. To study the effect of increasing the number of PWAS transducers on the percentage errors of the calculated impact points coordinates, six networks with a different number of PWAS transducers were investigated.

3.3.1 NETWORKS OF PWAS TRANSDUCERS

In this experiment, nine PWAS transducers are distributed across the interested area. Six networks are obtained from these sensors to localize the impact points. The first system (network 1) contains four PWAS transducers. The second system (network 2) is created by adding the fifth PWAS transducer to the first system as shown in the Figure 3.3. The same procedure is used to obtain the rest of networks:

1. Network 1 (4 PWASs: #1, #3, #5, #7)
2. Network 2 (5 PWASs: #1, #3, #5, #7, #2)
3. Network 3 (6 PWASs: #1, #3, #5, #7, #2, #6)
4. Network 4 (7 PWASs: #1, #3, #5, #7, #2, #6, #4)
5. Network 5 (8 PWASs: #1, #3, #5, #7, #2, #6, #4, #8)
6. Network 6 (9 PWASs: #1, #3, #5, #7, #2, #6, #4, #8, #9)

3.3.2 TIME OF FLIGHT (TOF) OF AN IMPACT SIGNAL

Two possible options exist for determining the TOF value of an impact signal:

(a) TOF = starting point of the signal (method 1)

(b) TOF = location of the maximum signal value (method 2)

The Continuous Wavelet Transform (CWT) of the signal is calculated with AGU-Vallen Wavelet, a freeware software program [50]. It has a Gabor function as the "mother" wavelet.

The CWT plot is very helpful to determine the time of flight (TOF). Also, it is explaining the features (TOF, frequency, and amplitude) of signals. In this work, the TOF by method 1 is determined at frequency 58 kHz and by method 2 is determined at frequency 22 kHz. Figure 3.4 shows the waveform and the CWT plot of the signal of impact point#1 received by PWAS #1.

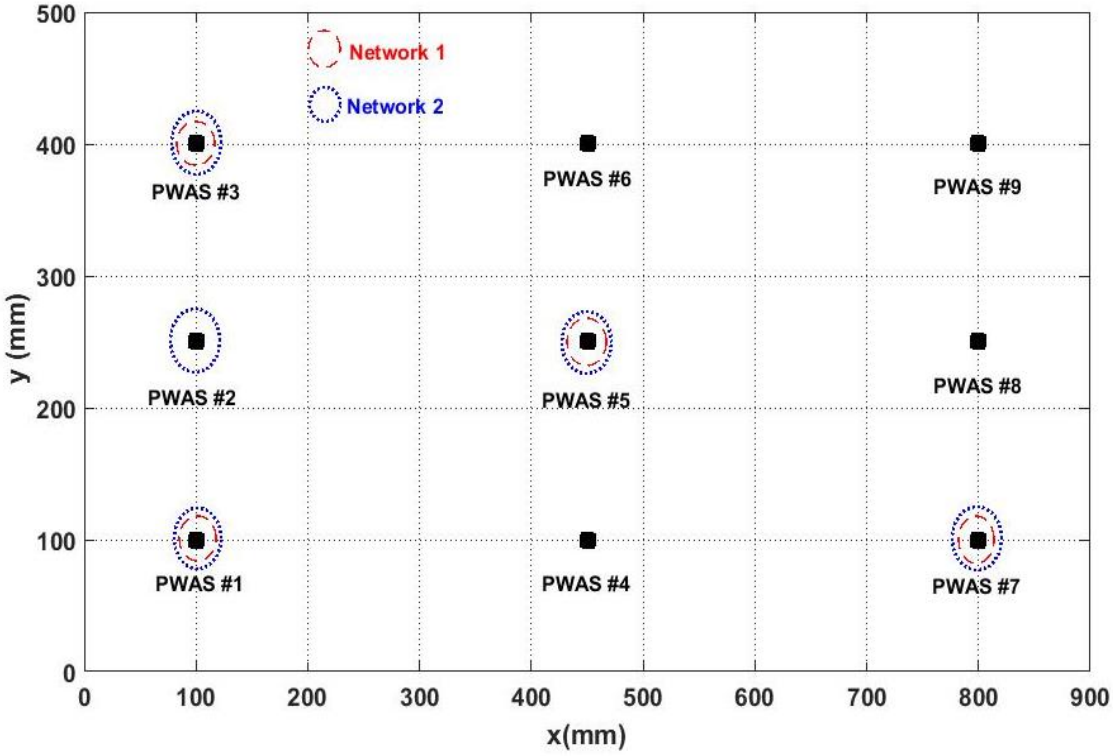

Figure 3.3: Identifying the network 1 and network 2.

3.3.3 FLOWCHART ALGORITHM

The idea of this part of work is to predict the impact source point by using the method 1 and method 2 of determining the time of flight (TOF). For every method, six networks were used separately to determine the coordinates of impact points. Figure 3.5 shows the flowchart of using triangulation algorithm, methods of calculated time of flight and the sensors network for localization the impact points.

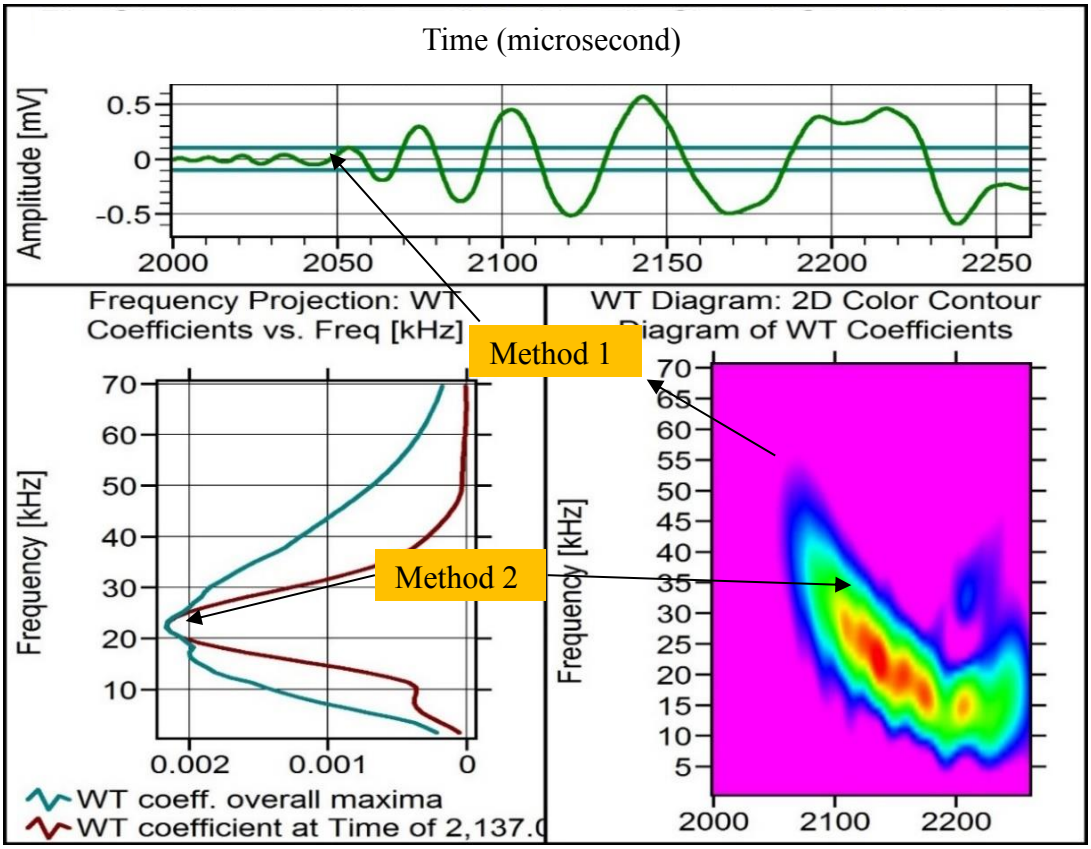

Figure 3.4: The time domain and wavelet transform of an impact signal to determine the time of flight (TOF).

3.3.4 Results and Discussion of Triangulation Algorithm

Three impact points point#1 (275, 287.5), point#2 (600, 300) and point#3 (700, 150)) are detected experimentally using nine PWAS transducers and triangulation algorithms. Figure 3.6a, b shows the waveform signals of impact point #1 and #3, respectively, received by nine PWAS transducers. From the first figure, we can guess that the impact point#1 is closed to the position of PWAS transducers #2, #3, #5 and #6 because their signals have higher amplitudes (higher energy) than other signals. The analysis window is used to calculate continues wavelet transform (CWT) for the incident wave part of the signals and to indicate the TOF of these signals using method 1 and method 2. The

wavelet transform is determined for six signals of the impact point #1 are shown in Figure 3.7.

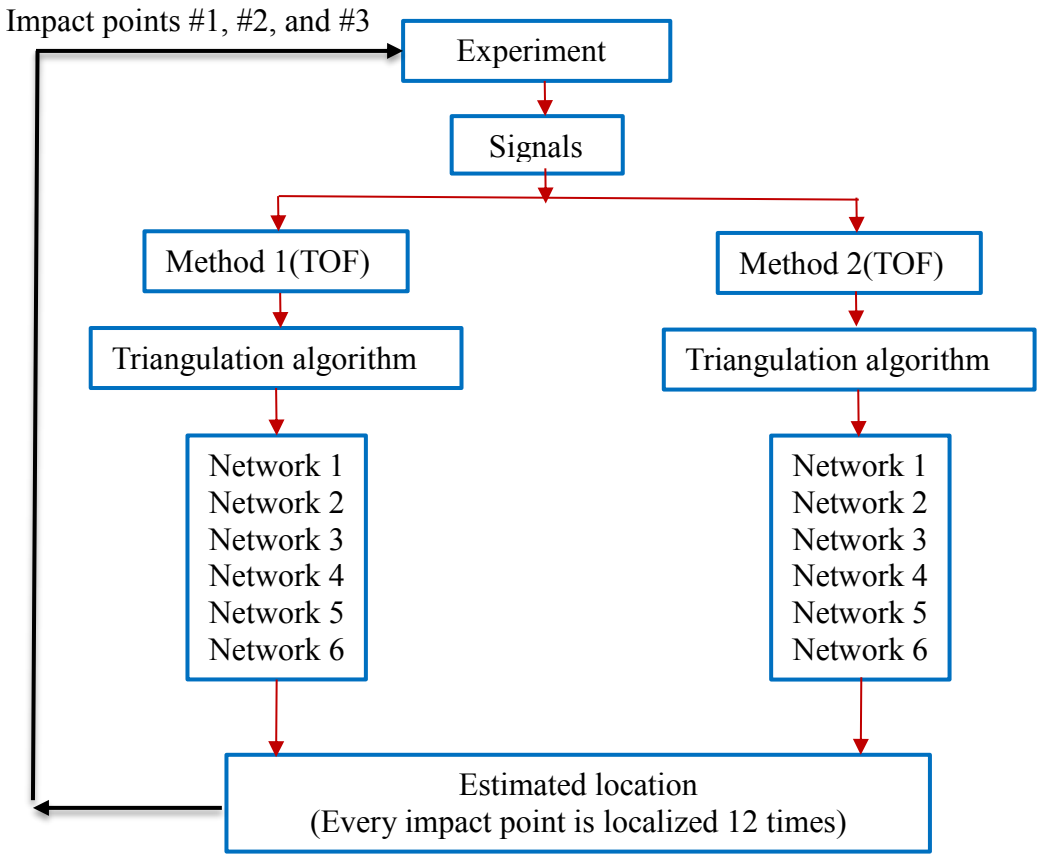

Figure 3.5: The flowchart of localization impact points using triangulation algorithm.

A MATLAB code was implemented to solve Eq.(3.1) and find the unknowns (x, y, c, t_0) . The expression of the objective function is expressed as

$$fcns = \sum_{i=1}^{N} \left((x_i(i) - x)^2 + (y_i(i) - y)^2 - (c.(t_i(i) + t_0))^2 \right)$$
$$N = 4, \ldots, 9 \qquad (3.2)$$

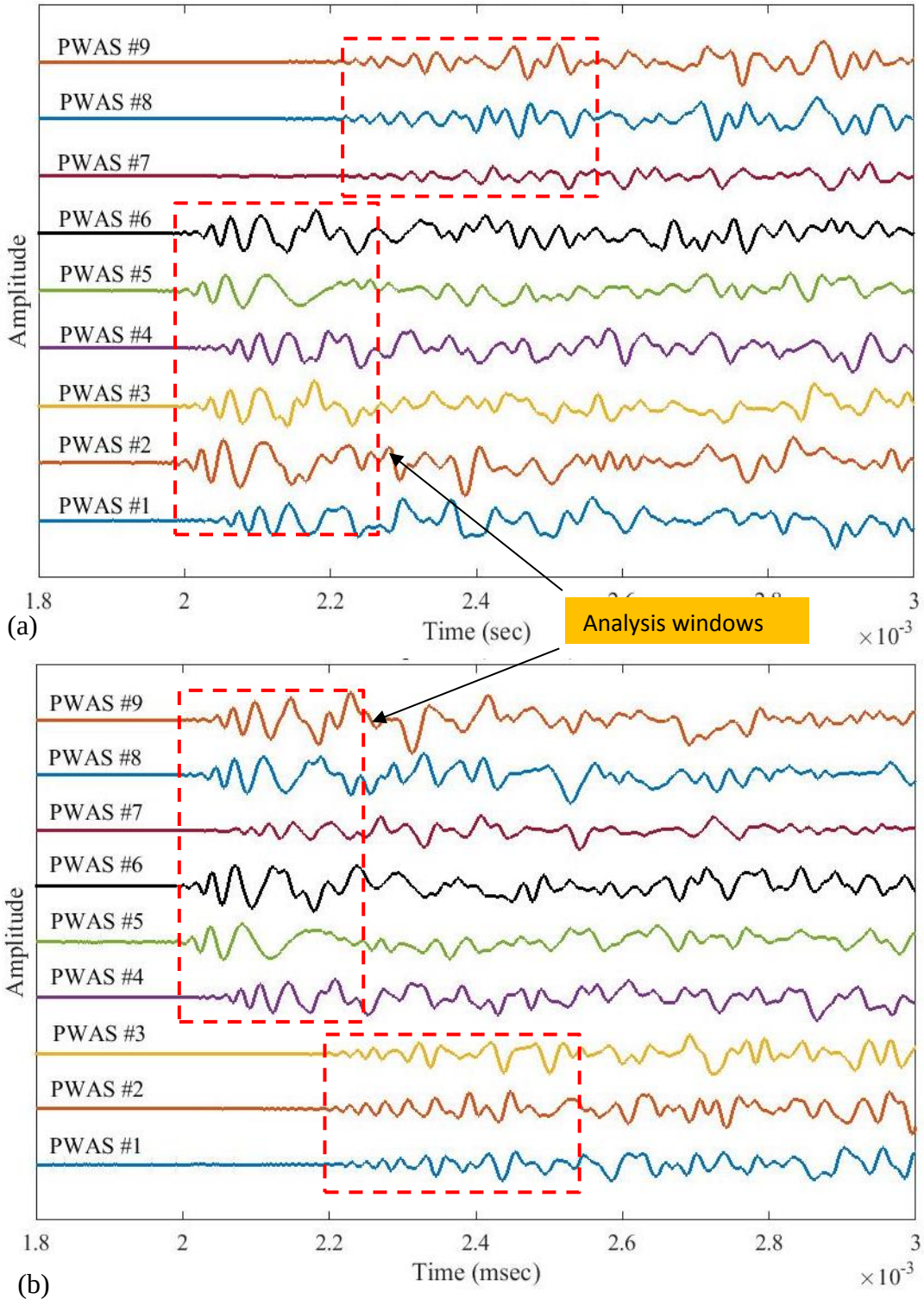

Figure 3.6: Time domain of signals received by 9 PWAS transducers for impact points; (a) point#1; (b) point#3.

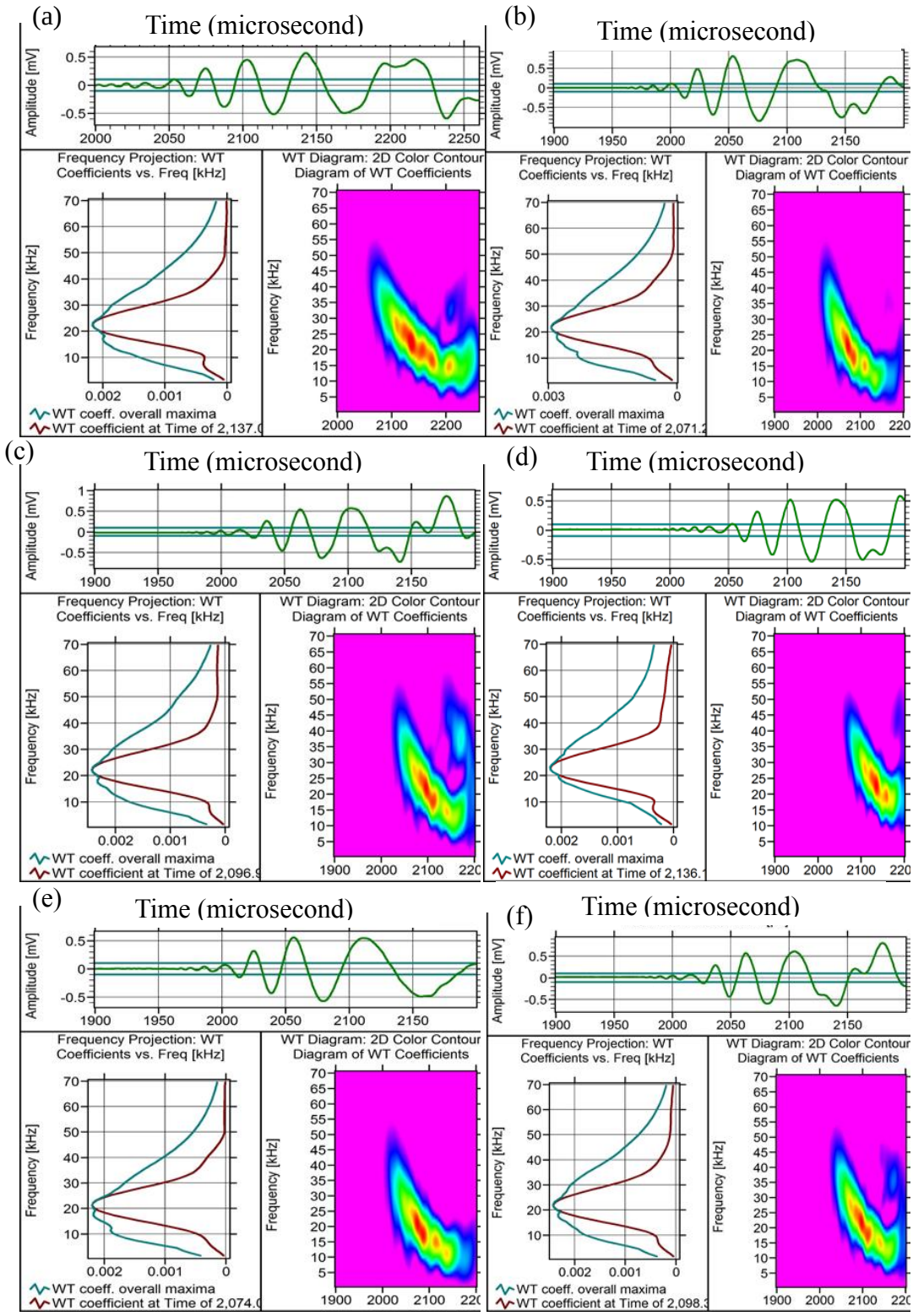

Figure 3.7: Wavelet transform of signals of impact point#1 received by sensors: (a) PWAS #1; (b) PWAS #2; (c) PWAS #3; (d) PWAS #4; (e) PWAS #5; (f) PWAS #6.

The location errors (δ) of calculated impact points are determined by using the following equation [7]

$$\delta = \sqrt{\left((x_{real} - x_{calculated})^2 + (y_{real} - y_{calculated})^2\right)} \tag{3.3}$$

where, (x_{real}, y_{real}) is the real impact location and $(x_{calculated}, y_{calculated})$ is the calculated impact location of the same point. The percentage error of the calculated location is determined using the following equation

$$error\% = \frac{\delta}{d} \tag{3.4}$$

Where, *d* is the mean value of diagonal distances A and B of the quadrilateral which has PWAS transducers #1, #3, #7 and #9 on its corners. With Eq.(3.4), the percentage error becomes independent with the location of the reference point.

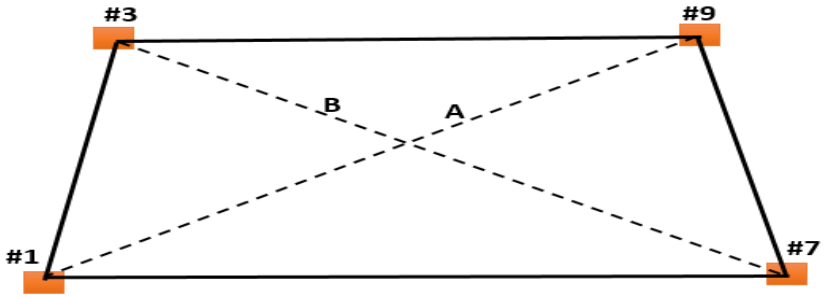

Figure 3.8: Determination of the mean value *d*.

Based on the two methods of determining the TOF of impact signals, the calculated location for every impact point is determined two times and based on the six networks, the estimated location for every impact point is determined six times. So, every impact point is localized twelve times. Table 3.3 and Table3.4 show the results of calculated coordinates Table3.4of impact point#1 using six networks for method 1 and method 2, respectively. The results of the current work are presented in the Figure 3.9. This plot shows the

percentage errors as a function of the number of PWAS transducers using the method 1 and method 2 for three impact points.

Table 3.3: Results of the impact point #1 using method 1 (unit: millimeter).

Networks	(x_{real}, y_{real})	$(x_{calculated}, y_{calculated})$	Location error (δ)	Error %
Network#1	(275,287.5)	(273.8, 285)	2.7	0.35%
Network#2		(275.6, 285.1)	2.4	0.31%
Network#3		(276, 286)	1.9	0.25%
Network#4		(275.8, 286.6)	1.2	0.15%
Network#5		(275.9, 287.1)	1	0.13%
Network#6		(275.9, 287.5)	0.7	0.09%

Table3.4: Results of the impact point #1 using method 2 (unit: millimeter).

Networks	(x_{real}, y_{real})	$(x_{calculated}, y_{calculated})$	Location error (δ)	Error %
Network#1	(275,287.5)	(273.5, 283.7)	4	0.52%
Network#2		(273.9, 283.8)	3.9	0.51%
Network#3		(275.2, 285.5)	2	0.26%
Network#4		(274.8, 286.2)	1.3	0.17%
Network#5		(274.8, 286.4)	1.1	0.14%
Network#6		(274.8, 286.8)	0.7	0.09%

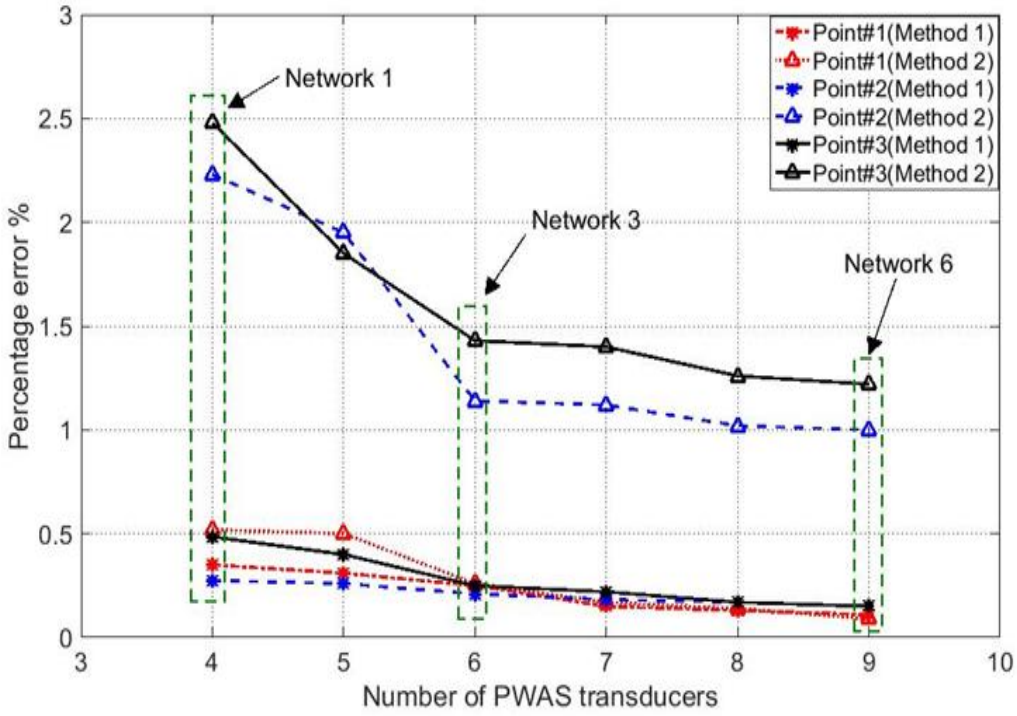

Figure 3.9: Percentage errors of calculated impact points as a function of the number of used PWAS transducers.

The Network 6 has fewer percentage errors (best result) than other networks. The method 1 has fewer percentage errors than method 2. The source location results for three impact points on the whole plate are shown in the Figure 3.10 with the zoom in local areas of the impact points: point#1 and point#3.

3.4 IMAGING METHOD

The imaging algorithms are sufficiently used to localize the defects in a structure like plate using guided waves. In recent years, many works have been implemented for damage localization using spares array of sensors, guided waves and imaging process. There are different shapes of orbits or loci which define the position of defects or an acoustic emission sources. The circular, elliptical and hyperbolic orbits can be created for

a pair of actuator-sensor or sensor-sensor based on Lamb wave signals captured by these sensors. In this work, the hyperbolae paths and imaging process are used to indicate the impact source point. The idea of this method is to use the synthetic signals and synthetic time reversal approach for enabling the hyperbolic paths between pairs of two sensors. The intersection point of these hyperbolic paths gives the location of impact source point.

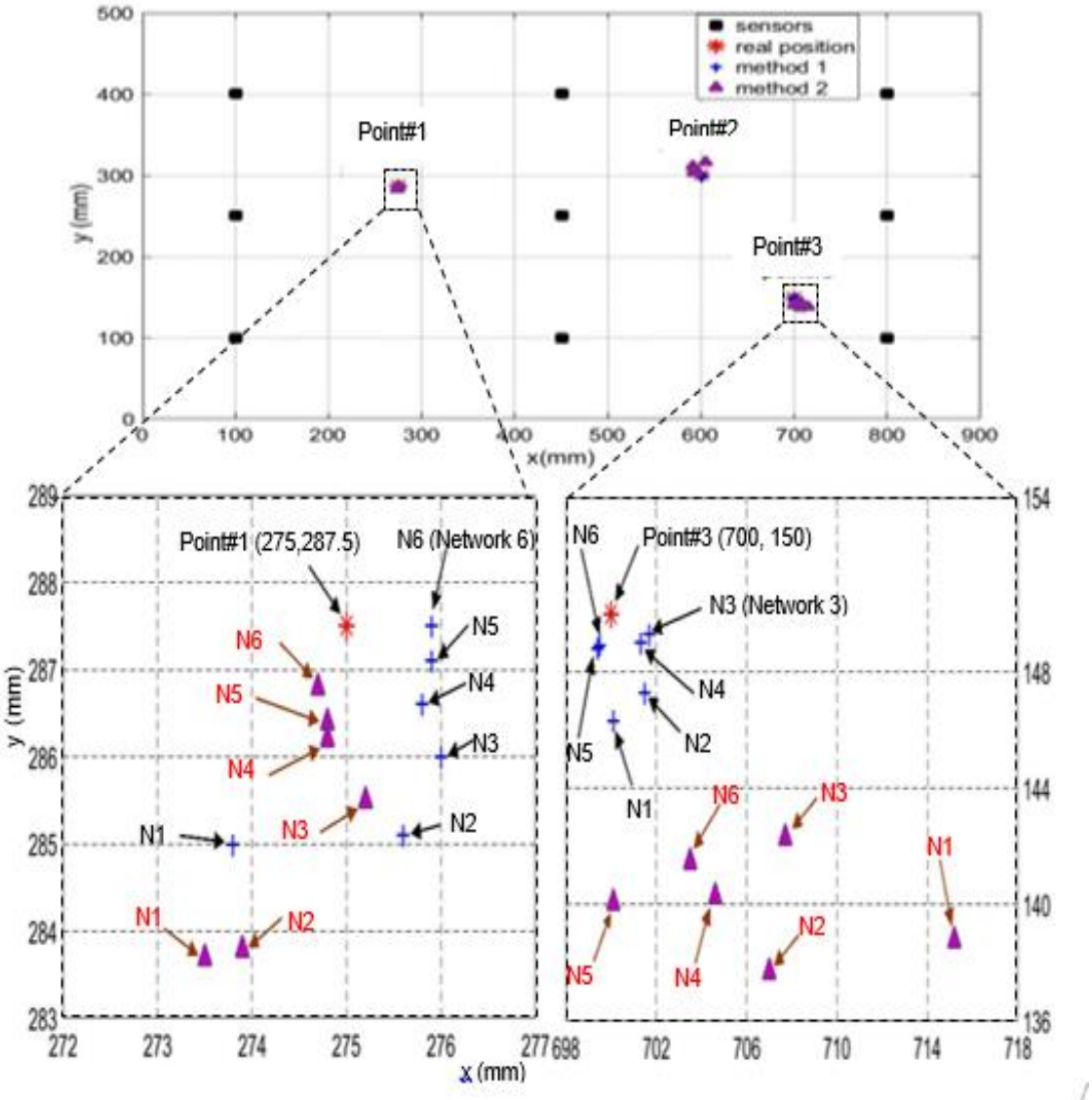

Figure 3.10: Calculated impact points on the whole plate with zoom in around the local area of point#1 and point#3.

3.4.1 HYPERBOLIC PATH

The hyperbolic path can be defined between two sensors. This path has two arms. The location of a defect or an acoustic emission source point is always on arm which is closed to the sensor which receives the signal early [1]. To define the hyperbola path between two sensors, which is shown in Figure 3.11, we need to determine the difference in time of flight (TOF) between the pair of sensors (PWAS#1 and PWAS#2)

$$\Delta t_{12} = t_{D-S1} - t_{D-S2} \tag{3.5}$$

$$\Delta t_{12} = \frac{L_{D-S1}}{v_1} - \frac{L_{D-S2}}{v_2} \tag{3.6}$$

Where L_{D-S1} and L_{D-S2} are the distances among the sensors $S1$, $S2$ and the impact source point D as shown in Figure 3.11. v_1, v_2 are the group velocities of propagated waves which received by sensors $S1$ and $S2$. For isotropic material the group velocities are equal in all directions. So, the Eq.(3.6) can also be simplified as

$$\Delta t_{12} = (\sqrt{\left((x_D - x_{S1})^2 + (\mathrm{y}_D - y_{S1})^2\right)} - \sqrt{\left((x_D - x_{S2})^2 + (\mathrm{y}_D - y_{S2})^2\right)}) / v \tag{3.7}$$

So for creating individual hyperbola path, the Eq. (3.7) is used to define hyperbolic path between sensors $S1$ and $S2$. The hyperbolic path has two arms with two foci (the position of sensors one and two) as shown in Figure 3.11b. The damage is always located on the arm which is closed to the sensor who received the signal early. The other arm is undesirable. The undesirable arm can be canceled as shown in Figure 3.11c.

3.4.2 IMAGING CONCEPT

The idea of using imaging methods for finding the location of defects or acoustic emission source points is to define the defect orbits (paths).

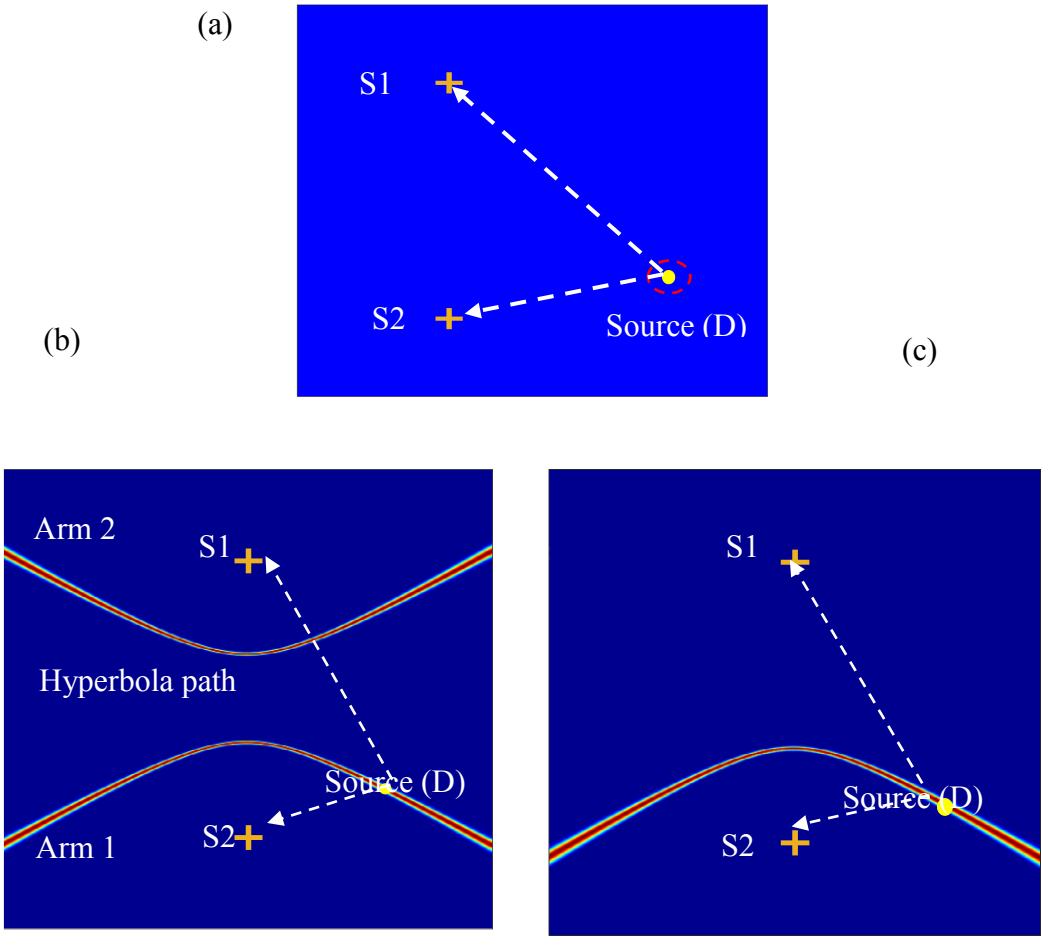

Figure 3.11: Hyperbolic orbit; (a) two sensors and signal source; (b) hyperbolic orbit with two arms; (c) hyperbolic orbit with one arm.

The intersection points of some orbits (paths) represent the defect location or the acoustic emission source point. The defect orbit can be defined as an elliptic, a circular, a hyperbolic or a straight-line path. To localize the defect on the interested area, it is divided into pixels. The pixel function is responsible about mapping the damage orbits (straight line, circular, etc.) on the image. A pair of two sensors can establish the hyperbola path. The intersection points of two paths (three sensors) is defined as a defect or acoustic emission source point as shown in Figure 3.12. For more clarifying the image concept, the second arms of hyperbolae paths are not being showed as showing in Figure 3.11c.

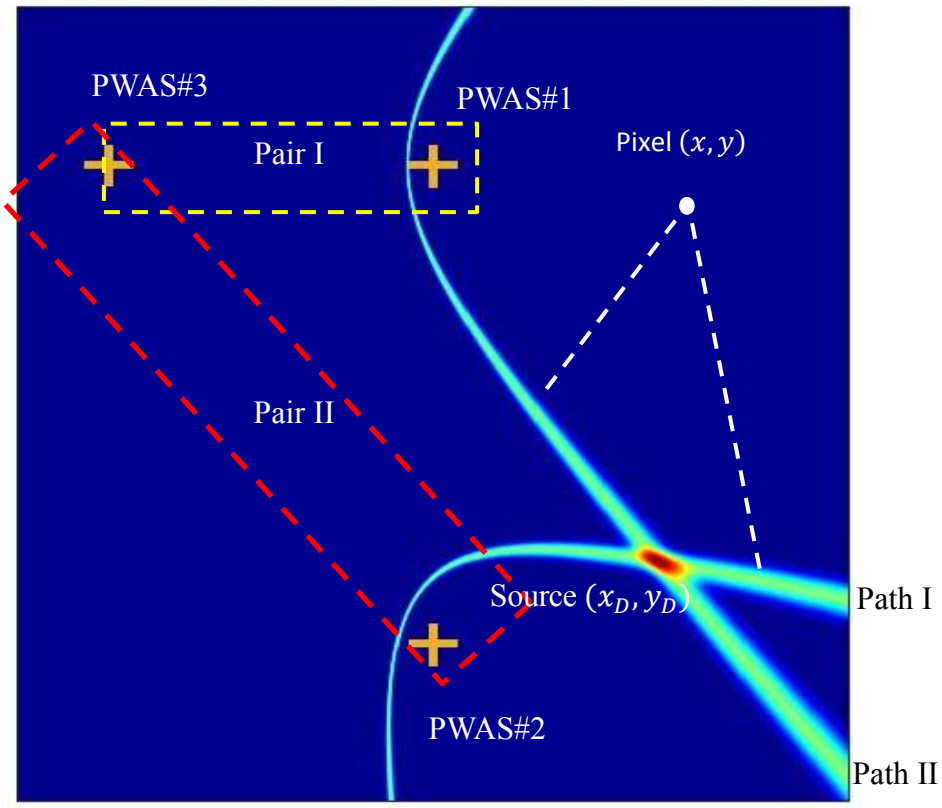

Figure 3.12: Imaging concept for localization an impact point.

So, every pair of sensors has a hyperbola pixel function as

$$f_I = sn_1(\Delta t_{31}(x, y)) \tag{3.8}$$

$$f_{II} = sn_2(\Delta t_{32}(x, y)) \tag{3.9}$$

where, f_I, f_{II} are the pixel functions for path I and path II respectively, sn_1, sn_2 are synthetic signals for enabling paths I and II. $\Delta t_{31}(x, y)$, $\Delta t_{32}(x, y)$ are the hyperbolae equations of path I (pair I) and path II (pair II) as

$$\Delta t_{31} = (\sqrt{\left((x_D - x_{S3})^2 + (y_D - y_{S3})^2\right)} - \sqrt{\left((x_D - x_{S1})^2 + (y_D - y_{S1})^2\right)}) / v_g \tag{3.10}$$

$$\Delta t_{32} = (\sqrt{\left((x_D - x_{S3})^2 + (y_D - y_{S3})^2\right)} - \sqrt{\left((x_D - x_{S2})^2 + (y_D - y_{S2})^2\right)}) / v_g \tag{3.11}$$

where, $x_{S1}, y_{S1}, x_{S2}, y_{S2}, x_{S3}, y_{S4}$ are the coordinates of sensors $S1, S2, S3$ respectively. Figure 3.12 shows the imaging concept. The values of pixel functions f_I, f_{II} are determined as follow

$$f_I = \begin{cases} 1 \;\; if\,(x, \mathrm{y}) \in \mathrm{pathI} \\ 0 \;\; else \end{cases}$$
$$f_{II} = \begin{cases} 1 \;\; if\,(x, \mathrm{y}) \in \mathrm{pathII} \\ 0 \;\; else \end{cases} \tag{3.12}$$

The source point is located at the intersection of path I and path II. To calculate this intersection, we can combine f_I, f_{II} either by summation or multiplication to calculate the field value of every pixels of interested area, i.e,

$$P_{sum}(x, y) = f_I(x, y) + f_{II}(\mathrm{x}, \mathrm{y}) = \begin{cases} 2 \;\; if\,(x, y) = (x_D, y_D) \\ 1 \;\; if\,(x, y) \in pathIorpathII \\ 0 \;\; else \end{cases} \tag{3.13}$$

$$P_{mult}(x, y) = f_I(x, y).f_{II}(\mathrm{x}, \mathrm{y}) = \begin{cases} 1 \;\; if\,(x, y) = (x_D, \mathrm{y}_D) \\ 0 \;\; else \end{cases} \tag{3.14}$$

where $P_{sum}(x, y)$, $P_{mult}(x, y)$ are the total field value of a pixel point (x, y) using summation or multiplication process.

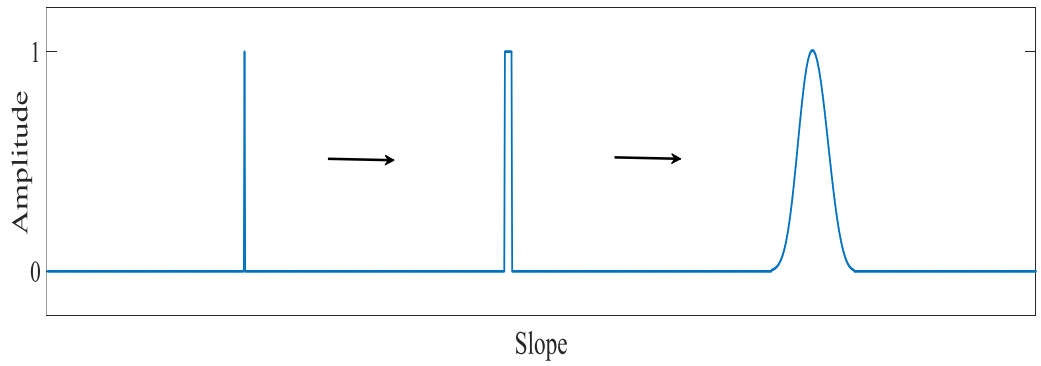

Figure 3.13: Different windows of synthetic signal.

Because the experimental data has noise, the $0,1$ images are not perfect. Hence, we need to reduce the effect of noise by using a smearing method of defusing the pixel function with a smoothing window as shown in Figure 3.13. These synthetic signals have maximum amplitude value at the magnitude of difference in time of flight between two sensors.

We can use also a data fusion concept by adding information from more than two paths, say a total of N paths to write,

$$P_{sum}(x,y) = \sum_{i=1}^{N} f_i(x,y)$$
$$P_{mult}(x,y) = \prod_{i=1}^{N} f_i(x,y) \tag{3.15}$$

3.4.3 Results of Imaging Method

The same impact points are localized using imaging method. The time of flight (TOF) of signals received by the nine sensors due to impact at point #1 are determined at the maximum signals amplitude. Figure 3.14 shows the time projection of wavelet transform coefficients of these signals at frequency 22 kHz. Table 3.5 shows the time of flight values of signals received by nine sensors due to impact at point #1. The difference in time of flight are determined for some pairs of sensors as shown in Table 3.6. Based on these values, synthetic signals are created as shown in Figure 3.15 which have maximum amplitude value at the certain value of difference in time flight. The synthetic signals are created with a Gaussian distribution function

$$f(x) = \frac{1}{\sqrt{2\pi}\sigma} e^{-\frac{(x-\mu)^2}{2\sigma^2}} \tag{3.16}$$

where σ is the standard deviation width and μ is the mean value. These synthetic signals are used for determining the pixels field values of interested images of various sensing

paths. Figure 3.16 shows various images of localization the impact point #1 (275, 287.5). In first image, two hyperbolae paths (every path has one arm) for three sensors intersect to localize the source point #1. The image shows a good indication for impact point #1 even it outside the sensors network. In second image, three paths (one arm for every path) for three sensors intersect at the source point #1 which is inside the sensors network. The zoom in image shows a good result. In third and fourth images, nine sensors are used. The difference between these images is the number of paths arms. The third image has eight paths with sixteen arms. However, the fourth image has eight paths with eight arms. Both images come up with the same accurate results.

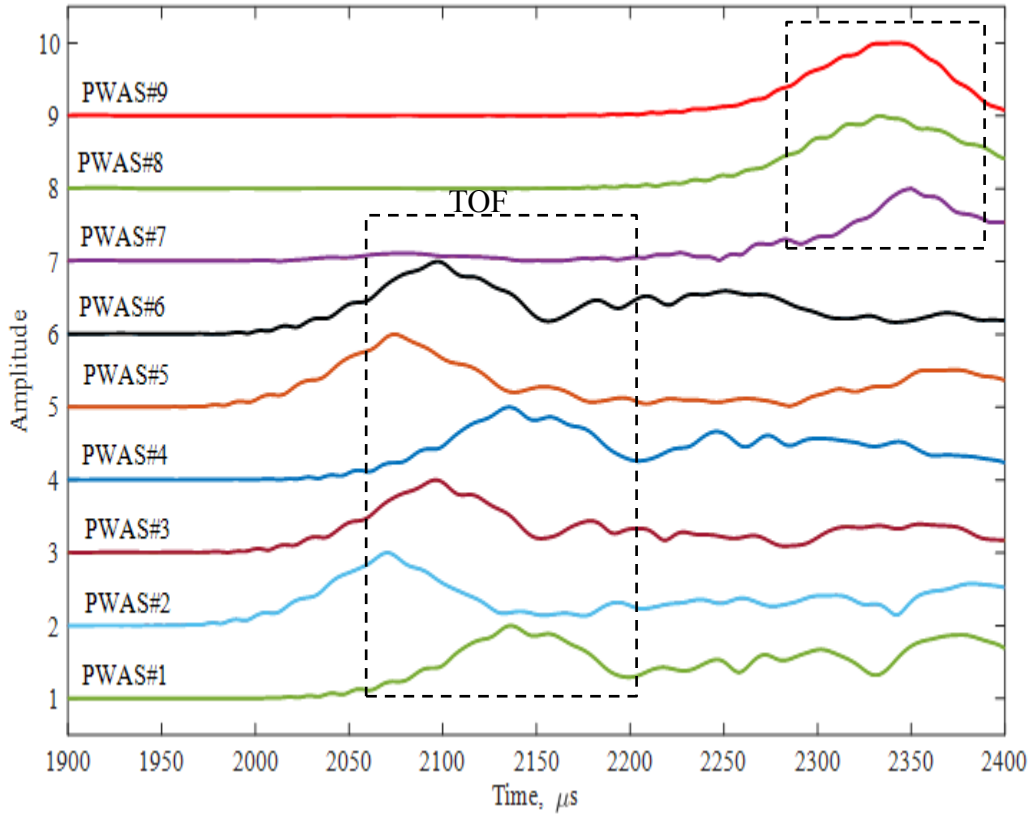

Figure 3.14: Time projections of wavelet transform at frequency 22 kHz for signals of impact point #1.

Table 3.5: TOF of signals due to impact point #1.

PWAS No.	$S1$	$S2$	$S3$	$S4$	$S5$	$S6$	$S7$	$S8$	$S9$
TOF (µs)	2137	2071	2097	2136	2074	2098	2350	2333	2340

Table 3.6: Difference in TOF of signals received by nine sensors (impact point #1).

Time difference	Δt_{12}	Δt_{13}	Δt_{14}	Δt_{15}	Δt_{16}	Δt_{71}	Δt_{81}	Δt_{91}
Value (µs)	66	40	1	63	39	213	196	203

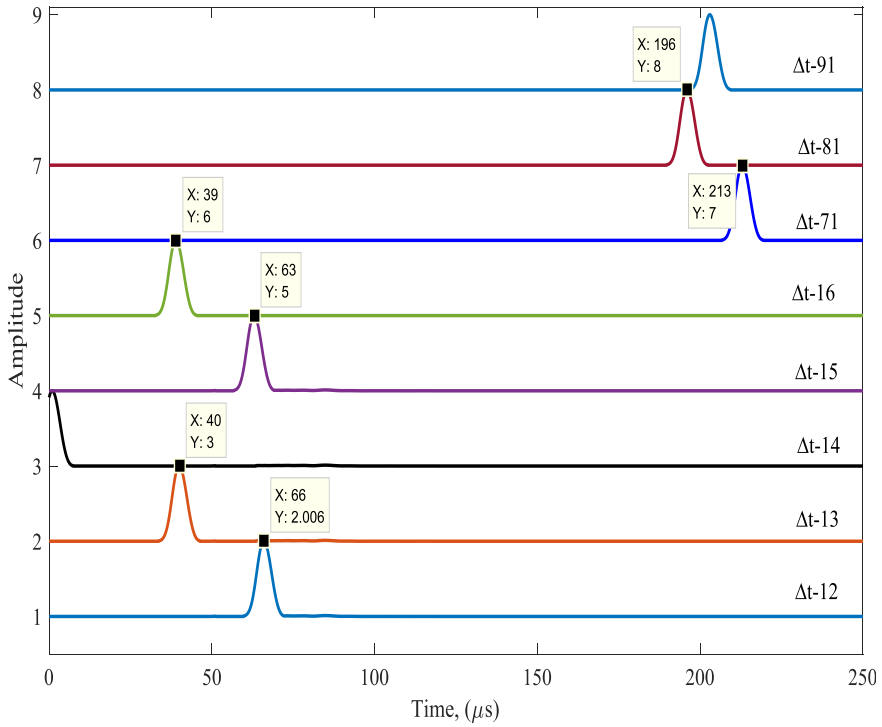

Figure 3.15: Synthetic signals have maximum amplitude at difference in TOF values.

The images of localization the impact point #2 are shown in Figure 3.17. In the first image, the impact point is outside the network of sex sensors *(S1, S2, S3, S4, S5, S6*). From these sensors, five paths with five arms are created to indicate the source point #2.

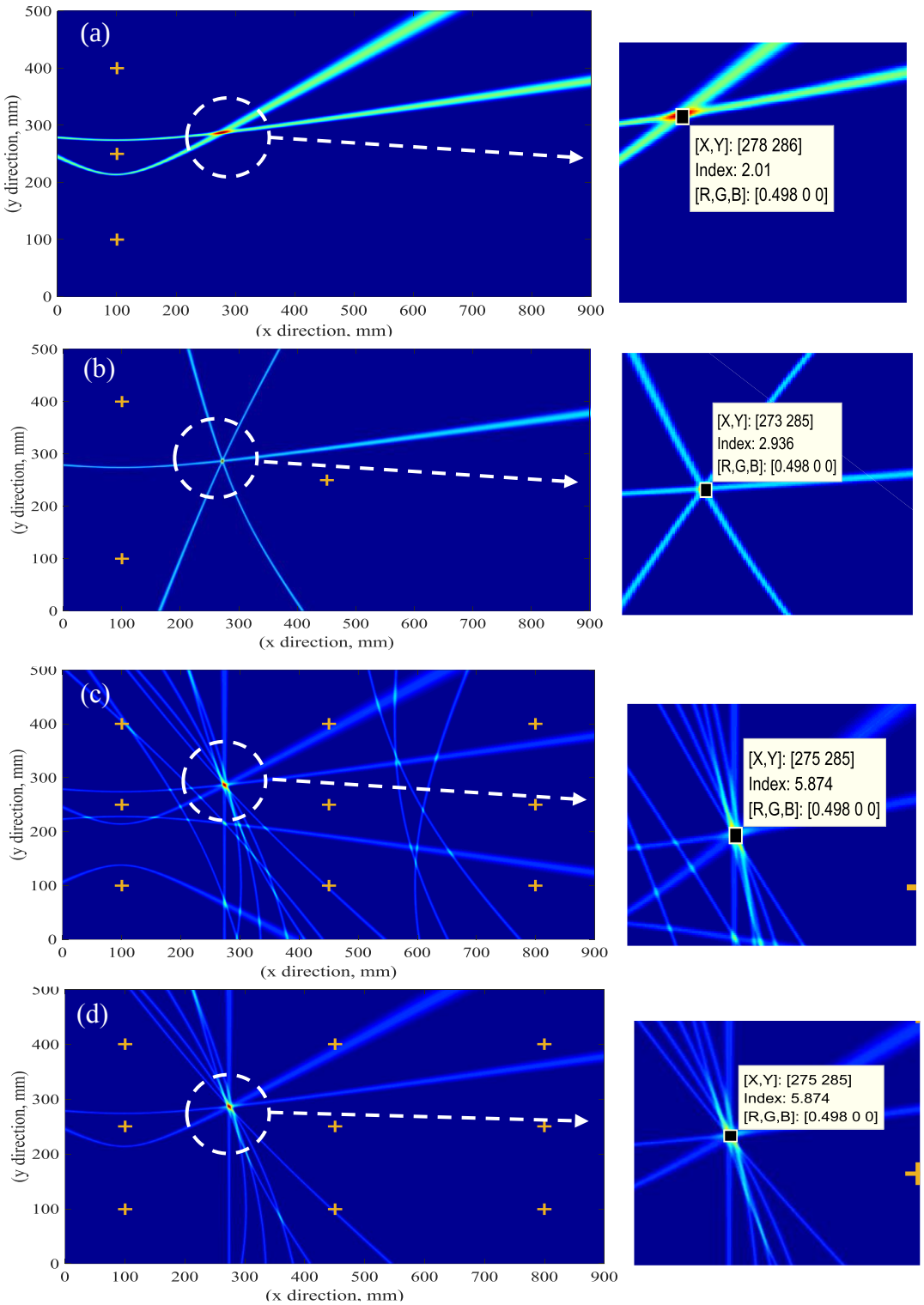

Figure 3.16: Imaging results of localization impact point #1(275, 287.5) mm using different number of used sensors: (a) 3sensors (2 paths); (b) 3sensors (3paths); (c) 9 sensors (8 paths-16 arms); (d) 9 sensors (8 paths-8 arms).

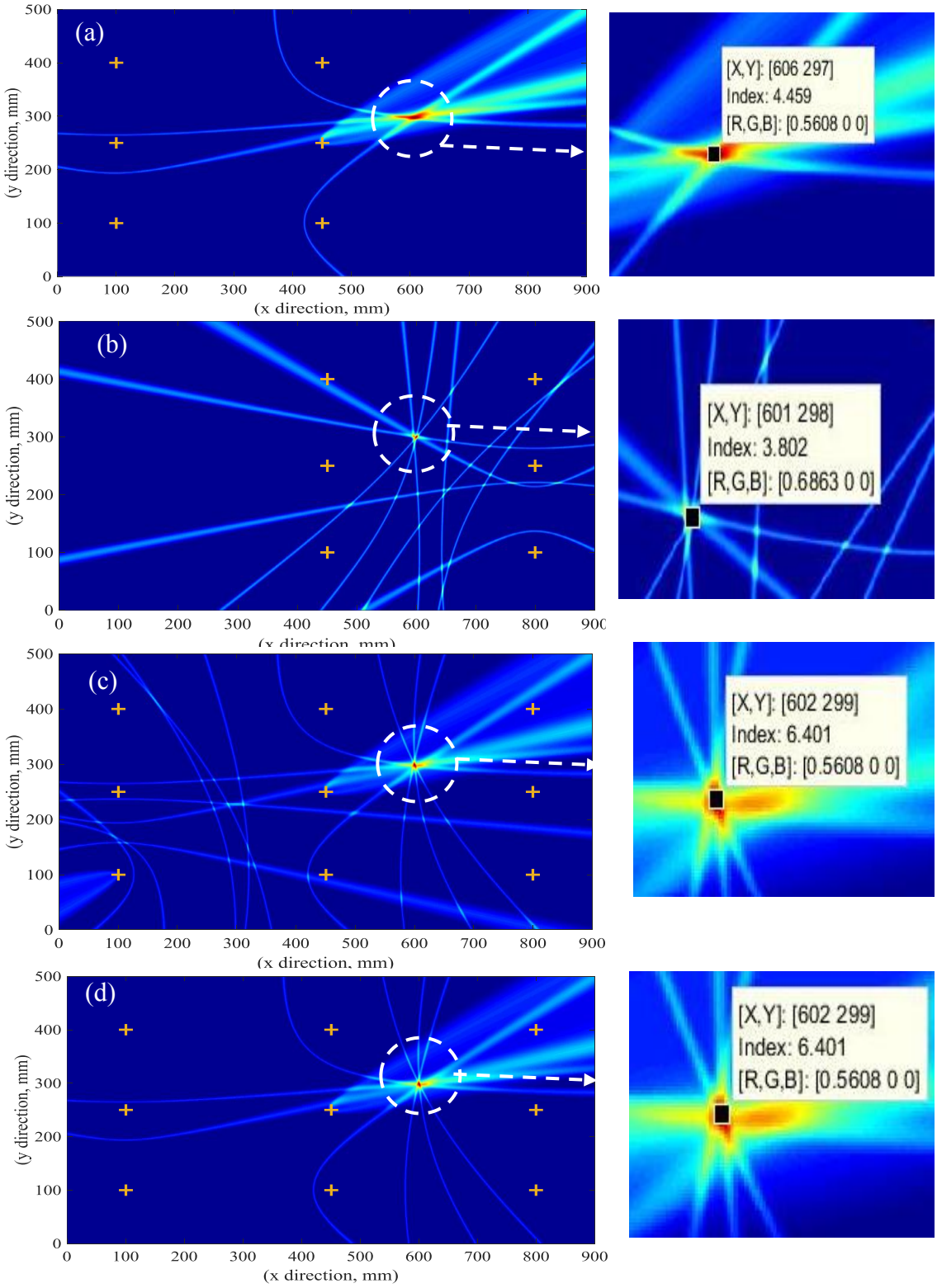

Figure 3.17: Imaging results of localization the impact point #2 (600, 300) mm using different number of sensors: (a) 4 sensors; (b) 5 sensors; (c) 9 sensors (7 paths-14 arms); (d) 9 sensors (7 paths-7 arms).

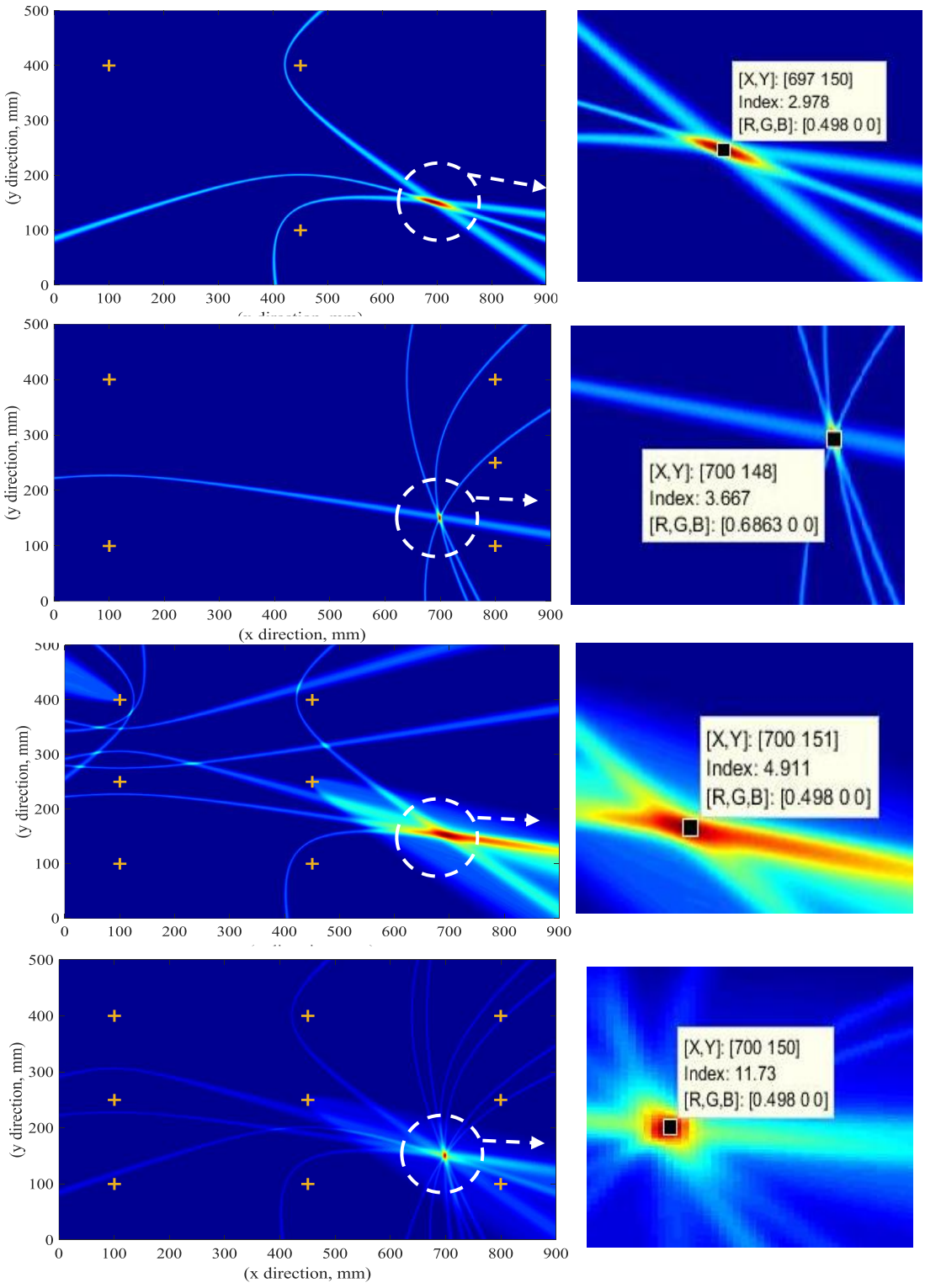

Figure 3.18: Imaging results of localization the impact point #3 (700, 150) mm using different number of sensors: (a) 3 sensors; (b) 5 sensors (4 paths); (c) 5 sensors (5 paths); (d) 9 sensors(12 paths).

In the second image, the source point is inside the network of sensors (S4, S5, S6, S7, S8, S9) which has five paths with ten arms. This image comes up with accurate result and best than the result of first image. For the third and fourth images eight paths with eight and sixteen arms respectively are used to localize the source point. A better results for source localization are got in these images. The images of localization the impact point #3 are shown in Figure 3.18. These images come up with better results.

CHAPTER 4
IMPACT SOURCE LOCALIZATION ON COMPOSITE PLATES

In this chapter, the impact sources on a composite plate are localized experimentally. In this experiment, the impact sources are generated by pencil lead breaks at different locations on a composite plate. Six piezoelectric wafer active sensors (PWAS) are used to acquire the generated pencil lead break signals. These sensors are distributed in two clusters on the plate. The time of flight (TOF) of acquired signals are estimated at the starting points of these signals. The continuous wavelet transforms (CWT) of received signals are calculated with AGU-Vallen wavelet program to get the accurate values of the TOF of these signals. First, we assume unknown material properties (its group velocity profile is unknown). In this case, we used numerical and imaging methods for localization the impact source points. The numerical methods are based on solving two linear equations (Kundu's approach) or solving a set of nonlinear equations (developed triangulation algorithm) to find the impact source point. The imaging methods are based on the Kundu's approach and synthetic signals to find the intersection point of two straight paths which represents an impact source point. Second, we assume known material properties, in this case the hyperbola paths-based image method is used to localize the impact source points. The results of all methods show good indications for the location of impact points.

4.1 INTRODUCTION

The sources of acoustic emission are different from structure to another structure which depend on the function of systems. It can be generated from impact between two

objects, break down a part of system or crack formation such as delamination in composite material [38]. The acoustic emission techniques record and analyze the AE signals to localize their sources. Any system works in serious environment such as the composite structure of airplane should be inspected continuously to make sure it works in healthy situation and highest efficiency. The passive and active modes should be worked sequentially to survive the structure through its design life. For example, the passive system is used to localize the acoustic emission source due to the impact. Then after that the hot spot area is inspected carefully to make sure no damage in this area or to quantify the damage if any significant damage occurred.

The localization of an acoustic emission (AE) source which emitted from the structure damage area is important step for damage quantification [29]. Many methodologies have been achieved to detect and localize the damage on anisotropic materials. These methodologies do not require the knowledge of the direction-dependent velocity profile of propagating wave. The triangulation technique cannot be used to localize the AE source in anisotropic material due to dependent the velocity with the structure layup direction. An alternative method was developed to overcome this problem [51]. They developed a new algorithm for predicting the impact points on a composite plate using modified objective function.

A new linear technique is developed to localize the acoustic source in an anisotropic plate without knowing its direction dependent velocity profile using six sensors which are distributed in two clusters [38]. Most of methods for source localization in anisotropic materials assume straight-line propagation wave across the sensing paths. A new approach was developed to localize the acoustic emission source in a composite plate which has non-

circular wavefront [36]. In this approach, three sensors installed in one cluster to obtain the direction vectors of wavefronts based on difference in time of flight among these three sensors. The results show the accurate prediction of acoustic emission source on an anisotropic plate without knowing its material properties.

Piezoelectric wafer active sensors (PWAS) compared with conventional ultrasonic transducers are small, light-weight, unobtrusive transducers that can be permanently bonded on host structures and could be used both as sensors and actuators [52]. In recent years, different imaging algorithms are performed for damage localization in structures like plates using sparse array of sensors and guided waves. The basic idea of these work is to find the scattered signal from subtraction the measured signal (damaged signal of a pair of transmitter and receiver sensors) from baseline signal (healthy signal of the same sensing paths). The first arrival (scattered echo from a defect) of scattered signal (residual signal) can be used to construct an ellipse path (transmitter and receiver sensors as foci) which represent the defect orbit. The intersection point of three paths from three sensors gives the damage point [10]. The early time packet in scattered signal (residual signal) should be stronger than other packets to construct clear damage image [15].

In this work, impact source signals, which are generated by pencil lead breaks (PLB) on the composite specimen, are localized using numerical methods and imaging methods. In numerical method, the group velocity profile of propagating wave is assumed to be unknown. In imaging methods, we have two cases. The first case, the group velocity profile is assumed to be unknown while it is assumed to be known in the second caseTable 4.1 contains the coordinates of PWAS transducers. In this work five impact points across the plate are investigated.

4.2 EXPERIMENTAL SETUP

The following experiment was implemented to predict the impact sources which were generated by pencil lead breaks at different points on the plate. In this experiment, a 5-Harness woven thermoplastic composite plate with dimension 0.5 m ×0.5 m×0.001 m instrumented with six PWAS transducers as shown in Figure 4.1 (a). These sensors receive the impact signals and connect with two oscilloscopes to record the experimental data.

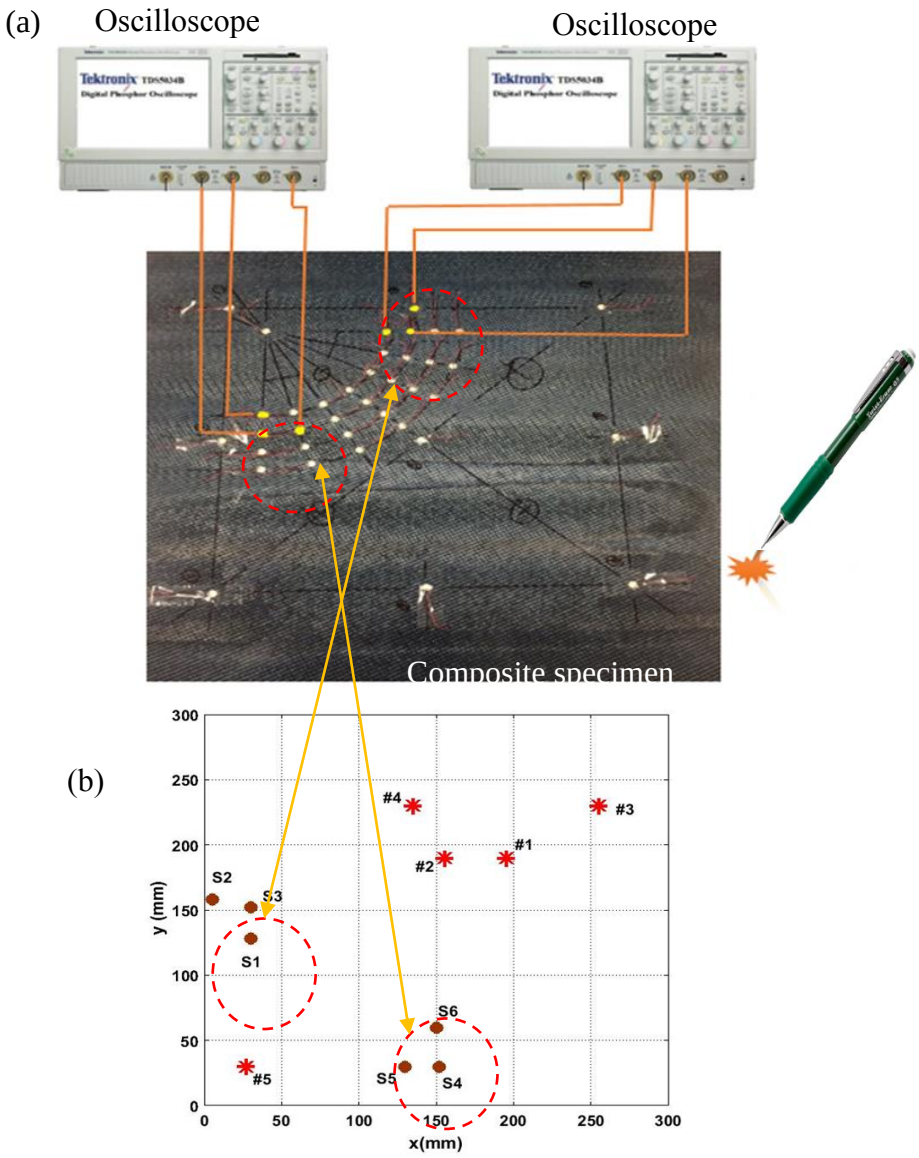

Figure 4.1: (a) Experimental setup; (b) interested area.

Table 4.2 shows the real coordinates of investigated points. The interested area, PWAS transducers and the real coordinates of impact source points on the plate are illustrated in Figure 4.1 (b). The TOF of the received signals are determined at the starting points of these signals. The Continuous Wavelet Transform (CWT) of the signals are determined with AGU-Vallen Wavelet, a freeware software program [50]. This program has a Gabor function as the "mother" wavelet. The CWT plot is very helpful to determine the features of a signal (time of flight (TOF), frequency, and amplitude). The TOF are indicated at frequency 60 kHz. The intersection point between the threshold line and an impact signal amplitude represents the starting point of this signal and the TOF is determined at this point. Figure 4.2 shows the waveform signals of impact point#1 and point#3 received by the six PWAS transducers. The CWT is determined for the analysis window (the incident wave part of the signal) to indicate the TOF of this signal. Figure 4.3 shows the wavelet coefficients for signals of impact point#1 received by six sensors.

Table 4.2 shows the real coordinates of investigated points. The interested area, PWAS transducers and the real coordinates of impact source points on the plate are illustrated in Figure 4.1 (b). The TOF of the received signals are determined at the starting points of these signals. The Continuous Wavelet Transform (CWT) of the signals are determined with AGU-Vallen Wavelet, a freeware software program [50]. This program has a Gabor function as the "mother" wavelet. The CWT plot is very helpful to determine the features of a signal (time of flight (TOF), frequency, and amplitude). The TOF are indicated at frequency 60 kHz. The intersection point between the threshold line and an impact signal amplitude represents the starting point of this signal and the TOF is determined at this point. Figure 4.2 shows the waveform signals of impact point#1 and

point#3 received by the six PWAS transducers. The CWT is determined for the analysis window (the incident wave part of the signal) to indicate the TOF of this signal. Figure 4.3 shows the wavelet coefficients for signals of impact point#1 received by six sensors.

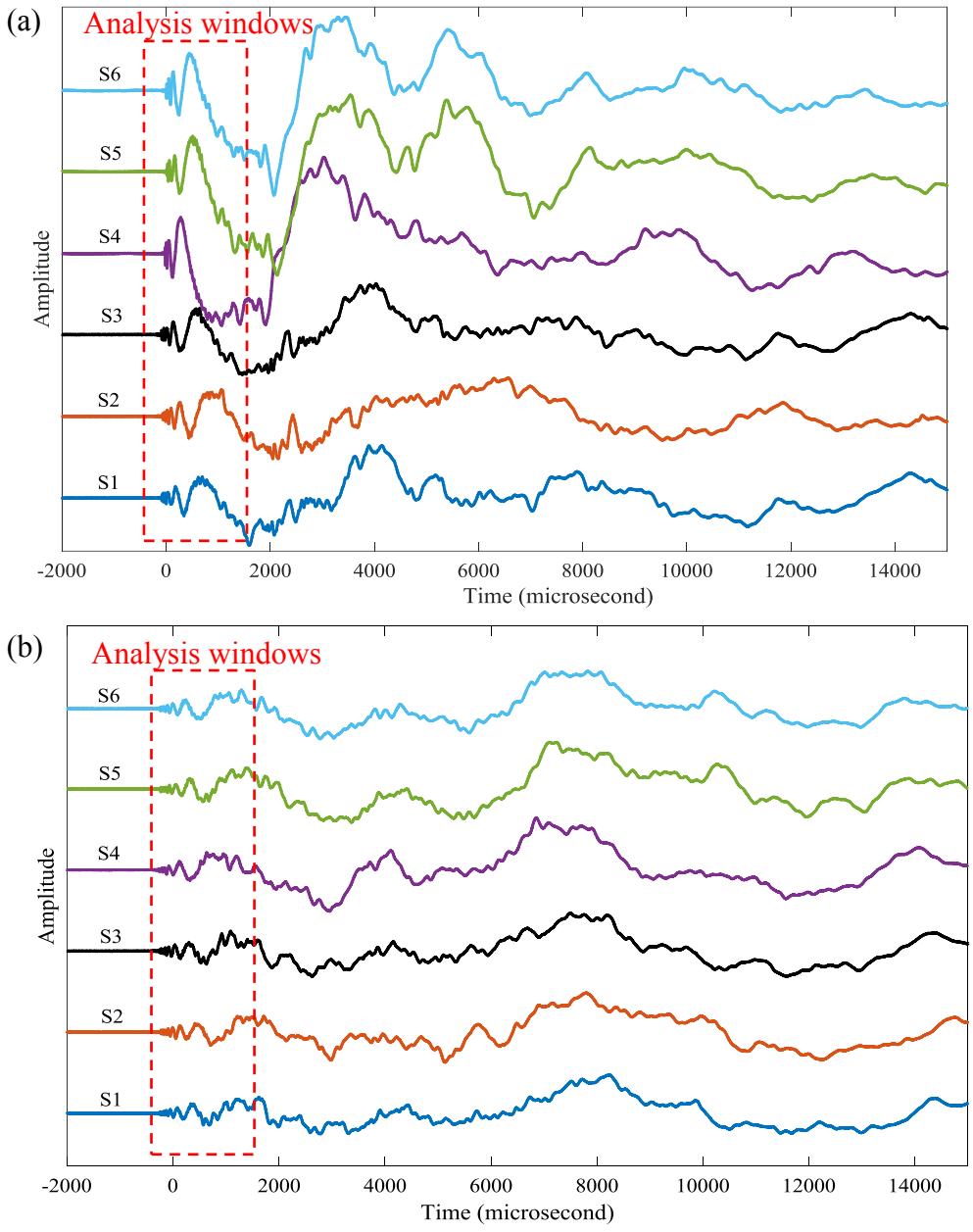

Figure 4.2: The waveform signals of impact sources at: (a) point #1; (b) point#3.

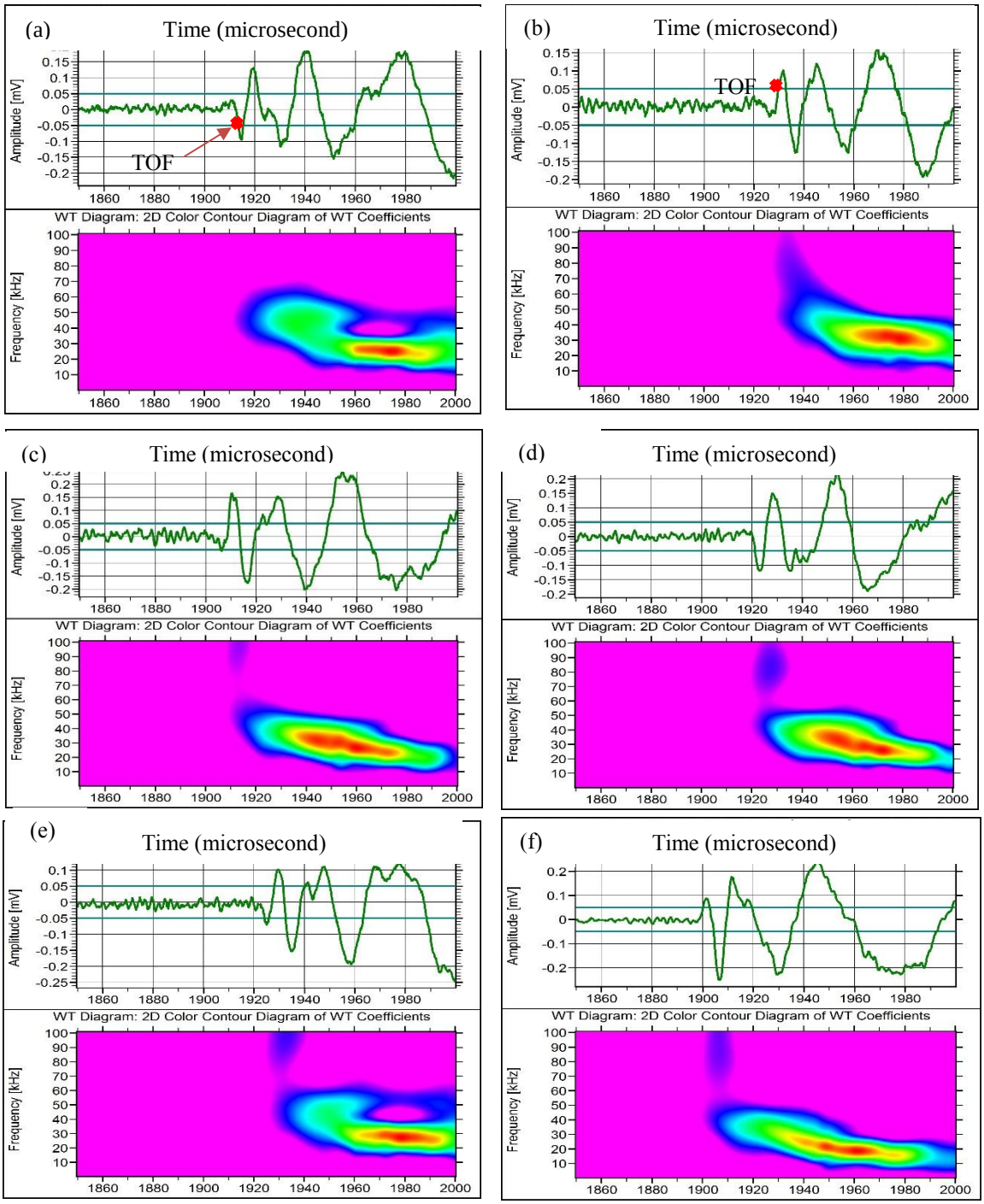

Figure 4.3: Wavelet transform of signals for impact point#1 received by transducers, (a) *S1*; (b) *S2*; (c) *S3*; (d) *S4*; (e) *S5*; (f) *S6*.

In this work, two methods are used for localizing impact source points. First, we use the numerical methods (traditional methods) to localize the impact points by solving a

set of linear or nonlinear equations. Second, we use developed imaging methods to image the impact point on the interested area. The developed imaging methods in conjunction with impact signals are used to find the source point.

Table 4.1: Sensors coordinates.

PWAS No.	S_1	S_2	S_3	S_4	S_5	S_6
x(mm)	30	0	30	152	130	150
y(mm)	128	155	152	30	30	60

Table 4.2: Real coordinates of impact points.

Point No.	#1	m	#3	#4	#5
x(mm)	195	155	255	135	27
y(mm)	190	190	230	230	30

4.3 NUMERICAL METHODS

Two numerical methods are used in this work to localize the impact source points. The first method (method 1) is the Kundu's approach (linear technique) [38]. This approach has two linear equations with two unknowns which represent the coordinates of an impact source point. The second numerical method (method 2) is the modified triangulation algorithm (nonlinear technique). This method has a set of nonlinear equations which should be solved to find the coordinates of an impact source point.

4.3.1 METHOD 1(LINEAR TECHNIQUE)

The new technique developed by Kundu [38] is used to localize the acoustic emission source in an anisotropic plate using six sensors. These sensors are distributed in two clusters with a particular distribution. This technique exists with two linear equations to calculate the coordinate of an acoustic source point. To explain this technique, six

sensors $(s_1, s_2, s_3, s_4, s_5, s_6)$ are distributed in two clusters on the specimen. The sensors of *ClusterI* (s_1, s_2, s_3) have the coordinates, (x_1, y_1), (x_2, y_2) and (x_3, y_3) respectively as shown in Figure 4.4. According to this technique, the distance among sensors are determined as follow

$$\begin{aligned} x_3 &= x_1 + d \\ x_2 &= x_1 \\ y_1 &= y_2 + d \\ y_3 &= y_1 \end{aligned} \tag{4.1}$$

Based on this technique, the distance between the acoustic emission source point $A(x_A, y_A)$ and the sensor s_1 *or* s_4 should be much larger than the distance *d* (it is the vertical or horizontal distance between two sensors). The inclination angles of the lines between point A and the sensors s_1, s_2, s_3 are assumed to be the same. Based on this assumption, the group velocities of AE signals received by these three sensors are also approximately the same

$$\begin{aligned} \theta_1 &\approx \theta_2 \approx \theta_3 \\ c_{g1} &\approx c_{g2} \approx c_{g3} \end{aligned} \tag{4.2}$$

The angle θ can be expressed by

$$\begin{aligned} \theta &= \theta_1 = \theta_2 = \theta_3 \\ \theta &= \tan^{-1}\left(\frac{y_1 - y_A}{x_1 - y_A}\right) = \tan^{-1}\left(\frac{y_2 - y_A}{x_2 - y_A}\right) = \tan^{-1}\left(\frac{y_3 - y_A}{x_3 - y_A}\right) \end{aligned} \tag{4.3}$$

Based on this assumption the wavefront of propagating signals received by cluster sensors is assumed to be circle as shown in Figure 4.5. The impact signals are received by PWAS transducers s_1, s_2, s_3 at the time of flight t_1, t_2, t_3, respectively. The propagating

distances k and f between the orbits of sensors S_1, S_3 and between the orbits of S_1, S_2, respectively are given by

$$\begin{aligned} k &= \Delta t_{13}.c_{g1} = d.\cos\theta \\ f &= \Delta t_{12}.c_{g1} = d.\sin\theta \end{aligned} \tag{4.4}$$

$$\begin{aligned} \tan\theta &= \frac{\Delta t_{12}}{\Delta t_{13}} \\ \theta &= \tan^{-1}\left(\frac{\Delta t_{12}}{\Delta t_{13}}\right) \end{aligned} \tag{4.5}$$

After adding the Eq.(4.3)and the Eq.(4.5), we can get

$$\begin{aligned} \tan^{-1}\left(\frac{y_1 - y_A}{x_1 - x_A}\right) &= \tan^{-1}\left(\frac{\Delta t_{12}}{\Delta t_{13}}\right) \\ \frac{y_1 - y_A}{x_1 - x_A} &= \frac{\Delta t_{12}}{\Delta t_{13}} \end{aligned} \tag{4.6}$$

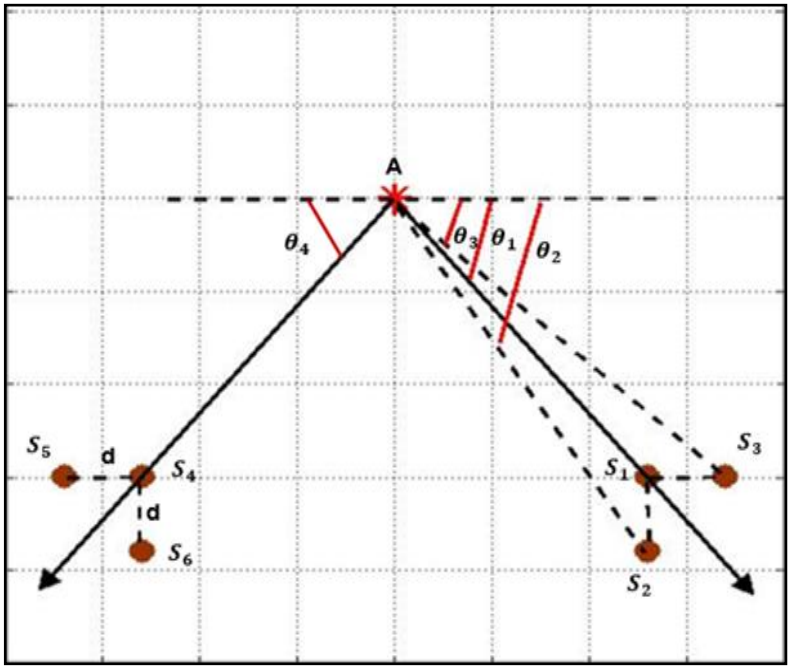

Figure 4.4: Six PWAS transducers are installed in two clusters to localize the impact point A(x, y) [38].

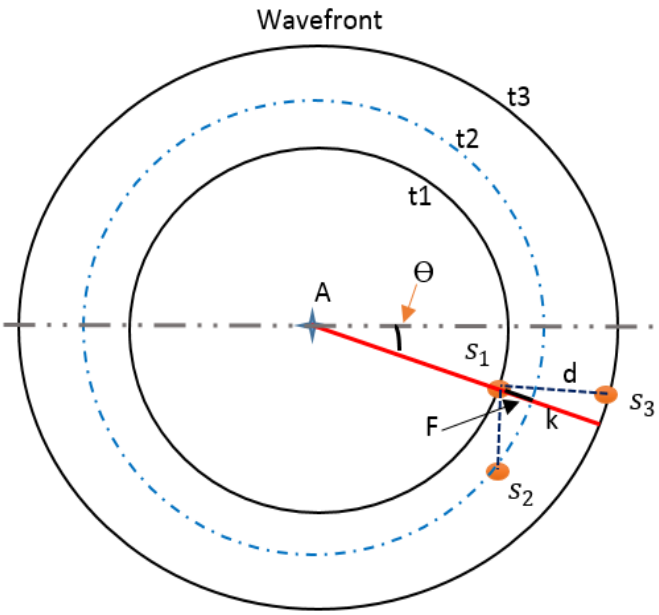

Figure 4.5: The wavefront of signals received by sensors S_1, S_2, S_3.

where Δt_{12} Δt_{13}, are the differences in time of flight among the signals received by sensors s_1 , s_2. and s_3. In the same manner, it can be doing for the second cluster to get

$$\frac{y_4 - y_A}{x_4 - x_A} = \frac{\Delta t_{46}}{\Delta t_{45}} \tag{4.7}$$

The two linear equations (Eq.(4.6), Eq.(4.7)) are solved together to get the coordinates of the impact point A.

4.3.2 METHOD 2 (NONLINEAR TECHNIQUE)

In this method, the triangulation algorithm is evoked and used to indicate the impact source points with same PWAS sensors configuration in linear method. Six PWAS sensors are embedded in two clusters (the same used sensors in the method 1) as shown in Figure 4.4. The inclination angles θ_1, θ_2 and θ_3 and the group velocities c_{g1}, c_{g2} and c_{g3} of sensors s_1, s_2 and s_3 are assumed to be the same. The sensors of the second cluster

s_4, s_5 *and* s_6 are also assumed to have the same inclination angles and group velocities. Based on this assumption, we get

$$c_{g1} \approx c_{g2} \approx c_{g3}$$
$$c_{g4} \approx c_{g5} \approx c_{g6} \tag{4.8}$$

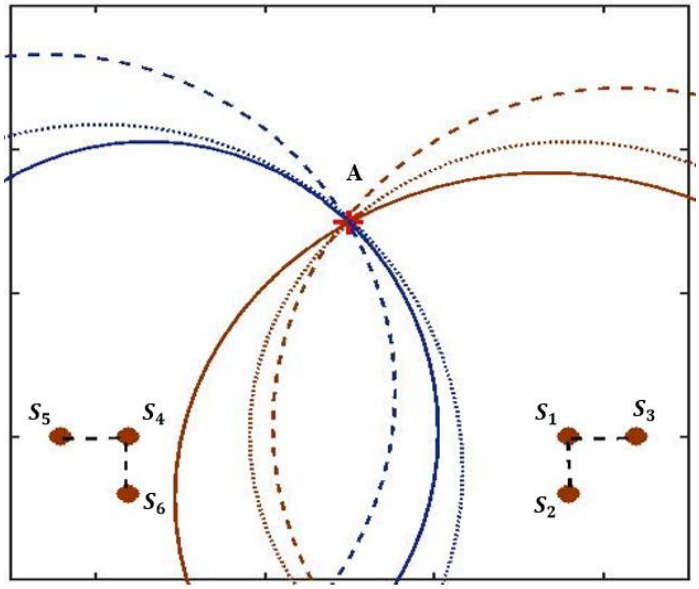

Figure 4.6: The triangulation algorithm representative.

The triangulation algorithm is used to calculate the coordinate of an impact source point [12]

$$(x_i - x_A)^2 + (y_i - y_A)^2 - [(t_i + t_0).c_{gi}]^2 = 0$$
$$i = 1, 2, ..., 6 \tag{4.9}$$

The above equation is a set of six nonlinear equations with five unknowns $(x_A, y_A, c_{g1}, c_{g4}, t_0)$. The unknown variables are the AE source location $A(x, y)$ the group velocities of the signals received by the PWAS transducers of the first and second clusters, c_{g1}, c_{g4} respectively, and the trigger delay t_0. The known terms are the sensors coordinates (x_i, y_i) and the time of flight of signals received by six sensors, t_i. The idea of

triangulation algorithm is to find the intersection point of a set of circular paths which represents the AE source point as shown in Figure 4.6.

4.3.3 RESULTS OF NUMERICAL METHODS

Five impact sources points were calculated experimentally using two different methods. Six PWAS transducers were used in conjunction with these two approaches. Two linear equations exist with the method 1. These equations are solved using MATLAB code to find the calculated coordinates of the impact source point as follow

$$\begin{aligned} &a.x_A - y_A = a.x_1 - y_1 \\ &b.x_A - y_A = b.x_4 - y_4 \\ &a = \frac{\Delta t_{12}}{\Delta t_{13}}, \mathrm{b} = \frac{\Delta t_{46}}{\Delta t_{45}} \end{aligned} \tag{4.10}$$

Based on method 2, the second MATLAB code was implemented to solve a set of six nonlinear equations with five unknowns $(x_A, y_A, c_{g1}, c_{g4}, t_0)$. These equations can be solved using error-minimization routine (the MATLAB function is fminsearch). In this code, the expression of the objective function is given by the following equation

$$\begin{aligned} fcns = &\sum_{i=1}^{3}\left((x_i - x)^2 + (x_i - x)^2 - (c_{g1}.(t_i + t_0))^2\right) \\ &+\sum_{i=4}^{6}\left((x_i - x)^2 + (x_i - x)^2 - (c_{g4}.(t_i + t_0))^2\right) \end{aligned} \tag{4.11}$$

The location error (δ) of calculated the location of a point is determined as the following equation [31]

$$\delta = \sqrt{\left((x_{real} - x_{calculated})^2 + \right)(\mathrm{y}_{real} - y_{calculated})^2} \tag{4.12}$$

In the above equation, (x_{real}, y_{real}) and $(x_{calculated}, y_{calculated})$ represent the real and calculated coordinates of an acoustic emission source point. The percentage error of calculated coordinate is determined using the following equation

$$error\% = \frac{\delta}{A} * 100\% \tag{4.13}$$

In the above equation, A represents the length of the straight line between the sensors s_1 and s_4 as shown in Figure 4.7.

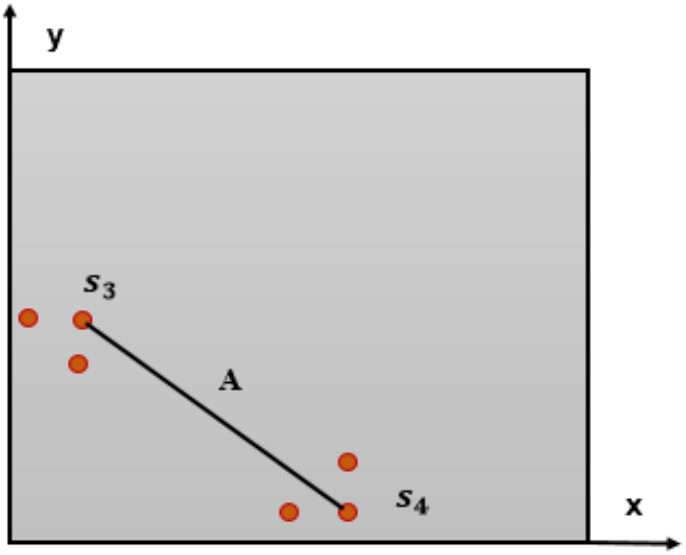

Figure 4.7: Distance A is the straight line between PWAS transducers s_1 and s_4.

Table 4.3 shows the real coordinate of five AE source points, the calculated coordinate of these points using method 1 (linear algorithm), the location errors and the percentage errors. The results of using method 2 (nonlinear algorithm) are shown in Table 4.4. The results show a good matching between these algorithms. The errors in the calculated locations are due to the errors in determining the TOF, and the assumption of

making the sensors in one cluster have the same group velocities. The source location results for five AE source points on the interested area of the plate is shown in Figure 4.8.

Table 4.3: Results of localization impact sources using the method 1 (linear algorithm).

Impact points	$(x_{real}, y_{real})mm$	$(x_{calculated}, y_{calculated})mm$	$(\delta)mm$	Percentage error %
Point #1	(195, 190)	(194.4, 191.1)	1.28	0.74%
Point #2	(155, 190)	(152.8, 190.5)	2.23	1.29%
Point #3	(255, 230)	(256.5, 227.5)	2.93	1.70%
Point #4	(135, 230)	(134.7, 229.1)	0.92	0.53%
Point #5	(27, 30)	(28, 30.5)	1.3	0.75%

Table 4.4: Results of localization impact sources using the method 1 (linear algorithm).

Impact points	$(x_{real}, y_{real})mm$	$(x_{calculated}, y_{calculated})mm$	$(\delta)mm$	Percentage error %
Point #1	(195, 190)	(192.4, 190.3)	2.6	1.5%
Point #2	(155, 190)	(152.2, 190.1)	2.15	1.24%
Point #3	(255, 230)	(251.3, 229.8)	3.7	2.13%
Point #4	(135, 230)	(135.6, 231.65)	1.8	1.04%
Point #5	(27, 30)	(27.1, 29.9)	0.9	0.52%

4.4 IMAGING METHODS

In recent years, many imaging algorithms are sufficiently used to quantify the defects in a structure like plate using guided waves. In this work, the developed imaging method is used to localize the impact source point. The basic idea of this method is to use the imaging concept in conjunction with slope equations (Kundu's approach) to create straight lines paths (damage paths). The intersection point of these paths gives the impact point location.

4.4.1 IMAGING CONCEPT

The idea of using imaging process for finding the location of defects or acoustic emission source points is to define the defect orbit (path). The intersection points of some orbits (paths) represent the defect or the acoustic emission source location. The defect orbit can be defined as an elliptic, circular, hyperbolic or straight-line path. To localize the defect in the interested area, it should be divided into small pixel points. To map the different kinds of paths on the interested area, we should find the field values of pixels points. The pixel function is responsible about mapping and presenting the defect path (straight line, circular, etc.) on the pixel points. In this work, two-lines paths are mapped from each cluster and intersected at the position of an acoustic emission source point as shown the Figure 4.9.

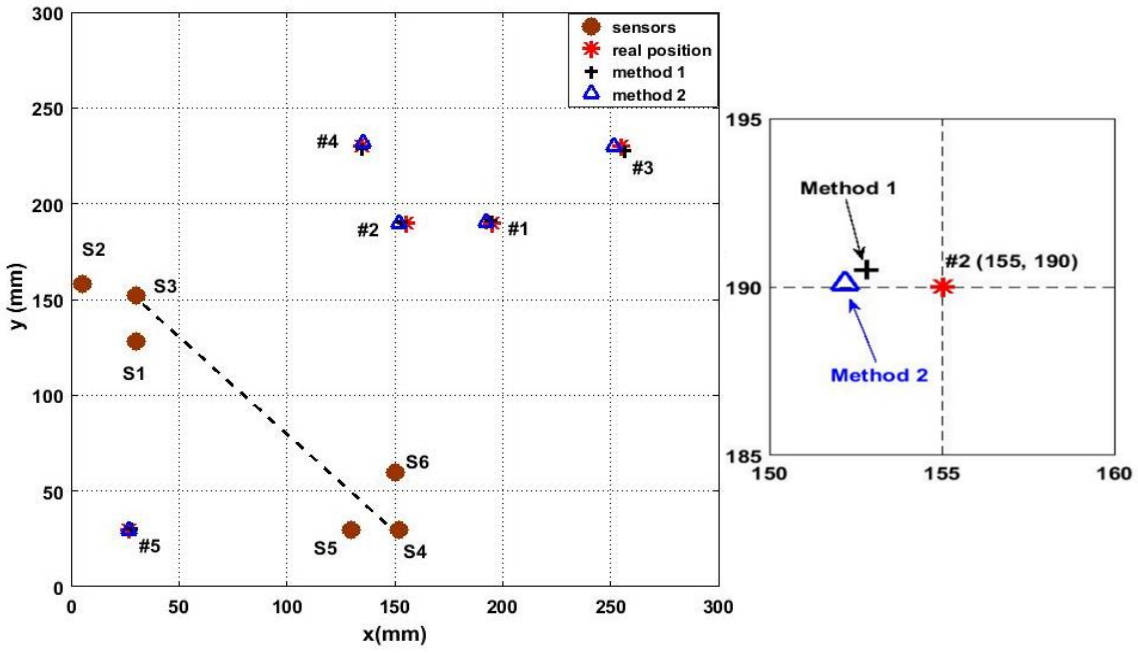

Figure 4.8: Source localization results on the interested area.

So, every cluster has a linear pixel function as follow

$$f_I = sn_1(\text{slope}_I(x,y))$$
$$f_{II} = sn_2(\text{slope}_{II}(x,y)) \tag{4.14}$$

where f_I, f_{II} are the pixel functions for line I and line II respectively, sn_1, sn_2 are synthetic signals for enabling lines I and line II. $Slope_I(x,y), Slope_{II}(x,y)$ are the slope equations of line I ($ClusterI$) and line II ($ClusterII$), i.e.

$$\text{Slope}_I(x,y) = \frac{y_3 - y}{x_3 - x}$$
$$\text{Slope}_{II}(x,y) = \frac{y_4 - y}{x_4 - x} \tag{4.15}$$

where $(x_3, y_3), (x_4, y_4)$ are the coordinates of sensors S_3 (in $ClusterI$) and S_4 (in $ClusterII$) respectively. The values of pixel functions f_I, f_{II} have two values as follow

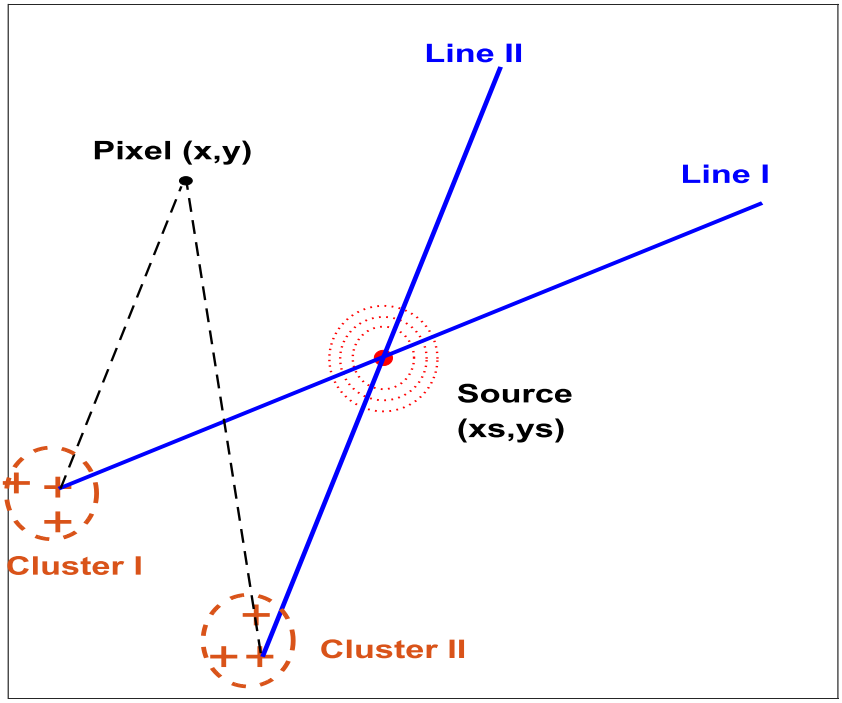

Figure 4.9: The developed Imaging concept.

$$f_I = \begin{cases} 1 & ,if\,(x,\mathrm{y}) \in \mathrm{pathI} \\ 0 & ,else \end{cases}$$
$$f_{II} = \begin{cases} 1 & ,if\,(x,\mathrm{y}) \in \mathrm{pathII} \\ 0 & ,else \end{cases} \qquad (4.16)$$

The impact point is located at the intersection point of path I and path II. To calculate this intersection point, we can combine f_I, f_{II} either by summation or multiplication (finding the total field value) of every pixel point in the area of interest, i.e

$$P_{sum}(x,y) = f_I(x,y) + f_{II}(\mathrm{x},\mathrm{y}) = \begin{cases} 2 & ,if\,(x,y) = (x_D, y_D) \\ 1 & ,if\,(x,y) \in pathIorpathII \\ 0 & ,else \end{cases} \qquad (4.17)$$

$$P_{mult}(x,y) = f_I(x,y).f_{II}(\mathrm{x},\mathrm{y}) = \begin{cases} 1 & ,if\,(x,y) = (x_D, \mathrm{y}_D) \\ 0 & ,else \end{cases} \qquad (4.18)$$

where $P_{sum}(x,y), P_{mult}(x,y)$ are the total field value of a pixel (x,y) using summation or multiplication methods. Because experimental data has noise, the 0, 1 images are not perfect. Hence, we need to reduce the effect of noise by using a smearing method of defusing the pixel function with a smoothing window as shown in Figure 4.10. These synthetic signals have maximum amplitude values at the certain slope magnitude of cluster paths.

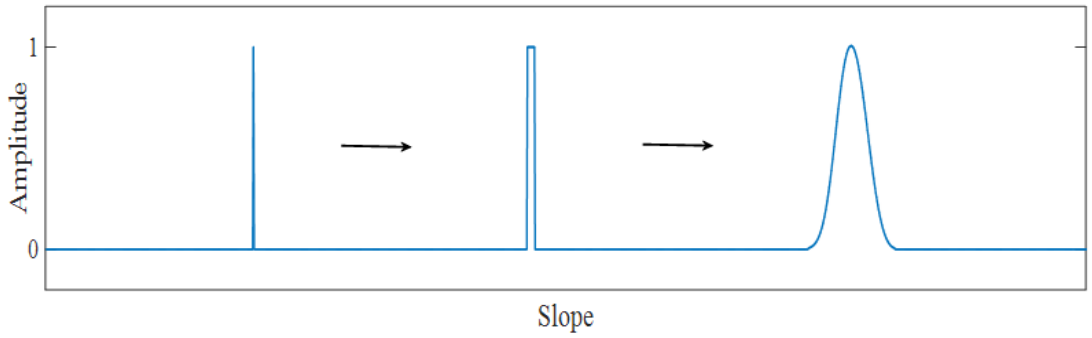

Figure 4.10: Synthetic signals with various windows.

In this experiment, the magnitudes of slopes for the cluster paths can be determined using Eq.(4.6) and Eq.(4.7) (Kundu's method) as follow

$$\begin{aligned} m_I &= \frac{\Delta t_{31}}{\Delta t_{32}} \\ m_{II} &= \frac{\Delta t_{46}}{\Delta t_{45}} \end{aligned} \tag{4.19}$$

where m_I, m_{II} are the slope values of *ClusterI* and *ClusterII* . We can use also a data fusion concept by adding or multiplying information from more than two clusters, say a total of N cluster to write,

$$\begin{aligned} P_{sum}(x,y) &= \sum_{i=1}^{N} f_i(x,y) \\ P_{mult}(x,y) &= \prod_{i=1}^{N} f_i(x,y) \end{aligned} \tag{4.20}$$

In this work, we develope two visual methods for source localization. In the first method (method v1), we use smoothing window synthetic signals for finding the pixels field values which is Gaussian distribution function

$$f(x) = \frac{1}{\sigma\sqrt{2\pi}} e^{-\frac{(x-\mu)^2}{2\sigma^2}} \tag{4.21}$$

where σ is the standard deviation width and μ is the mean value. For determination the total field values of pixels, summation and multiplication algorithms are used (Eq.(4.17), Eq.(4.18)). In the second method (method v2), we use rectangular window function (unite pulse) for enabling the cluster paths which is formed as follow

$$\prod_{a,b}(x) = \begin{cases} 1 & , \quad a < x < b \\ 0 & , \quad otherwise \end{cases} \tag{4.22}$$

The slope value is located at the middle distance between points a, b . The width of rectangular window function should be small as much as possible to get one intersection point. The summation algorithm (Eq.(4.17)) is used for imaging construction

4.4.2 DETERMINATION OF EXPERIMENTAL SLOPE VALUES

The time of flight of impact signals received by the sensors of cluster I and cluster II are determined in the Table 4.5. The difference in time of flight (TOF) between the sensors of same cluster are determined in Table 4.6.

Table 4.5: TOF of signals received by six sensors (impact at point#1(195, 190) mm).

PWAS No.	s_1	s_2	s_3	s_4	s_5	s_6
TOF ($\mu sec.$)	1914	1930	1909	1920	1925	1901

Table 4.6: The difference in TOF of received signals

Time difference	Δt_{31}	Δt_{32}	Δt_{45}	Δt_{46}
Value ($\mu sec.$)	-5	-21	-5	19

The slope of *ClusterI* (m_I) and the slope of *ClusterII* (m_{II}) are determined using Eq.(4.19)

$$m_I = \frac{\Delta t_{31}}{\Delta t_{32}} = 0.238$$

$$m_{II} = \frac{\Delta t_{46}}{\Delta t_{45}} = -3.8$$

The synthetic signals of method v1 and method v2 are determined for enabling the slope paths of *ClusterI* and *ClusterII* . These synthetic signals have peak amplitudes at slope values 0.238, -3.8 respectively as shown in Figure 4.11 and Figure 4.12. The width

of Gaussian windows of synthetic signals in Figure 4.11 can be optimized to get better imaging results. However, the width of rectangular window function of synthetic signals which are shown in Figure 4.12 should be small as much as possible to restrict the probability of localization the impact source in one-pixel point.

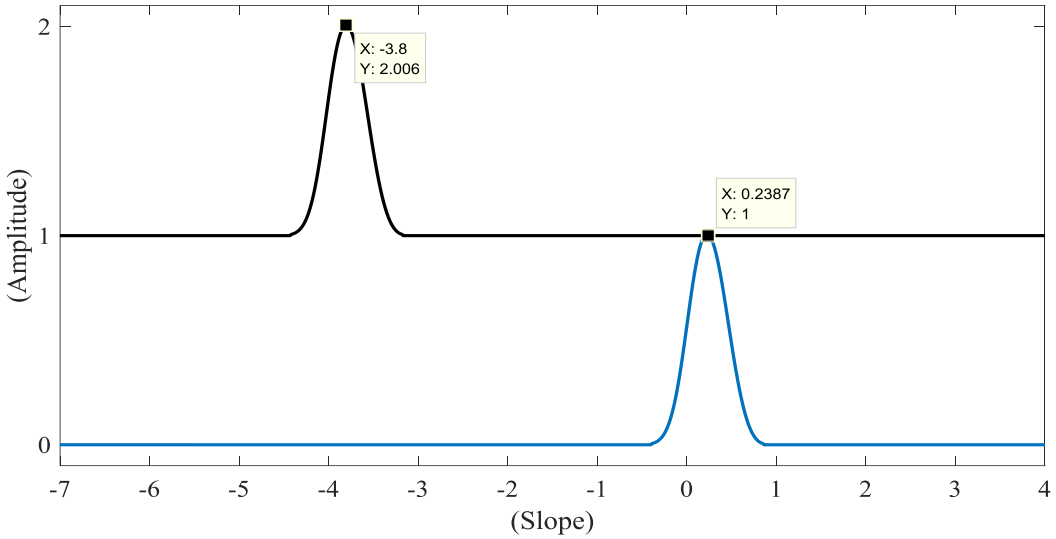

Figure 4.11: Synthetic signals of method v1 for imaging impact point#1.

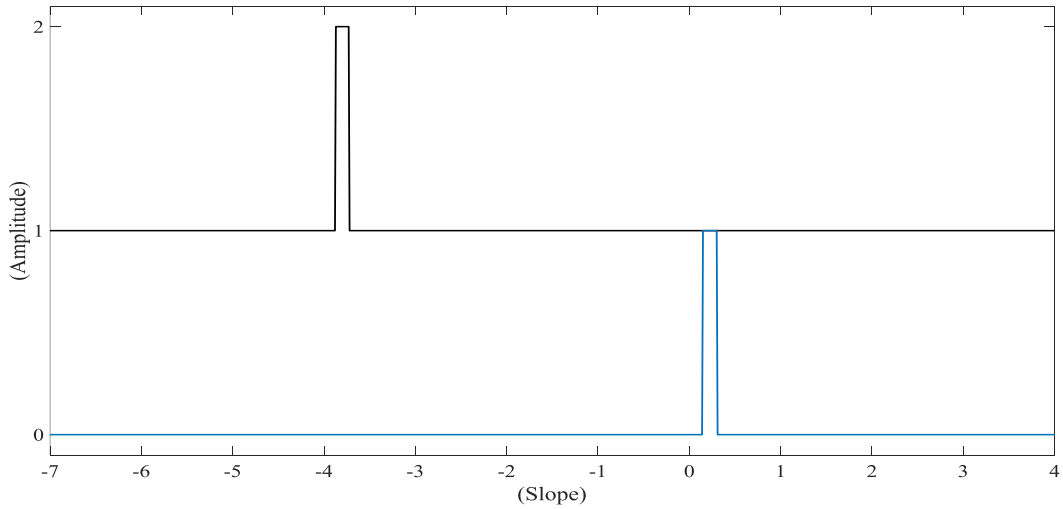

Figure 4.12: Synthetic signals of method v2 for imaging impact point#1.

4.4.3 RESULTS

The imaging results of localization the AE source point at point #1 (195, 190) mm are shown Figure 4.13. It can be seen two straight paths come from *ClusterI* (PWAS #3) and *ClusterII* (PWAS #4) and intersect at the impact source point as shown in Figure 4.13 (a), (c) (using summation algorithm). Figure 4.13 (b) shows just the intersection area of two slope paths (using multiplication algorithm).

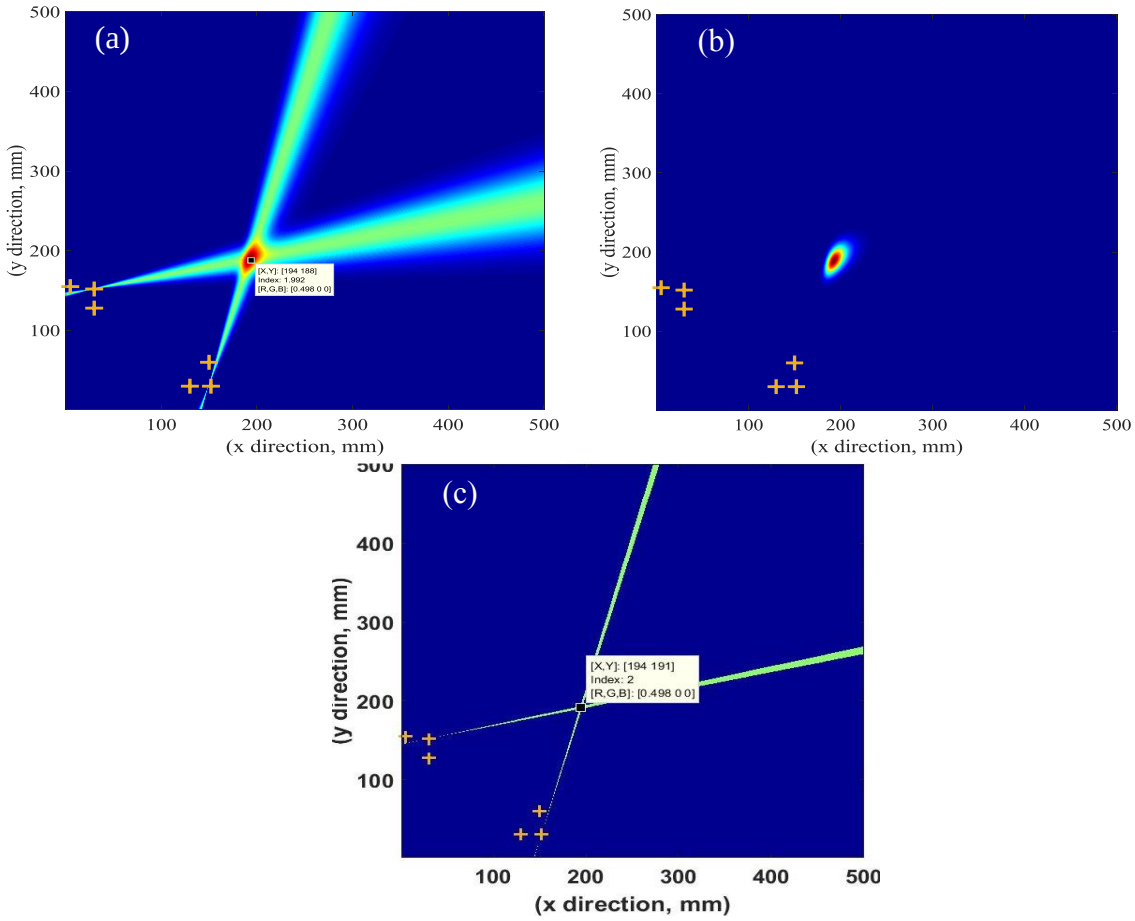

Figure 4.13: Imaging results of the impact source at point #1(195, 190) mm.

The pixel point with the higher field value at the intersection area represents the impact point as shown in Figure 4.13 (a), and Figure 4.13 (b). The result of method v2 is shown in Figure 4.13 (c). This figure shows one-pixel point at the intersection area which

represents the AE source point. If there are more than one-pixel point, we can control the width rectangular window function of synthetic signals as shown in the Figure 4.12 or determine the average value between two points.

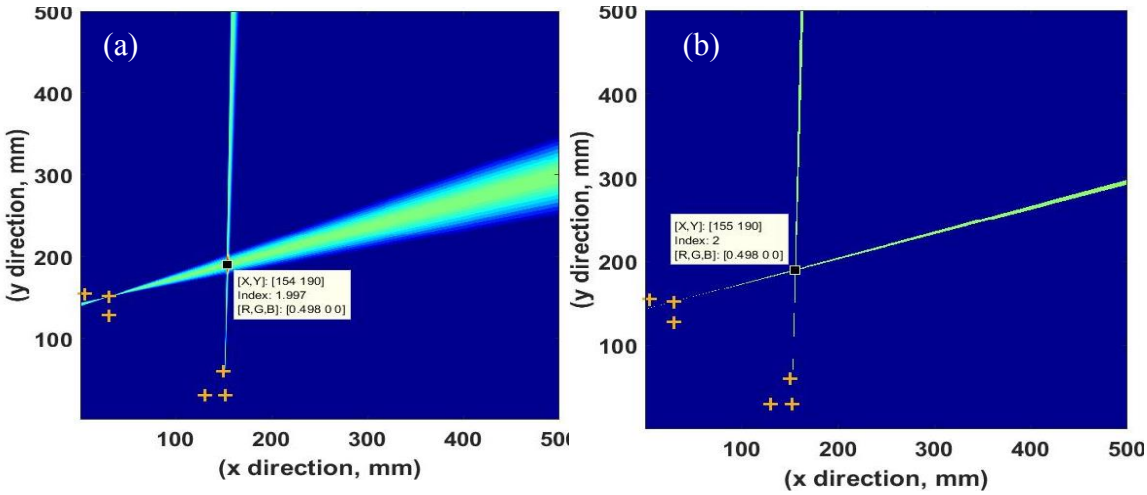

Figure 4.14: Imaging results of the impact source at point #2 (155, 190) mm.

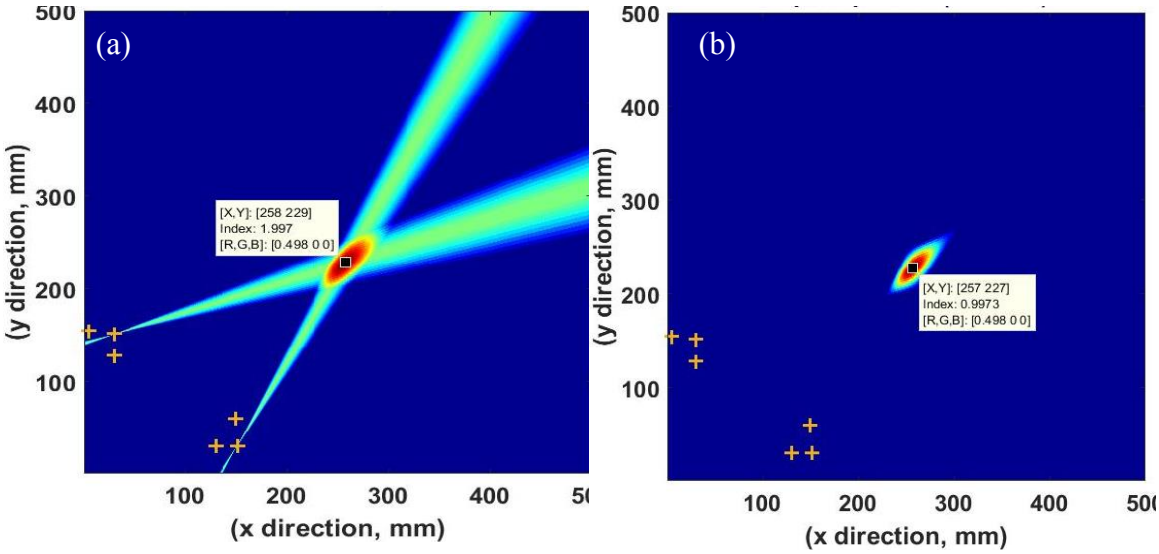

Figure 4.15: Imaging results of impact source at point #3 (255, 230) mm.

Figure 4.14 shows the imaging results of localization the impact source point #2 (155, 190) mm. These slope-based imaging results come up with accurate source localization result. In Figure 4.14 (a) (method v1), we see different size paths (thick and

thin paths). The path size (path width) is a function with its slope value (slope angle). When the slope has a small value (small angle), the path has a thick width. However, when the slope has a big value, the path has a thin width. In Figure 4.14b (method v2), we see very thin lines to get one-pixel point at the intersection area. The results of localization the impact source point #3 (255, 230) mm are shown in Figure 4.15. The Figure 4.15 (a) shows the result of method v1 with summation algorithm (using Eq.(4.17)). The paths have approximately the same size width because they apporximatly have the same slope values. Figure 4.15 (b) shows the image result of using method v1 with multiplication algorithm (using Eq.(4.18)). This figure shows a clear spot area with a high field pixel point which represents the AE source point. The results of all five investigated points using method v1 (sum. and multi. methods) are shown in Table 4.7. The results show a good matching between imaging methods and the numerical methods.

Table 4.7: Result of both imaging methods (unit: millimeter).

Impact points	Real points	Calculated points Method v1	Calculated points Method v1	Calculated points Method v2
Point #1	(195, 190)	(194, 188)	(194, 188)	(194, 191)
Point #2	(155, 190)	(154, 190)	(154, 190)	(155, 190)
Point #3	(255, 230)	(258, 229)	(258, 227)	(257, 229)
Point #4	(135, 230)	(134, 229)	(134, 229)	(135, 230)
Point #5	(27, 30)	(27, 29))	(27, 29)	(26, 30)

4.5 IMAGING METHODS WITH KNOWN MATERIAL PROPERTIES

In this part of localization the acoustic emission source points, we use time of flight of received signals-based imaging algorithm to create hyperbola locus between two sensors. The intersection point of two hyperbolae paths represent the impact source point. The

hyperbolae path, which is shown in Figure 4.16, between sensors PWAS#1 and PWAS#2 can be created as a function of difference in time of flight (TOF) of signals received by these two sensors using the following equation

$$\Delta t_{12} = (\sqrt{(x_D - x_{s1})^2 + (y_D - y_{s1})^2} - \sqrt{(x_D - x_{s2})^2 + (y_D - y_{s2})^2}) / v_g \qquad (4.23)$$

where Δt_{12} is the difference in TOF of the signals received by PWAS#1 and PWAS#2, (x_D, y_D) represents the coordinates of impact source point, $(x_{s1}, y_{s1}, x_{s2}, y_{s2})$ are the coordinates of PWAS#1 and PWAS#2 respectively, v_g represents the group velocity of propagation waves.

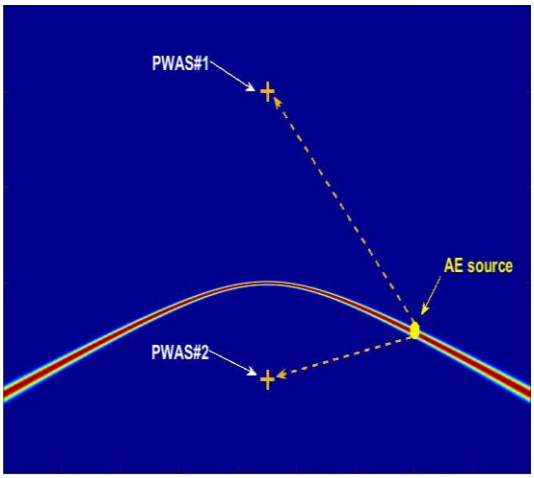

Figure 4.16: Imaging result of hyperbola path between two sensors.

The direction-dependent velocity profiles (group velocity profile) of Lamb waves are determined analytically for the interested specimen based on the material properties. The wavelet transforms of received signals reveal the frequency domain and the Lamb wave mode type of these signals. For the signals of impact point #1, the Lamb wave mode is A0 and the time of flight is determined at frequency 60 kHz. Figure 4.17 shows the group velocity profile of A0 mode at frequency 60 kHz.

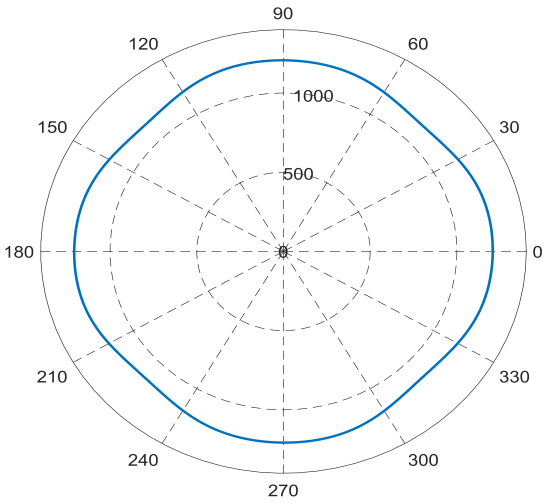

Figure 4.17: The group velocity profile of A0 mode at 60 kHz.

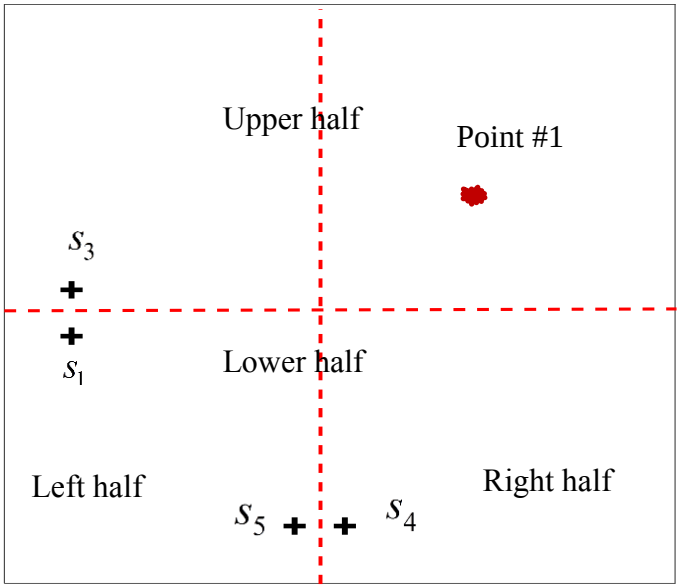

Figure 4.18: Indicating the location of an impact point.

In this method, we use four sensors to localize the AE source point as shown in Figure 4.18. We assume that every pair of sensors have the same wave velocity. To guess the group velocity value for every pair of sensors, we need to predict the location of impact source point on the interested area.

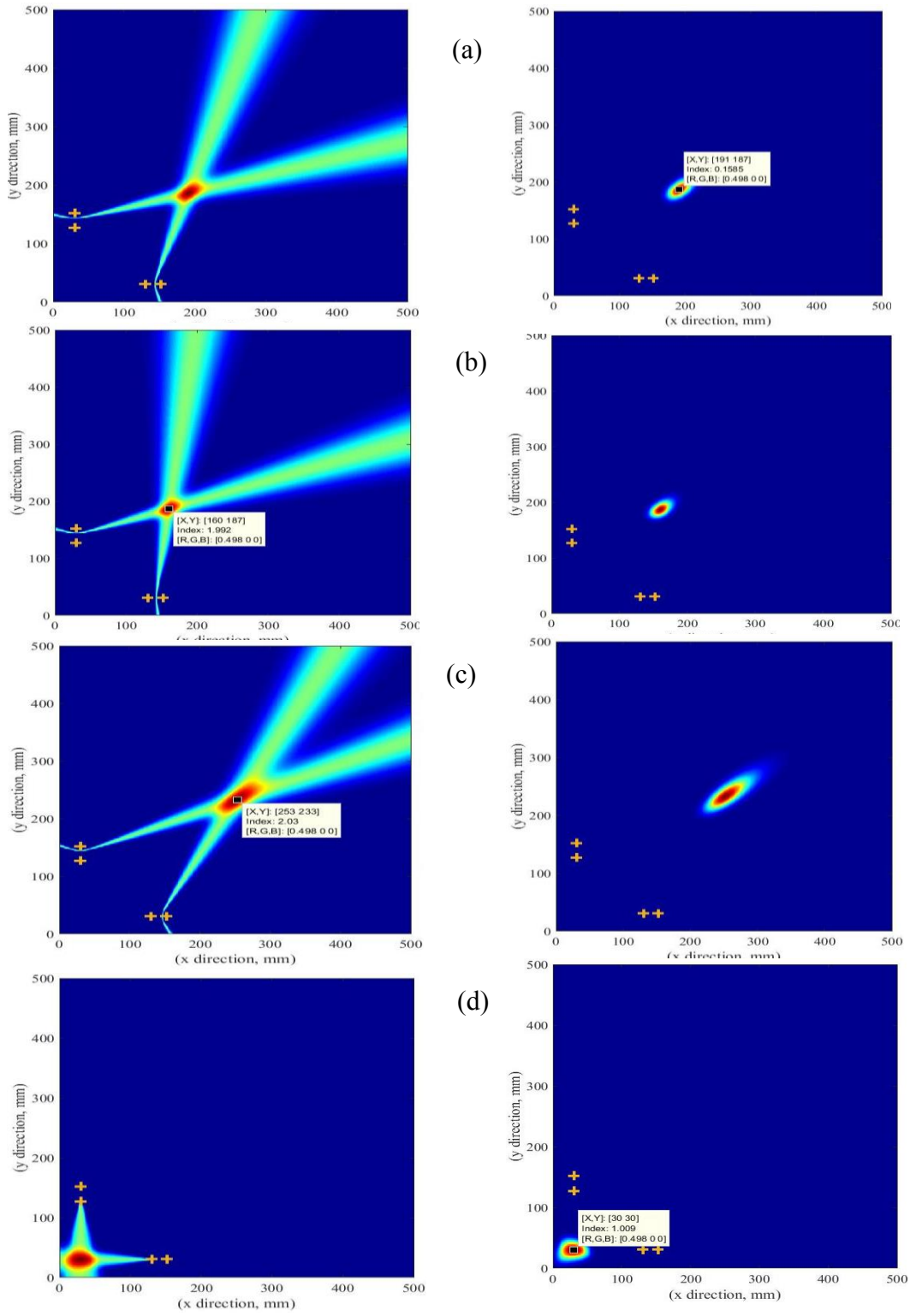

Figure 4.19: Hyperbola-based imaging results for: (a) point#1(195,190); (b) point #2(155,190); (c) point #3(250, 235); (d) point#5 (27, 30).

The interested area was divided into four segments to find the location of an impact source point based on the values of time of flight of signals received by these four sensors. To predict the location of impact source point#1, because the time of flight of sensor s_3 is less than TOF of sensor s_1, the impact point is on the upper half part of the plate and because the TOF of sensor s_4 is less than the TOF of sensor s_5, the impact point is on right half part. So, the location of the impact source point #1 is on the upper right quarter.

The Gaussian distribution function is used to estimate the field value of pixel points. The summation algorithm (Eq.(4.17)) and multiplication algorithm (Eq.(4.18)) are used to determine the total field values of the pixel points of the final image.

The imaging results of impact sources points are shown in the Figure 4.18. The visual results show the powerful of developed imaging methods for localization the impact sources points. The errors in the estimation results are due to the errors in determining the group velocity values of propagating signals and the assumption of making a pair of sensors have the same group velocities. The results value of impact source points coordinates are listed in the Table 4.8.

Table 4.8: Result of both imaging methods (unit: millimeter).

Impact points	Real points	Calculated points
Point #1	(195, 190)	(194, 188)
Point #2	(155, 190)	(154, 190)
Point #3	(255, 230)	(258, 229)
Point #4	(135, 230)	(134, 229)
Point #5	(27, 30)	(27, 29))

4.6 PART I: SUMMARY AND CONCLUSION

The experiment of impact localization on metallic plate was implemented. Nine PWASs were distributed across the plate to receive the propagating signals due to the impact of a small steel ball at three different locations. Two different methods were developed to indicate the location of the impact source points which are the triangulation algorithm method and imaging method. For triangulation algorithm method, the impact points were localized and studied using two ideas. In the first idea, the time of flight of impact signals were determined at the starting point of a signal (Method 1) and the maximum amplitude of a signal (Method 2). In the second studied idea, the effect on increasing the number of used sensors on the result accuracy of localization the impact points were approved. The results of triangulation algorithms show that both methods of determining the time of flight have accurate results for localization the impact points. Also, these results were approved that the percentage errors of localization the impact points decrease with increasing the number of used sensors.

The developed imaging method, was used to localize the impact or acoustic emission source points using hyperbolic paths and imaging process. The basic idea of this developed method is to indicate the intersection point of some hyperbolic paths (at least two paths) which represents the impact source point. Based on the Gaussian distribution function, a synthetic signal was obtained for mapping the hyperbola path between two sensors. The synthetic signal has maximum amplitude (mean value) at the difference in time of flight value of received signals by these two sensors. The imaging results shows the ability of this method for localization the impact points which are inside or outside the sensors networks.

The impact points due to pencil lead breaks on the composite specimen were localized. The properties of this specimen were assumed to be unknown in the first case of localization and assumed to be known in the second case of localization. In the first case of localization, numerical methods (traditional methods) and visuals methods (new method) were used to indicate the AE source points. The method 1 (numerical method) is the Kundu's approach for localization the AE source point using two linear equations (independent with group velocity profile of interesting material). The second numerical method (method 2) is triangulation algorithm with a set of sex nonlinear equations to find five unknowns (the coordinate of an impact point, the group velocities of two clusters and the time delay of received signals). Both of the numerical methods came up with good results. The imaging methods are based on Kundu's approach, synthetic signals and imaging process. The method v1 (imaging method) has two smooth synthetic signals (one synthetic signal for each path) as a function of a slope value. The method v2 (imaging method), has two square synthetic signals. The square synthetic window has two values (one at path slope and zero otherwise). The idea of these methods is to obtain two straight paths for two clusters. The intersection point of these two paths is the AE source point. The results of imaging methods indicate the location of impact points. In the second case, the hyperbola path-based image method was used to localize the impact points using four sensors. The results of this case were interesting.

PART II: DAMAGES DETECTION IN METALLIC STRUCTURES

CHAPTER 5
DAMAGE IDENTIFICATION IN METALLIC PLATES USING SPARSE ARRAY OF SENSORS AND IMAGING METHODS

In this chapter, the SHM technique is used with imaging method to identify crack and hole damages in aluminum plates by implementing two different experiments. The first experiment is to quantify the identification of a crack in an aluminum plate using a sparse array of eight sensors and imaging method. The pitch-catch and pulse-echo modes are used separately in this experiment to determine the measured signals for different sensing paths. The field values of image pixels are determined by scattering signals and synthetic time reversal method or by determining the time of flight values of scattered waves and Gaussian distribution function. For both pitch-catch and pulse echo modes, the image results quantify the crack information (position, size, and orientation of the crack). For the second experiment, a network of sparse array of six sensors with imaging methods is used to quantify a hole damage. Both pitch-catch and pulse-echo modes are used to obtain the measured signals. The same imaging steps of the first experiment are used in the second experiment. The hole damage are well identified by imaging results.

5.1 INTRODUCTION AND STATE OF THE ART

The aluminum material is a common material in the aerospace structure. Cracks are one of the most common defect types in aluminum aircraft structures [14]. The Lamb wave technique is widely used in SHM and NDT techniques for inspection large structure like a plate. The Lamb waves can propagate long distance with less energy loss and are sensitive

to detect small structural defects. In recent years many efforts have been implemented to investigate the ability of Lamb waves for damage detection in structures like plates.

Numerical and experimental studies were implemented to investigate the interaction of Lamb waves with a notch. The results show the sensitivity of Lamb waves for notches detection [53]. The interaction of Lamb modes with vertical and horizontal defects are studied experimentally. The author studied the stress fields of different Lamb modes across the plate thickness. Based on these studied, the efficient Lamb wave mode can be chosen to detect which type of structure flaw [54]. An experimental and a theoretical study were performed on the interaction of Lamb waves with rivet hole crack. The authors found that the scattered field around the hole significantly changes with the presence of crack [55]. In recent years, a network of sensors is used in conjunction with Lamb waves to detect different kinds of structural defects. Array-image SHM methodologies have been developed for vision the identification of flaw structure. A system of an electromagnetic acoustic transducer (EMAT) array was designed for inspection large area of the metallic plate using symmetric Lamb wave mode. The authors demonstrated the sensitivity of this system for detection artificial defects [56]. An approach of Phased array filters using piezoelectric sensors was developed for damage detection in the large isotropic plate. Based on this approach, the area of damage can be localized using low-frequency Lamb wave [57]. The phased array-imaging algorithms were developed [10]. In this study, the authors used linear and square arrays of sensors for damage detection and localization on the large isotropic plate. For quantitatively identification of a damage in the plate, a sparse array of sensors in conjunction with imaging process methods have been developed for vision the damage in a plate. A distributed network of sensors and new imaging method

were used for localization and sizing the structural damages. The sensors operate in pitch-catch and pulse-echo modes. Based on the principle a synthetic time-reversal method, the field values of image pixels are determined [11]. A sparse array of piezoelectric transducers was used to detect through thickness-hole in a large area of the aluminum plate using imaging algorithm. The results show the efficiency of an imaging method for damage localization using only four sensors. Also, the results show that the applying bandpass filters at various frequencies can improve imaging results and can accurately localize the damage [12]. A focusing array algorithm was developed in both experimental and simulation studies to quantify the simulated crack in an aluminum plate. The results show the ability of the array to detect the damage within or outside the network. The imaging results visualize the crack as two highlighted spots which represent the two tips of crack [14].

5.2 CRACK SIZE ESTIMATION

5.2.1 EXPERIMENTAL SETUP

A large aluminum plate-like specimen with dimensions 1220 mm × 1220 mm × 1.6 mm was used. A sub inspection area of 610 mm × 610 mm was instrumented with an active network of eight PWAS transducers as shown in Figure 5.1. This sub inspection area contained a very narrow slit which was manufactured by using a 0.25 mm thin dental cutting disk. This is a simulated crack; for convenience, we will call it hereafter as “crack”. The crack length was about 10 mm and oriented horizontally. The zoomed-in view of the crack is shown as inset of Figure 5.1. The center of the horizontal crack was located at (303 mm, 300 mm) with the left bottom corner of the sub-area as the origin. The sensor network circumscribed the crack at the center. The PWAS transducers of the network were

distributed with equal radial and angular distances. The diameter of the circular network was 300 mm. The diameter of each PWAS transducer was 7 mm and the thickness was 0.2 mm. A function generator was used to generate 3-count tone burst excitation signal at a center frequency of 450 kHz. This frequency was chosen based on the tuning curve of PWAS. At this frequency-thickness product, the symmetric Lamb wave (S0) was dominant in this plate specimen. The same PWAS transducer can be used as a transmitter and a receiver of Lamb wave signals. An Oscilloscope recorded the received Lamb wave signals. The specimen edges of the sub-area were covered with damping clay to minimize the edge-reflected wave signals. Two experimental modes were used: (1) pitch-catch and (2) pulse-echo modes. In pitch-catch modes, each PWAS transducer acted as a transmitter whereas the rest of them in the network acted as receivers. In the pulse-echo mode, each PWAS transducer was served as a transmitter and the same PWAS acted as a receiver. In both experimental modes, the imaging methods were performed for crack detection and quantification as discussed next.

5.2.2 IMAGING METHODS

Two imaging methods were implemented by using the scattered wave signals. The first method involved synthetic time reversal to determine the field values of each pixel using the scattered signals amplitude. This method is hereafter referred to as “method A”. The flow chart of method A is illustrated in Figure 5.2. The concept of synthetic time reversal method was first presented by Wang et. Al [11]. In this study, summation, multiplication and combined algorithms were used in conjunction with synthetic time reversal concept. The second method involved the Gaussian distribution function and scattered signals. This method is hereafter referred to as “method B”.

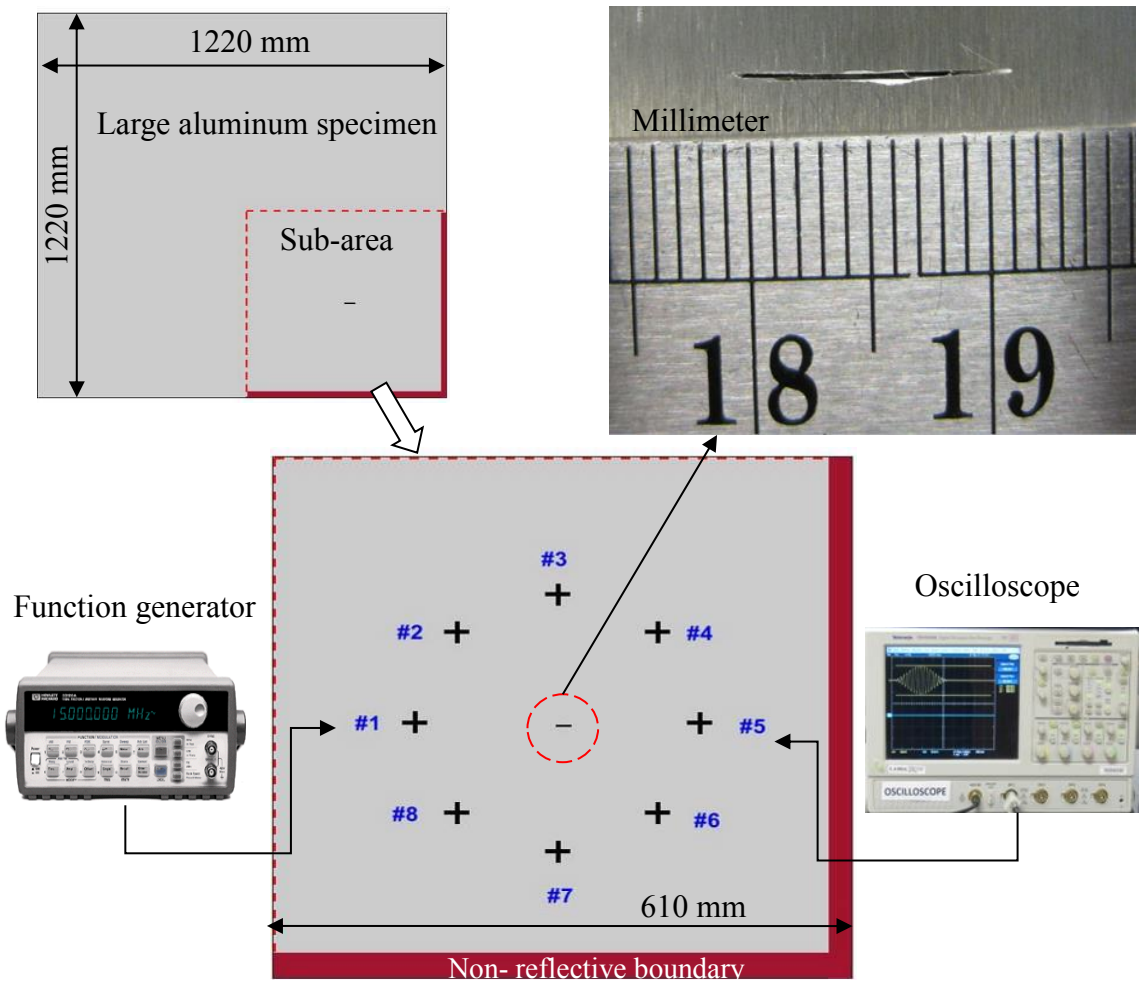

Figure 5.1: Experimental setup of using SHM technique for crack detection.

The flow chart of method B is illustrated in Figure 5.3. In this method, at first, the scattered wave signals were determined using pitch-catch and/or pulse-echo experimental mode/s. The interested area was divided into pixels. The time-of-flight (TOF) of every pixel was determined using the equation of ellipse/circle. The pitch-catch experimental mode involved elliptical orbit (Figure 5.4a) and the TOF can be determined by using the Eq. (5.1)

$$t_{ij} = \frac{\sqrt{(x_T - x_i)^2 + (y_T - y_j)^2}}{v_g} + \frac{\sqrt{(x_i - x_R)^2 + (y_j - y_R)^2}}{v_g} \quad (5.1)$$

where t_{ij} is TOF of scattered signal, x_T, y_T, x_R, y_R, x_i, y_j are the coordinates of transmitter sensor, receiver sensor, and pixel, respectively, v_g is the group velocities of Lamb wave mode. When the pixels lay on the damage orbit of a sensing path then, $t_{ij} = t_d$. The pulse-echo experimental mode involved circular orbit (Figure 5.4b) and the TOF can be determined by using the Eq.(5.2). This orbit has one sensor in its center works as a transmitter and receiver in the same time.

$$t_{ij} = \frac{2\sqrt{(x_i - x_{T,R})^2 + (y_j - y_{T,R})^2}}{v_g} \quad (5.2)$$

The hyperbola orbit obtained by a pitch-catch mode among three sensors (one sensor works as an actuator and the rest of sensors work as receivers) or pulse-echo experiment with two sensors. For the pitch-catch experiment, the hyperbola path can be defined based on the difference in TOF of scattered wave received by two receiver's sensors using the following equation

$$\Delta t_{R12} = \frac{\sqrt{(x_i - x_{R1})^2 + (y_j - y_{R1})^2}}{v_g} - \frac{\sqrt{(x_i - x_{R2})^2 + (y_j - y_{R2})^2}}{v_g} \quad (5.3)$$

where Δt_{R12} is the difference in TOF of scattered signals received by two sensors R1 and R2, $x_{R1}, y_{R1}, x_{R2}, y_{R2}$ are the coordinates of sensors R1 and R2, respectively, v_g is the group velocities of incident S0. Figure 5.4 (c) shows a hyperbola path which is obtained by three sensors and pitch-catch mode. This path has two arms and two foci which represent the two receiver sensors. The damage is located on the arm which is closed to the

sensor who receives the signal early. The second arm is undesirable arm which can be canceled.

For the pulse-echo experiment, two receiver transducers are used to make a hyperbola path using Eq.5.2 (see Figure 5.4d). One of two hyperbola arms represents the damage orbit. The field value of each pixel was determined by using the Gaussian distribution function [27]. The equation of Gaussian distribution function is shown below:

$$f_{ij}(x,y) = \frac{1}{\sigma\sqrt{2\pi}} e^{-\frac{(x-\mu)^2}{2\sigma^2}} \tag{5.4}$$

where $f_{ij}^{k}(x,y)$ is the field value of every pixel $P(x,y)$ of the image of a particular sensing path $T_m - R_n$ (transmitter T_m and receiver R_n), x represents the time of flight at each pixel point $t_{ij}(x,y)$ for the sensing path $T_m - R_n$, μ represents the time of flight of scattered wave packet for sensing path $T_m - R_n$ which can be determined experimentally. The standard deviation, σ which describes the variability or dispersion of a data set, which was taken as half of the time range of wave packet. m,n represent the index of transmitters and receivers, respectively which vary from 1 to total number of transmitters (N_T) and receivers (N_R), such as, $m = 1,2,3,....N_T$ and $n = 1,2,3,....N_R$

To fuse all the images of different sensing paths, we can use summation [12] or multiplication algorithms [58] as follow

$$\begin{aligned} P_{sum}(x,y) &= \sum_{i=1}^{N}\sum_{j=1}^{M} f_{ij}(x,y) \\ P_{mult}(x,y) &= \prod_{i=1}^{N}\prod_{J=1}^{M} f_{ij}(x,y) \end{aligned} \tag{5.5}$$

where $P_{sum}(x,y), P_{mult}(x,y)$ are the total field values of each pixel point using summation or

multiplication algorithm.

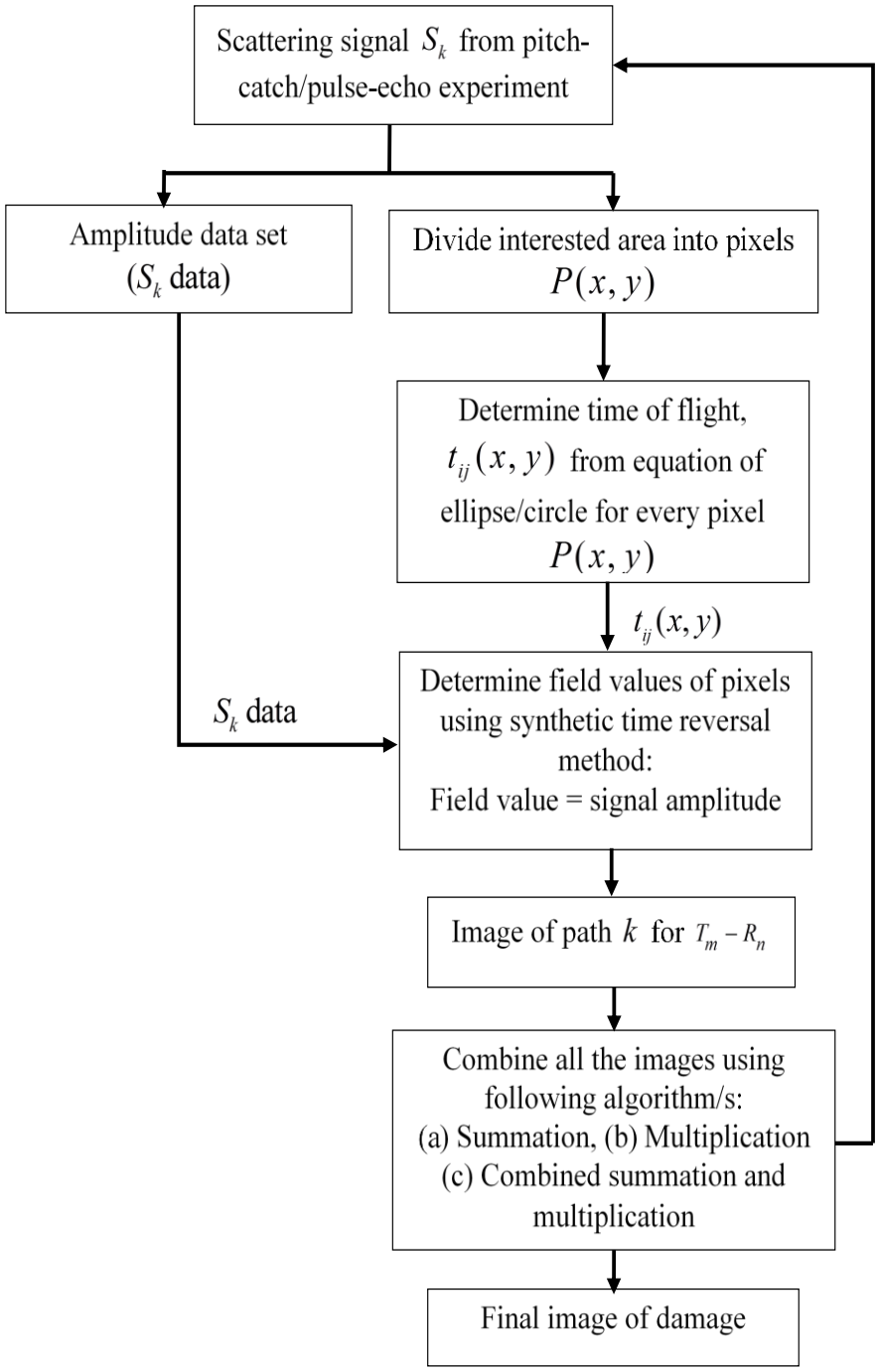

Figure 5.2: Flowchart of imaging method based on synthetic time reversal (method A).

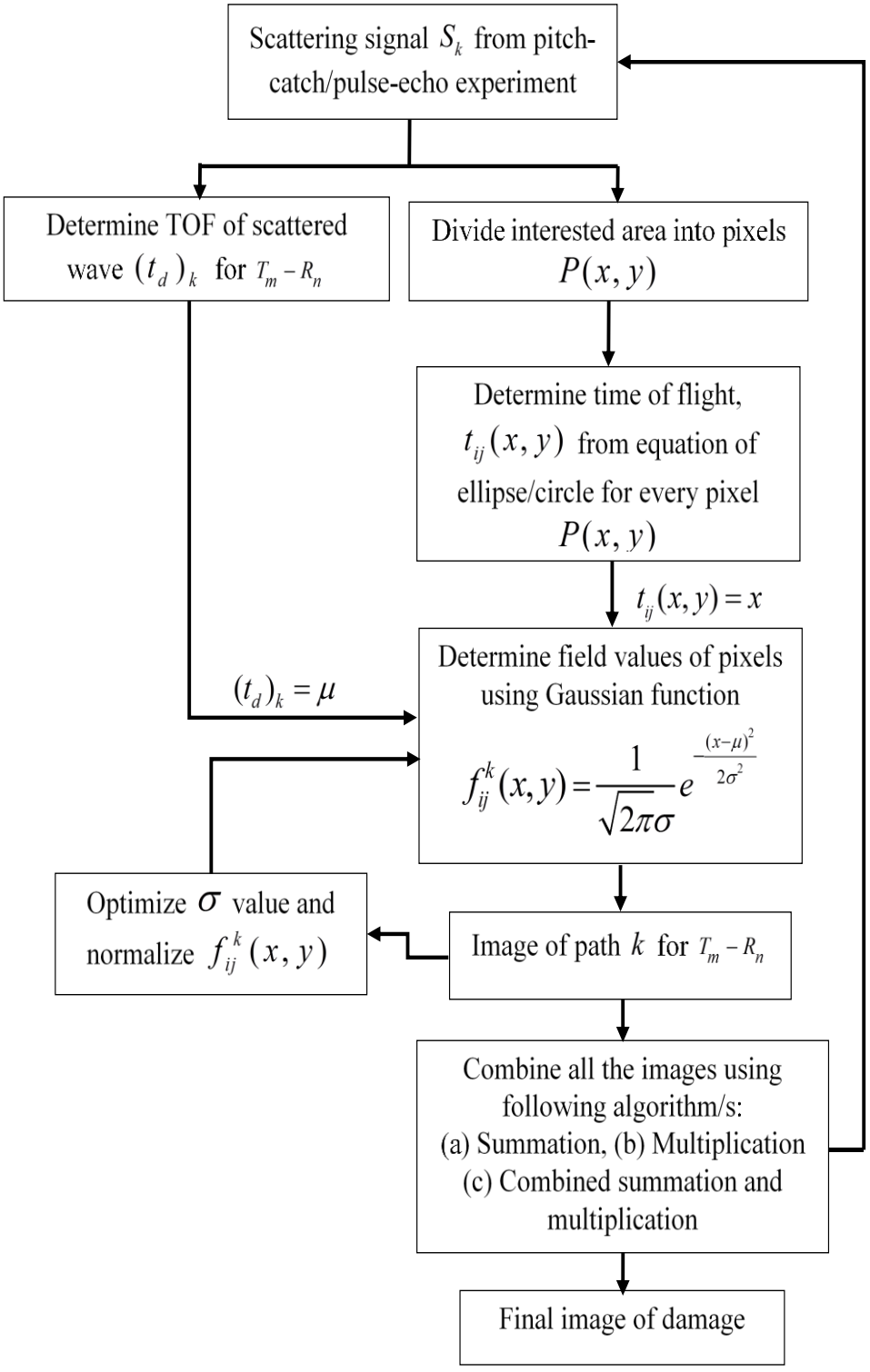

Figure 5.3: Flowchart of imaging method based on Gaussian distribution function (method B).

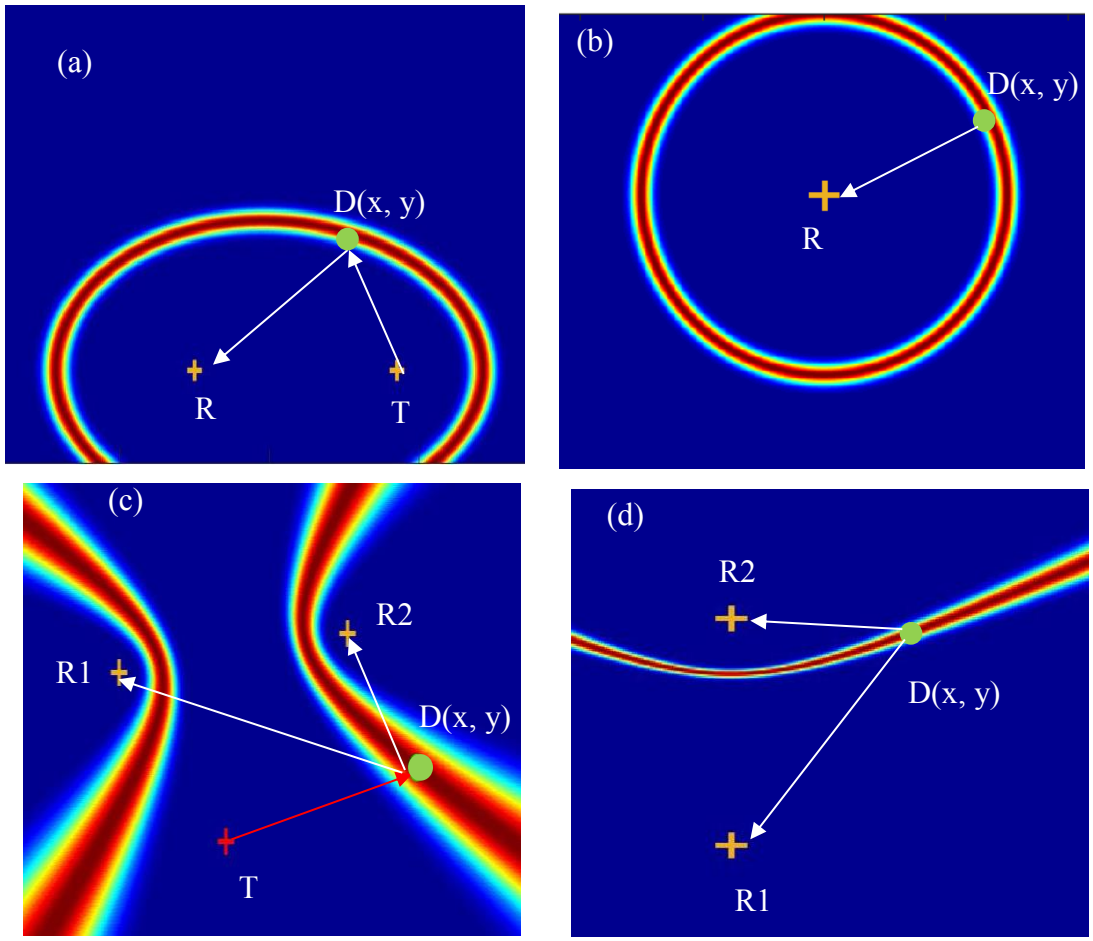

Figure 5.4: Damage orbits; (a) ellipse orbit; (b) circle orbit; (c) hyperbola orbit with pitch-catch mode; (d) hyperbola orbit with pulse-echo mode.

5.2.3 Results of Pitch-Catch Mode

A pitch-catch experiment is performed for pristine plate to measure the baseline signals of different sensing paths. Figure 5.5 (a) shows the baseline signals of different sensing paths where PWAS #3 represents the transmitter, and the rest of sensors represent the receivers. Form this figure; we can indicate that the symmetric Lamb mode (S0) is dominate at center frequency 450 kHz. After measuring the pristine signals, 10-mm horizontal crack centered at (303mm, 300mm) was created. The measured signal is determined for the same previous healthy paths as shown in Figure 5.5 (b).

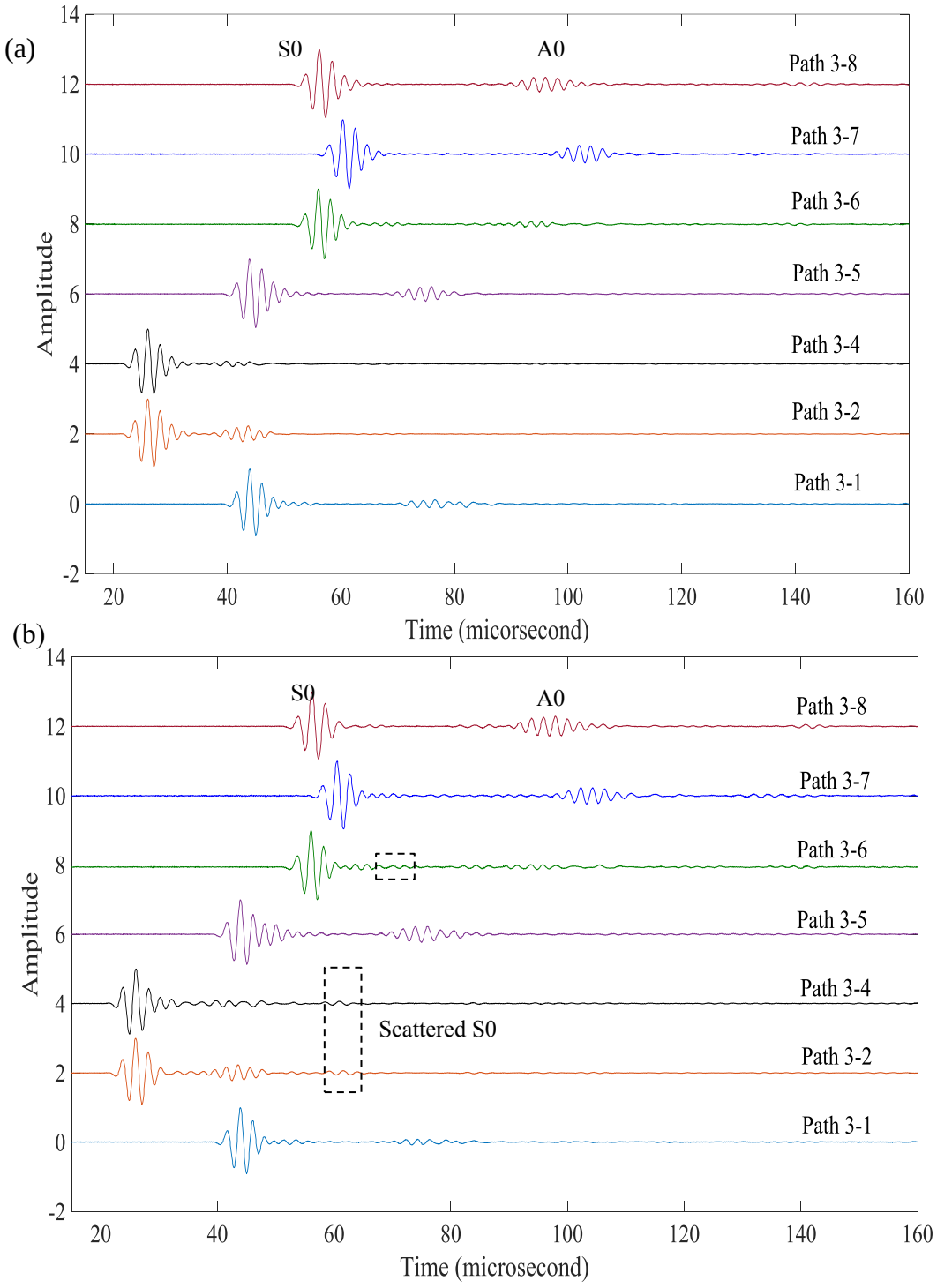

Figure 5.5: Waveform signals of pitch-catch modes: (a) baseline signals without any crack, (b) signals with 10-mm crack. (PWAS #3 as a transmitter and rest of the seven PWAS transducers as receivers).

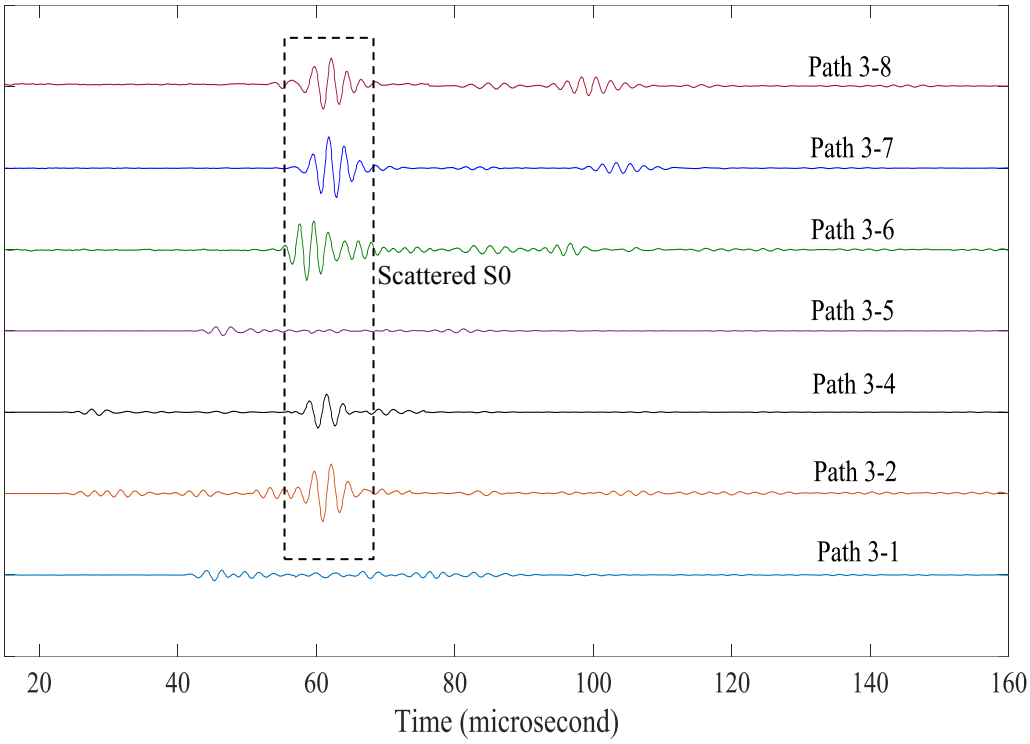

Figure 5.6 Scattered wave signals for various sensing paths. These signals were obtained by the subtraction of baseline signals from the signals with 10-mm crack.

The scattering signals can be obtained by the subtraction of baseline signals from the signals with 10-mm crack as shown the Figure 5.6. The scattering signals are used in conjunction with imaging methods to visualize the structural damage on the interested area. The idea of imaging concept is to find the field values of image pixels from the amplitude of scattering signals based on the synthetic time reversal concept [8]. The pixel with highest field value (brightest pixel) indicates the crack location. The effect of the incident directions on generated scattering waves and imaging results are studied. Figure 5.7 shows three images results of crack detection using three different incident wave's directions. For 0-degree incidence of S0 Lamb wave, the imaging result is very poor since the brightest pixel appeared near the transmitter (Figure 5.7a). This is because the scattered signals are very weak for 0-degree incidence. For 45-degree incidence of S0 Lamb wave, the imaging

result (Figure 5.7b) is fair since the scatter signals are relatively stronger. For 90-degree incidence of S0 Lamb wave (incident wave was perpendicular to the crack orientation), the imaging result (Figure 5.7c) is good since the scattered signals are the strongest of these three cases. One transmitter may not be sufficient to estimate the crack size, but it may predict the location of the crack when it is placed in the best location with respect to the crack.

For estimating the crack size, method A (with summation algorithm) imaging was used with a set of two transmitters (for each transmitter, rest of the seven PWAS transducers were the receivers). The imaging results are illustrated in Figure 5.8. The crack tips can be identified by using the sensing paths of two transmitters. Two dots with maximum field value (index value) can be obtained which represent the two crack tips. Figure 5.8a shows the imaging result after setting a threshold value (about 80% of maximum field value). This image was obtained by using the scatter wave signals of all the sensing paths of transmitter set PWAS #2 and #3. From the zoomed in image, two strong spots can be identified. The distance between the two spots is 9-mm which is close to the crack length. Also, it can be noted that the crack is oriented horizontally as seen from the imaging result. The similar procedure was repeated for transmitter set PWAS#2 and#6. In this case, both transmitters are oriented at 45° to the crack. Based on the imaging results as shown in Figure 5.8b. The crack length can be estimated to be 8-mm. This predicted crack length deviates from the actual crack length since the scatter wave signals were relatively weaker for the 45° incident Lamb wave. When PWAS#2 and #7 were used as transmitters, the predicted crack length was 12-mm as shown in Figure 5.8c.

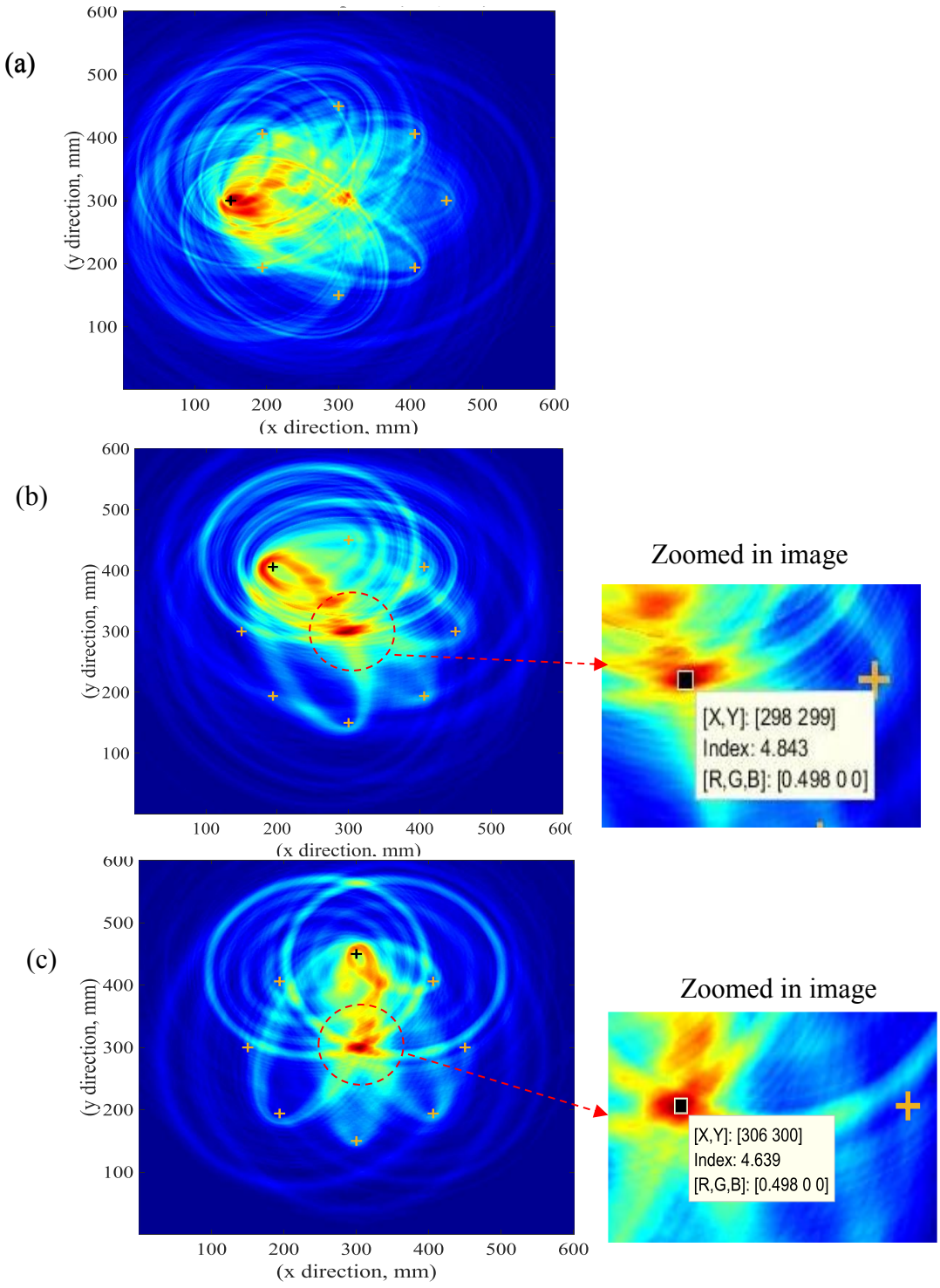

Figure 5.7: Directionality effect on the imaging results of method A. (a) 0° incident (transmitter PWAS #1), (b) 45° incident (transmitter PWAS #2), (c) 90° incident (transmitter PWAS #3).

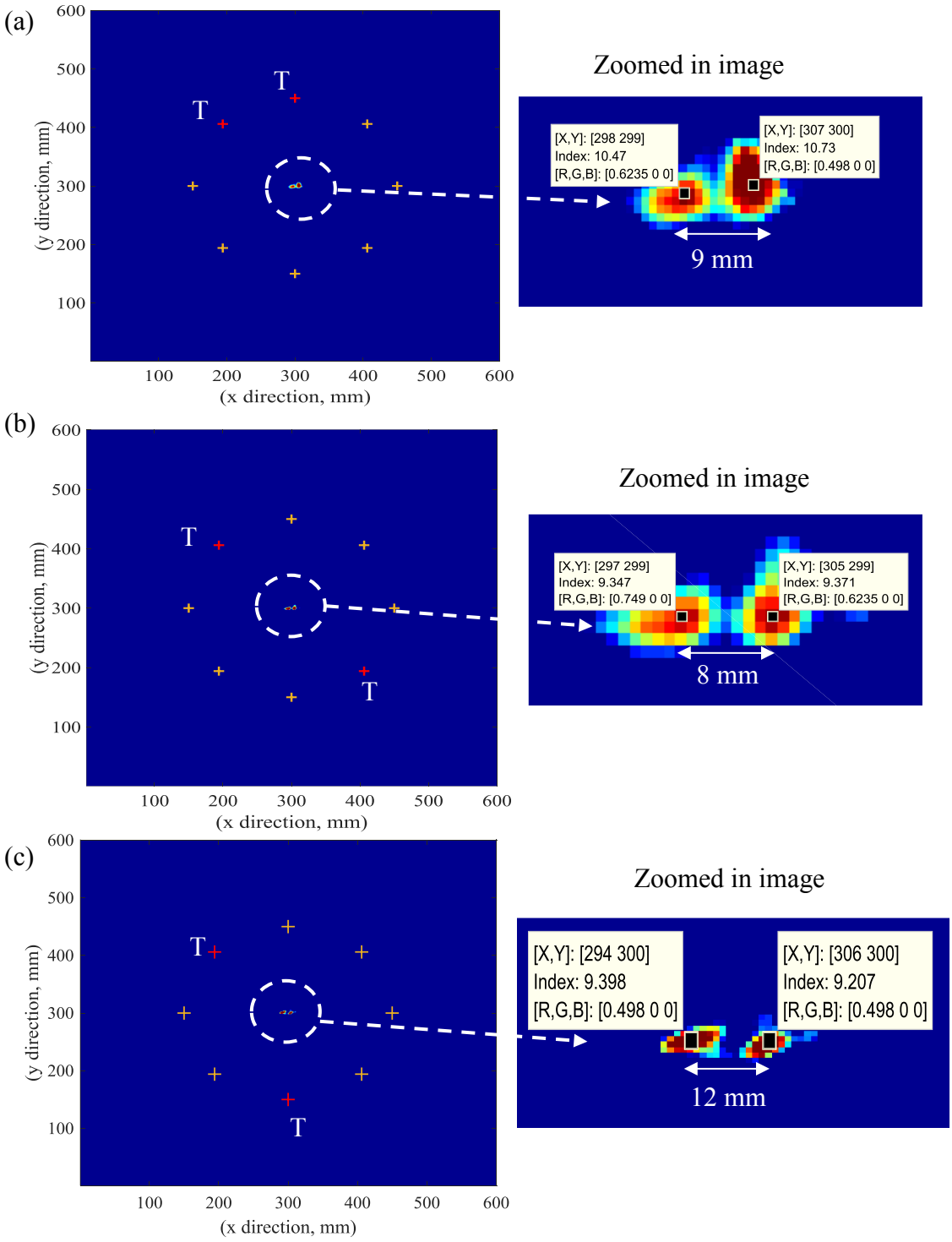

Figure 5.8: Estimation of crack size based on method A imaging results using sensing paths of two transmitters; (a) PWAS #2 and #3; (b) PWAS #2 and #6; (c) PWAS #2 and #7. "T" indicates the transmitter. A threshold value (80% of maximum field value) was set to obtain these images.

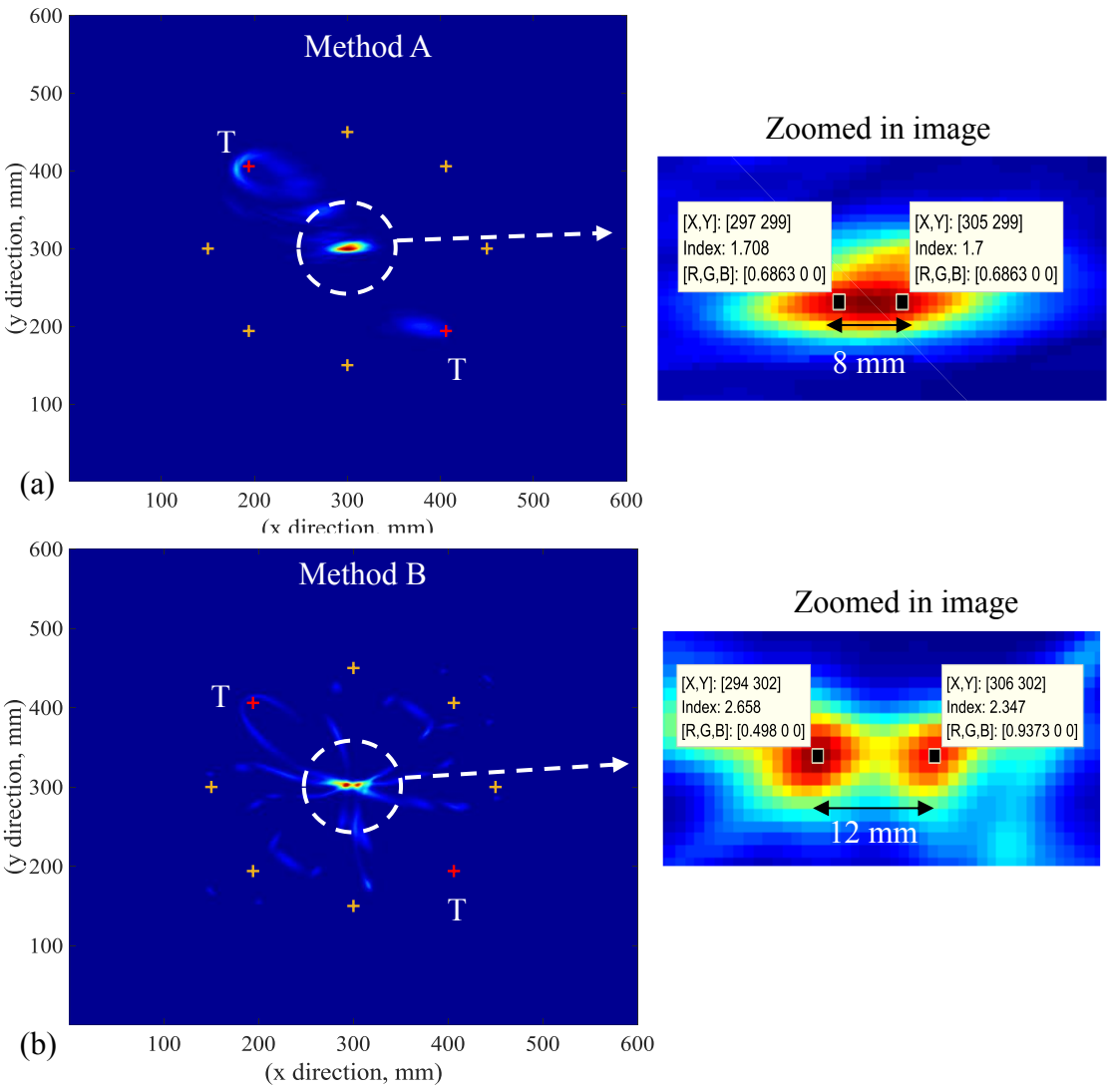

Figure 5.9: Estimation of crack size based on imaging (a) method A and (b) method B with combined summation and multiplication algorithms.

The crack size can also be determined by using a combined summation and multiplication algorithms for determining the total field values of pixels. The advantage of this method was no threshold setting was required. This combined algorithm was used with both method A and method B. The imaging results of both methods are illustrated in Figure 5.9. A set of two transmitters (PWAS#2 and #6) was used for this purpose. All seven sensing paths were used for each transmitter. First, the summation algorithm was applied

to generate the image for individual transmitter. Then, the multiplication algorithm was applied to these images to obtain the final image as shown in Figure 5.9. Hence, two images were fused together providing a clean image by this combined algorithm. Figure 5.9a shows the imaging results of method A which predicts the crack length of 8-mm. Figure 5.9b shows the imaging results of method B which predicts the crack length of 12-mm. Both methods show that the crack is oriented horizontally.

5.2.4 Results of Pulse-Echo

In the pulse-echo experimental mode, each PWAS transducers acted simultaneously as a transmitter and receiver. The S0 Lamb waves were originated from a PWAS, hit the crack and scattered back to the same PWAS. The pulse-echo signals were recorded by the Oscilloscope for all the sensors (PWAS#1,…,8). The waveform signals are shown in Figure 5.10. It can be observed that the path 3-3 and path 7-7 have the strongest scattering waveforms since they are directly perpendicular to the crack. The path 2-2, path 4-4, path 6-6 and path 8-8 have relatively weaker signal since they are at an oblique (45°) incidence. These signals appear to have a similar amplitude as expected. However, path 1-1 and path 5-5 have very weak scattered signals since they are parallel to the crack. Two sensors can be used to localize the damage points as shown in Figure 5.11. For Figure 5.11 (b), there are two intersection points; the first point is inside the inspection area which represents the damage point. The second point is outside the inspection area which represents undesirable point

To estimate the crack size the pulse-echo scattering waveforms were fed into the two imaging methods (method A, B). In both methods, the summation algorithm without any threshold setting was used to determine the total field value at a pixel. The imaging

results using method A and method B are illustrated in Figure 5.12 (a) and (b), respectively. It shows that the sensing paths were circular shapes. The intersecting sensing paths resulted in a horizontal band of bright dots where the field values were concentrated. This is because the scattering waves were originated from this region. From the zoomed in image, two intensive red spots can be identified which represent the crack tips. According to method A, the crack length can be estimated as 9-mm. According to method B, the crack length can be estimated as 12-mm. In both methods, the crack orientation appears to be horizontal. However, method A shows many pixels with a similar level of field values on both sides of the two highest field values along the crack length (which appear as a band of red pixels along the entire crack length. On the other hand, method B shows concentrated bright pixels at the two crack tips. In both experimental modes (pitch-catch and pulse-echo), it appears that method A slightly underestimate the actual crack length whereas method B slightly overestimate the actual crack length.

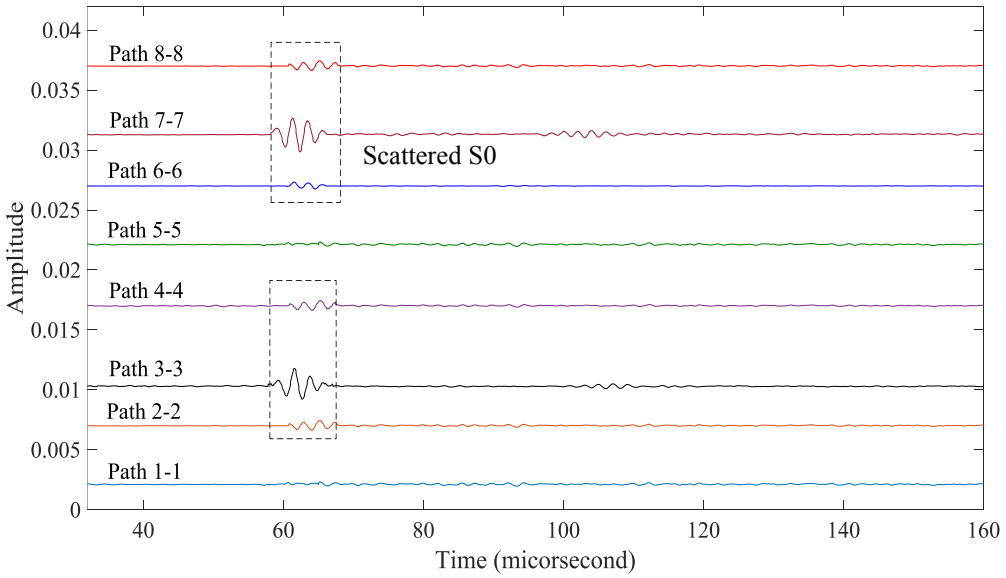

Figure 5.10: Waveform signals of pulse-echo experiment.

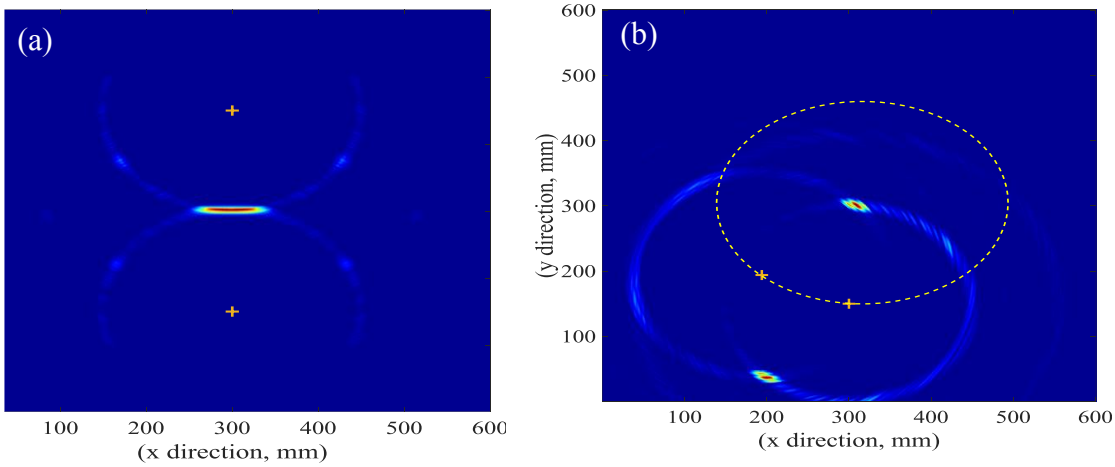

Figure 5.11: Imaging results using pulse-echo mode and two sensors; (a) PWAS #3 and #7; (b) PWAS #7 and #8.

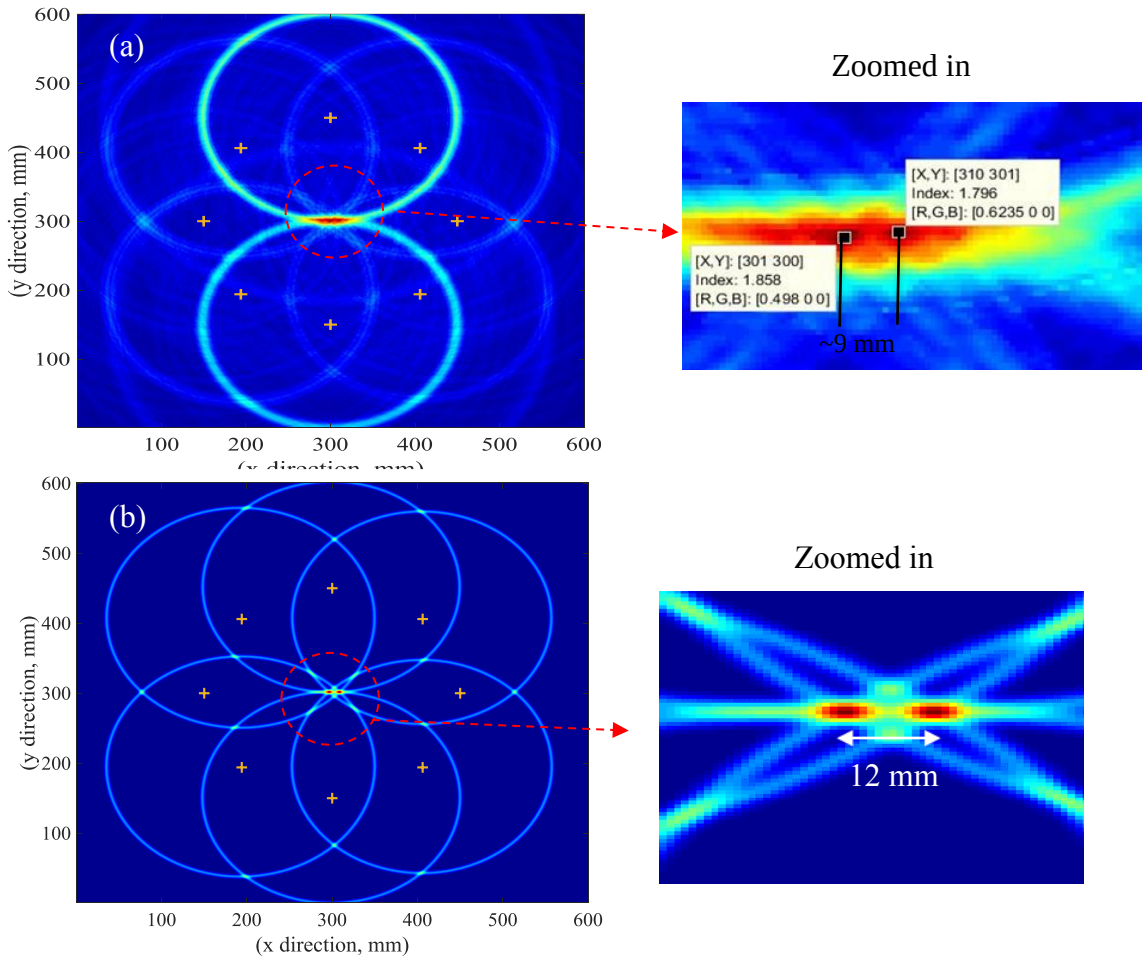

Figure 5.12: Crack size estimation for pulse-echo experimental mode by using (a) method A, (b) method B (both methods used the summation algorithm; no thresholding applied).

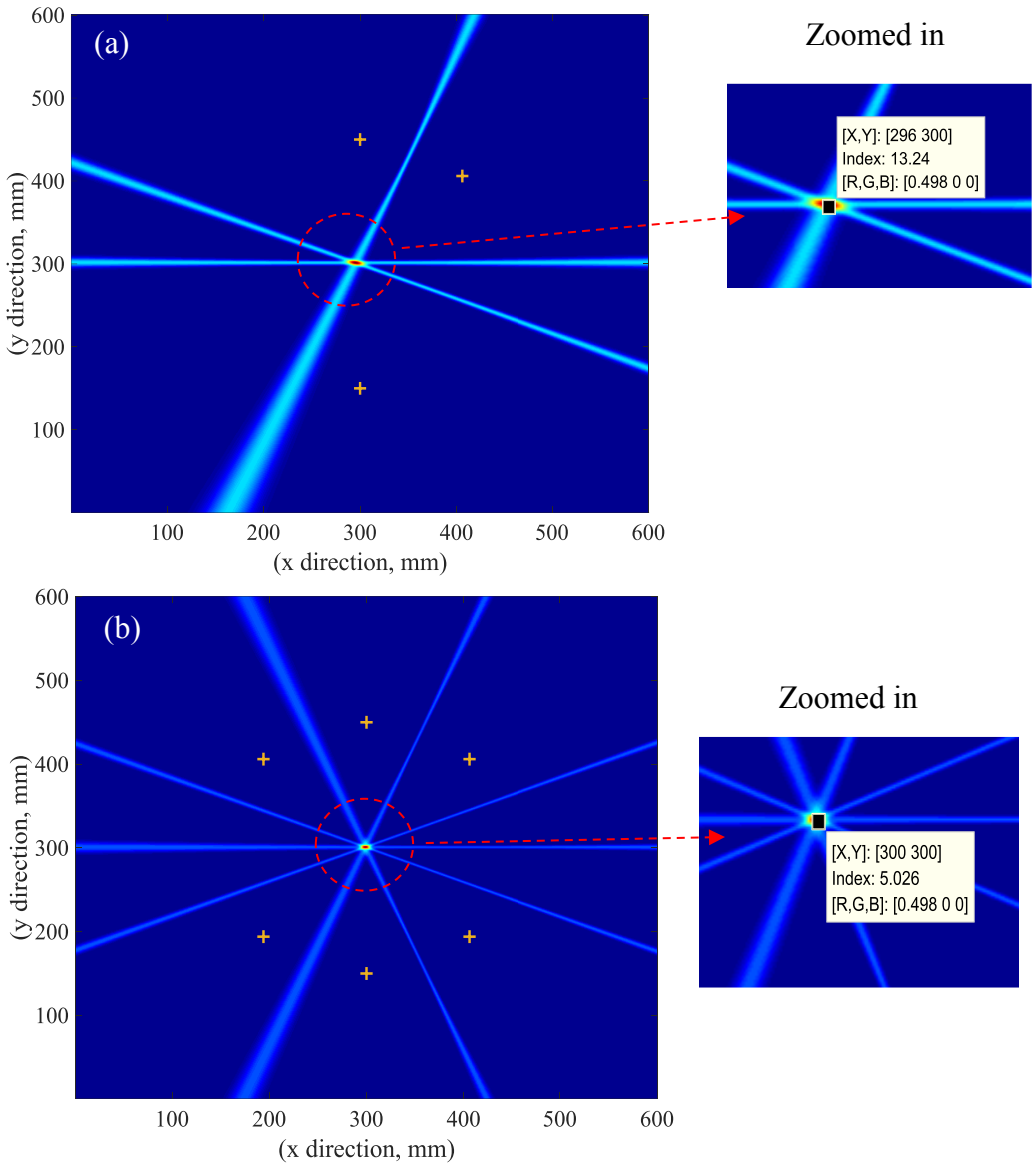

Figure 5.13 Crack localization using hyperbola path with pulse-echo experiment; (a) using three sensors; (b) using six sensors.

The hyperbola path can be used for identifying damage structure based on difference in time of flight of scattered waves received by two sensors. For the pulse-echo experiment, three sensors can localize the crack using the difference in TOF values and Gaussian distribution function as shown in Figure 5.13a. The imaging result becomes more accurate when the number of used sensors is increased as shown in Figure 5.13(b).

5.3 THROUGH-HOLE DETECTION AND SIZE ESTIMATION

Lamb wave-based imaging methods were used to detect through-thickness hole with various diameters. The pitch-catch experiments were conducted in a plate-like specimen. The details of the experimental setup and imaging results are discussed next.

5.3.1 EXPERIMENTAL SETUP

An aluminum plate-like specimen with dimension 600 mm × 600 mm × 1.6 mm was used in this experiment (Figure 5.14). A 1-mm through-thickness hole was manufactured at a location with coordinate (315 mm, 249 mm) while the bottom left corner was the origin. The specimen was instrumented with six PWAS transducers (PWAS#0, 1, 2… 5). These transducers were bonded at arbitrary locations around the hole. A function generator was used to generate 3-count tone burst signals at a center frequency 450 kHz and an Oscilloscope was used to record the signals. At this frequency-thickness product, the symmetric Lamb wave was dominant in the aluminum plate. The baseline signals were recorded for all possible sensing paths corresponding to the 1-mm hole. The hole size was enlarged gradually: starting from 1 mm to 1.5 mm, 2 mm, 2.5 mm, and 3 mm. The waveform signals were measured for each hole size at all possible sensing paths.

5.3.2 MEASURED WAVEFORMS AND IMAGING RESULTS FOR VARIOUS HOLE SIZES

The scattering waveforms are the key elements for imaging methods. The scattered waveforms were obtained by subtracting the baseline signals from the measured signals for various hole sizes. The measured signals for 1-mm and 1.5-mm hole are shown in Figure 5.15 (a) and (b), respectively. The signals received by all the five sensors (e.g., path 0-1, 0-2, 0-3, etc.) for PWAS#0 as a transmitter. The signals corresponding to 1-mm hole were taken as baseline signals. The waveforms in Figure 5.15 shows that all of them have a

strong S0 Lamb wave packet and weak A0 Lamb wave packet as expected at 450 kHz center frequency. The scattered waveforms for 1.5-mm hole are shown in Figure 5.16.

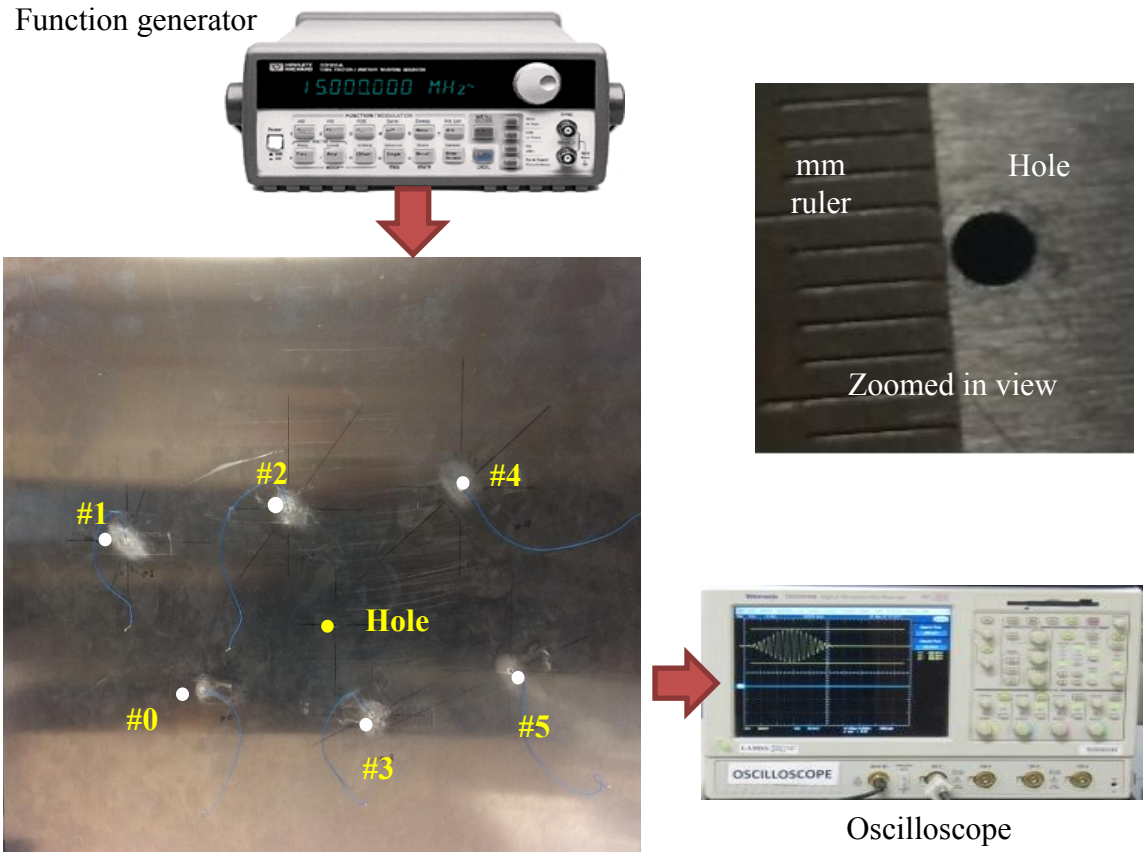

Figure 5.14: Instrumented aluminum plate with a through-thickness hole. The hole size was enlarged gradually: starting from 1 mm to 1.5 mm, 2 mm, 2.5 mm, and 3 mm.

It can be observed strong scattered waves (S0) in all the waveforms. Some paths have relatively stronger signal than others. For example, in this case, scatter signal of path 0-1 stronger than that of path 0-4. The hole-size significantly affects the scattering as illustrated in Figure 5.17. Two particular sensing paths 0-2 (transmitter PWAS#0 and receiver PWAS#2) and path 2-4 (transmitter PWAS#2 and receiver PWAS#4) were considered for illustration. Stronger scattered signals can be observed as the hole-size increases. Both paths show the similar results.

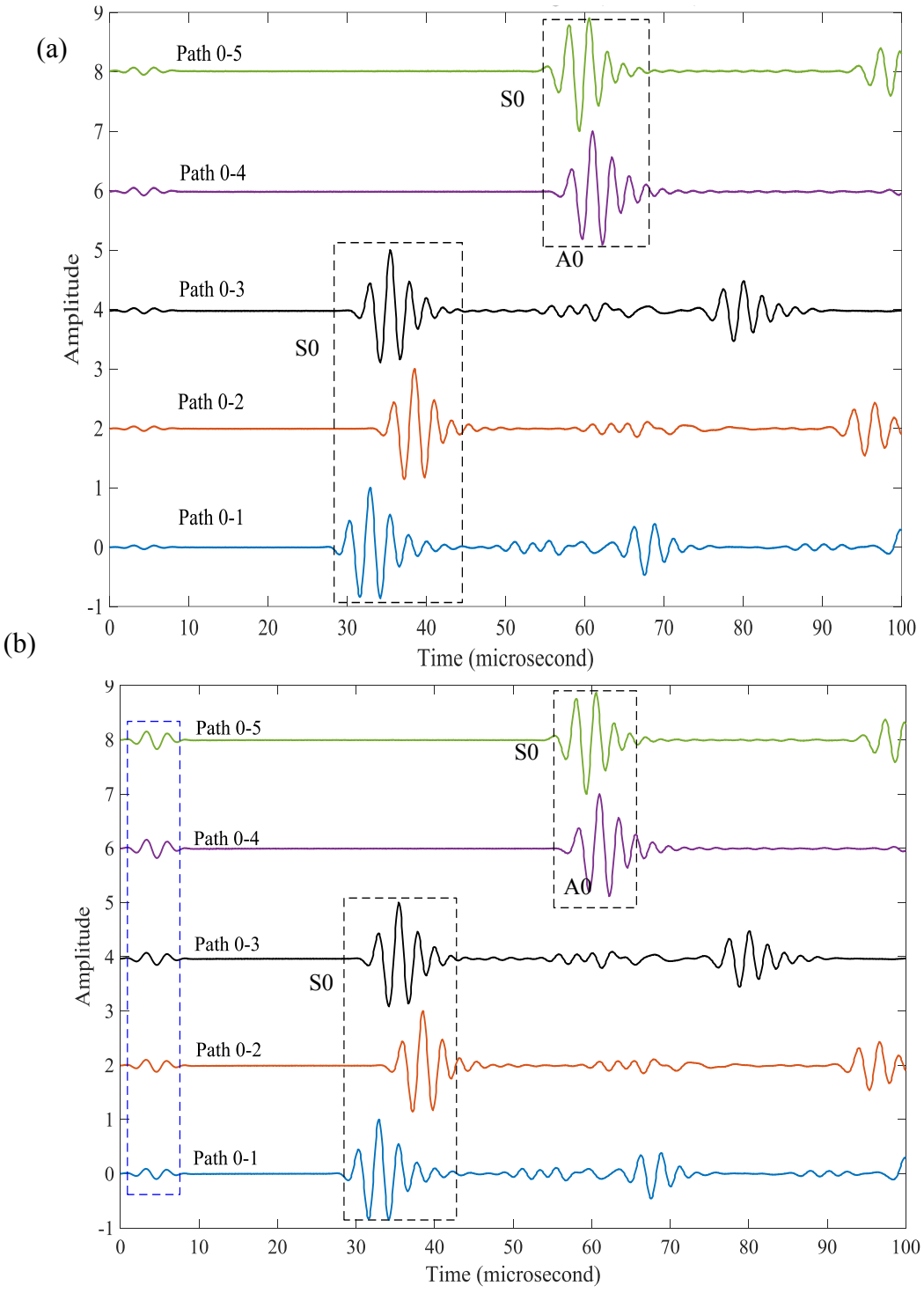

Figure 5.15: The waveform signals for (a) 1-mm hole, (b) 1.5-mm hole. The excitation signal was given from PWAS #0 and received by rest of the PWAS transducers

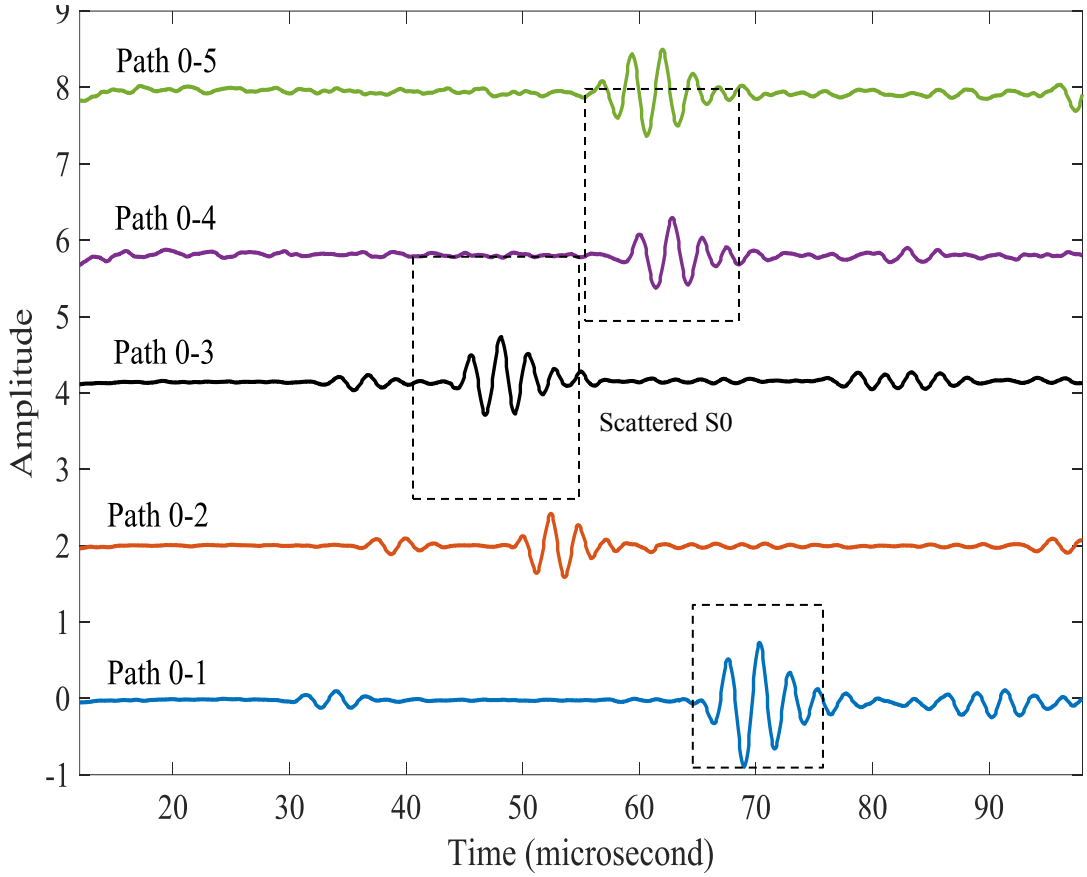

Figure 5.16 Scattering signals at various receivers for 1.5-mm hole while the excitation was given by PWAS #0. These scattered signals were determined by subtraction of baseline signals from the measured signals for 1.5-mm hole.

Method A imaging method was used for hole localization and size estimation. Both summation and multiplication algorithms were used. The imaging results for three hole sizes (2-mm, 2.5-mm, 3-mm diameter) are presented in Figure 5.18. The imaging results of summation algorithm are shown in the left side and that of multiplication algorithm are shown in the right side of Figure 5.18. The results of the multiplication algorithm are shown as a zoomed-in view for clarity. The sensing paths of four transmitters (PWAS#0, 2, 3, 4) were used to produces these images. These transmitters were chosen since they produced relatively stronger scattering waves.

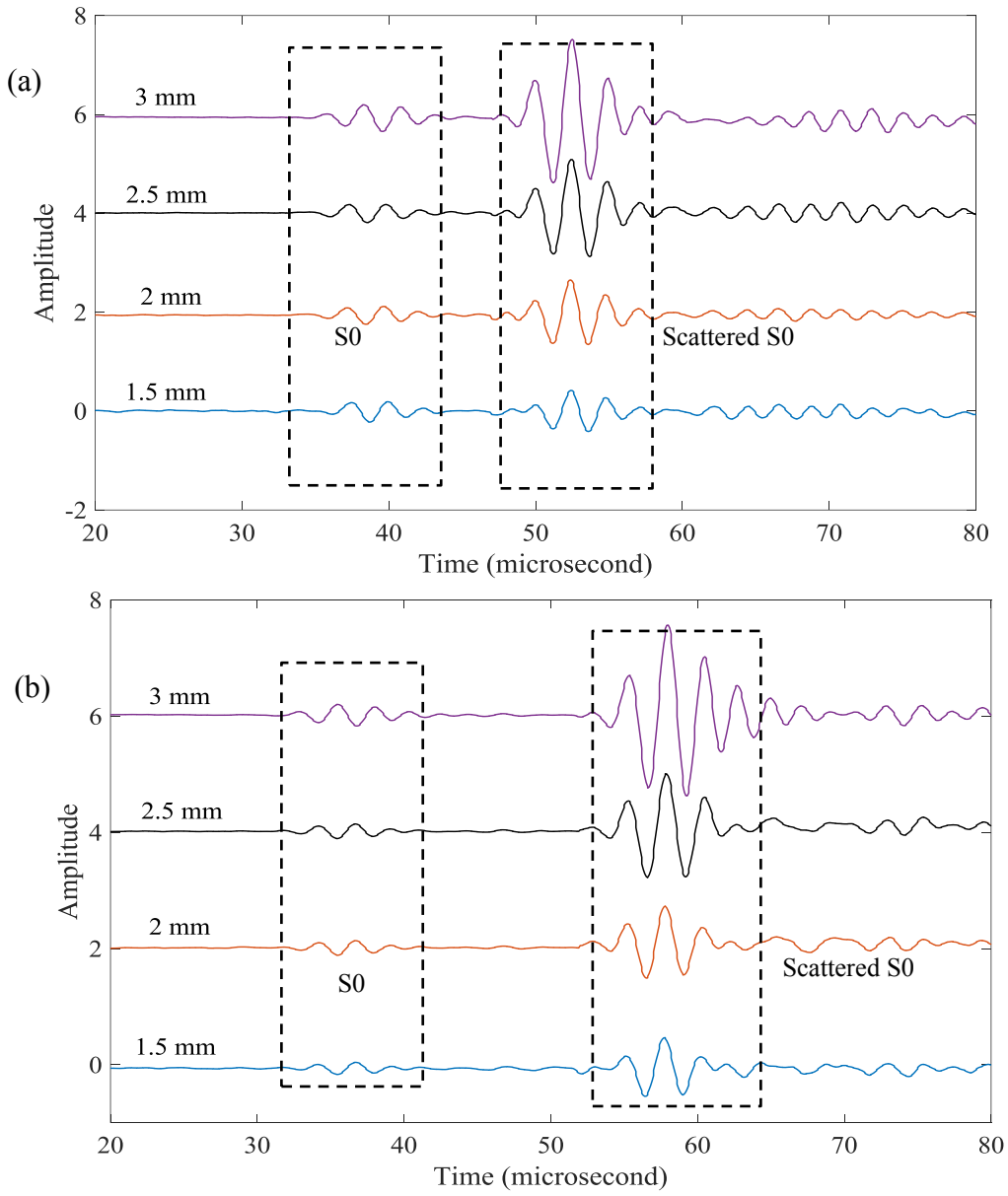

Figure 5.17: The scattering signals of different hole-plate diameters; (a) Sensing path 0-2; (b) Sensing path 2-4.

In Figure 5.18, it can be observed that as the hole size increases the imaging result gets better. Because larger hole produced stronger scattering waves. The hole can be localized based on the highest field value of pixels. For a larger hole, the brighter pixels become more concentrated and provide accurate localization. For example, the imaging

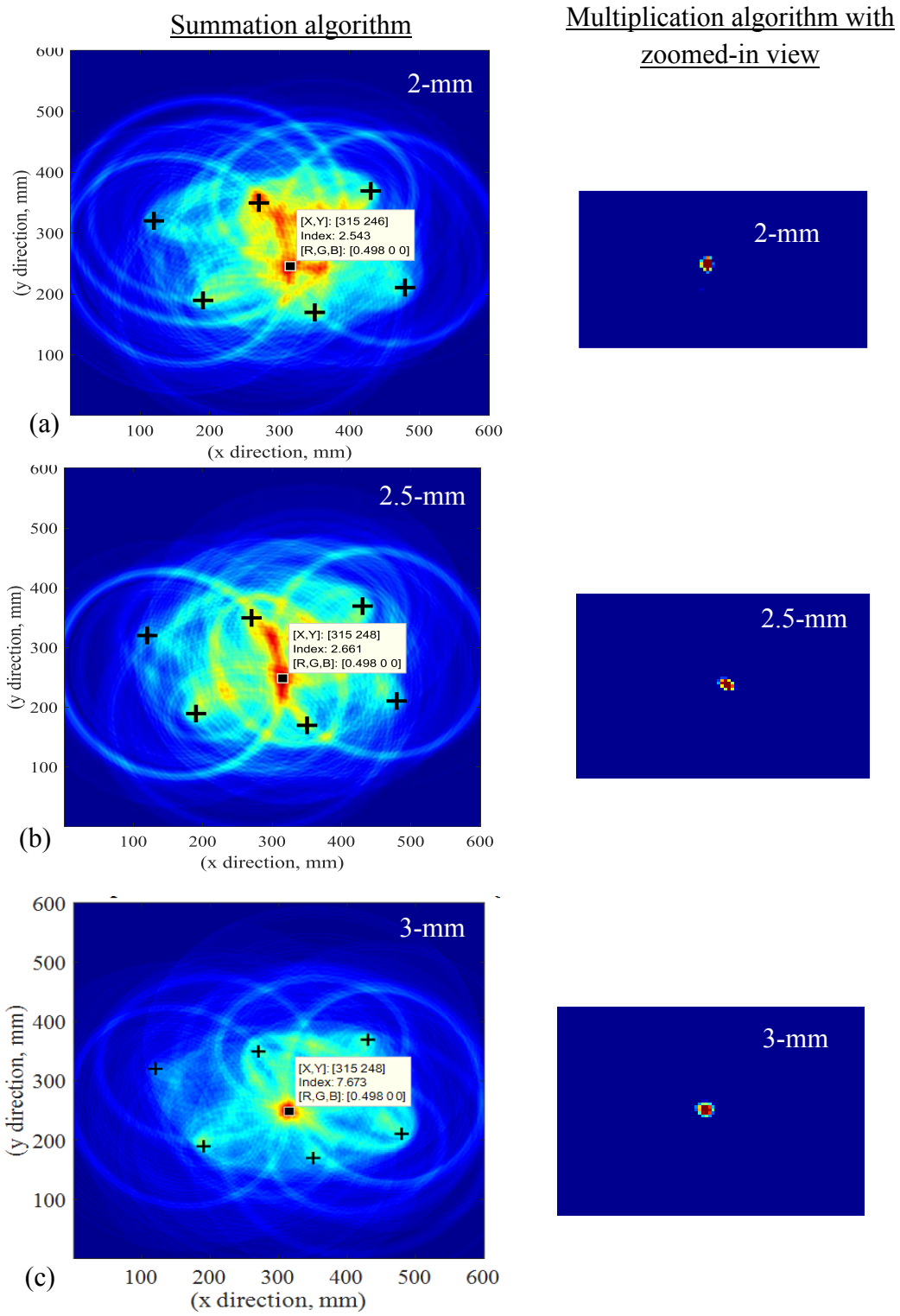

Figure 5.18: Imaging results using summation (left side) and multiplication (right side) algorithms for various hole-sizes: (a) 2-mm, (b) 2.5-mm, (c) 3-mm diameter.

localization result predicts the hole to be located at (315 mm, 248 mm) whereas the actual location of the hole is at (315 mm, 249 mm). The multiplication algorithm provided the similar results as the summation algorithm. The only difference is that the multiplication algorithm provides a cleaner image than the summation algorithm. The multiplication algorithm results of Figure 5.18 shows circular shape brighter pixels. These circular brighter pixels suggest that the damage is a point source or circular shape. However, in this case, the size of the hole is difficult to predict since the hole-size is very small. It may need further investigation to determine the smaller size holes. Despite, the imaging methods could successfully localize the smaller hole. Method B also predicted the similar results as method A and not repeated for the sake of brevity.

5.3.3 Pulse-Echo Results

Two sensors can be used to localize the damage defect in the interested area using pulse-echo experiment. In this work, a pulse-echo experiment was implemented using PWAS #0 and PWAS #3.

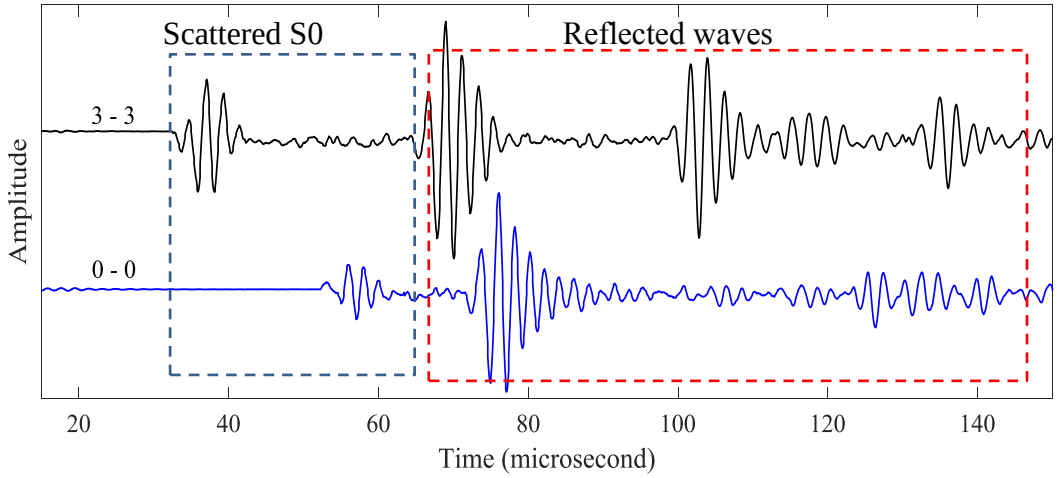

Figure 5.19: Pulse-echo signals of path 0-0 and path 3-3 at frequency excitation 450 kHz.

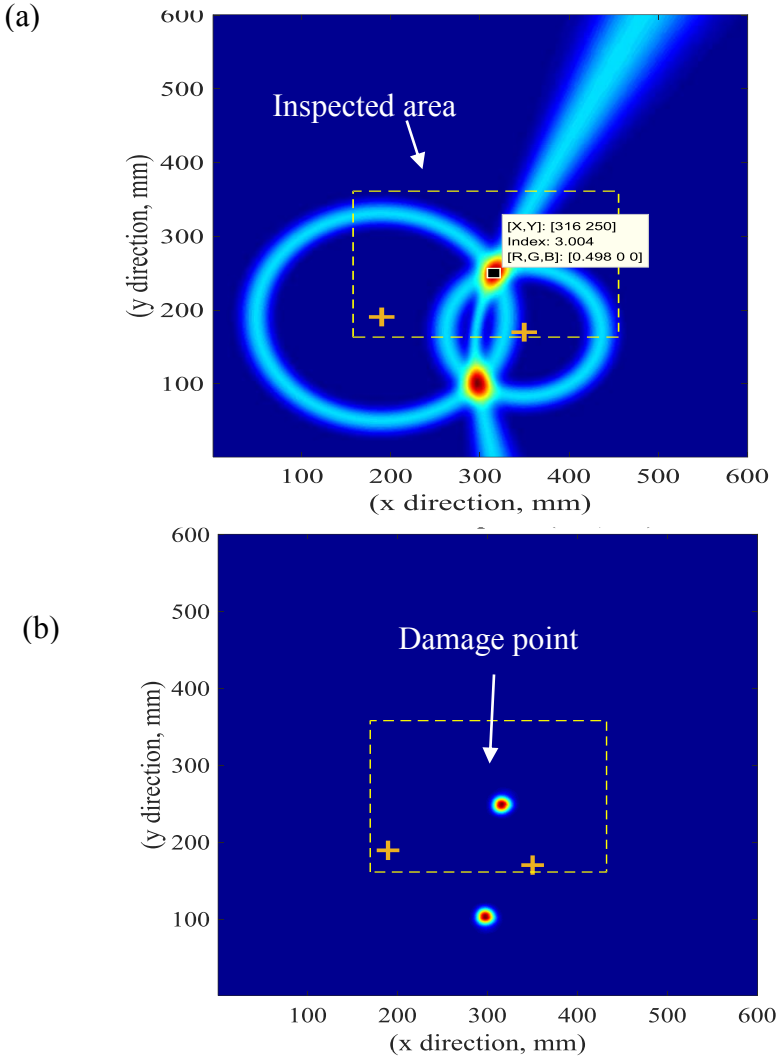

Figure 5.20: Imaging results of using two sensors with pulse-echo mode; (a) Using summation algorithm for image construction; (b) Using multiplication algorithm for image construction.

The excitation signal is 3-count tone burst at center frequency 450 kHz. Figure 5.19 shows two pulse-echo signals of sensing path 0-0, where the Lamb wave signal travel form PWAS #0 and received by the same sensor and path 3-3. We can observe the scattered waves of the damaged hole in both signals. From these two signals, we can generate three damage orbits, which are two circular orbits and one hyperbola orbit. These three paths

give two intersection points. The first point inside the interested area which represents damage point. The second intersection point is outside the interested area which represents an undesirable point. The Gaussian distribution function is used to determine the field values of pixels points of the interested area. To fuse all three images, we used summation and multiplication algorithms. The imaging results of using two sensors are shown in Figure 5.20. In Figure 5.20 (a), three paths (two circular paths and one hyperbolic path) are intersection at two points. The red spot point inside the interested area represents the damage point. The summation algorithm is used to fuse all the three images of these three paths. In Figure 5.20 (b), the multiplication algorithm is used to fuse the three images of these three paths to get two red spot points.

CHAPTER 6
FEM SIMULATION OF LAMB WAVES INTERACTION WITH CRACK IN METALLIC PLATE

In this chapter, the interaction of Lamb waves with crack damage are studied numerically using multi-physics finite element method (MP-FEM). The various incident wave are simulated to study the effect of an incident wave direction on the generated scattered wave. A hybrid global-local (HGL) approach was used in conjunction with the imaging methods for the numerical simulation. The HGL approach allowed fast and efficient prediction of scattering wave signals for Lamb wave interaction with crack from various incident directions. The simulation results showed the directionality effect of the scattering wave signals and suggested an optimum transmitter-sensor configuration. The scattering signals of different sensing paths are determined.

6.1 INTRODUCTION

The simulations of Lamb wave propagation on a plate using numerical methods are sufficient methods to understand the interaction of Lamb wave with damage [59]. The interaction of Lamb wave with various defects has been studied intensively in many researches. The wave propagation on isotropic plates are studied analytically, numerically and experimentally in 1-D and 2-D [60]. An analytical model was developed to get the time and frequency domain of pitch-catch signal. The authors used the multi-physics finite element method (MP-FEM) to simulate wave propagation for a pitch-catch mode. The results of waveform signals show a good matching among analytical, FEM and

experimental results. The emanated scattering waves from the interaction of Lamb waves with defects are characterized by Golato [61]. The results show that the scattering waves are strongly function of the crack size and the frequency. A new approach was developed by Shen and Giurgiutiu [62] to study the Lamb wave propagation and interaction with a damage. In this approach, the Analytical method is combined with Finite Element approach for local damage area to find an efficient solution for 2-D guided wave propagation and interaction with damage. The crack in the rivet hole is detected using global analytical with local FEM approach [63]. The authors developed the scatter cubes of complex-valued of wave-damage interaction coefficients which describe the three dimensions of interaction of Lamb wave modes with the damage. The results of scatter cubes, which are function of frequency excitation signal, incident direction and azimuth direction, are fed to into the exact analytical framework to get the time domain of sensing paths signals.

6.2 2D-FINITE ELEMENT MODELING

In this chapter we describe the FEM simulation of the experimental work which is explained in Chapter 5. The experimental setup shown in Figure 5.1 was modeled with a 2D FEM analysis as sketched in Figure 6.1. In this work, we use multi-physics finite element method (MP-FEM) to model the interaction of Lamb wave with horizontal crack. We used coupled field element (SOLID5-Ansys15) to simulate the piezoelectric effect of transmitter and receiver- PWAS. The Lamb waves are generated by applying the electric field on the surface of PWAS transmitter. The propagating signals are received as electric signals by PWAS receivers. For meshing the whole plate, we use eight node structure element (SOLID45). For construction non-reflective boundaries NRB around the plate, we used COMBIN14 spring-damper element to die out the reflected waves from the boundary

edges. The width of non-reflective boundary across the plate surface is 40 mm which determined based on the criteria developed by Shen and Giurgiutiu [64]. The 18 mm-crack is created between two discontinuous volumes. After the meshing these two volumes, there are two discontinuous sets of nodes cover the distance along the crack faces. So, the solid elements are disbanded along the crack faces. The size of element is adopted 1-mm across the surface and 0.5-mm across the thickness. A 3-count tone burst signal at center frequency 450 kHz is used to excite the transmitter. The time step is 0.2-microsecond. The details of full scale of FEM simulation is shown in the Figure 6.2.

In this simulation, we studied the effect of the incident wave direction on the interaction of Lamb wave with the crack damage. Figure 6.3 shows the snapshot images of Lamb wave transmits from PWAS#5 (0° incident wave direction.) and interacts with the crack damage. The snapshot image at 10-microsecond shows two independent Lamb wave modes S0 and A0. For 35-microsecond snapshot image, we can see a weak scattered S0 wave at the crack tip which is generated from the interaction of incident S0 mode with the crack damage. Also, we can see a very weak scattered wave emanated from PWAS#4 after hitting it by the incident S0 mode. In the second simulation, we used PWAS#4 as a transmitter to get 45° incident wave direction. In this case, the generated scattered S0 from the crack damage becomes strong and apparent as shown in 32-microsecond snapshot image of Figure 6.4. The scattered A0 (slower mode) becomes apparent around the crack damage as shown in the 65-microsecond snapshot image. For both scattered modes, the maximum scattering amplitude occurred when the Lamb waves were scattered at 45°. In the second simulation, we used PWAS#3 as a transmitter to get 90° incident wave direction. The generated scattered waves are the strongest among all the cases of various incident

Lamb wave directions. Figure 6.5 show the snapshot images at different time of flight. We can observe very strong scattered waves generated by the crack damage. In this case, the maximum scattering amplitude occurred when the Lamb wave is scattered at 90°. Based on the above results, we can conclude that the 90° incident wave direction is the best case to give the strongest scattered waves.

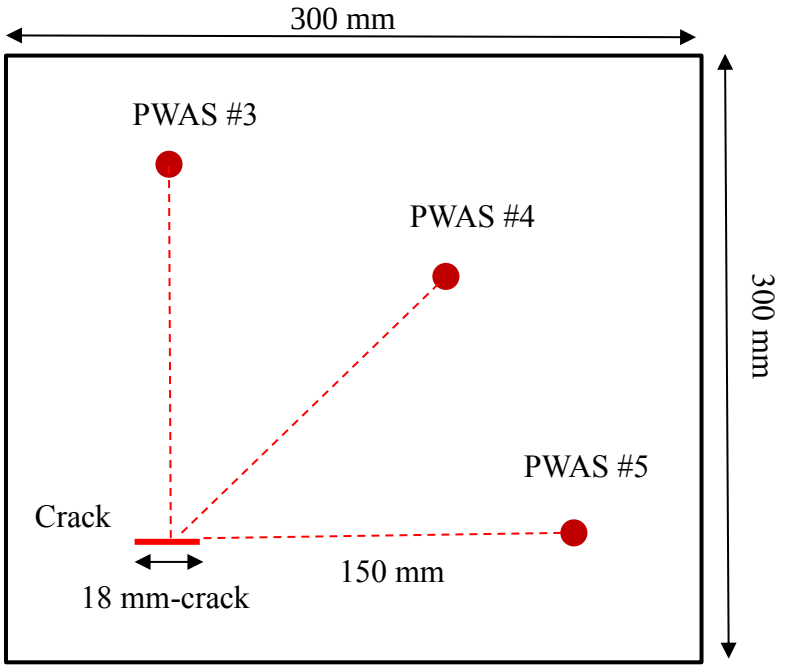

Figure 6.1: The configuration of the model for 2-D multi-physics FEM simulation.

6.3 HYBRID GLOBAL ANALYTICAL WITH LOCAL FEM APPROACH

In the past, many efforts have been made to develop analytical or numerical models of waves propagation and interaction with damages [65] [66]. Numerical and experimental studies were adopted to analyze a crack damage which is located at structural interface. This crack is subjected to pure shear loading and ultrasonic loading. The results show the scattered waves generated by the interaction of elastic waves with the crack [67]. The Local Interaction Simulation Approach (LISA) was developed to study the nonlinear interaction

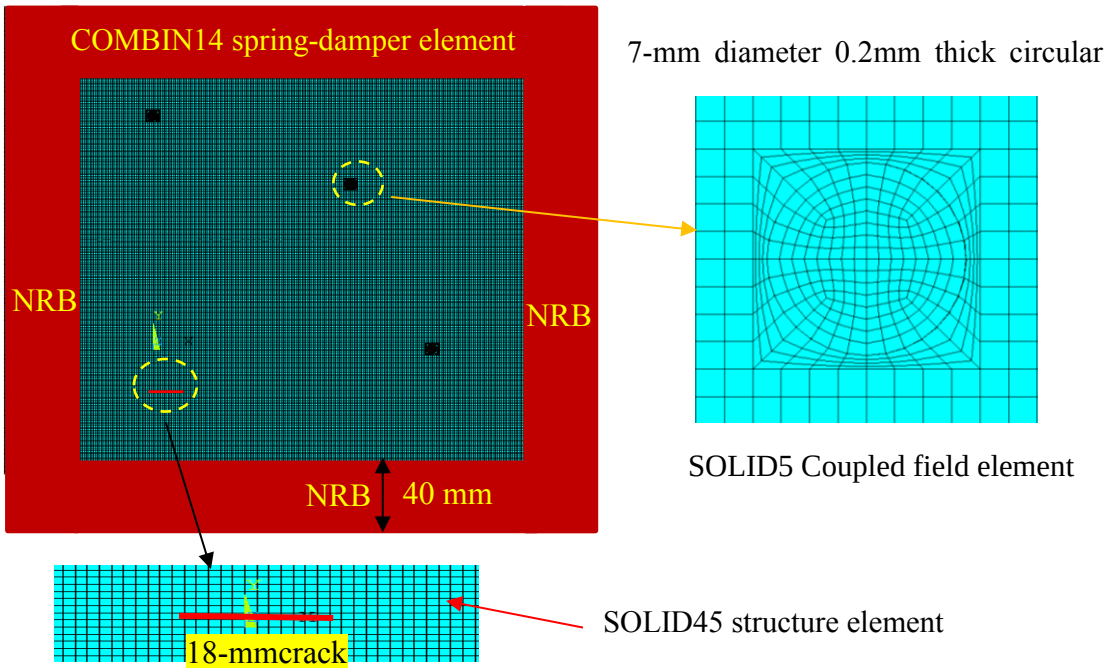

Figure 6.2: Multi-physics FEM modeling using commercial FEM ANSYS 17.

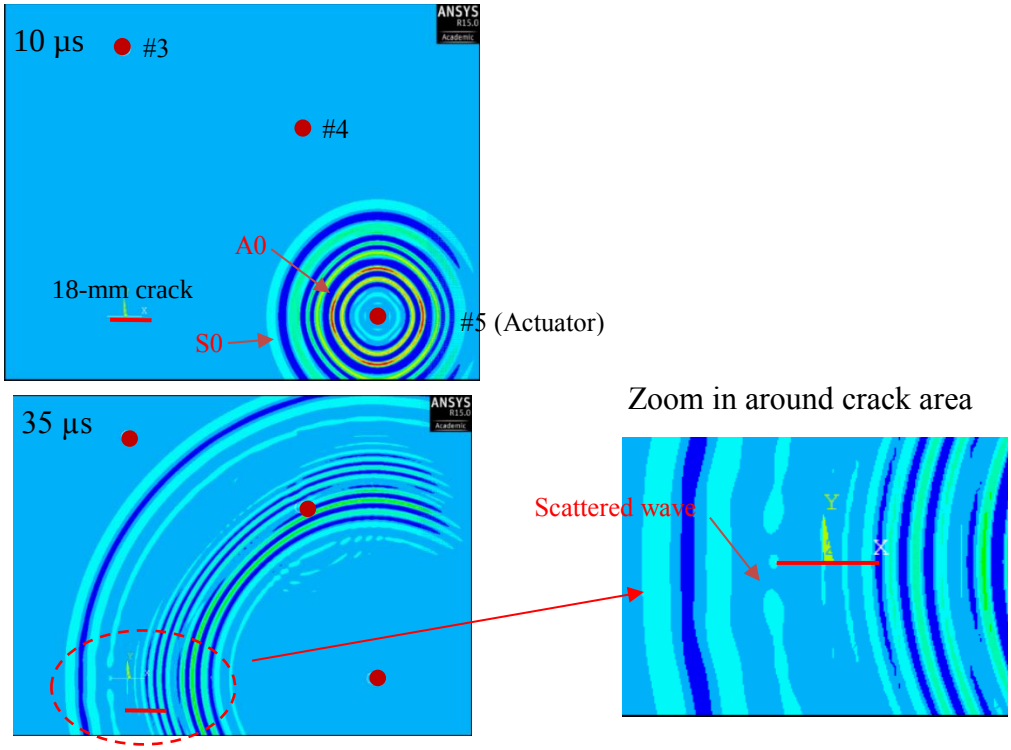

Figure 6.3: Snapshots of simulation 0° incident Lamb wave propagating and interaction with a crack.

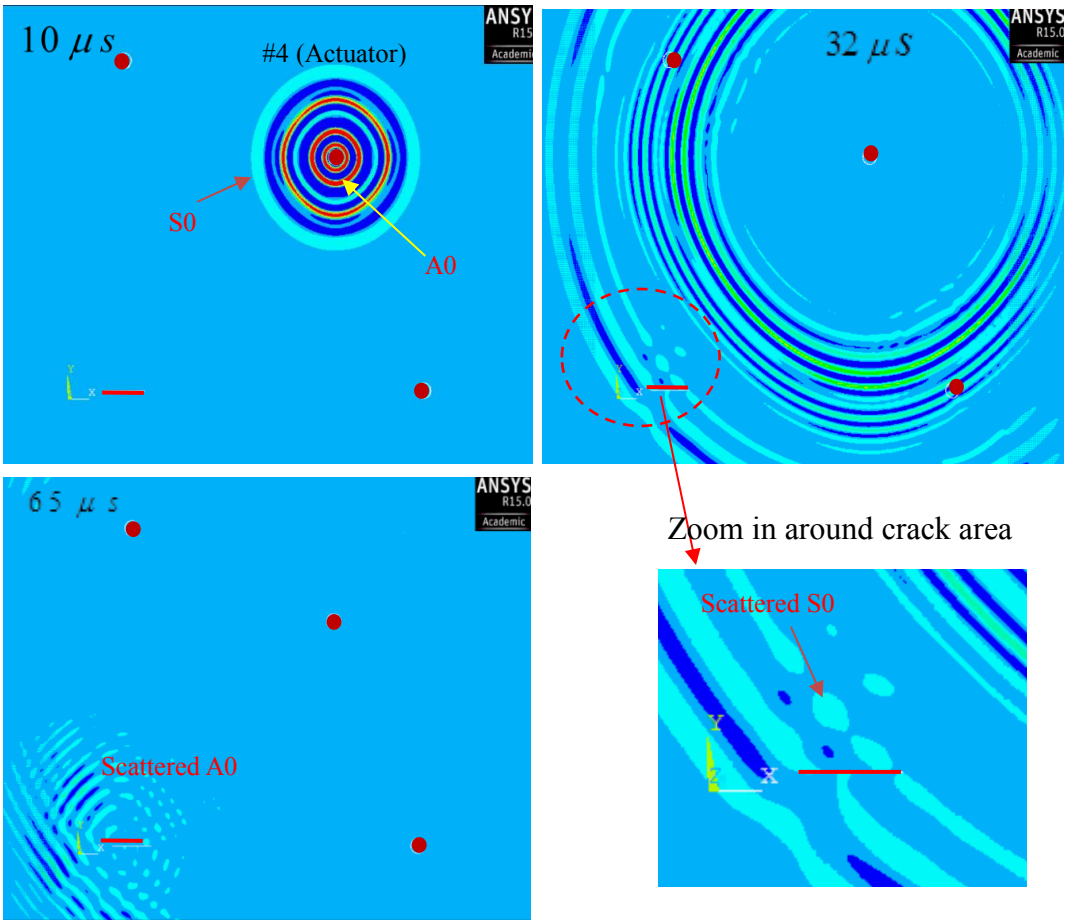

Figure 6.4: Snapshots of simulation 45° incident Lamb wave propagating and interaction with a crack.

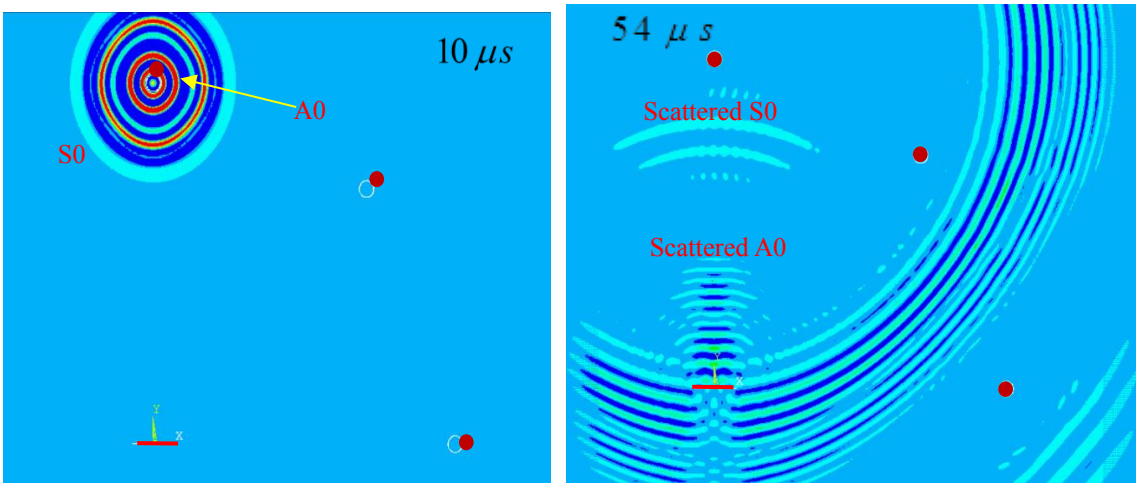

Figure 6.5: Snapshots of simulation 90° incident Lamb wave propagating and interaction with a crack.

of guided waves with fatigue cracks. The results show the nonlinear higher harmonics and mode conversion phenomena during the wave interaction with crack [68] [69].

In this work, a hybrid global-local (HGL) simulation approach [70] [71] has been used for the numerical study. A schematic illustration of the HGL simulation is shown Figure 6.6. A set of eight PWAS transducers were used as numbered from 1 to 8. Each of them was located at equal distance of 150 mm from the center of crack. The crack length was 18 mm. The Lamb waves were generated from the transmitter PWAS. The transmitter PWAS (T1, T2, T3) were located at 0°, 45°, 90° to the crack. For each transmitter, the rest of the PWAS transducers were acted as receivers. The directionality of incident Lamb wave and scattered wave was studied.

The HGL approach involved local FEM simulation of the damage site accompanied with exact analytical solution outside the damage region. The dimensions of the local FEM models were. A non-reflective boundary (NRB) was modeled using spring-damper elements surrounding the plate edges as in ref. [64] to minimize the edge reflected waves. The overview of the entire HGL process is illustrated in Figure 6.7 (a) following ref. [70]. The wave damage interaction coefficients (WDIC) were obtained from the local FEM analysis and then inserted into the global analytical framework. The WDICs were obtained for three separate FEM models (0°, 45°, 90° crack orientation) as shown in Figure 6.7 (b), (c) and (d). The FEM model parameters were chosen based on the ref. [72].

The WDIC is the measure of Lamb wave interaction with crack and is a complex-valued parameter. The WDIC polar plots for all three incident directions of Lamb waves are shown in Figure 6.8. Both amplitude and phase of WDIC show that the scattered waves from the crack have directionality effect. For example, when Lamb waves were incident at

45° to crack, the maximum scattering amplitude occurred at 135° to crack. This means a receiver sensor would pick up stronger scattering signals when it would be installed in this direction. It can also be noticed that maximum WDIC occurs when the Lamb waves were incident perpendicular (90°) to the crack. For 0° Lamb wave incident, weak WDIC occurred. This study of directionality effect suggested using the optimum transmitter and receiver combination for the imaging method as discussed later. The scattering waveforms for 0°, 45° and 90° Lamb wave incident (transmitter T1, T2, T3) are illustrated in Figure 6.9 (a), (b) and (c). The strongest scattering signal was observed for path 2-4 (transmitter, T2- receiver, R4), which corresponds to 45° Lamb wave incident and scattering wave received at 135°, which is expected based on the WDIC profile (Figure 6.8).

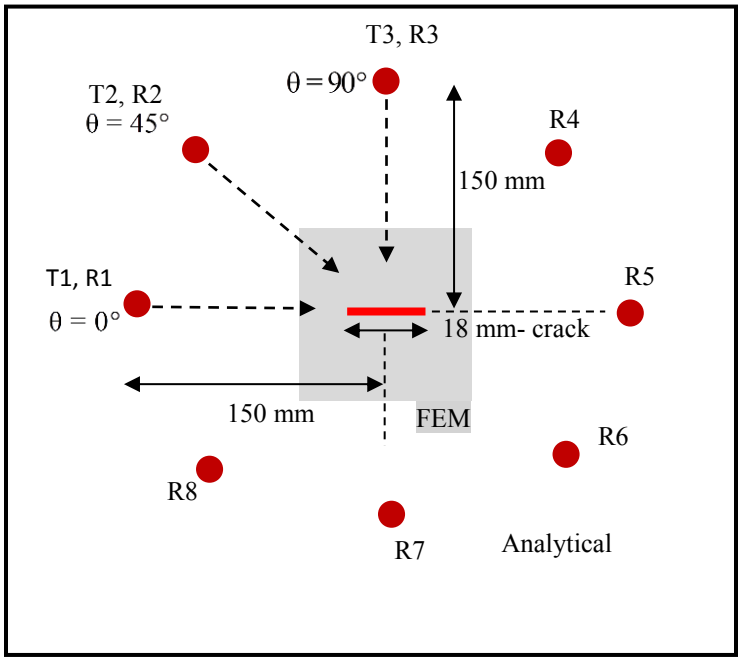

Figure 6.6: Schematic illustration of the hybrid global-local (HGL) simulation.

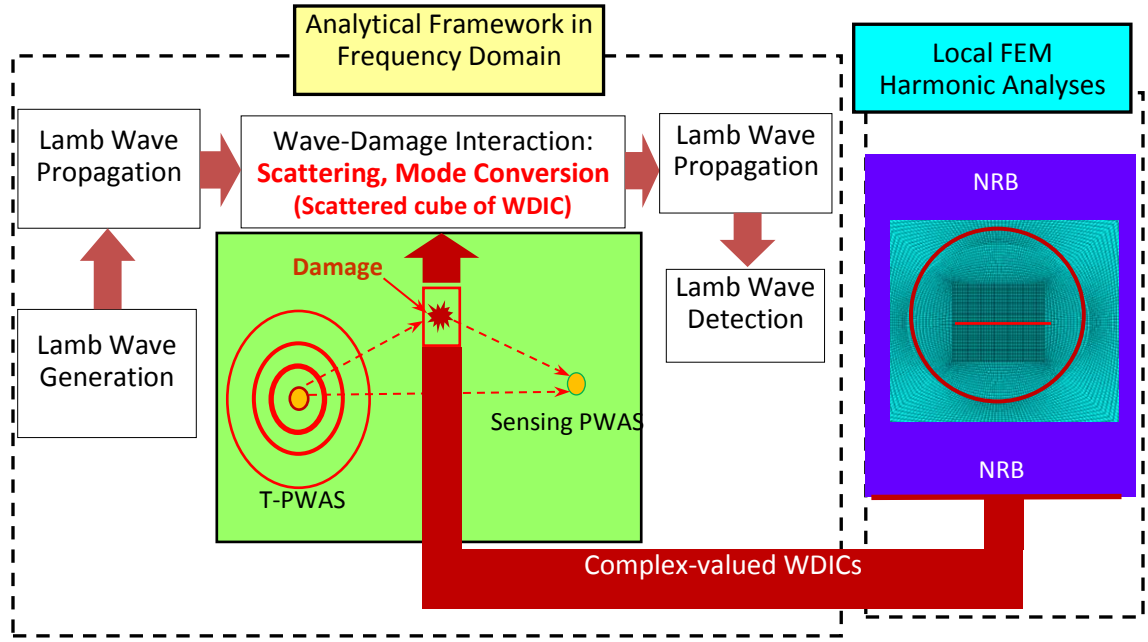

(a) Overview of combined global analytical and local FEM analysis [70].

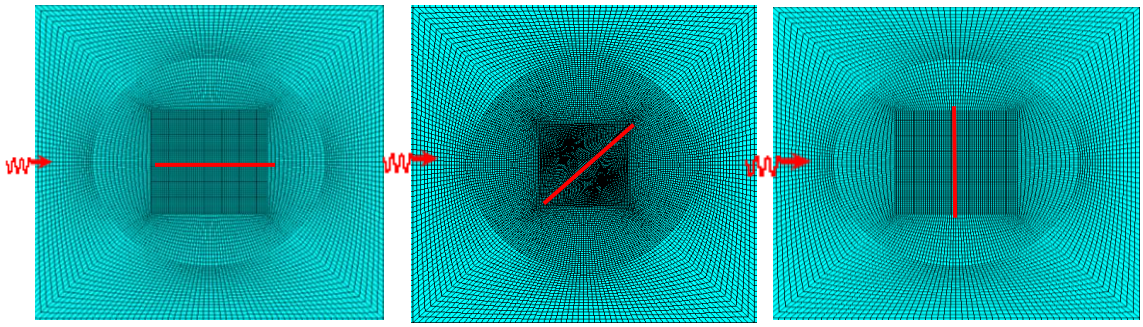

(b) 0° crack orientation (b) 45° crack orientation (b) 90° crack orientation

Figure 6.7: (a) Overview of combined global analytical and local FEM analysis, (b) Three local FEM models for 0°, 45°, 90° crack orientation with incident Lamb wave.

The scattering waveform for path 3-3 (transmitter, T3- receiver, R3) also shows the stronger scattering signals, which corresponds to 90° Lamb wave incident and scattering wave received at 90°. Please note, WDICs of scattered S0 Lamb wave mode for incident S0 Lamb wave (S0_S0) was plotted in Figure 6.8. The scattered shear horizontal (SH0) mode does exist for incident S0 Lamb wave, but not shown here.

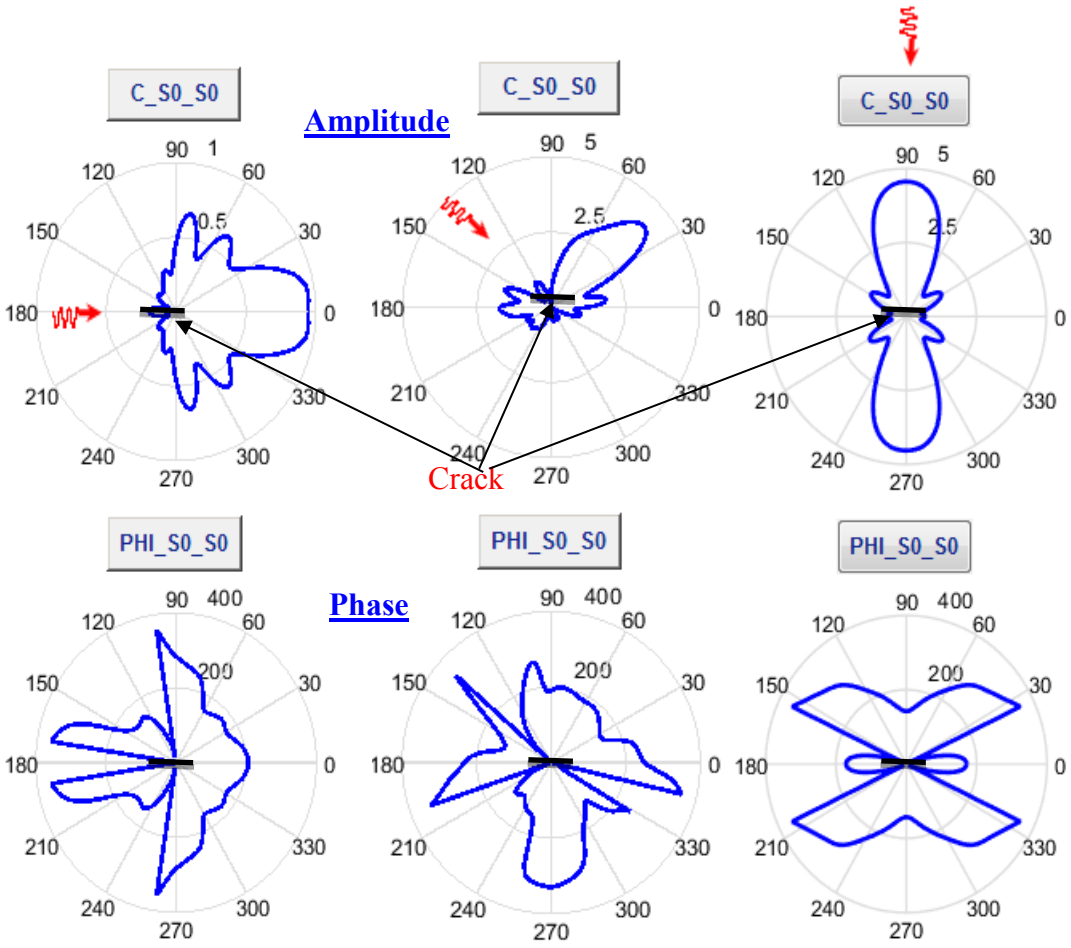

(a) 0° LW incidence (b) 45° LW incidence (c) 90° LW incidence

Figure 6.8: WDIC directivity plot (amplitude and phase) at 450 kHz for three different directions (0°, 45°, 90°) of Lamb wave (LW) incident ("S0_S0" means scattered S0 Lamb wave for incident S0 Lamb wave).

6.3.1 Imaging Results Based on HGL Approach

For imaging methods, the sensing signals at receivers for two incident directions (45° and 90°) were used. The imaging results of the simulated signals are illustrated in Figure 6.10. The combined summation and multiplication was adopted to produce better images of the crack. It can be observed that both imaging methods predict the crack size to be 16-mm, whereas the simulated crack size was 18-mm.

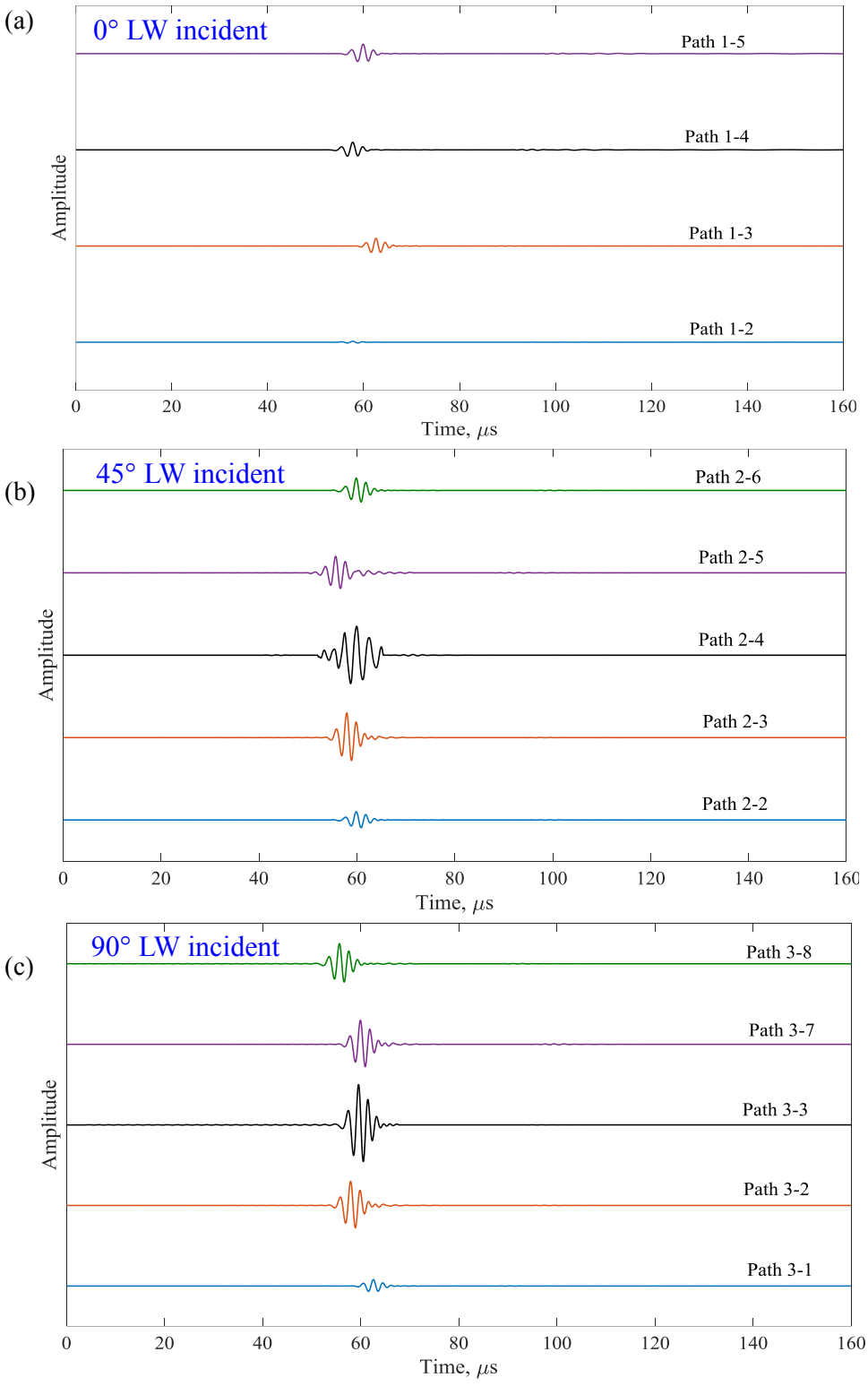

Figure 6.9: Scattering waveforms at various receivers for: (a) 0° Lamb wave (S0) incident; (b) 45° Lamb wave (S0) incident; (c) 90° Lamb wave (S0) incident.

The simulated results also show the horizontal orientation of the crack. It should be noted that during the simulation the scattering signals were not affected by any confounding factors (sensor bonding, environmental noise, electrical connections, temperature-humidity, etc.) commonly encountered in practice.

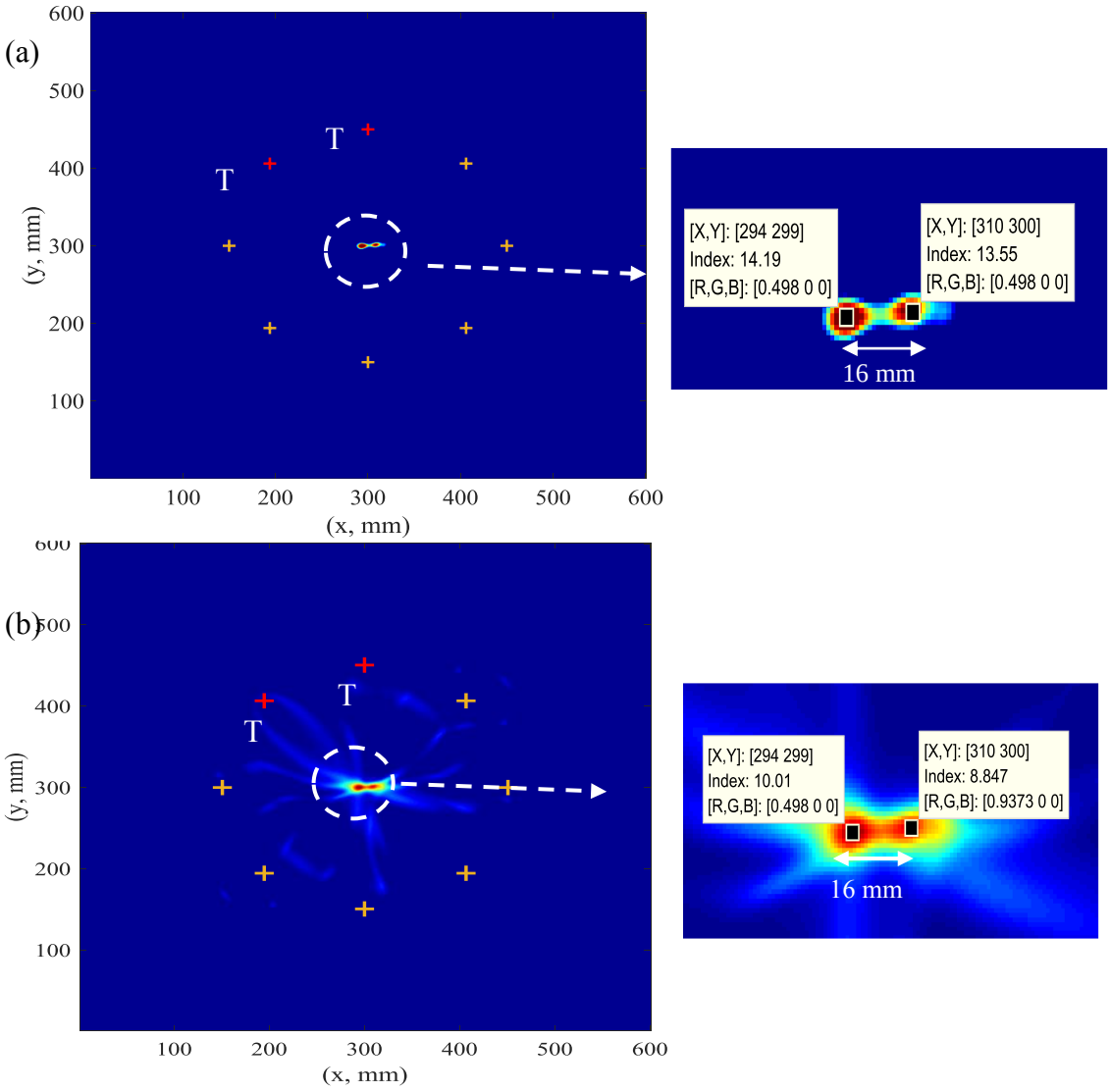

Figure 6.10: Estimation of crack size based on imaging (a) method A and (b) method B with combined summation and multiplication algorithms ("T" means transmitter, two transmitters at 45°, 90° were used, all the receivers for each transmitter were used).

6.4 PART II: SUMMARY AND CONCLUSION

This part briefly explained the principles of two imaging methods by presenting two flow charts. Numerical simulations were performed with HGL approach and imaging methods (method A and B). Method A involves synthetic time reversal concept and method B involves Gaussian distribution function. Several local FEM simulations were performed for various Lamb wave incidences (0°, 45°, 90° to the crack). The directionality effect and imaging results were studied. Two experimental investigations of two types of damage situations were considered: (1) crack, (2) through-thickness hole. The first experiment involved a sparse array of eight PWAS transducers to quantify the crack size by using the imaging methods. Pitch-catch and pulse-echo experimental modes were considered for each imaging method. The scattered waveform and imaging results were presented for both methods in each experimental mode. The second experiment involved a network of sparse array of six PWAS transducers to quantify hole size by using the same imaging methods. The pitch-catch experimental mode was used to obtain the scattered signals. The relation between the hole size and the scattered signals was studied. The imaging results identify (the location, size and shape) when the hole damage has 2-mm, 2.5-mm and 3-mm. Two sensors with pulse-echo mode or combined pulse-echo and pitch-catch mode were used to localize the hole plate. The imaging results give two intersection point. The point inside the interested area represents the damage point. The second point outside the interested area can be canceled

The hybrid global-local (HGL) approach with imaging methods provided fast and efficient simulation of crack size estimation. The polar plot of simulated WDICs revealed the directionality effect of the scattered wave signals emanated from the crack. Both

incident and sensing direction of Lamb waves affect the scattered wave signals which eventually affect the quality of imaging results. The flowcharts of two imaging methods were developed. The simulations and experiments show that both imaging methods successfully quantify the crack size, shape, and orientation within an acceptable level of accuracy. The experiment involved confounding factors which affect the measurement of scatter wave signals. These scattered signals play an important role in crack quantification. Stronger scattered waves result in better imaging results.

The optimum sensor configuration results in better scattered signals which eventually give better damage quantification. For pitch-catch mode, the sensing paths of two transmitters in optimum locations may be enough to quantify the crack size. The synthetic time reversal-based imaging method (method A) can be used with threshold setting and without threshold setting. The use of combined summation and multiplication algorithm may eliminate the need for thresholding for better crack imaging. Both pitch-catch and pulse-echo modes show that the scattered waves are stronger when incident waves are perpendicular to the crack. In both experimental modes, the Gaussian distribution-based imaging method (method B) seems to overestimate the crack size. In an attempt of smaller (1-mm to 3-mm) through thickness-hole size estimation, it was found that smaller crack produces relatively weaker scatter waves. These scattered waves can be used for hole detection and localization but may not be sufficient to quantify the hole size.

PART III: DAMAGES DETECTION IN COMPOSITE STRUCTURES

CHAPTER 7
NDT AND SHM TECHNIQUES FOR IDENTIFYING THE DELAMINATION IN COMPOSITE PLAT

In this chapter, two damaged composite plates were inspected. The first composite plate, which is cross-ply eight layers of carbon/epoxy laminate, has three different sizes of simulated circular delaminations. These simulated delaminations are inserted at different locations across the plate area and the same thickness depth. The second composite plate is thirty layers of unidirectional carbon/epoxy laminate, has three same sizes of simulated circular delaminations, which are inserted at different locations across the plate area and different thickness depths. Four different techniques were used to detect and quantify the delamination in these specimens. First, The NDT technique was used to inspect these two plates using Rollerform and Omniscan devices. The Omniscan extracts the results as C-scan image, B-scan image and A-scan plot which identify the delamination areas. Second, the SHM technique in conjunction with imaging method is used to inspect these plates. A network of PWAS transducers, Lamb waves and imaging methods were used to identify the delamination in the composite plates. Third, The SLDV technique was used to study the guided waves propagation and interaction with delamination areas for both specimens.

The time-space, frequency-wavenumber and wavefields images results are studied for quantifying the delamination areas of both specimens. Fourth, the local vibration-based technique was used to detect the delamination areas using SLDV and linear chirp excitation

signal. The structural operational vibration shapes at resonance frequencies remarkably detected and quantified the delamination areas.

7.1 INTRODUCTION

The composite material is widely used in many applications due to their high strength and stiffness combined with low weight. In recent years, most of aerospace structure are made from laminate composite material. These materials are oversensitive to different kind of damage such as delamination, crack and disbanding which may be induced during manufacturing, by external impact, or by aging. These defects may grow and subsequently cause structural failure [73]. Lamb wave is emerging technology can be used to detect and localize different kinds of structural defects. Lamb waves are ultrasonic guided waves that can propagate in solid structures with boundaries.

Delamination in composites can be detected by reflected Lamb waves using pulse-echo mode or pitch-catch mode. If the delamination exist, additional reflection waves can be observed, and the delamination can be located by measuring the arrival time of the reflection wave and the wave velocity [74]. Different structural health monitoring techniques are used to identify the structural damages such as ultrasonic testing, radiographic testing, electromagnetic testing, etc. [75]. Guided ultrasonic waves technique is widely used in structural health monitoring because of its sensitivity for damage detection and monitoring large area [76]. The mechanical properties of composite plates such as inhomogeneity, the anisotropy and the multi-layered construction make the wave propagation in composite plate more complex. The Lamb waves propagating in a composite plate are dispersive, their velocities depends on a plate thickness and the frequency of excitation signal, and dependent on its fiber direction and laminate layup

configurations [77].The guided ultrasonic waves have been demonstrated as an effective tool for structural health monitoring. In recent years, many works have been implemented about using guided waves for damage detection and localization in isotropic and composite materials [78] [79] [80]. The group velocity and characteristic wave curves of wave propagation in composite material, are investigated theoretically and experimentally. In experimental results, the higher multiple Lamb wave modes were determined by the excitation of ultrasonic frequencies. The three-dimensional (3-D) elasticity theory were solved numerically to determine the dispersion curves. Both experimental and theoretical results show a good agreement [81]. The interaction of symmetric Lamb wave mode with the delamination at different location across the composite plate thickness was studied experimentally [82]. The results show that the amplitudes of symmetric Lamb waves reflect from delamination are dependent on the delamination depth.

A network of piezoelectric sensors was used as actuators and sensors to localize a delamination in composite plate. The outgoing modes from interaction the Lamb waves with delamination are studied. The wavelet transform is used to determine the time delay between the incident mode and the specific outgoing mode. The results identified the delamination area with accurate information [83]. The Lamb wave-based imaging approach was developed to identify the structural damage in both isotropic and composite plates. The experimental results demonstrated the effectiveness of this approach [27].

7.2 SPECIMENS CONFIGURATION

Two in-house composite plates with different delamination damages and stacking sequences were manufactured. In the present study, six cases of delamination of different sizes and depths were investigated. The first specimen is 1.6 mm thick in-house cross-ply

carbon fiber-reinforced polymer (CFRP) composite plate with a stacking sequence of $[0/90]_{2S}$. Three delamination damages are generated by inserting different sizes of Teflon films between the first ply and second ply before autoclave processing. The sizes of simulated circular delaminations are 25 mm, 50 mm, and 75 mm in diameter, respectively. Figure 7.1 shows the schematic of the composite plate with simulated delamination damages. The dimension of the specimen is 700 mm × 700mm × 1.6 mm. The engineering elastic properties of the unidirectional prepreg are given in Table 7.1.

The second specimen is a 5 mm thick in-house unidirectional CFRP composite plate with a stacking sequence of [0]30. The configuration of the unidirectional composite plate is given in Figure 7.2. The dimension of the specimen is 700 mm × 700m × 5 mm. The unidirectional prepreg is the same as the first specimen. This specimen has three simulated delamination at different depths across the plate thickness, which are created by inserted three circular Teflon films with the same size (75 mm in diameter). The delamination A (near the top surface) is created between plies 7 and 8. Similarly, the delamination B (near the mid-plane) is generated between plies 18 and 19, and the delamination C (near the bottom surface) is made between plies 28 and 29, as shown in Figure 7.2.

Table 7.1: Engineering constants of the unidirectional prepreg.

E_{11}	E_{22}	E_{33}	ν_{12}	ν_{13}	ν_{23}	G_{12}	G_{13}	G_{23}	ρ
140.8 GPa	11.3 GPa	11.3 GPa	0.31	0.31	0.5	5.7 GPa	5.7 GPa	3.4 GPa	1640 kg/m^3

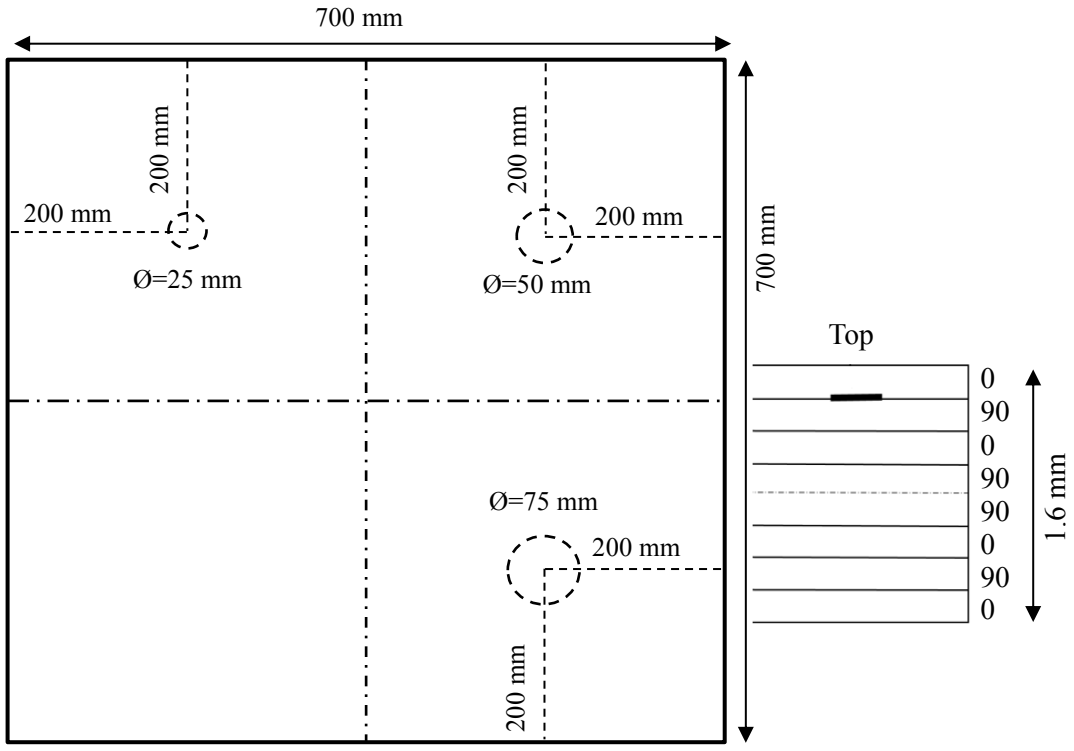

Figure 7.1: Schematic of 1.6 mm cross-ply $[0/90]_{2S}$ CFRP composite plate with three simulated delamination of various sizes at the same depth.

7.3 WHEEL-PROBE INSPECTION OF COMPOSITE PLATE USING OMNISCAN

The Olympus Roller form is a new phased array wheel probe design for zero-degree C-scan inspection of aerospace composite, aluminum panels and similar components. This tool can be used for thickness measurement, material loss, detection and sizing of delamination and internal porosity [13]. The Rollerform scanner features a phased array probe enclosed in a water chamber and an encoder sensor as shown in Figure 7.3 (a). The wheel probe is designed to be with smooth surface to contact the interested area with minimal water. The acoustic wheel has a transparent material which closely matches the acoustic impedance of water. The water delay line of wheel chamber is 25-mm which

allows you to perform inspections on composites that are up to 50-mm thickness. This scanner is also capable of performing thickness measurements in part thicknesses as small as 2-mm [14]. The width of coverage across the probe, which depends on the element selection of the phased array group, is approximately 49-mm. So, based on this value, we can divide the inspection area into lines scan. Every line scan has 49-mm width.

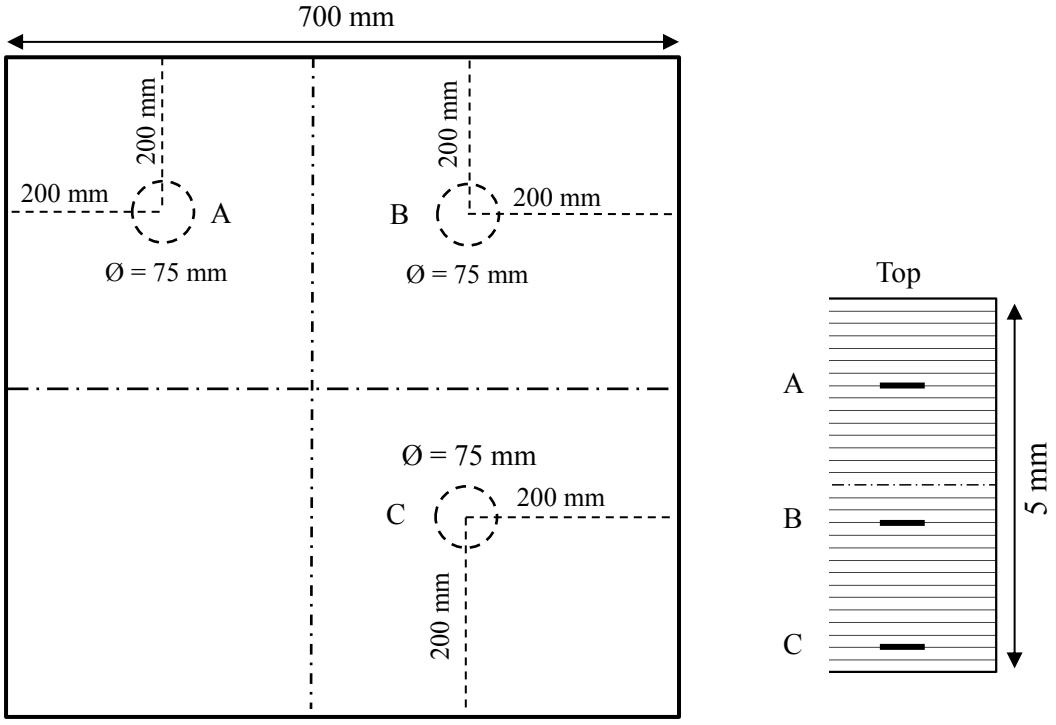

Figure 7.2 Schematic of 5 mm unidirectional $[0]_{30}$ CFRP composite plate with three same size delamination at various depths.

The Rollerform can inspect surface curvatures of 50-mm, ranging from 100 mm outer diameter to flat surfaces. Its near-surface resolution ranges from 1-mm, when using a 5 MHz phased array probe, to 1.5 mm, when using a 3.5 MHz phased array probe with delamination detection capacity of 3 mm × 3 mm [84]. The Omniscan instrument processes the received signal and generates A-scan, B-scan and C-scan representations of the signal.

The A-scan represents the plot of amplitude of waveform signal as a function with time. This amplitude can be either rectified or non-rectified. The B-scan can be defined as a two-dimensional image of ultrasonic data plotted as reflector depth or distance based on the beam position.

The c-scan represents a two-dimensional view of ultrasonic amplitude or time/depth data displayed as a top view of the inspection area. The probe elements send phased array beam (pressure wave) which is perpendicular on the inspection area. The front wall signal is generated when the phased array beam hits the top surface of inspection area and the back-wall signal is generated when the phased array beam hits the bottom surface. The interaction of the phased array beam is shown in the Figure 7.3 (b). The experimental setup of inspection two specimens using NDT technique is shown in the Figure 7.4. The tire chamber should fill with distilled deionized water a day before inspection to allow the water to completely degas. The OmniScan devise should be set up for Rollerform wheel probe inspection. The Rollerform wheel probe should be completely wet using a light water spray. We can inspect the whole or part of inspection area.

In this work, three damaged sub-areas of the specimen 1 are inspected as shown in Figure 7.5. The first area (area 1) with 550 mm × 49 mm has the small circular delamination area (25-mm diameter). The second area (area 2) with 400 mm × 49 mm has no delamination defect (healthy area). So, these areas have one-line scan because their widths are equal to the phase array beam width (49-mm). The third area with 550 mm × 98 mm has two different sizes of circular delamination areas. This sub-area is divided in two scan lines. Each scan line has 49-mm width. The visualization results of scan area 2 are shown in Figure 7.6. In this result, we can see C-scan image, A-scan plot and S-scan image. From

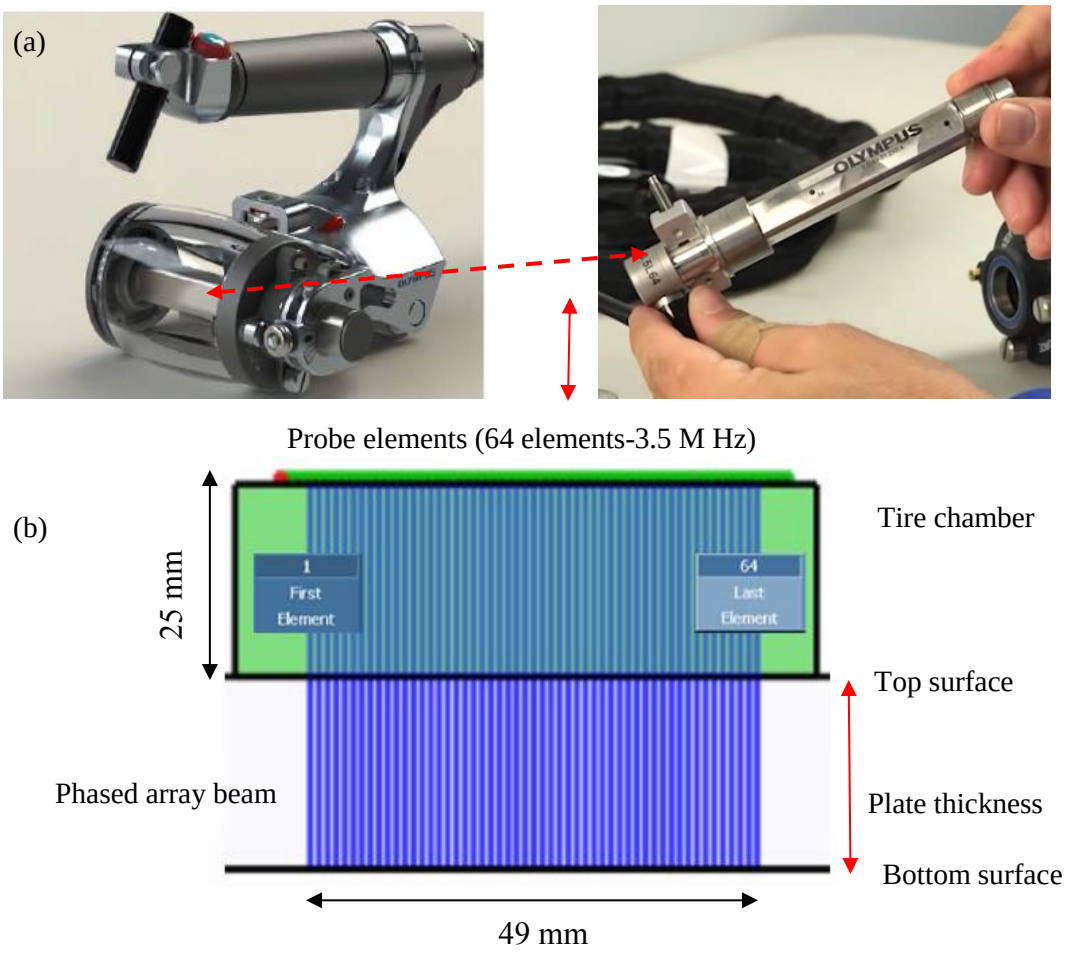

Figure 7.3: Tire-chamber configuration of the Olympus Roller form; (a) Tire-chamber; (b) Phased array beam [84].

C-scan image (which represents the top view of inspection area), we can indicate that the scanned area is very clean and there is no defect in this area. The section view across the line I, which represent the S-scan image contains the top surface and bottom surface cross-sectional image with high intensive color which means these surfaces have strong reflected signals as seen in the A-scan plot. While the area between top and bottom surfaces has very low field color map which means there is no defect between them. The A-scan plot show the reflected signals from the top and bottom surfaces. Figure 7.7 shows the imaging results of scan area 1.

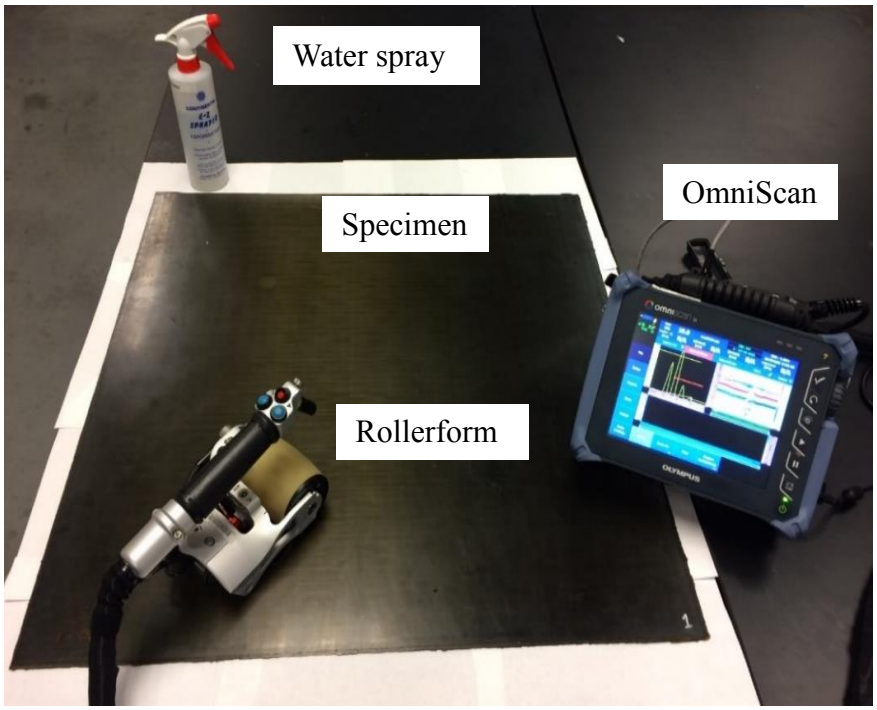

Figure 7.4: Experimental setup for NDT technique.

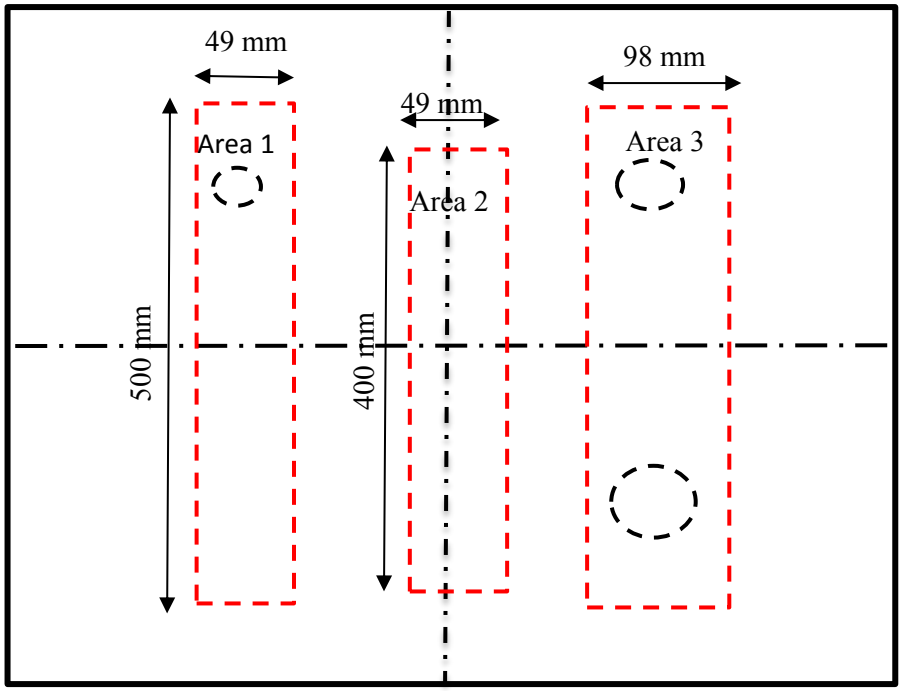

Figure 7.5: Interested areas of specimen 1to be scanning by NDT technique.

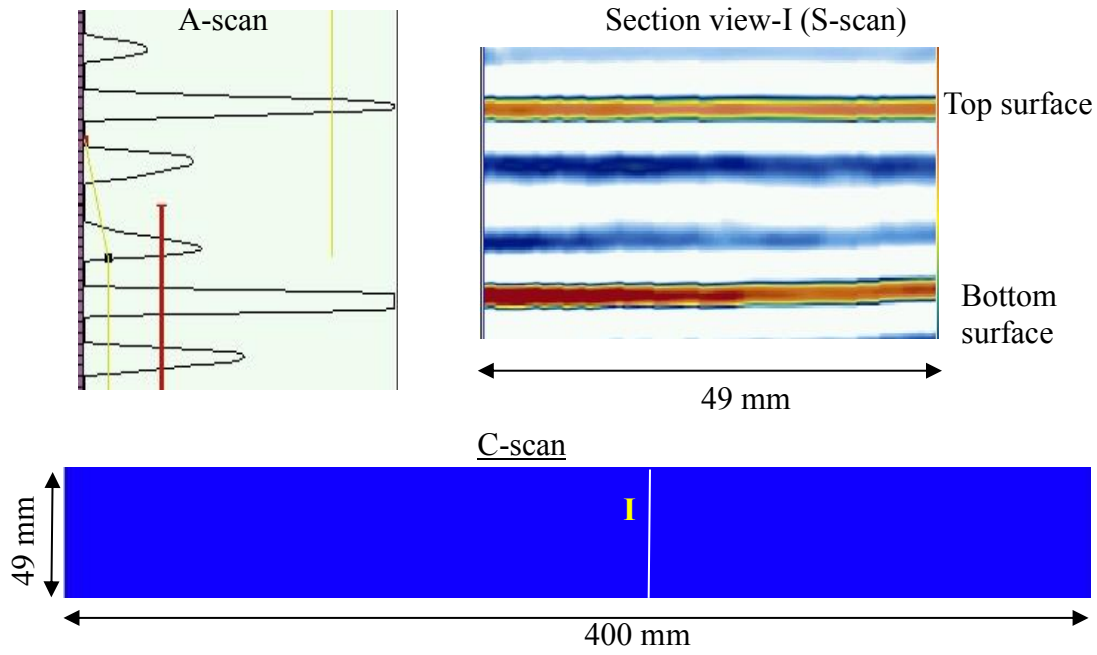

Figure 7.6: Imaging results of NDT technique for inspection area 2 (specimen 1).

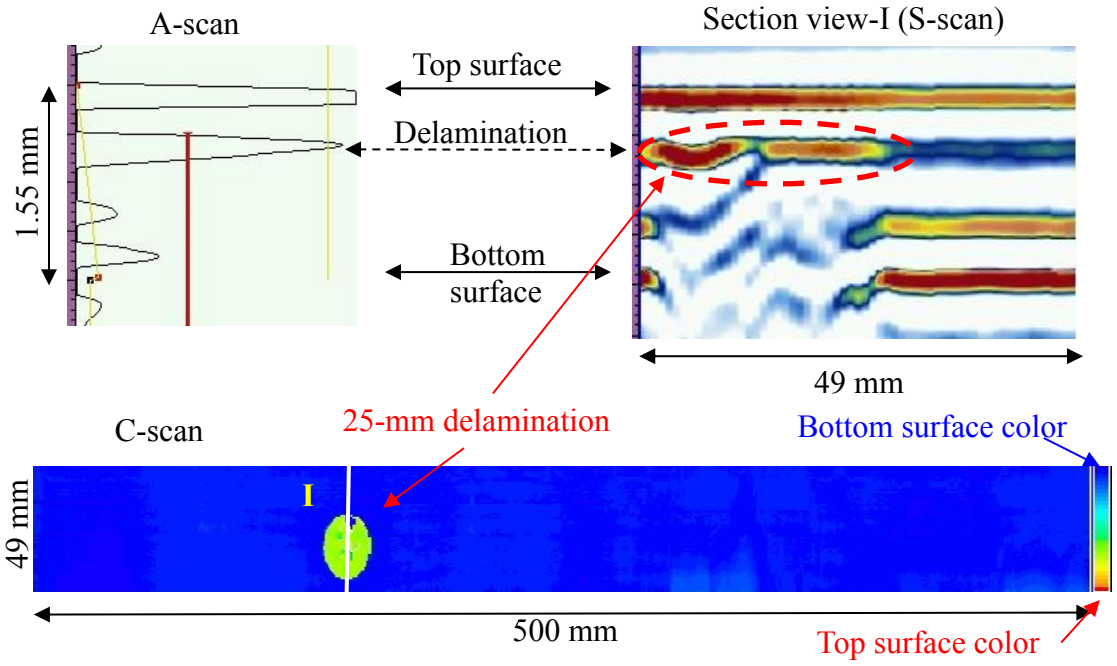

Figure 7.7: Visualization results of the first inspection area on the cross-ply $[0/90]_{2s}$ CFRP composite plate: pristine area and 25-mm delamination.

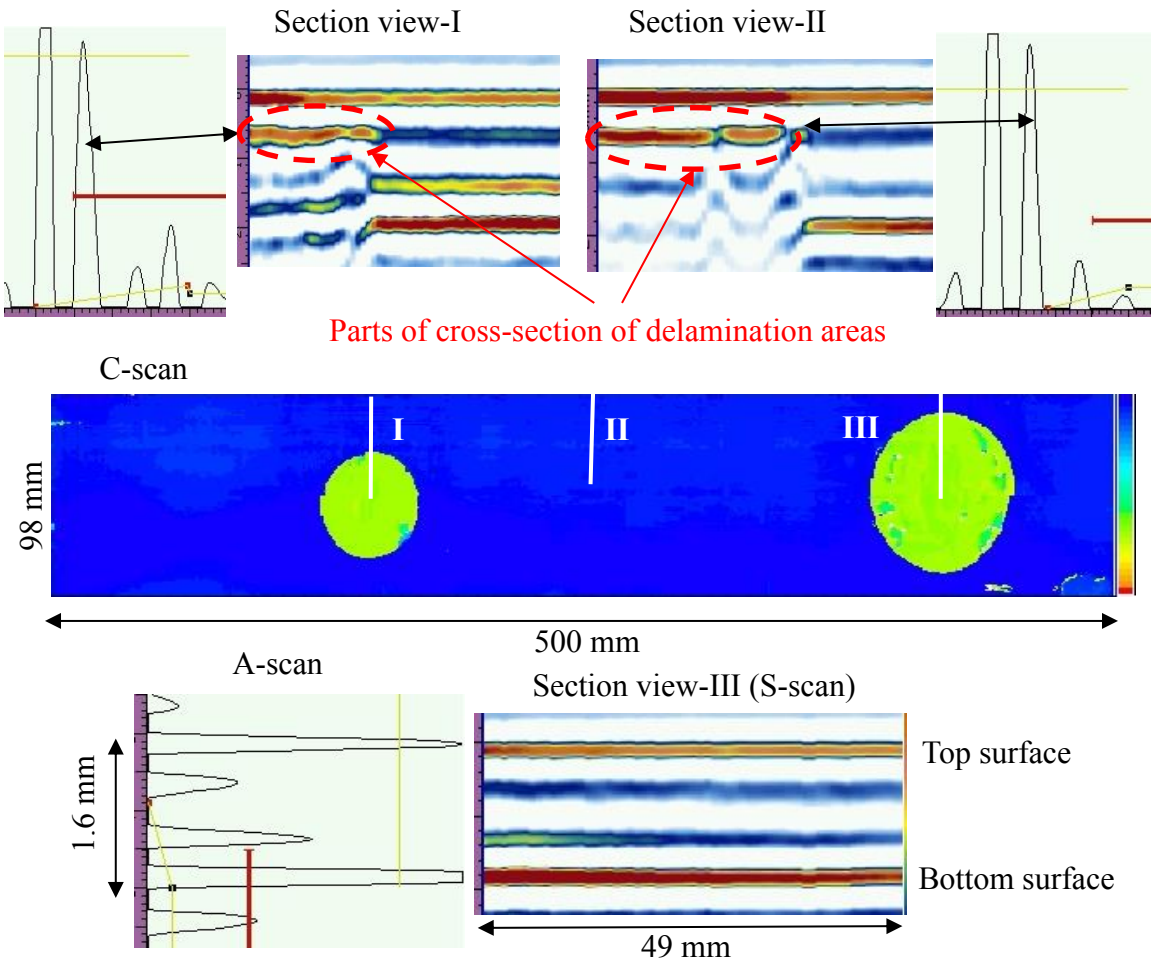

Figure 7.8: Visualization results of the second inspection area on the cross-ply $[0/90]_{2s}$ CFRP composite plate: 50-mm delamination and 75-mm delamination.

The C-scan image shows the small circular delamination area (25 mm diameter). Based on the color map, we can extract the location of delamination area across the thickness.

The section view-I (S-scan) across the delamination area shows the cross section of delamination area under the top surface. The delamination area prevents the phase array beam to hit the bottom surface of plate under this area. However, we can see the cross-section of bottom surface out the delamination area. The results of scanning area 3 are shown in the Figure 7.8. From C-scan result, we can see two different size of delamination

areas (50 mm and 75mm diameters). These delamination areas have the same color because they are inserted at the same thickness depth. The section views I and II show the parts of cross-section areas of delamination defects. So, we can indicate the lengths of delamination and their depths.

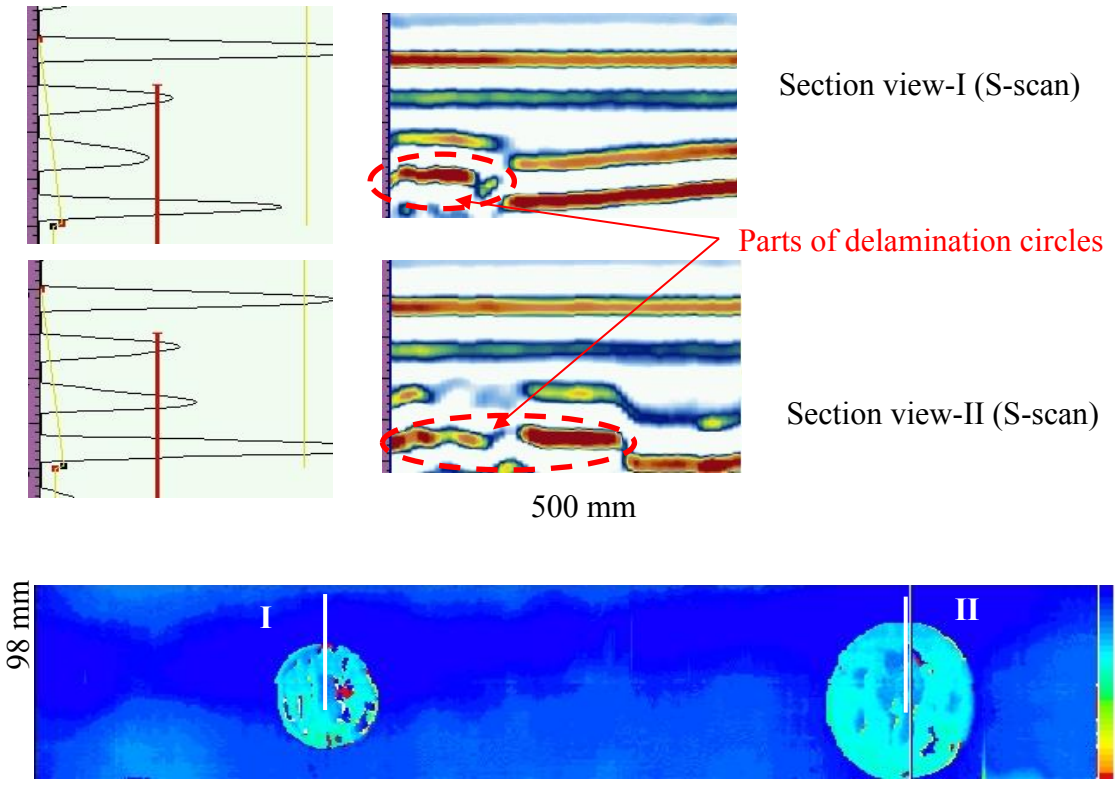

Figure 7.9 Visualization results of the second inspection area on the cross-ply $[0/90]_{2s}$ CFRP composite plate: 50-mm delamination and 75-mm delamination (bottom side).

After scanning the areas from the top plate surface, we did the same experiment and scanned it from the bottom surface. Figure 7.9 shows the imaging results of area 3 after scanning it from the bottom surface. The C-scan of this area show different color for the delamination areas compere with the C-scan result of Figure 7.8. In this case, the delamination are near the bottom surface as shown in section views I and II.

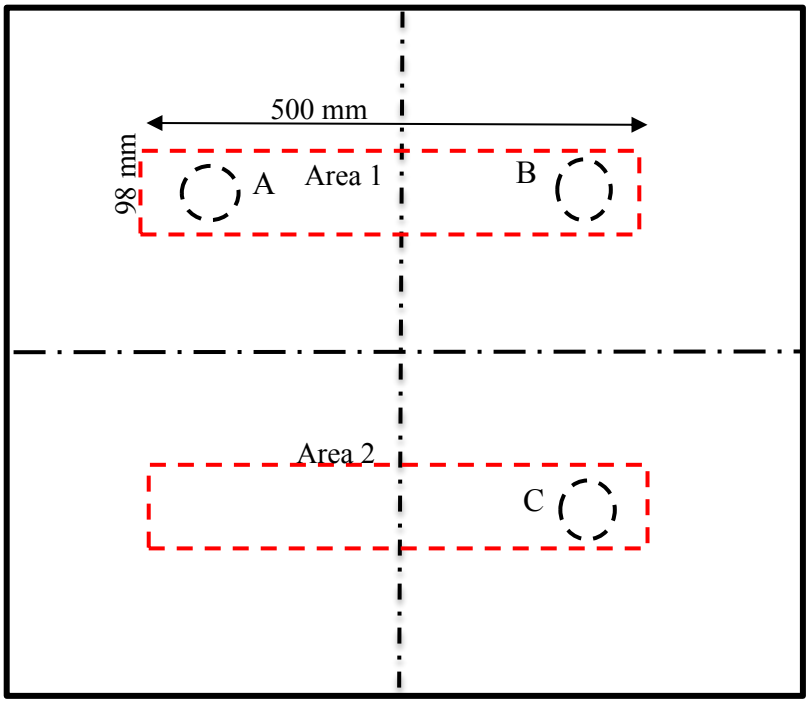

Figure 7.10: Interested areas of specimen 2 to be scanning by NDT technique.

For specimen 2, two areas (550 mm × 98 mm) are scanned as seen in the Figure 7.10. The area 1 has two circular delamination A and B, while area 2 has one circular delamination C. These delamination areas have the same size and they are inserted at different depths. The imaging results of scanning area 2 are shown in Figure 7.11. From C-scan image, we can see two equal sizes of circular delamination areas with different color map. So, we can localize these delamination areas in three dimensions and indicate the size and shape of these delaminations. The S-scan image of delamination B with green color shows the cross-section of half circular delamination area under the middle line of plate thickness (at the second half thickness). The A-scan plot shows the reflected signal from delamination with strong amplitude while the back-wall signal is very weak because it is under the delamination area. The cross-section image (S-scan) of circular delamination

area with yellow color map shows the location of this delamination in first half of plate thickness. The A-scan shows the reflected signal from delamination area. The imaging results of inspection area 1 are seen in Figure 7.12. The C-scan image shows the circular delamination area C with color map closed to the color of plate bottom surface which means the delamination is near the bottom surface. The section I (S-scan) shows the cross-section area of delamination C which is closed to the bottom surface. The section II shows the cross-section image in healthy area.

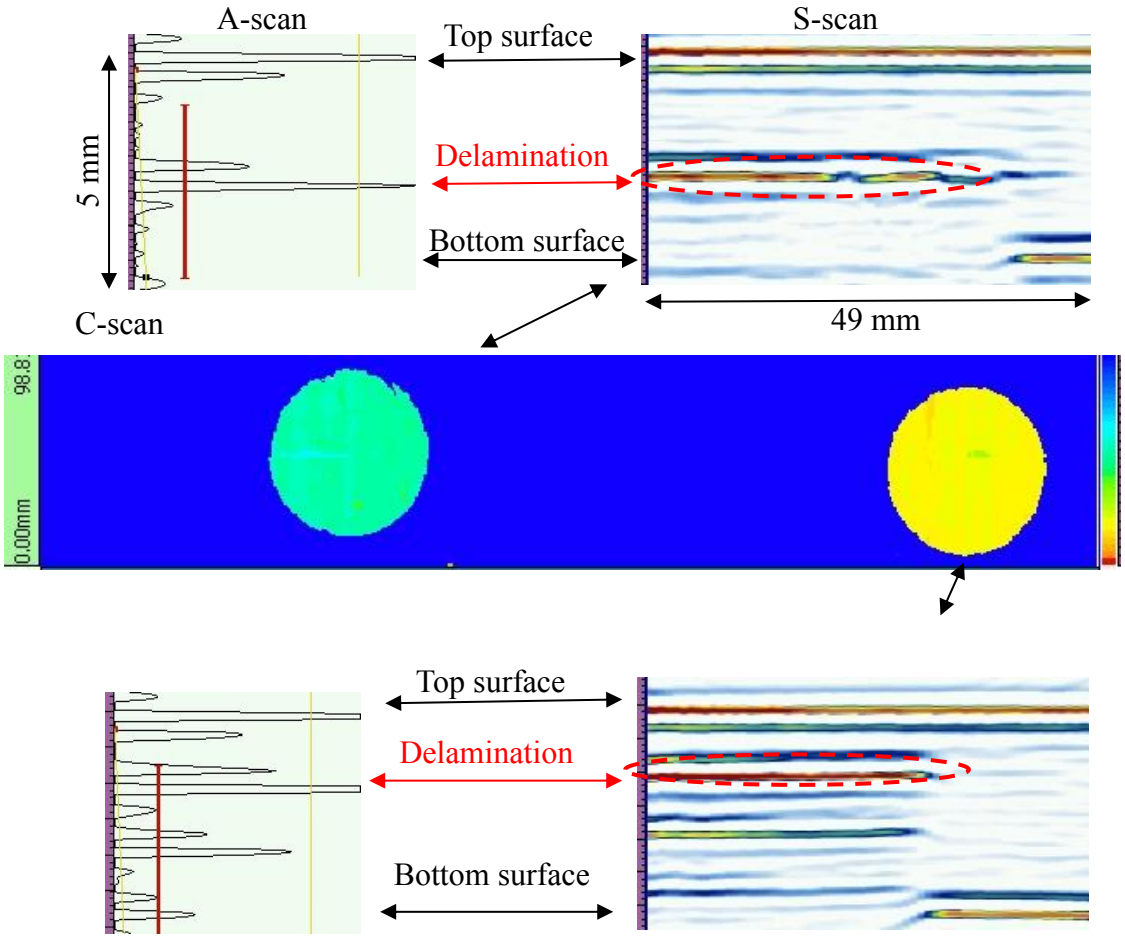

Figure 7.11: Visualization results of the first inspection area on the unidirectional $[0]_{30}$ CFRP composite plate: top and middle 75-mm delamination.

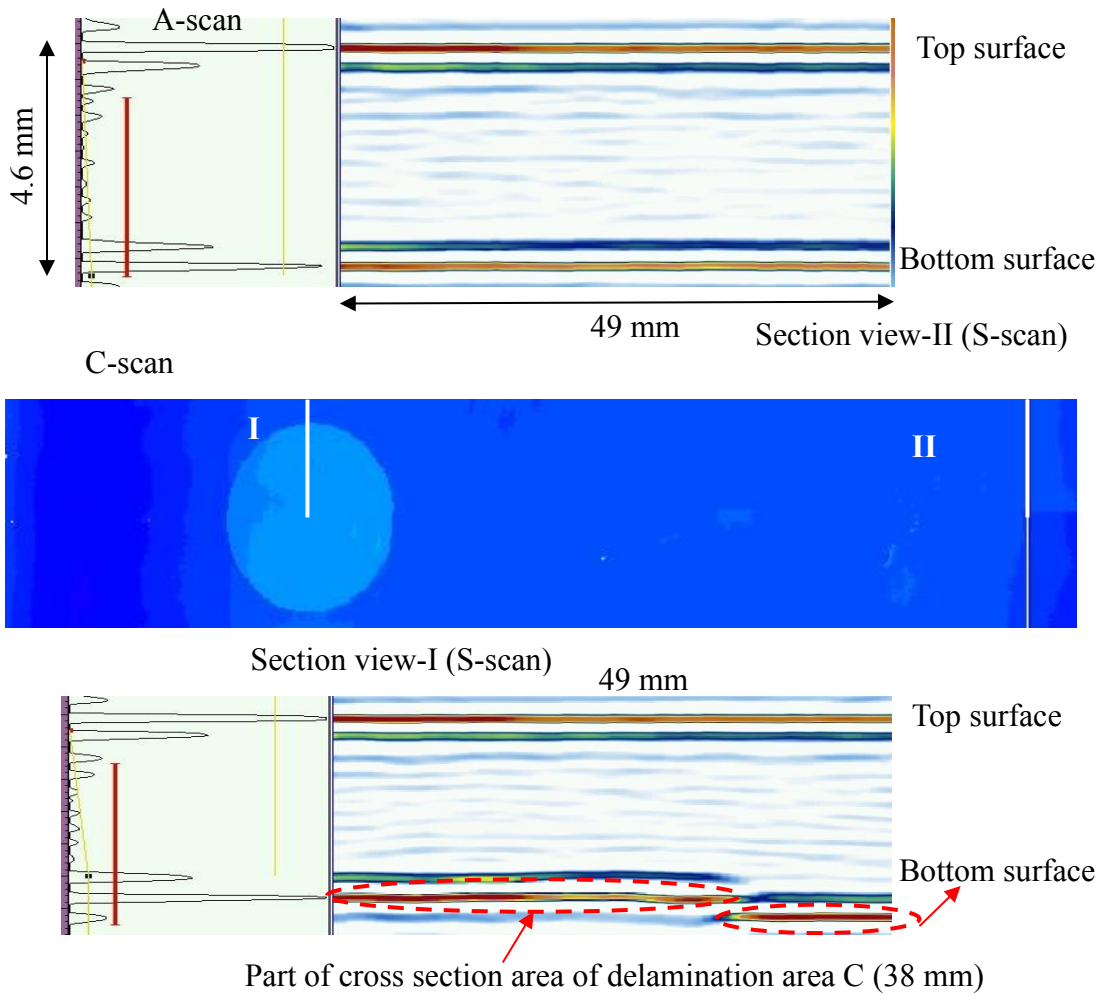

Figure 7.12: Visualization results of the second inspection area on the unidirectional $[0]_{30}$ CFRP composite plate: bottom 75-mm delamination.

7.4 SHM TECHNIQUE FOR INSPECTION SPECIMEN 1

7.4.1 EXPERIMENTAL SETUP

The experimental setup of using SHM techniques for inspection the cross ply composite plate (specimen 1) is shown in the Figure 7.13. A network of twenty-two of PWAS transducers are embedded across the plate. The plate has non-reflective boundaries by putting a clay around its edges to die out the reflected waves. An Agilent 33120A Arbitrary Waveform Generator was used to generate a 3-count Hanning window modulated

tone burst excitation signal at center frequency 330 kHz. Oscilloscope records the received signals.

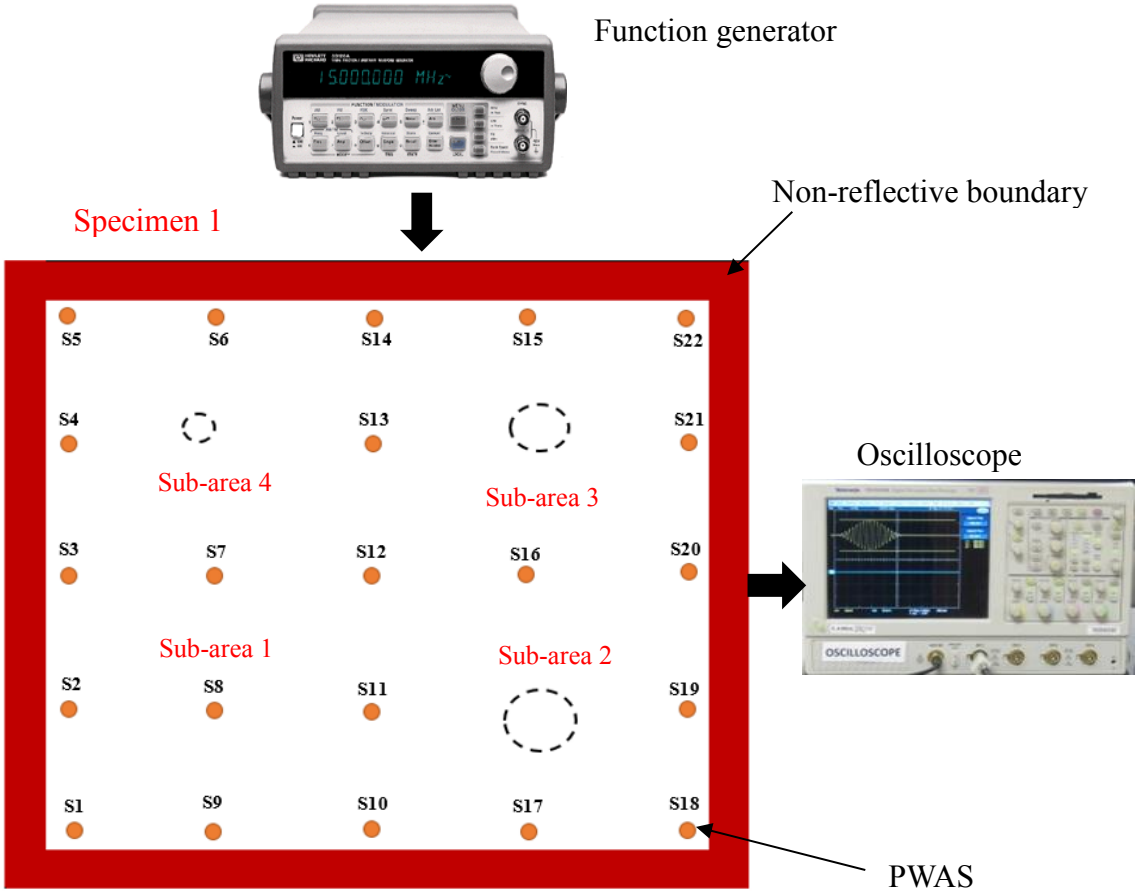

Figure 7.13: Experimental setup of using SHM technique for inspection specimen 1.

7.4.2 Group Velocity Dispersion and Tuning Curves

Before studying the interaction of Lamb wave with the defects on composite plate, we should obtain the experimental tuning and group velocities dispersion curves of propagating Lamb waves on the interested specimen to understand the behavior of propagating Lamb wave modes as function of frequencies and propagating directions. Figure 7.14 (a) shows the tuning curves of Lamb modes propagating in 0° direction. We can observe symmetric (S0) and antisymmetric (A0) Lamb wave modes. The S0 is the

dominant mode around frequency 330 kHz. Figure 7.14 (b) shows the tuning curves of Lamb wave modes propagating in 45° direction. We can recognize the symmetric (S0), shear horizontal (SH0) and antisymmetric (A0). The S0 and SH0 are the dominant modes around the frequency 330 kHz. Figure 7.14 (c), (d) show the experimental dispersion curves of A0, S0 and SH0 modes. We can observe that S0 is the faster mode and SH0 has a group velocity closed to the group velocity of S0 for the 45° direction. Based on the above curves, we can choose the frequency value 330 kHz to excite the S0 mode as dominant guided wave mode.

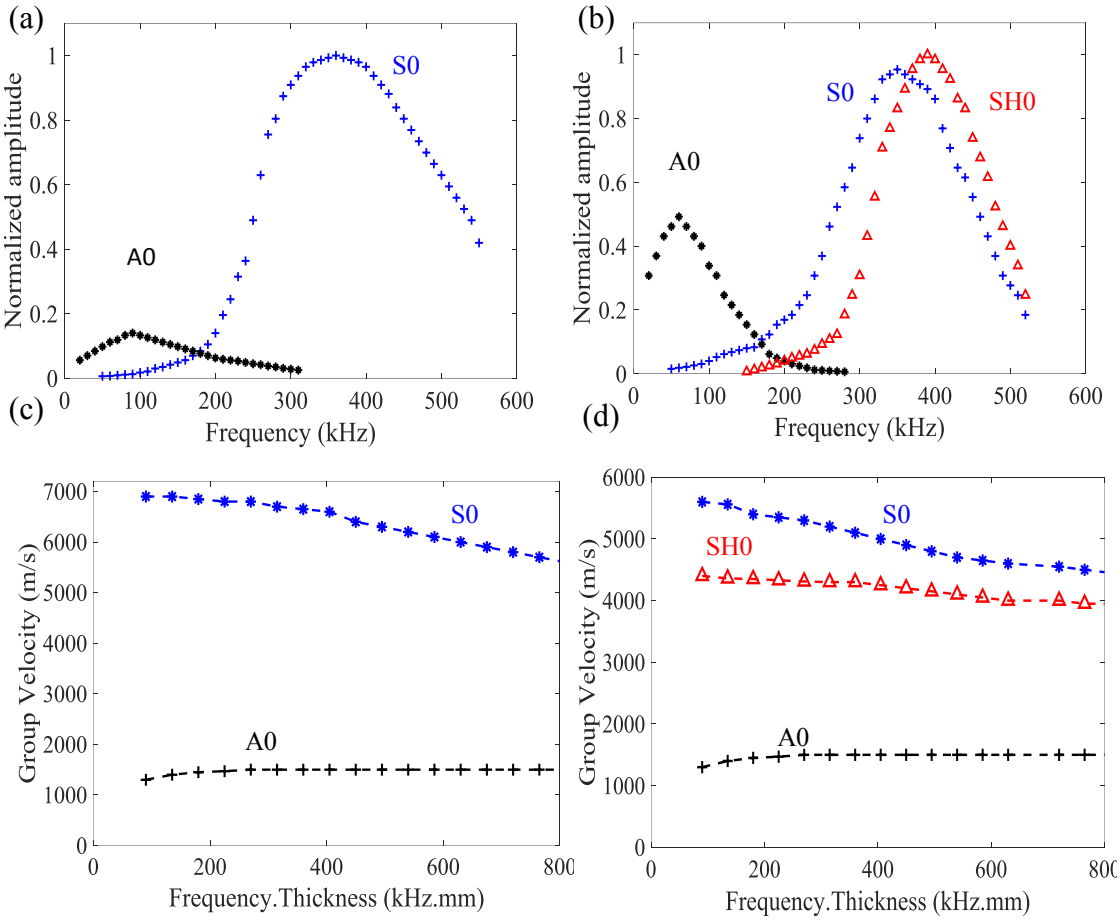

Figure 7.14: Experimental dispersion and tuning curves of the cross-ply CFRP composite plate; (a) 0° direction tuning curves; (b) 45° direction tuning curves; (c) 0° direction dispersion curves; (d) 45° direction dispersion curves.

7.4.3 Interaction of Lamb Wave with Delamination Area

A pitch-catch experiment is implemented between sensor S12 (transmitter) and sensor S14 (receiver). The length of this sensing path is 270-mm. A 3-count tone burst signal at center frequency 330 kHz is excited the transmitter. From Figure 7.15, we can see, the incident waves S0. Also, we can see two new scattered waves (scattered S0 and scattered SH0) due to interaction of Lamb wave with delamination area.

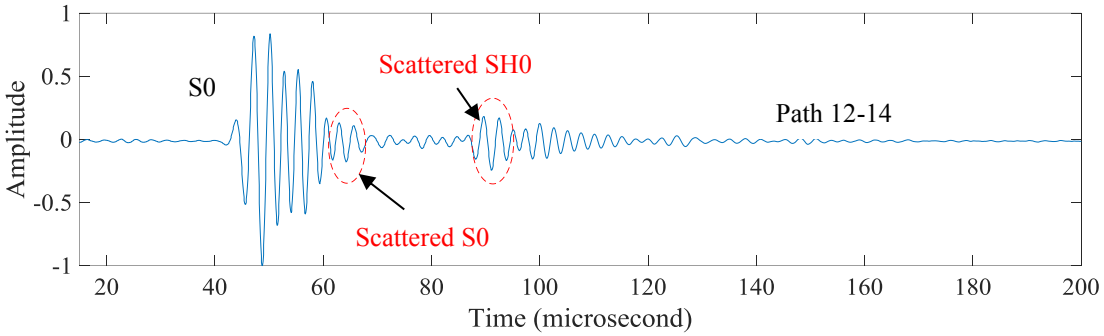

Figure 7.15: The waveform signal of sensing path 12-14.

7.4.4 Results

In this experiment, the twenty-two sensors are distributed across the plate to divide it into four sub-areas. The first sub-area is a pristine area. The baseline signal can be determined from this area. The other three sub-areas have different sizes of circular delamination as shown in Figure 7.13. Before imaging the delamination, we should indicate the location of damages points on the plate. This step helps us to determine the direction of incident and scattered waves of different sensing paths. A pulse-echo experiments were implemented to study the scattering waves around the damage point. From the Figure 7.16, we can observe that the pulse echo signals received by sensor *S16* (path 16-16) and sensor *S15* (path 15-15) have approximately the same TOF of scattered waves. Also, the sensors *S13* and *S21* have the same TOF. The difference in TOF of two scattered signals received

by two sensors located in horizontal or vertical lines is equal to zero. We can estimate the location of defect point which is at the center of interested area as shown in Figure 7.16 (b).

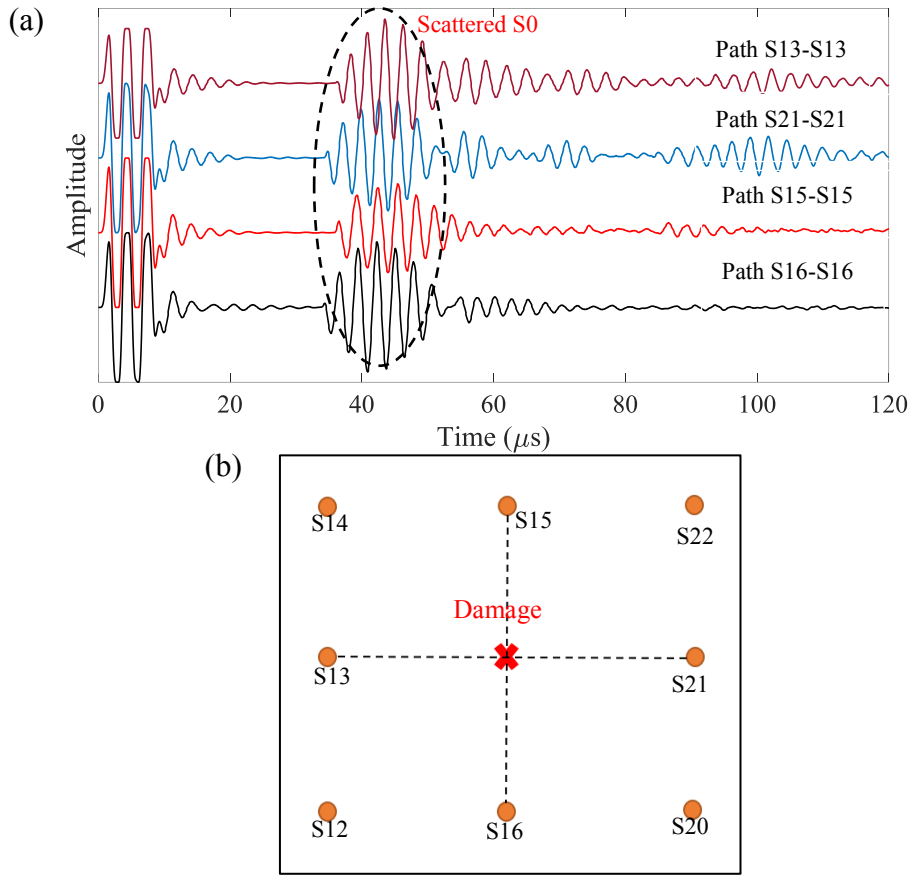

Figure 7.16: The methodology of prediction the location of damage point of sub-area 2; (a) pulse–echo signals for some sensors at center frequency 330 kHz; (b) estimation the location of damage point.

A pitch-catch experiment was implemented to identify the delamination areas. The excitation signal is 3-count tone burst signal at center frequency 330 kHz. In this experiment, we worked with short sensing path. The short distance paths can catch the scattered signals from defects. Also, for short distance sensing path, the scattered S0 packet is overlap with the incident waves. In this case, we will work with scattered SH0. Figure

7.17 shows the measured signals of sensing paths 19-17 and 19-16 compared with pristine signal of path 3-8. It can be easily recognized the scattered SH0 of 75-mm delamination for both measured signals. The scattered SH0 of 50-mm delamination can be recognized for the sensing paths 15-13 and 15-21 as shown in the Figure 7.18.

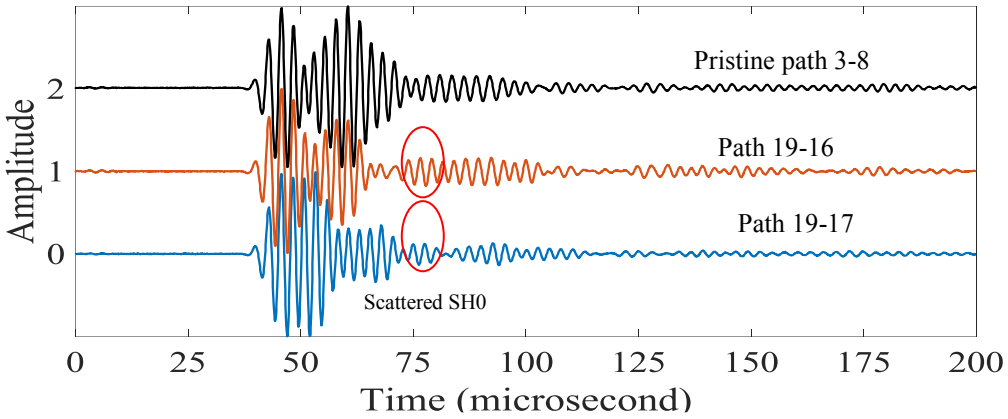

Figure 7.17: Measured signals of sensing paths 19-17 and 19-16 compared with pristine signal of sensing path 3-8.

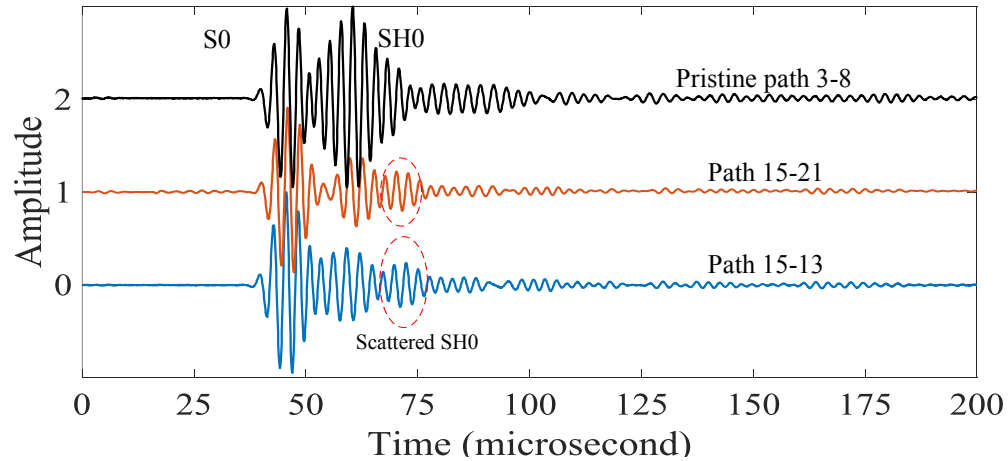

Figure 7.18: Measured signals of sensing paths 15-13 and 15-21 compared with pristine signal of sensing path 3-8.

Based on the time of flight of scattered SH0 waves, the imaging method is used to quantify the damage areas on the plate. The basic idea of imaging method is to divide the

interested area into pixels and to find the field values of the pixels for each image of sensing paths. After that we should fuse all the images from different paths in one image using summation or multiplication algorithms. The semi-elliptical orbit in the Figure 7.19 can be extracted using the following equation

$$t_D = \frac{\sqrt{(x_T - x_D)^2 + (y_T - y_D)}}{V_{S0}} + \frac{\sqrt{(x_D - x_R)^2 + (y_D - y_R)}}{V_{SH0}} \tag{7.1}$$

where t_D is TOF of scattered signal, $x_T, y_T, x_R, y_R, y_D, x_D$ are the coordinates of transmitter sensor, receiver sensor and damage point, respectively, v_{S0}, v_{SH0} are the group velocities of incident S0 and scattered SH0, respectively.

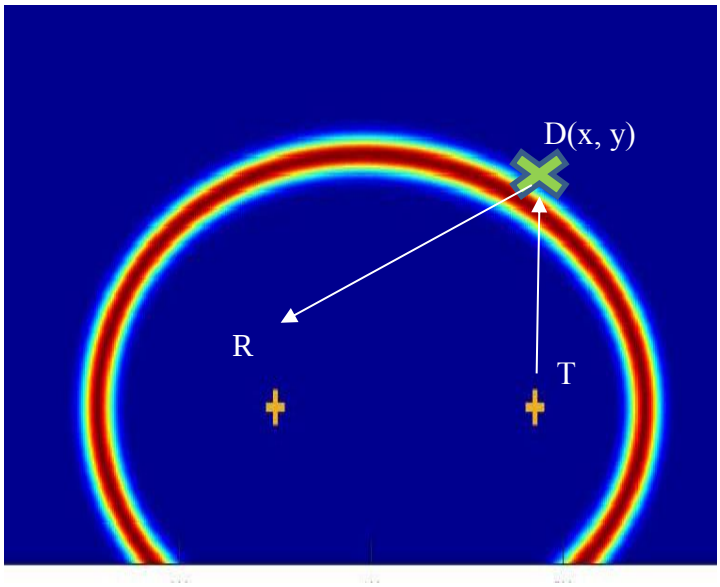

Figure 7.19: Semi-elliptical orbit which has the transmitter and receiver sensors as foci.

We modified the flow chart of imaging method which shown in chapter 5. In this modified flow chart, we add a methodology of determining the group velocities of incident and scattering waves as is shown in Figure 7.20. The Gaussian distribution equation is used

to determine the field values for image pixels as follow

$$f_{ij}^{k}(x,y)=\frac{1}{\sigma\sqrt{2\pi}}e^{-\frac{(x-\mu)^2}{2\sigma^2}} \tag{7.2}$$

where $f_{ij}^{k}(x,y)$ is the field value of every pixel $P(x,y)$ of the image of a particular sensing path $T_m - R_n$ (transmitter T_m and receiver R_n), x represents the time of flight at each pixel point $t_{ij}(x,y)$ for the sensing path $T_m - R_n$, μ represents the time of flight of scattering wave packet for sensing path $T_m - R_n$ which can be determined experimentally. The standard deviation, σ which describes the variability or dispersion of a data set, which was taken as half of the time range of wave packet. m,n represent the index of transmitters and receivers, respectively which vary from 1 to total number of transmitters (N_T) and receivers (N_R), such as, $m=1,2,3,....N_T$ and $n=1,2,3,....N_R$.

The pixel points which located on the locus of damage orbit have the maximum field values (they have 100% of the probability of defect presence). The field value decreases with increasing the distance between the pixel point and damage locus. To fuse all the images of different sensing paths, we can use summation [11] or multiplication [17] algorithms as follow

$$\begin{aligned} P_{sum}(x,y)&=\sum_{k=1}^{N} f_{ij}^{k}(x,y) \\ P_{mult}(x,y)&=\prod_{k=1}^{N} f_{ij}^{k}(x,y) \end{aligned} \tag{7.3}$$

where $P_{sum}(x,y), P_{mult}(x,y)$ are the total field values of each pixel point using summation or multiplication algorithm. N represents the total number of sensing paths.

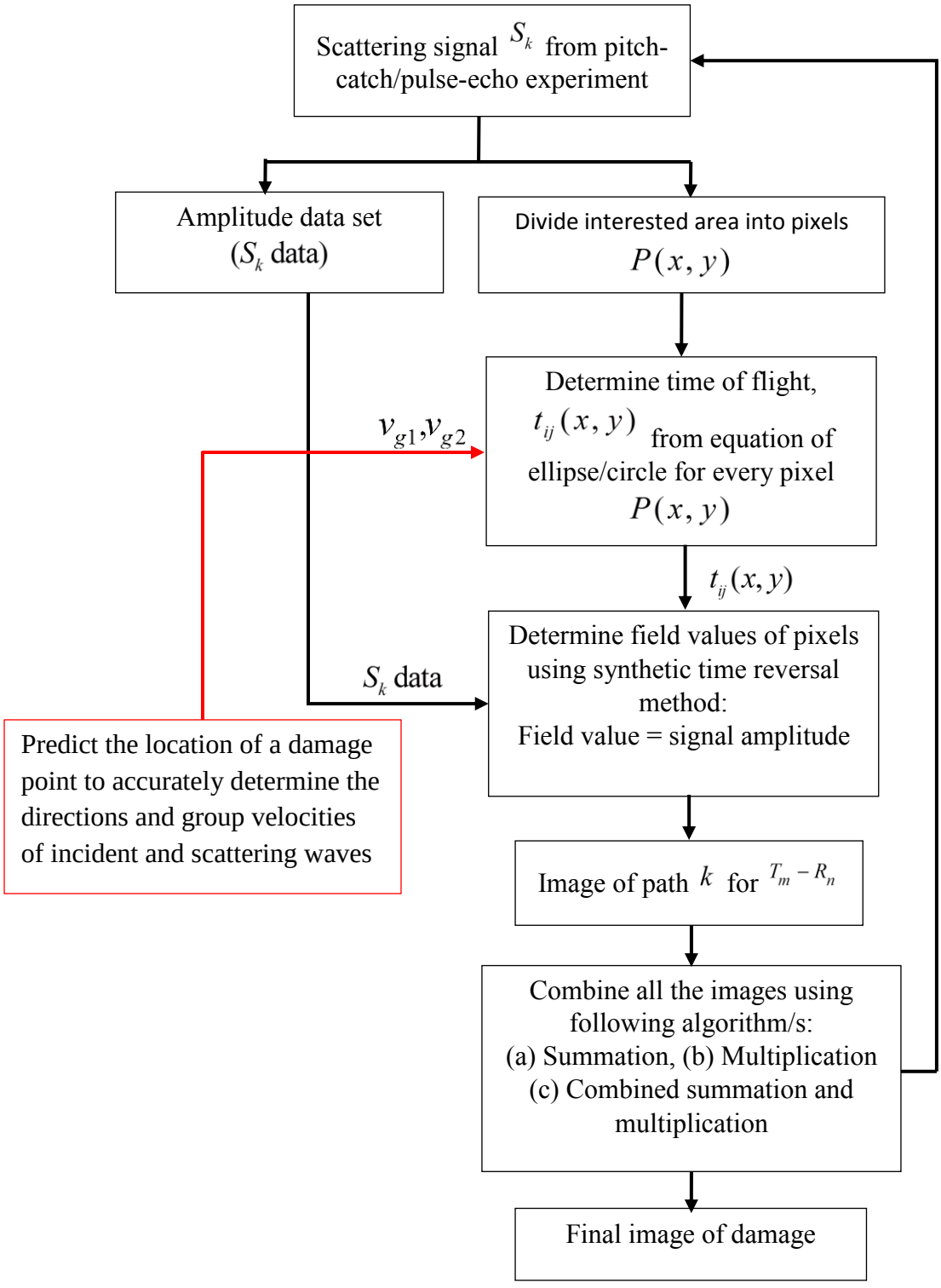

Figure 7.20: Flowchart of imaging method for identfying a damage of interested area.

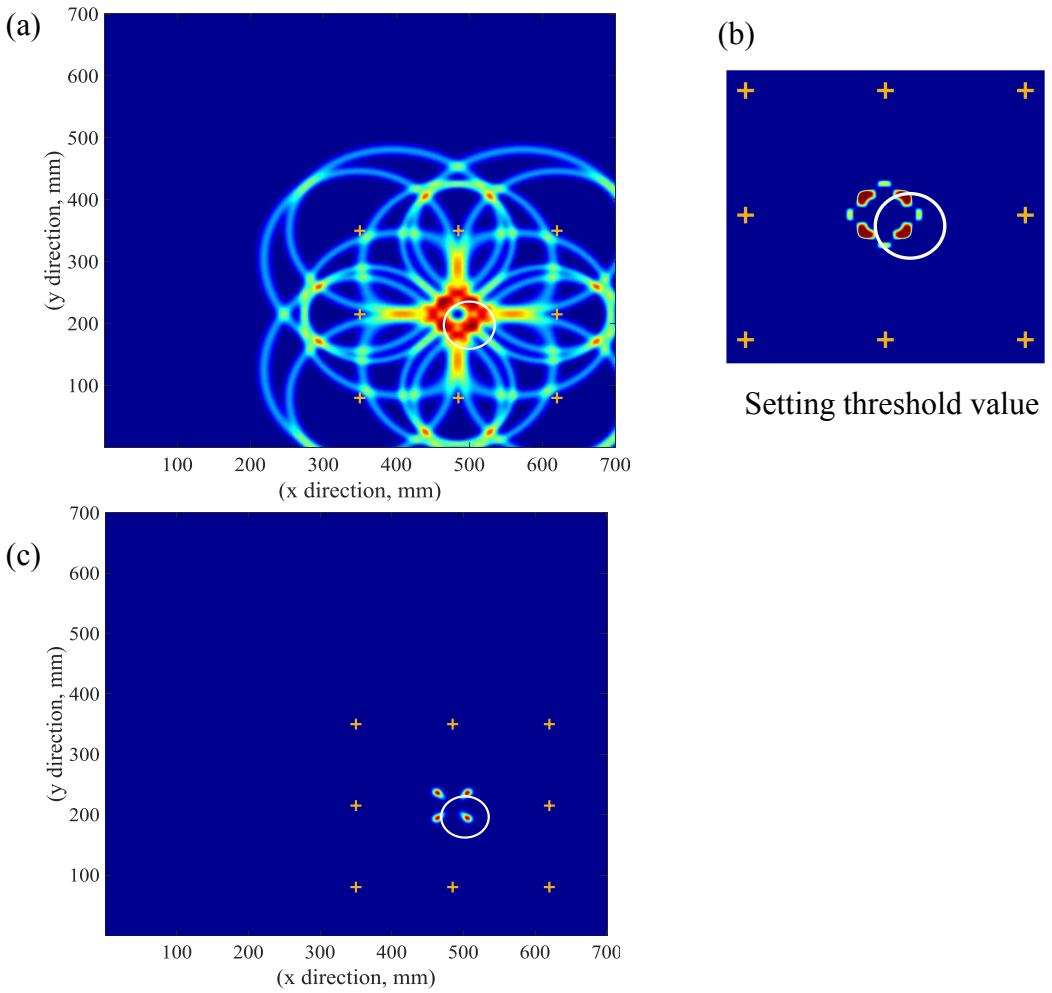

Figure 7.21: Imaging results of sub-area 2 (75-mm delamination); (a) using summation algorithm; (b) setting threshold value; (c) using combined of summation and multiplication algorithms

The imaging results of sub-area 2 are shown the Figure 7.21. Figure 7.21 (a) shows the image of 75-mm delamination area which extracted using summation algorithm. We can see the edges of circular delamination area. Figure 7.21 (b) shows the delamination area after setting threshold value (about 80% of maximum field value). From this image, we can indicate the size and the shape of delamination area. We have developed a methodology of visualizing the structural damage without setting threshold value. In this methodology, the summation and multiplication imaging algorithms are combined to fuse

all the images of various sensing paths. Firstly, we use summation algorithm to find the total field values of sensing paths of every actuator. After that, we use the multiplication algorithm to fuse all the images of all used actuators. From the Figure 7.21 (c), we can see the delaminations sizes are identified by four red spots which represent the edges of delamination area. In the same manner, we visualize the delamination area of sub-area 3. Figure 7.22 (a) show the result image of identifying 50-mm delamination area. The shape and size of delamination can be quantified after setting threshold value which is seen in Figure 7.22 (b). Also, we can use both of summation and multiplication algorithms to map the delamination area as shown in the Figure 7.22 (c). For the 25-mm delamination of sub-area 4, the imaging results show a small red spot with a size approximately equal to the size of delamination area as shown in Figure 7.23. The final images of identifying multiple damages on the whole plate are seen in Figure 7.24. For Figure 7.24 (a), the combined of summation and multiplication algorithms were used to extract the final image without setting threshold value. For Figure 7.24 (b), the summation algorithm was used to extract the final image of the whole plate after setting threshold value.

7.5 SHM TECHNIQUE FOR INSPECTION SPECIMEN 2

The experimental setup of inspection specimen 2 is like the setup of specimen 1 as shown in Figure 7.25: Experimental setup of using SHM technique for inspection the specimen 2. A network of twenty-two of PWAS were installed across the plat with 135-mm distance between two sensors. The plate has non-reflective boundaries by putting a clay around its edges to die out the reflected waves. An Agilent 33120A Arbitrary Waveform Generator was used to generate a 3-count Hanning window modulated tone burst excitation signal. The frequency of excitation signal was swept between 30 kHz to

420 kHz. An Oscilloscope records the received signals.

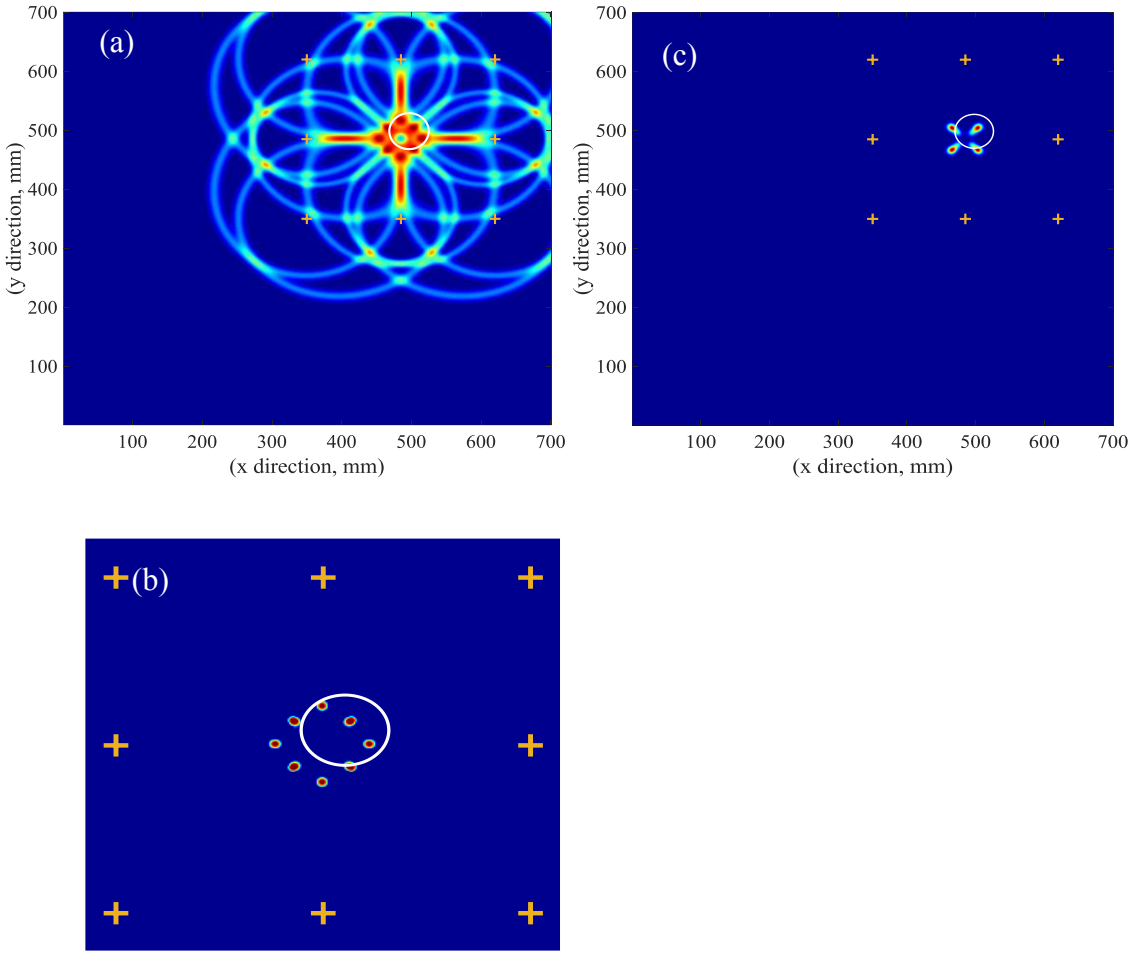

Figure 7.22: The imaging results of sub-area 3 (50-mm delamination); (a) using summation algorithm; (b) setting threshold value; (c) using combined of summation and multiplication algorithms.

7.5.1 Group Velocity Dispersion and Tuning Curves

The group velocity dispersion curves and tuning curves are determined experimentally for Lamb wave propagating on 5-mm thickness unidirectional composite laminates. Figure 7.26 (a), (b) show the waveform and short-time Fourier transform (STFT) spectrum of Lamb wave modes propagating in the fiber direction (0° direction) at frequency 180 kHz. It can be observed a good matching among analytical slowness curves

and STFT spectrum of experimental signal. The symmetric Lamb mode (S0) is strongest mode at this frequency.

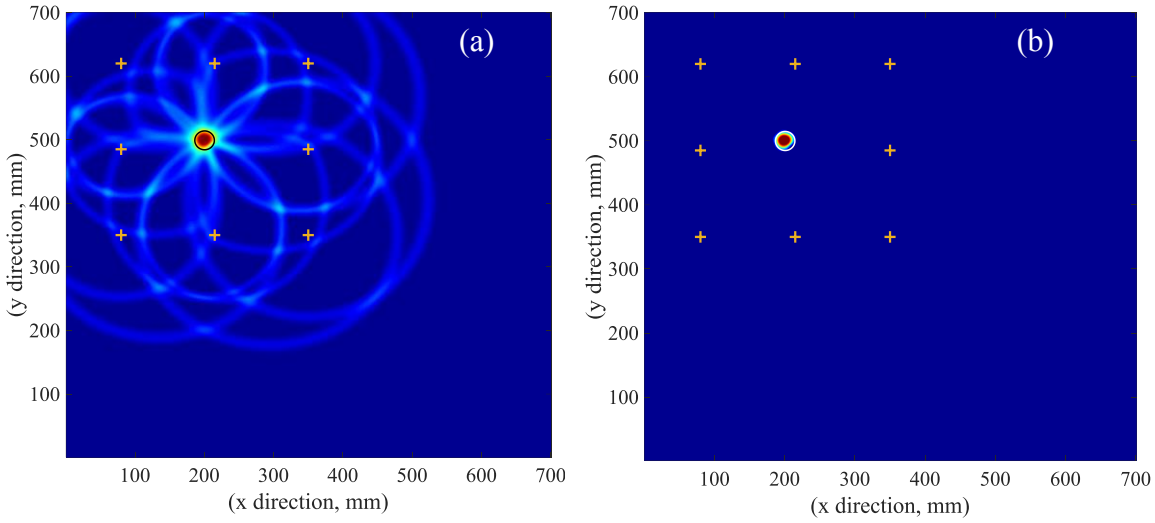

Figure 7.23: Imaging results of sub-area 4 (25-mm delamination); (a) using summation algorithm; (b) using combined of summation and multiplication algorithms.

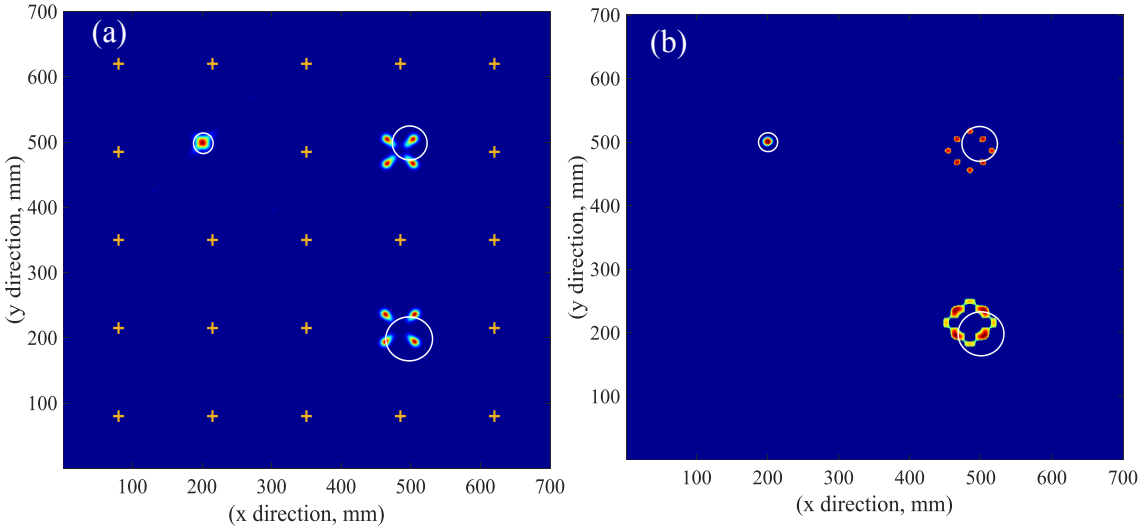

Figure 7.24: Imaging results of the whole area; (a) using combined of summation and multiplication algorithms; (b) setting threshold value.

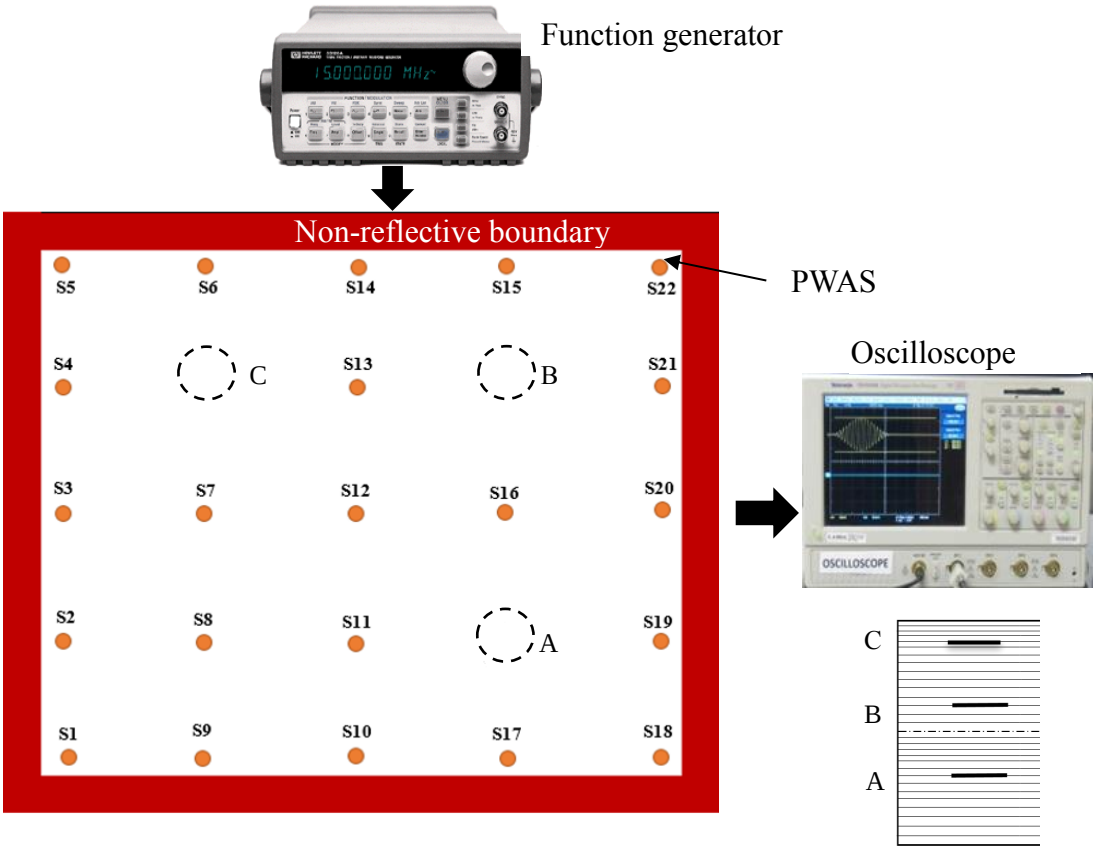

Figure 7.25: Experimental setup of using SHM technique for inspection the specimen 2.

Figure 7.27 (a), (b) show the waveform and short-time Fourier transform (STFT) spectrum of propagating Lamb waves in transverse direction (90° direction) at frequency 180 kHz. It can be observed a good matching among analytical slowness curves [15] and STFT spectrum of experimental signal. Furthermore, we can observe that SHS0 is the dominant mode in the transverse direction at frequency 180 kHz. Figure 7.28 shows the analytical and experimental group velocity dispersion curves of some Lamb waves propagating in fiber and transverse directions. Figure 7.28 (a) shows a good matching among the analytical [85] and experimental group velocity dispersion curves in fiber direction for some Lamb wave modes. Figure 7.28 (b) shows the analytical and experimental group velocity dispersion curves in transverse direction.

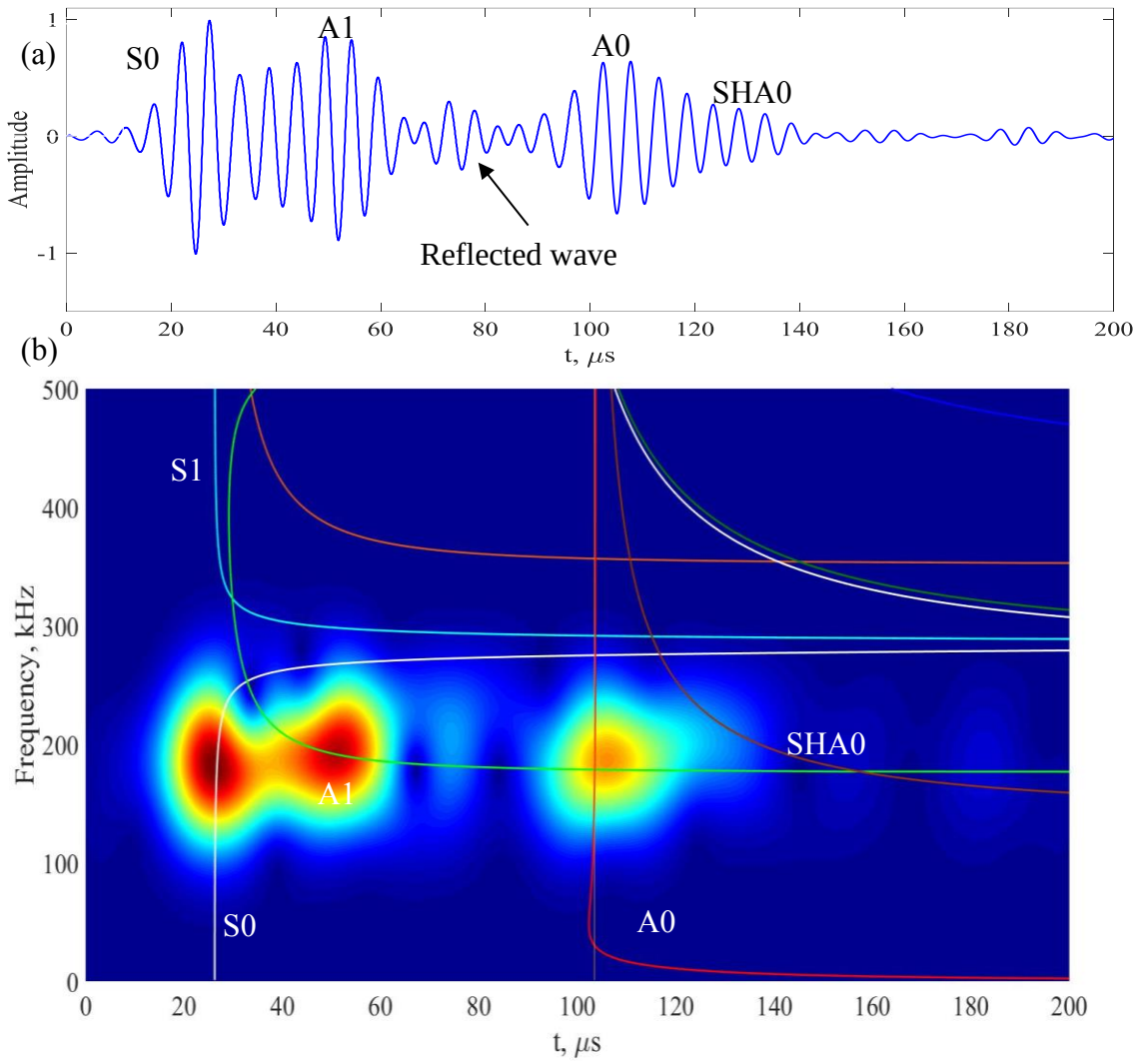

Figure 7.26: Lamb wave propagating in fiber direction of unidirectional composite plate; (a) signal time domain; (b) time frequency spectrum combined with analytical slowness curves [15].

We can observe a good matching between analytical and experimental results. The tuning curves were determined for some Lamb waves which are propagating in three different directions as shown in Figure 7.29. Figure 7.29 (a) shows the analytical [85] and experimental fiber direction tuning curves of some Lamb wave modes. The A1 is the strongest and dominant mode at the frequency range 280-400 kHz. Figure 7.29 (b) shows the Lamb waves tuning curves in transverse direction (90^0).

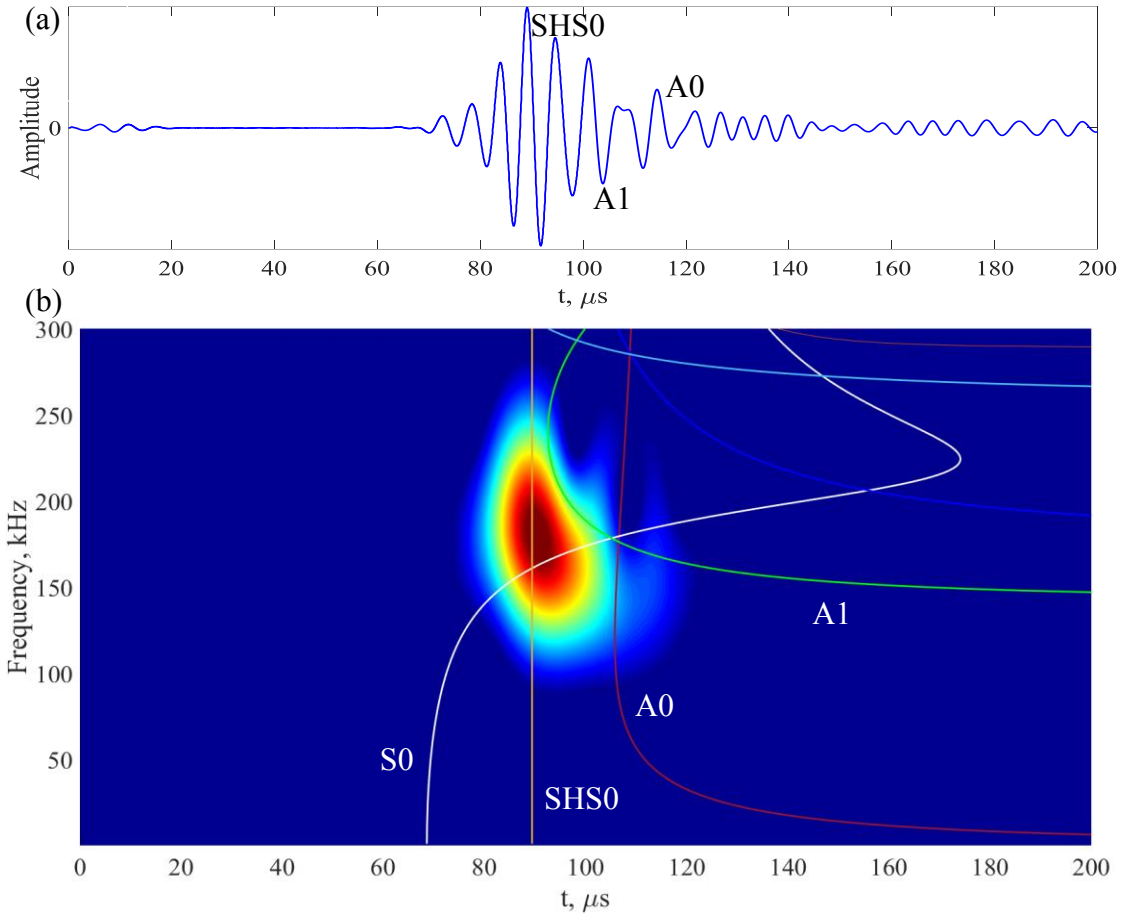

Figure 7.27: Lamb wave propagating in transverse direction of unidirectional composite plate; (a) signal time domain; (b) time frequency spectrum combined with analytical slowness curves [15].

We can observe a good matching between analytical and experimental results. The SHS0 is the dominant mode for Lamb waves propagating in transverse direction at the frequency range 180-400 kHz. Figure 7.31 (c) shows the experimental results of tuning curves for propagating Lamb waves in 45^0 direction. The SHS0 is the dominant mode at frequency range 150-220 kHz. Based on these tuning curves for three different directions, we can choose the frequencies of excitation signals. For sensing paths in fiber direction, we choose 300 kHz as an excitation signal frequency. The A1 is the dominant mode at this frequency. For the sensing paths in transverse direction (90^0), we choose 180 kHz as an

excitation signal frequency where SHS0 is the dominant mode. Figure 7.30 shows dominant lamb waves at different frequencies and directions.

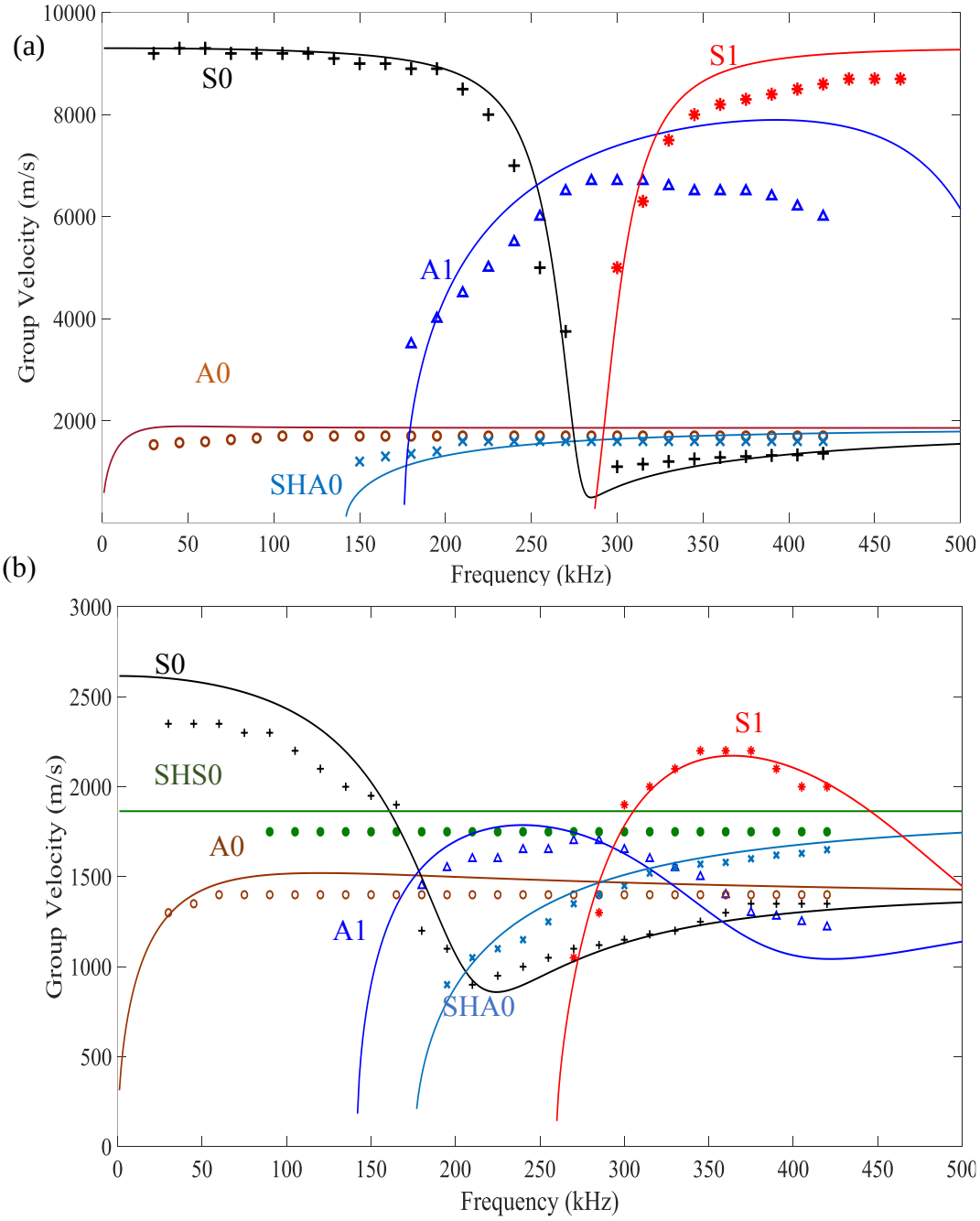

Figure 7.28: Analytical [15] and experimental group velocity dispersion curves of unidirectional composite laminate for two directions; (a) fiber direction (0^0); (b) transvers direction (90^0).

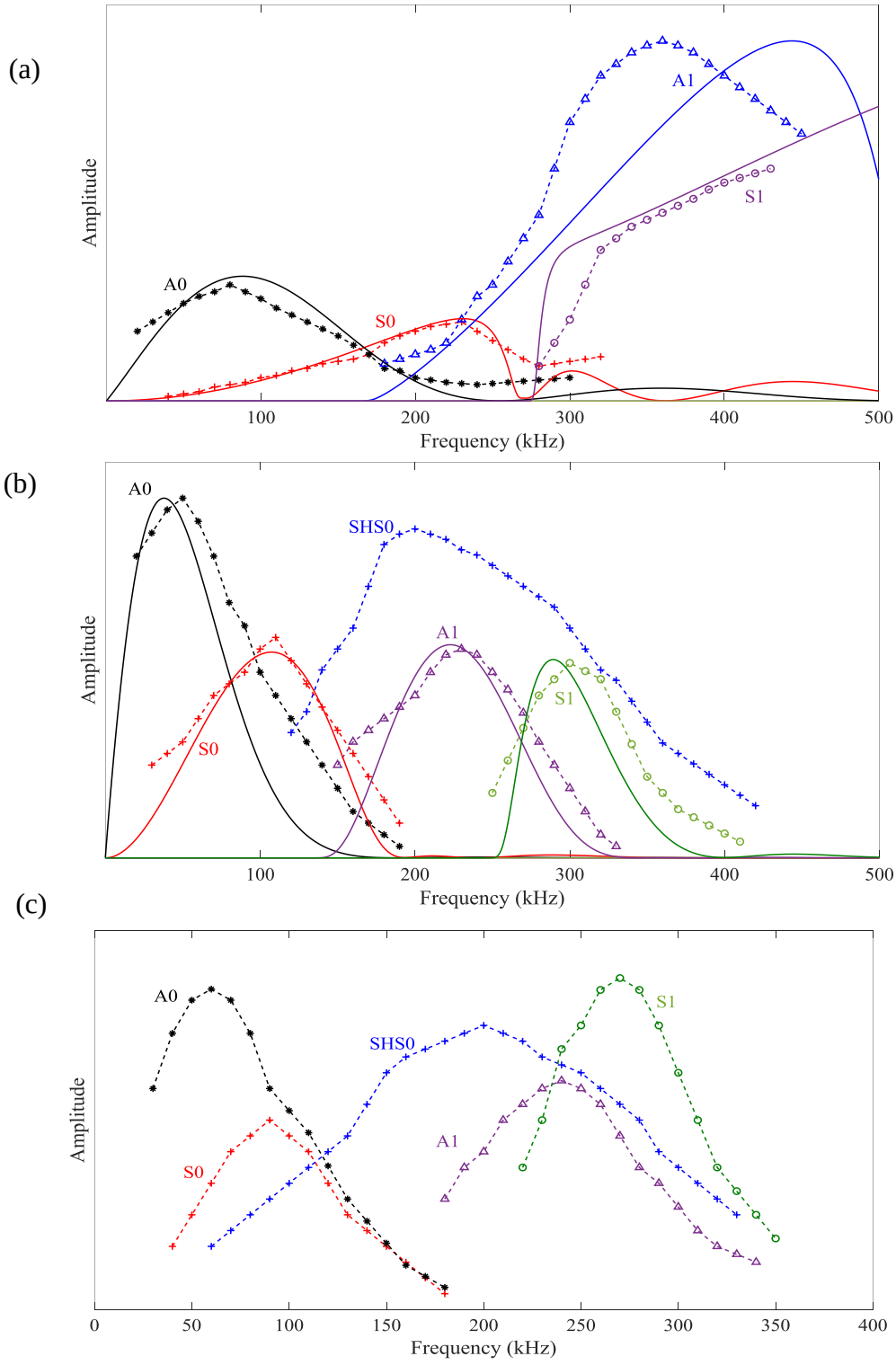

Figure 7.29: Analytical [15] and experimental tuning curves of Lamb waves for 5-mm unidirectional composite laminate at three directions; (a) fiber direction (0^0); (b) transvers direction (90^0); (c) experimental results at 45^0direction.

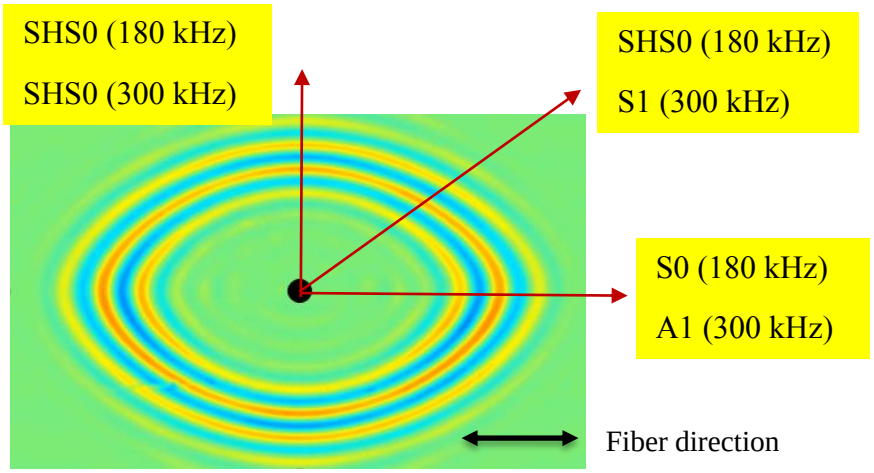

Figure 7.30: Dominant Lamb wave modes at different frequencies and directions for 5-mm unidirectional composite laminates.

7.5.2 Pitch-Catch Experimental Results

A pitch-catch experiments were implemented after setting up a network of twenty-two sensors and choosing the appropriate frequencies of excitation signals. The effect of delamination depth on the energy of scattering waves is studied. Figure 7.31 shows the scattering waves of different delamination areas. The scattering waves of delamination C have the highest energy among the scattering waves of other delamination areas. It is important step to analyze and define the mode types of scattering waves to predict and size the damages. The TOF of scattering wave packet consist of two parts. The first part is TOF of incident wave form the transmitter to the damage point. The second part is TOF of scattering wave from the damage to the receiver. To determine the TOF of scattering we should know the propagating distance from the transmitter to the damage point and the distance from the damage point to receiver. Also, we should know the group velocity of dominant incident and scattering waves. Based on tuning curves, we can define the dominant incident modes at certain frequencies and directions. The delamination has multiple scattering waves. The scattering waves depend on the incident waves and the

scattering waves directions. Figure 7.32 (a) shows the direction of incident and scattering waves of sensing path between transmitter sensor *S13* and receiver *S12*. The measured signal between these two sensors which is shown in the Figure 7.32 (d) has two scattering waves. The incident signal which propagate in fiber direction at certain frequency 300 kHz hits the delamination area and generates scattering waves. These scattering waves propagate in 45^0 to be received by the sensor *S12*.

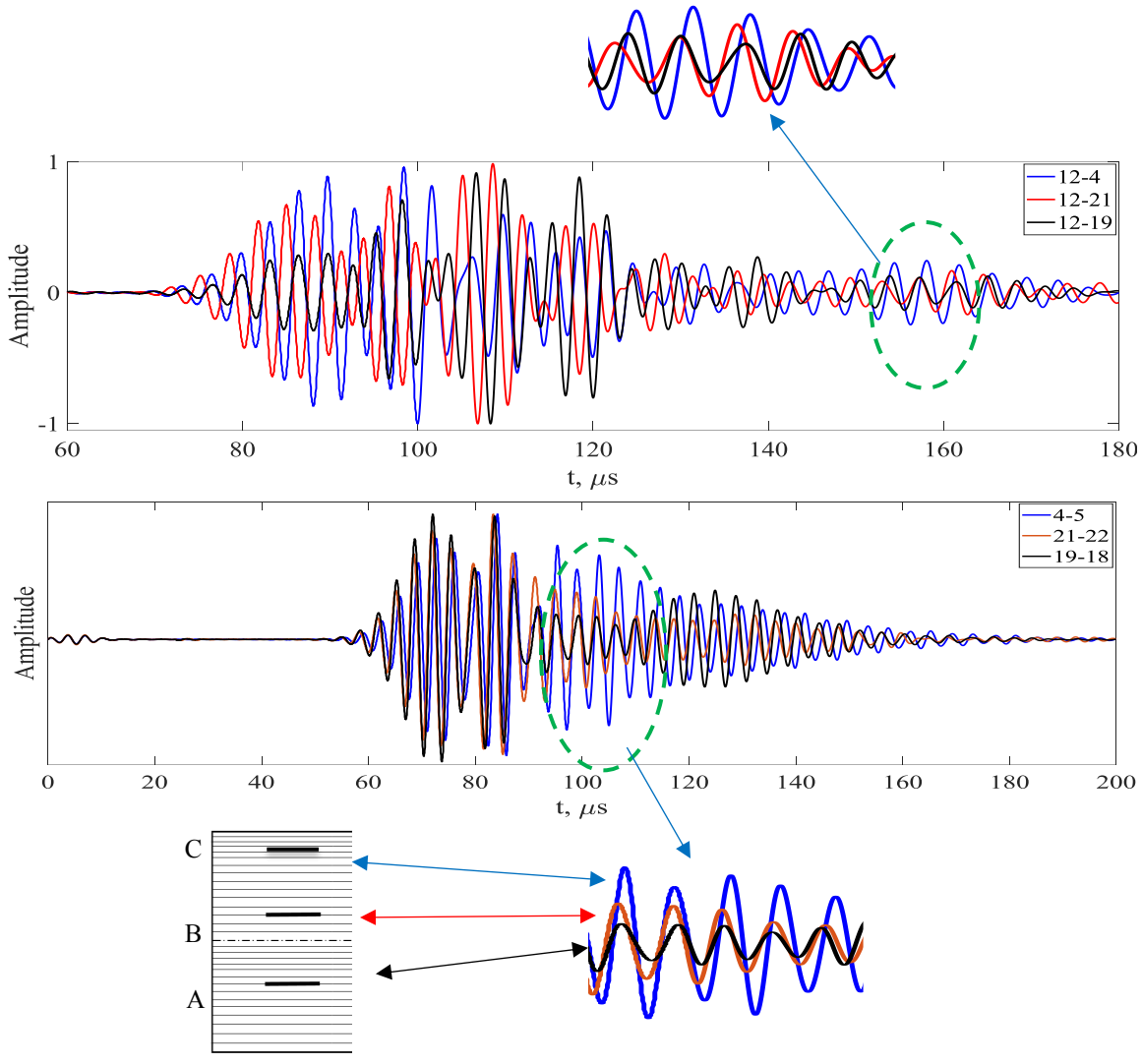

Figure 7.31: The effect of delamination depth on scattering wave amplitude.

We should define the scattering modes to localize the delamination area. Based on tuning curves of Lamb modes propagation in 45^0 direction and a pristine signal of a sensing path in 45^0 direction which is shown in Figure 7.32b, the modes S1 is dominant mode at frequency 300 kHz as shown in Figure 7.32c. Also, we can see other two modes A1 and SHS0. So, we should check all these three modes to help us defining the scattering modes as the following three cases:

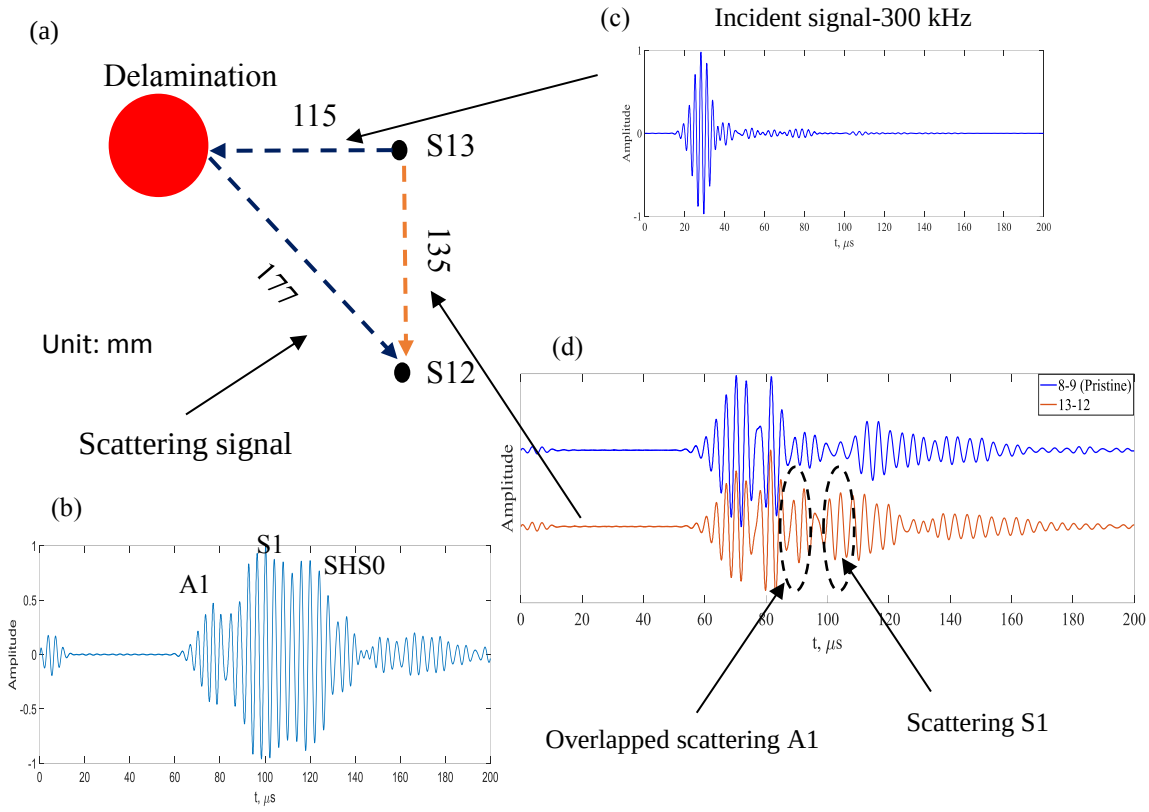

Figure 7.32: Determining the TOF and identifying of scattering wave modes.

1. Case (1): The incident wave mode is A1 and the scattering mode is A1

$$TOF_{Scattered}\left(Exp.\right)=103\ \mu s$$

$$TOF_{Scattered}=\frac{L_{T-D}}{V_{A1\left(0^{\circ}\right)}}+\frac{L_{D-R}}{V_{A1\left(45^{\circ}\right)}}=\frac{115}{6.5}+\frac{177}{2.7}=83\,\mu s$$

2. Case (2): The incident wave mode is A1 and the scattering mode is S1

$$TOF_{Scattered}\left(Exp.\right)=103\ \mu s$$

$$TOF_{Scattered}=\frac{L_{T-D}}{V_{A1(0^\circ)}}+\frac{L_{D-R}}{V_{S1(45^\circ)}}=\frac{115}{6.5}+\frac{177}{2}=106\,\mu s$$

3. Case (3): The incident wave mode is A1 and the scattering mode is SHS0

$$TOF_{Scattered}\left(Exp.\right)=103\ \mu s$$

$$TOF_{Scattered}=\frac{L_{T-D}}{V_{A1(0^\circ)}}+\frac{L_{D-R}}{V_{SHS0(45^\circ)}}=\frac{115}{6.5}+\frac{177}{1.6}=127\,\mu s$$

Based on the above results, we can observe that case (2) reached the experimental TOF of scattering wave.

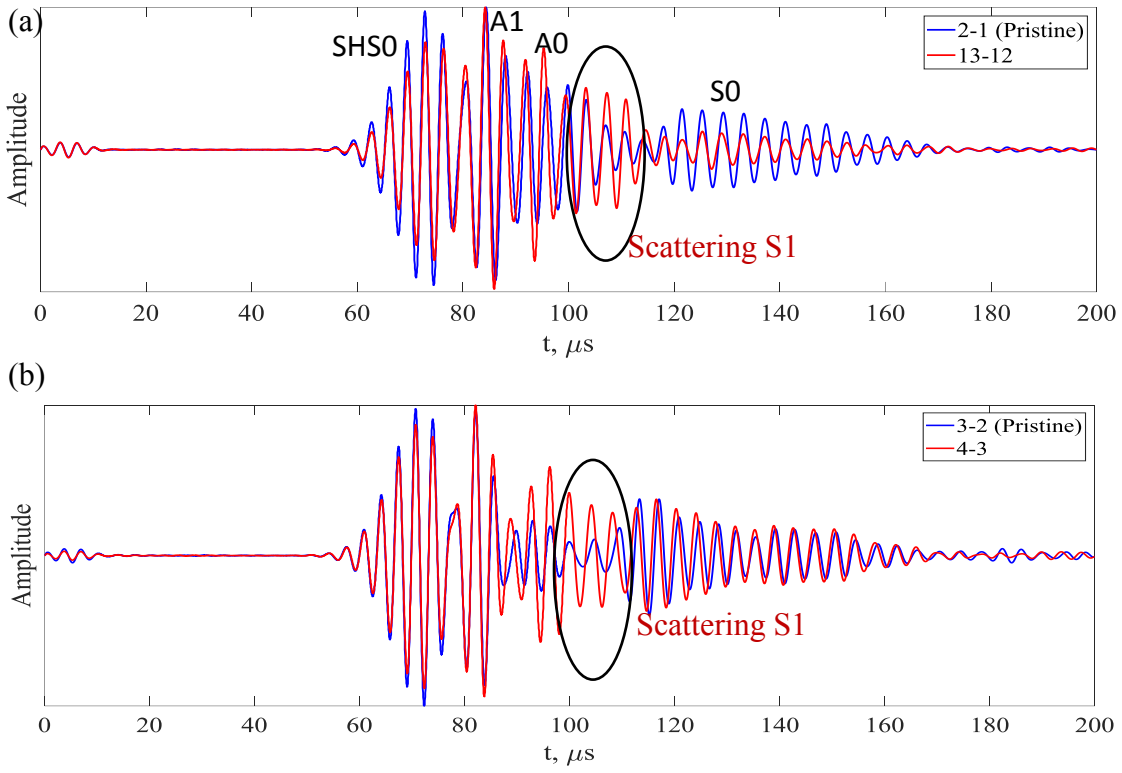

Figure 7.33: Pristine and measured signals of sensing paths in transverse direction at frequency 300 kHz; (a) pristine path 2-1 and measured path 13-12; (b) pristine path 3-2 and measured path 4-3.

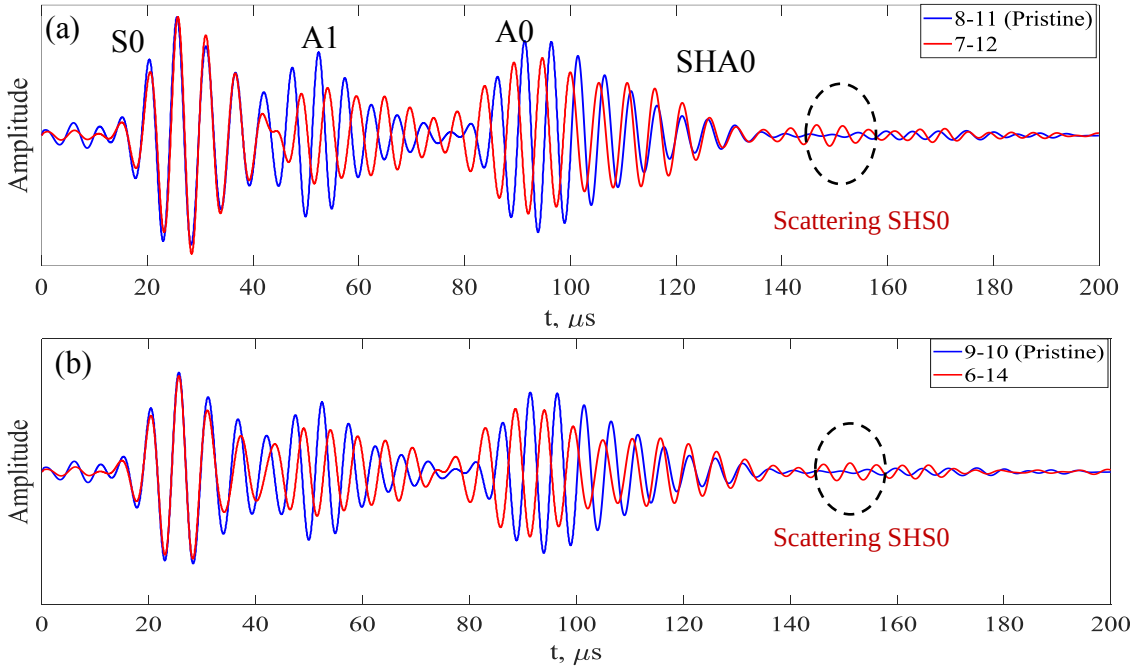

Figure 7.34: Pristine and measured signals of sensing paths in fiber direction at frequency 180 kHz; (a) pristine path 8-11 and measured path 7-12; (b) pristine path 9-10 and measured path 6-14.

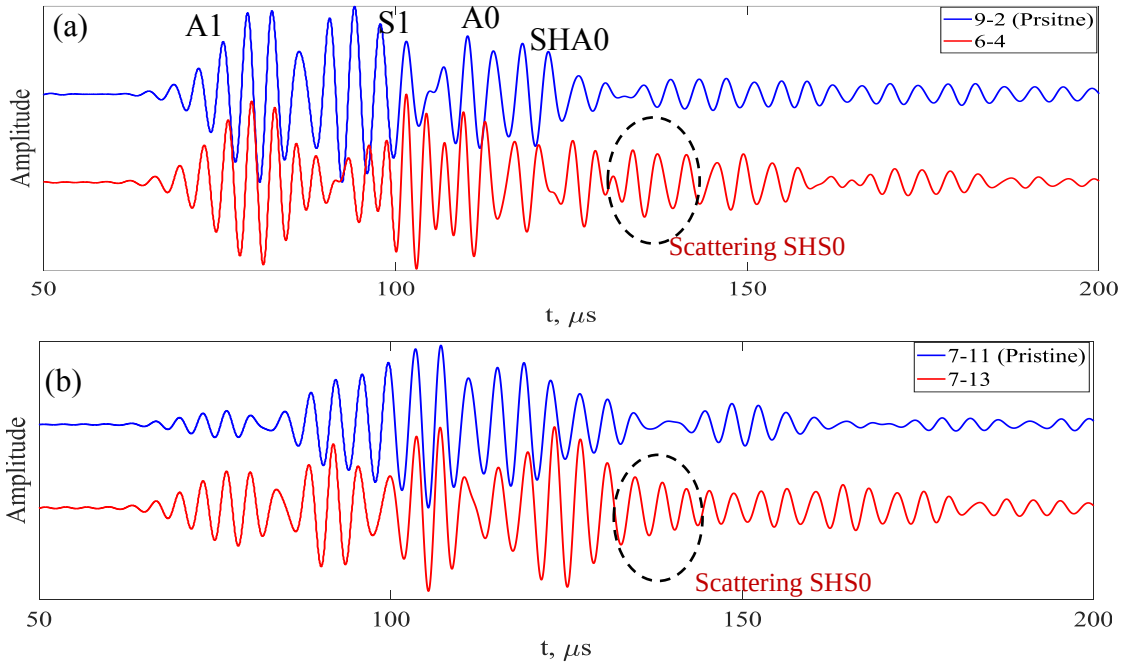

Figure 7.35: Pristine and measured signals of sensing paths in 45° direction at frequency 300 kHz; (a) pristine path 9-2 and measured path 6-4; (b) pristine path 7-11 and measured path 7-13.

The TOF of case (1) reached the TOF of overlapped scattering wave. We can conclude that the scattering modes have the same types of dominant modes in 45°. Based on these results, we can predict the scattering modes based on the dominant incident modes and the dominant modes of scattering direction. We should deal with the damage as a point and predict its location firstly to identify the directions of incident and scattering waves. To do that, we should study the scattering waves of sensing paths signals around the delamination areas. Figure 7.33 shows the measured and pristine signals in transvers direction of sensing paths around delamination C. It can be observed that the scattering waves have the same TOF values. Figure 7.34 shows the measured signals of the sensing paths in the fiber direction at frequency 180 kHz. The scattering waves of both sensing paths have same TOF value. Figure 7.35 shows two measured signals at frequency 300 kHz of 45^0 sensing paths around delamination C. The scattering waves of these signals have the same TOF value. Based on the difference in the TOF values of scattering waves of two horizontal and vertical sensing paths, we can detect the location of damage points. In this work, the damage points located at the centers of three sub-areas as shown in the Figure 7.36. After this methodology of prediction damages locations, the scattering modes types and the direction of incident and scattering waves and their group velocity can be determined.

7.5.3 Sizing of Delamination Areas Using Imaging Methods

The imaging methods are used to identify the delamination areas. The inspected specimen is divided into small pixels. To investigate pixels whether they have the damage or not, the TOF of pixels are determined using three different elliptical equations as shown in the Figure 7.37.

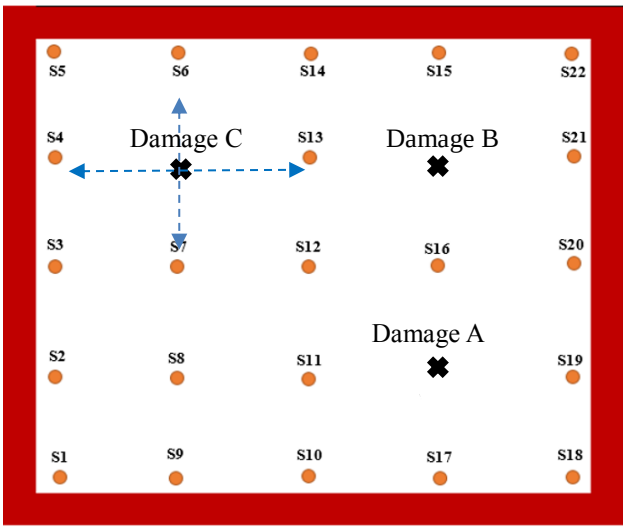

Figure 7.36: Prediction of damage locations using developed methodology.

Figure 7.37 (a) shows the scattering wave direction of a transverse sensing path where A1 is the incident mode at 300 kHz and S1 is the scattering mode. Figure 7.37 (b) shows the pattern of sensing paths in 45^0 direction where A1 is incident mode at 300 kHz and SHS0 is the scattering mode. Figure 7.37 (c) shows the scattering waves map of a fiber direction sensing path where SHS0 is the incident mode at 180 kHz and A1 is the scattering mode. The following elliptical equations represent the TOF of scattering waves for three different cases of sensing paths:

Case (1): The incident wave mode is A1, and the scattering mode is S1

$$t_{ij} = \frac{\sqrt{(x_T - x_i)^2 + (y_T - y_j)^2}}{v_{A1}} + \frac{\sqrt{(x_i - x_R)^2 + (y_j - y_R)^2}}{v_{S1}} \tag{7.4}$$

Case (2): The incident wave mode is A1, and the scattering mode is SHS0

$$t_{ij} = \frac{\sqrt{(x_T - x_i)^2 + (y_T - y_j)^2}}{v_{A1}} + \frac{\sqrt{(x_i - x_R)^2 + (y_j - y_R)^2}}{v_{SHS0}} \tag{7.5}$$

Case (3): The incident wave mode is SHS0 and the scattering mode is A1

$$t_{ij} = \frac{\sqrt{(x_T - x_i)^2 + (y_T - y_j)^2}}{v_{SHS0}} + \frac{\sqrt{(x_i - x_R)^2 + (y_j - y_R)^2}}{v_{A1}} \tag{7.6}$$

where t_{ij} is TOF of scattered signal, x_T, y_T, x_R, y_R, x_i, y_j are the coordinates of transmitter sensor, receiver sensor, and pixels, respectively, v_{S1}, v_{A1}, v_{SHS0} is the group velocities of symmetric and antisymmetric Lamb waves and symmetric shear horizontal wave.

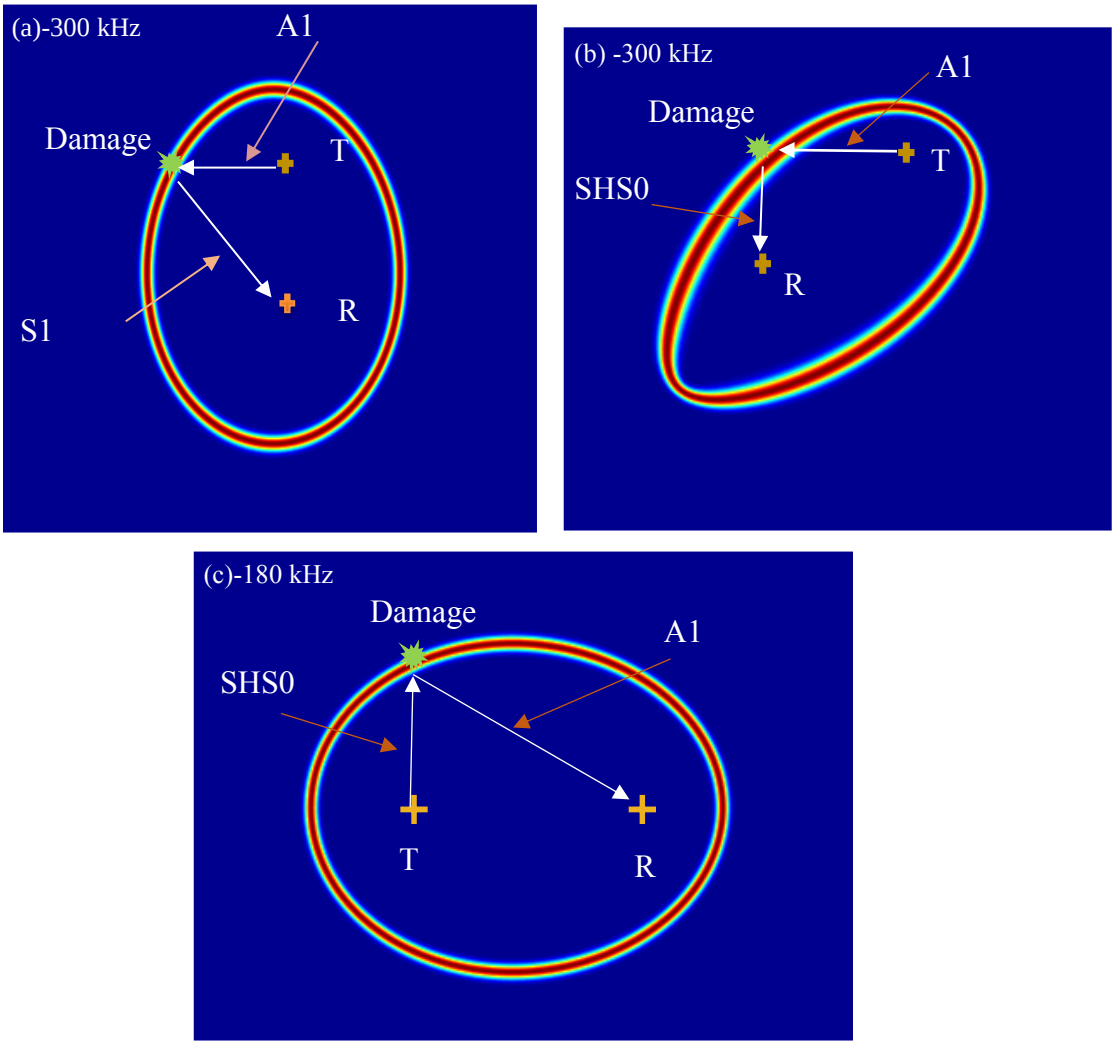

Figure 7.37: Three different cases of determining the TOF of scattering waves for three different directions of sensing paths: (a) transverse direction; (b) 45° direction; (c) fiber direction.

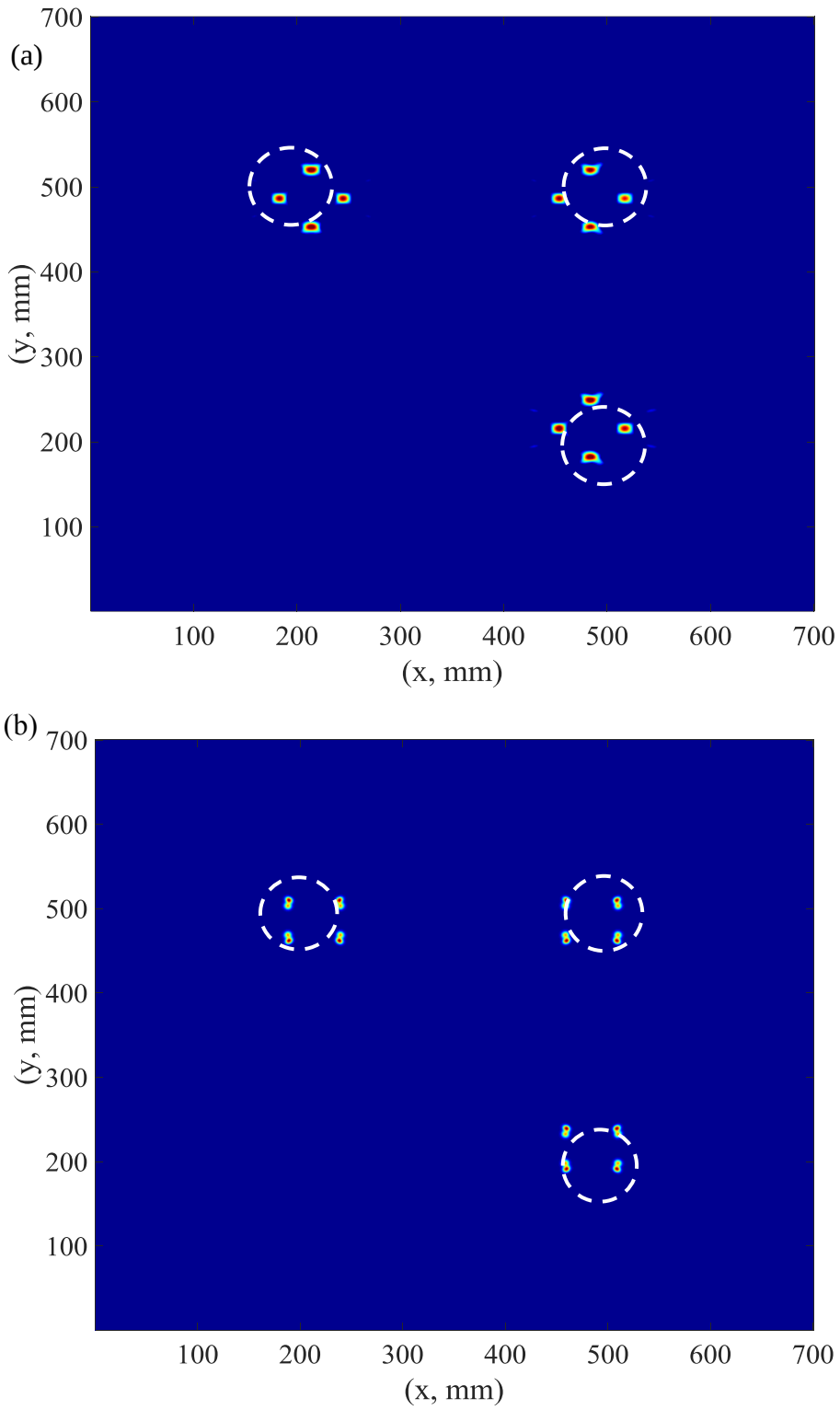

Figure 7.38: Imaging results: (a) using summation algorithm and setting threshold value (80% of maximum threshold value); (b) using combined of summation and multiplication algorithms without sitting threshold value.

The pixels field values of a sensing path image were determined by using the Gaussian distribution function. To collect pixels field values of all sensing paths, we use summation algorithms, multiplication algorithms or both (Eq.(7.3)). The final images of localizing and sizing delamination areas are shown in the Figure 7.38. To methods were used to extract the final images of identifying the delamination areas. In the first method (method 1), we used summation algorithm to add all the individual images of sensing paths. We set a threshold value which is 80% of maximum field value to extract the final image as shown in the Figure 7.38 (a). The second method (method 2), we used combined of summation and multiplication algorithms to extract the final image without setting a threshold value as shown in the Figure 7.38 (b). The results show good matching between real and calculated location and size of delamination.

7.6 SLDV TECHNIQUE FOR INSPECTION COMPOSITE PLATES

The aerospace composites are exposed to different kinds of unexpected damages due to impact or cycles load. The hidden delamination is one of the comment internal defects that take place in composite structure during their lifetime [86]. The SHM and the non-distractive techniques are the best and reliable methods for detecting and quantifying the invisible damages in metallic and composite structures [22] [87]. In recent years, many research have been implemented about using guided waves as effective methods for damage detection in metallic and composite structures [88] [23]. The Lamb wave interaction with composite defects are studied experimentally using guided wave images and wavenumber analysis [89]. The SLDV was used to study the effect of delamination damage on the Lamb wave amplitude and determine the damage size [87]. The delamination size and its location across the thickness were quantified using local

wavenumber domain analysis [90]. The delamination damage due to impact was quantified using guided wave field data and special wavenumber image [91]. The guided waves interaction with complex geometry of delamination were studied experimentally using LDV and numerically using EFIT method.

The results match fairly well in wavenumber domain [90]. Because the delamination damage is complex volume, we can see multiple reflection from this region when guided wave- damage interaction occur [92]. When the guided waves interact with delamination area, a considerable energy is trapped in above and down delamination area. The trapped waves were studied experimentally using LDV. The wavefield images clearly showed the trapped waves on the delamination area [93].

7.6.1 SLDV Technique for Inspection Specimen 1

The experimental setup of scanning Laser Doppler vibrometer is shown in Figure 7.39. In this experiment, The PWAS transducer is used to excite guided waves. The function generator is used to generate 3-count tone burst signal at frequencies 120 kHz and 240 kHz. The excitation signal is amplified to 50 V using amplifier. The amplifier relates to PWAS transducer to excite the guided waves. The scanning laser Doppler vibrometer is used to acquire the time-space wavefields over the scanning area. The laser head generates laser beam which is perpendicular to scanning area to measure out of plan motion. Four areas were scanned in this experiment. The first area is pristine area. The other three areas are the damaged areas as shown in the Figure 7.40. The scanned areas were covered with special tap to improve the surface condition. The guided waves interaction with damage can be visualized using the hybrid PWAS transducer- SLDV. So, we can visualize 1-D scan along a certain line of points or 2-D scanning with points in a certain area.

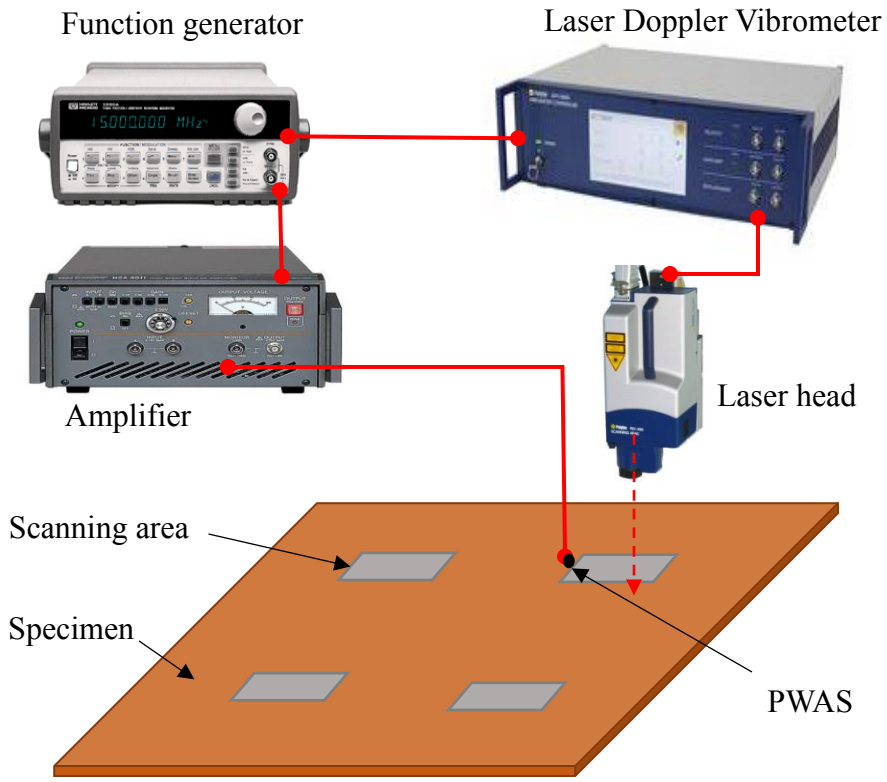

Figure 7.39: Experimental setup of scanning laser Doppler vibrometer.

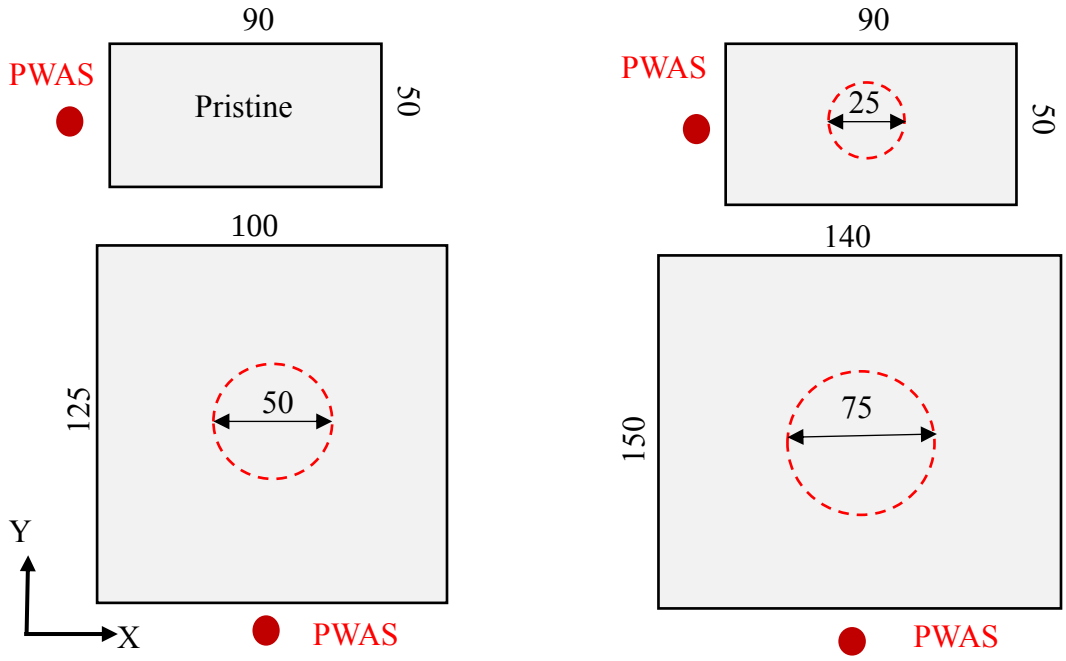

Figure 7.40: Configuration of scanning areas (Unit is millimeter).

Figure 7.41 shows the time-space wavefield and wavenumber-frequency domains which are measured for a line scan points along the x-direction of pristine area. Figure 7.41 (a) shows the time-space of asymmetric Lamb mode (A0) which excited at frequency 120 kHz. Figure 7.41 (b) shows the wavenumber-frequency domain of asymmetric Lamb mode (A0) at the same frequency. Figure 7.41(c), (d) show the time-space and wavenumber-frequency domains of symmetric and antisymmetric Lamb modes for the excitation signal at center frequency 240 kHz. From all these figures, we cannot observe any reflected or trapped waves.

Figure 7.42 shows the time-space domains for a line scan points along the horizontal center line of 25-mm delamination area. Figure 7.42 (a) shows the time space domain at certain frequency 120 kHz. We can see that the A0 mode is stronger than S0 mode and the reflected waves due to interaction of Lamb wave with delamination area. Figure 7.42 (b) shows the time-space domain at certain frequency 240 kHz. We can see both S0 and A0 modes. S0 mode is faster than A0. Also, we can see the trapped waves of S0 mode over 25-mm delamination area. The wavenumber-frequency domain of wavefields points along the center-line of 25-mm delamination are shown in Figure 7.43. From Figure 7.43 (a), (b), we can observe new components for both A0 and S0 modes due to interaction them with delamination area. The snapshots of wavefields over 25-mm delamination are shown in the Figure 7.44 (a), (b). From these figures, we can observe the trapped waves over delamination. So, we can quantify the location and size of delamination. The signals amplitude profiles for the points along the center lines of 25 mm delamination are shown the Figure 7.45 (a), (b). We can observe that signals of scanning points over the delamination area have higher amplitude values than other points. For both amplitude

profiles of scanning points along propagating waves direction (X-axis) and transverse direction (Y-axis), we can determine the lengths of delaminations. Figure 7.46 shows the time-space and frequency-wavenumber domains of wavefields along the center line of 50-mm delamination at frequencies 120 kHz and 240 kHz.

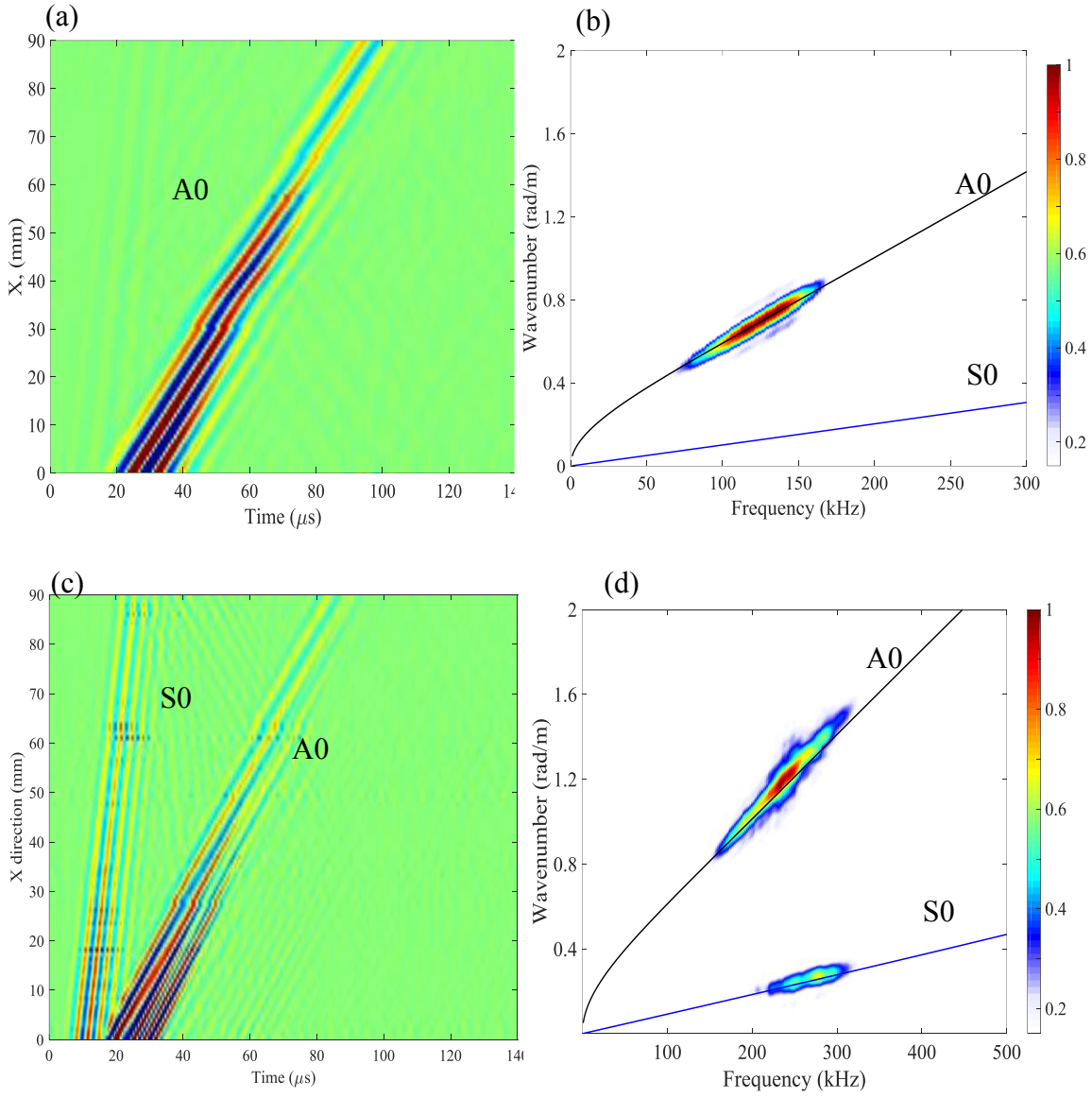

Figure 7.41: 1-D scanning pristine area using SLDV: (a) and (b) are the time-space and wavenumber-frequency domains at center frequency 120 kHz, (c) and (d) are the time-space and wavenumber-frequency domains at center frequency 240 kHz.

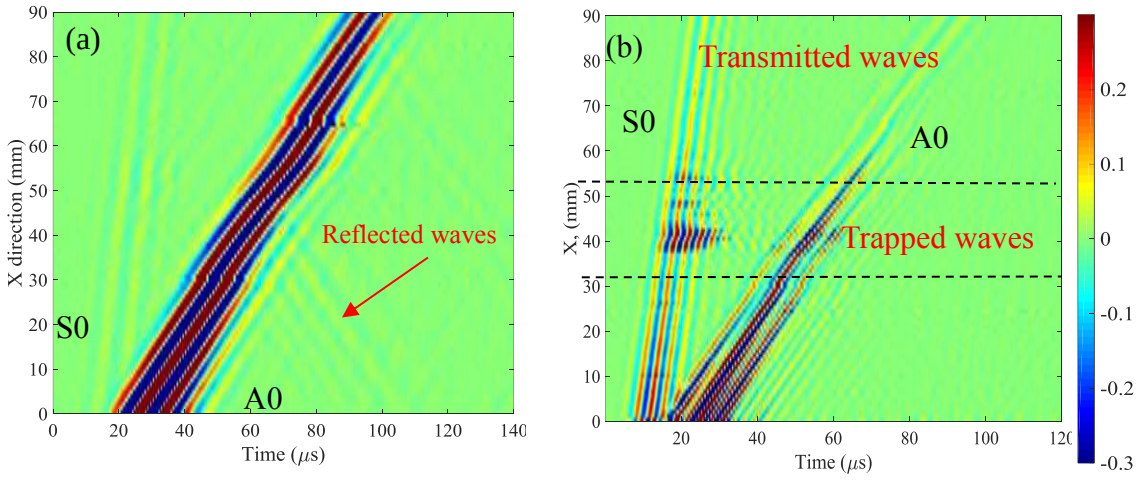

Figure 7.42: Time space domain measured from 1-D scanning with points along the center-line of 25 mm-delamination area at frequencies; (a) 120 kHz; (b) 240 kHz.

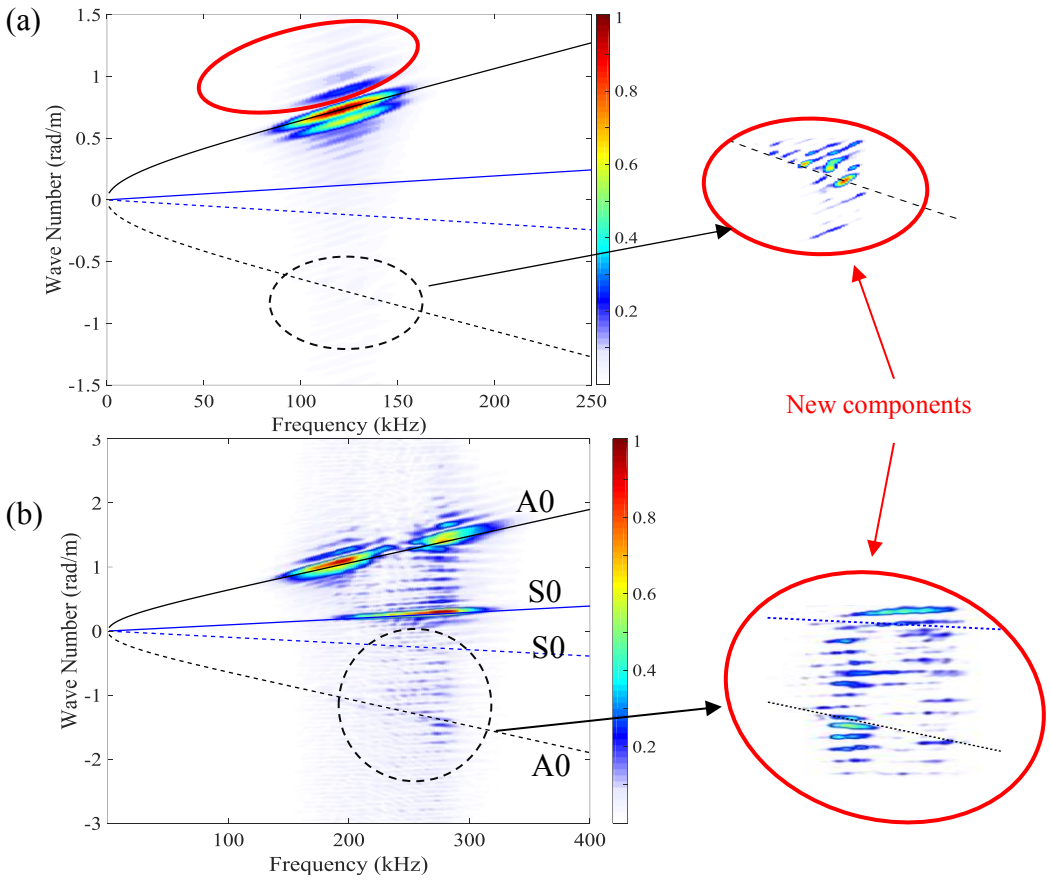

Figure 7.43: Wave-number domain measured from 1-D scanning with points along the center-line of 25 mm-delamination area at frequencies; (a) 120 kHz; (b) 240 kHz.

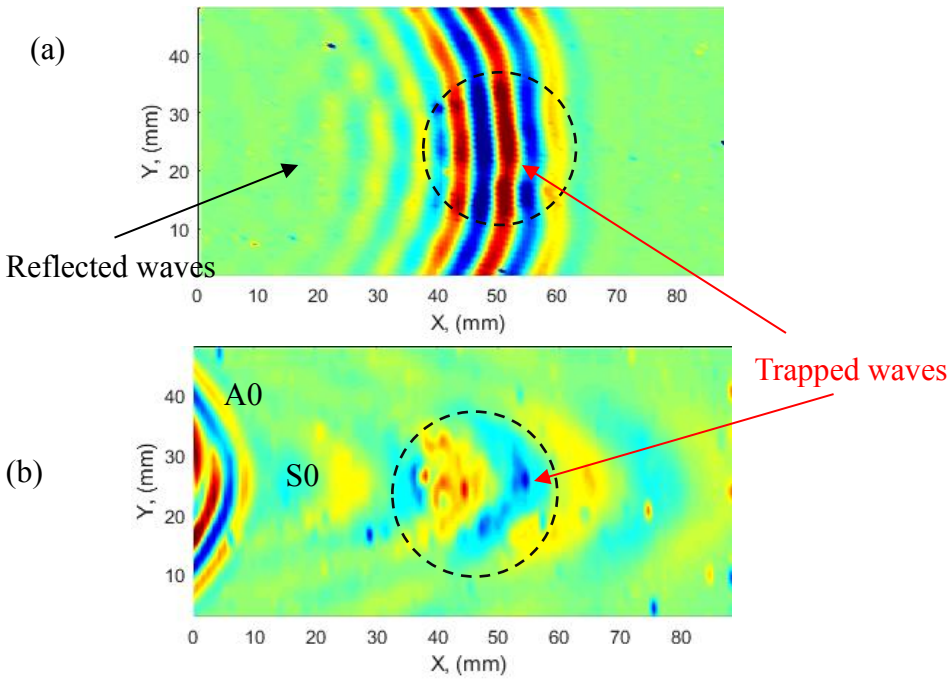

Figure 7.44: Measured time-space wavefield for the 2-D scanning of 25-mm delamination area at frequencies; (a) 120 kHz; (b) 240 kHz.

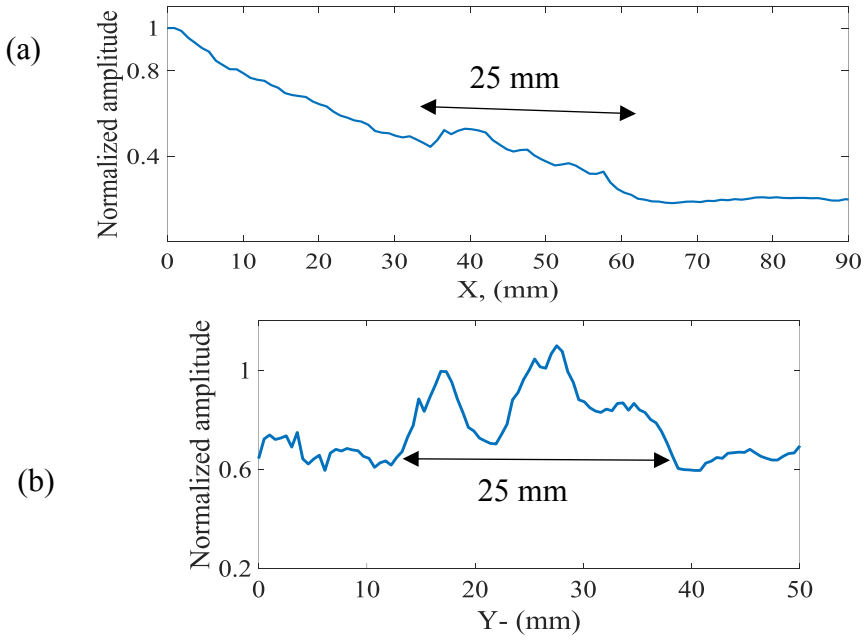

Figure 7.45: Maximum signals amplitude along the center lines of 25-mm delamination in; (a) X-direction; (b) Y-direction.

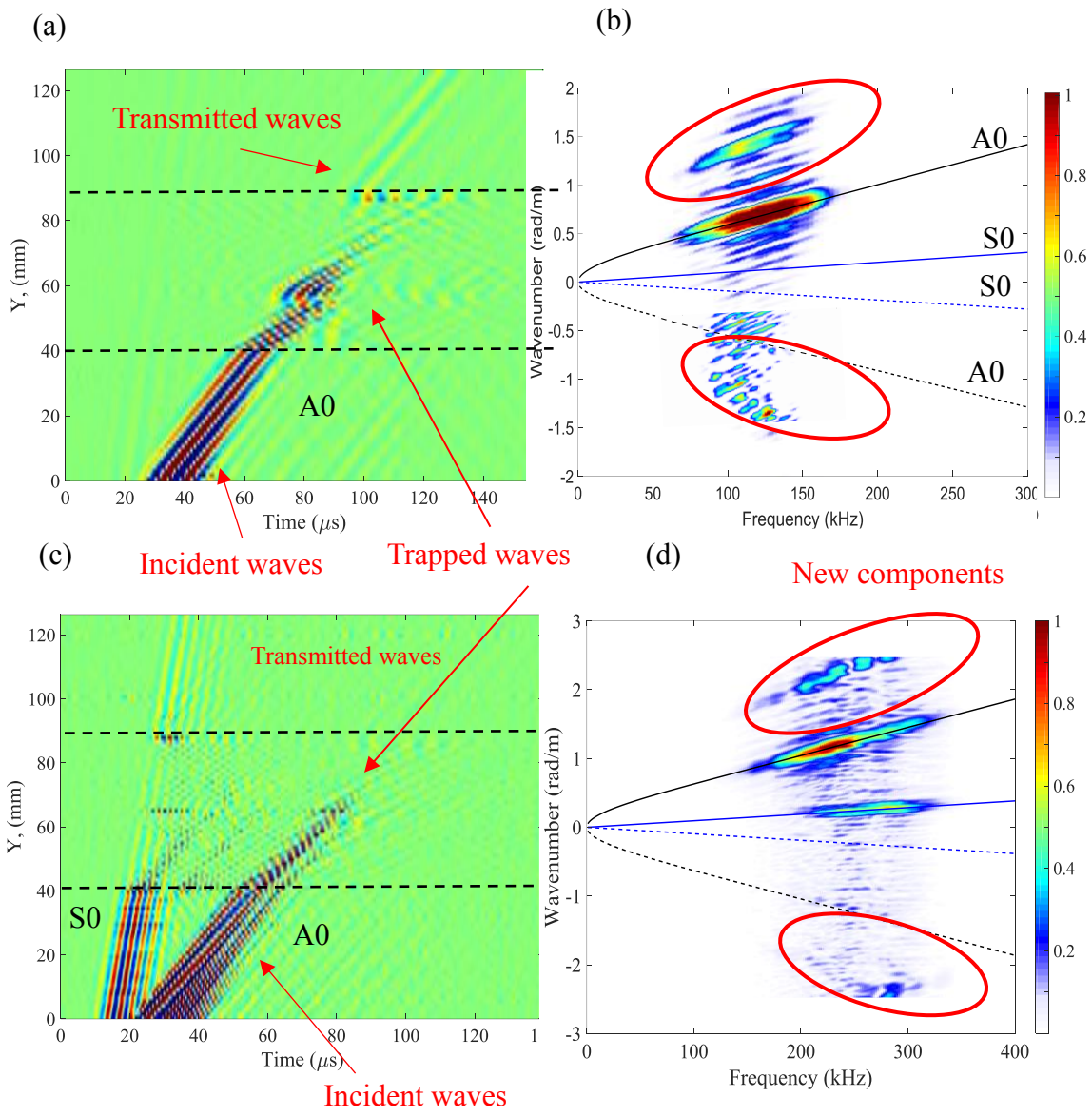

Figure 7.46: 1-D scanning of 50-mm delamination area using SLDV: (a) and (b) are the time-space and wavenumber-frequency domains at center frequency 120 kHz, (c) and (d) are the time-space and wavenumber-frequency domains at center frequency 240 kHz.

It can be clearly seen the trapped waves due to Lamb wave interaction with 50-mm delamination as shown in Figure 7.46 (a), (c). From these two figures, we can observe the length of delamination area. Form the frequency-wavenumber domains which are shown in Figure 7.46 (b), (d), we can see new components of trapped and reflected waves. Figure 7.49 shows snapshot images of wave propagation over 50-mm delamination sensing by

SLDV at frequencies 120 kHz and 240 kHz. Trapped waves due to interaction of antisymmetric Lamb wave mode with delamination area can be shown in Figure 7.47 (a), (b).

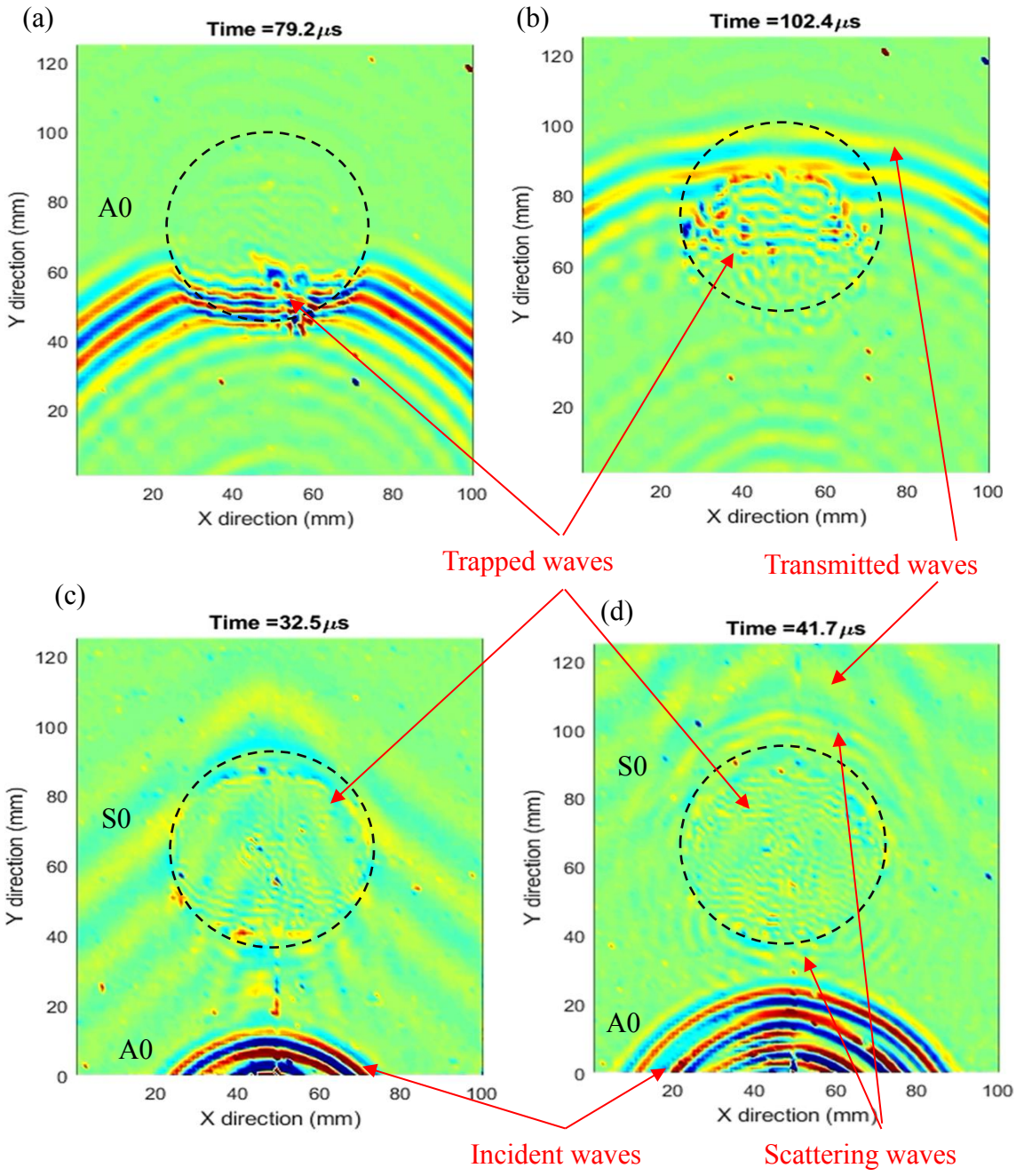

Figure 7.47: Snapshots of measured time-space wavefields for the 2-D scanning of 50-mm delamination; (a) wavefield image at 79.2 μs and 120 kHz; (b) wavefield image at 102.4

μs and 120 kHz; (c) wavefield image at 32.5 μs and 240 kHz; (d) wavefield image at 41.7 μs and 240 kHz.

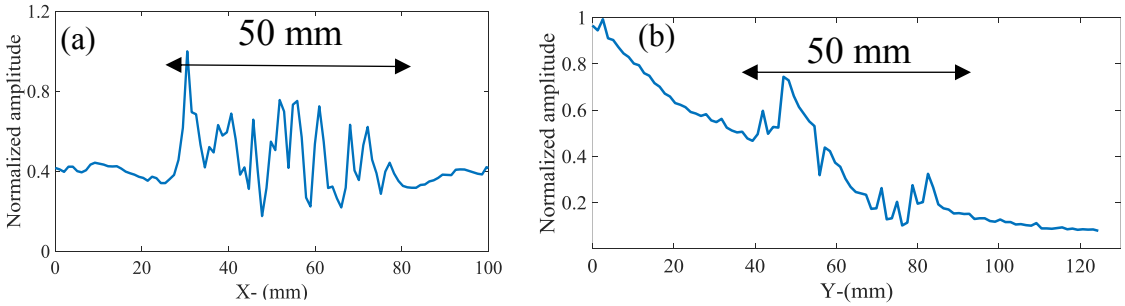

Figure 7.48: Maximum signals amplitude profile along the center lines of 50-mm delamination area in; (a) X-direction; (b) Y-direction.

We can clearly see the location, size and shape of 50-mm delamination. This delamination has significant trapped waves. Figure 7.47 (c), (d) show the trapped waves due to interaction of symmetric (S0) Lamb wave mode with 50-mm delamination at different times. We can observe the size, shape and location of 50-mm delamination area. However, the energy of symmetric trapped waves is less than antisymmetric trapped wave. The size and location of 50-mm delamination can be determined from the maximum signals amplitude profiles of data along the center lines of scanning area as shown in the Figure 7.48. The time-space domains and wavenumber-frequency domain along the center line of 75-mm delamination area are shown in the Figure 7.49. Figure 7.49 (a), (c) show the time-space domain at frequencies 120 kHz and 240 kHz respectively. We can observe a significant amount of trapped wave energy over 75-mm delamination area and estimate the length of delamination. Also, we can observe the reflected waves from the delamination area. The new components of trapped waves and reflected wave can be clearly observed at wavenumber frequency domain which is shown in the Figure 7.49 (b), (d). The snapshot images of 2-D wave propagation and interaction with 75-mm delamination areas at different time and frequencies are shown in the Figure 7.50. We can see the symmetric and

antisymmetric trapped and reflected waves over 75-mm delamination area. These snapshot images quantify the size, shape and location of 75-mm delamination area. The wavefield amplitude profiles for the points along the center lines of the 75-mm delamination area help us to indicate the size and the location of delamination area. The size and location of 75-mm delamination area also, can be determined from the maximum signals amplitude profile over the delamination area as shown in the Figure 7.51.

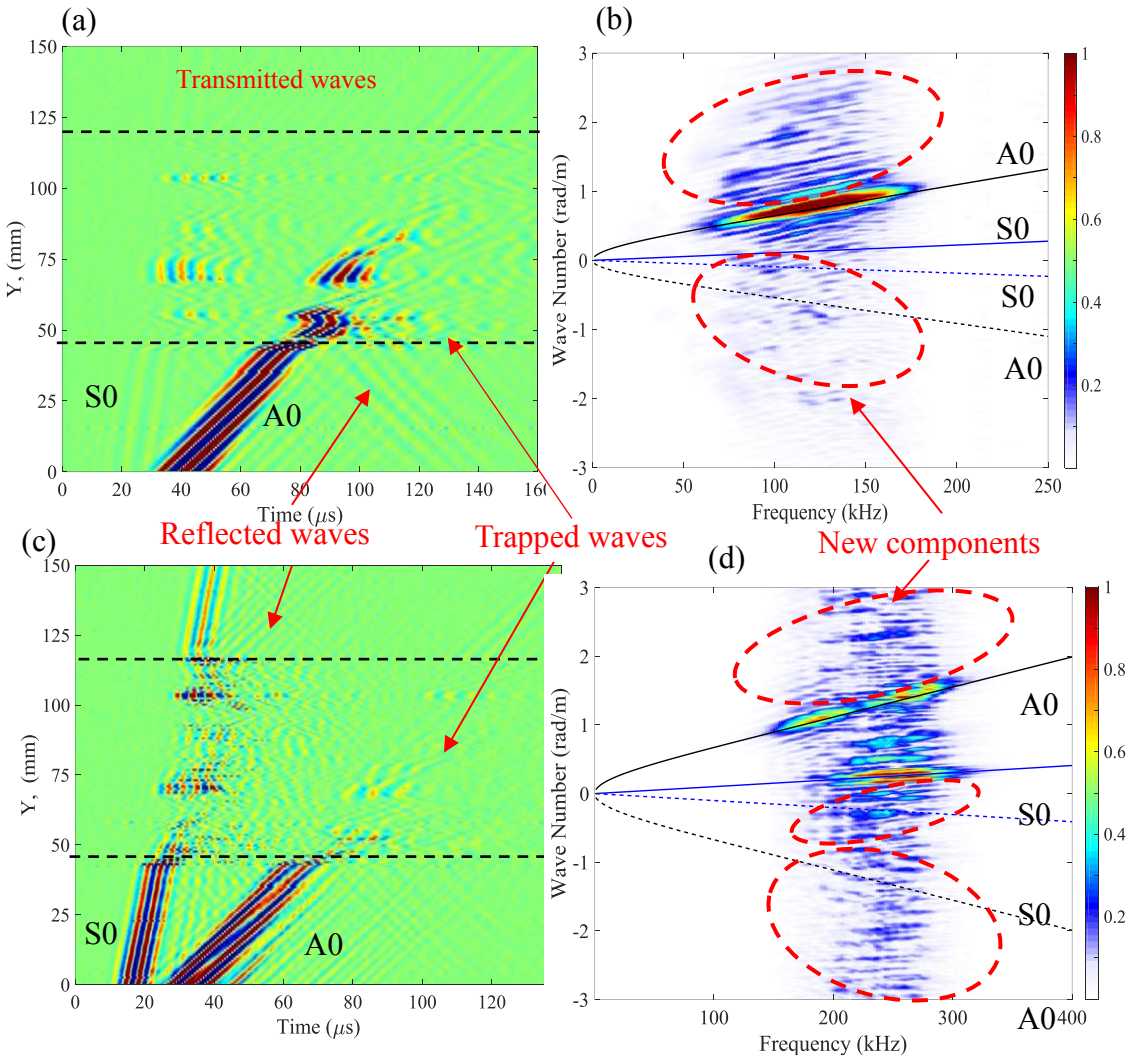

Figure 7.49: 1-D scanning of 75-mm delamination; (a) and (b) time-space and wavenumber-frequency domains at certain frequency 120 kHz; (c) and (d) The time-space and wavenumber-frequency domains at center frequency 240 kHz.

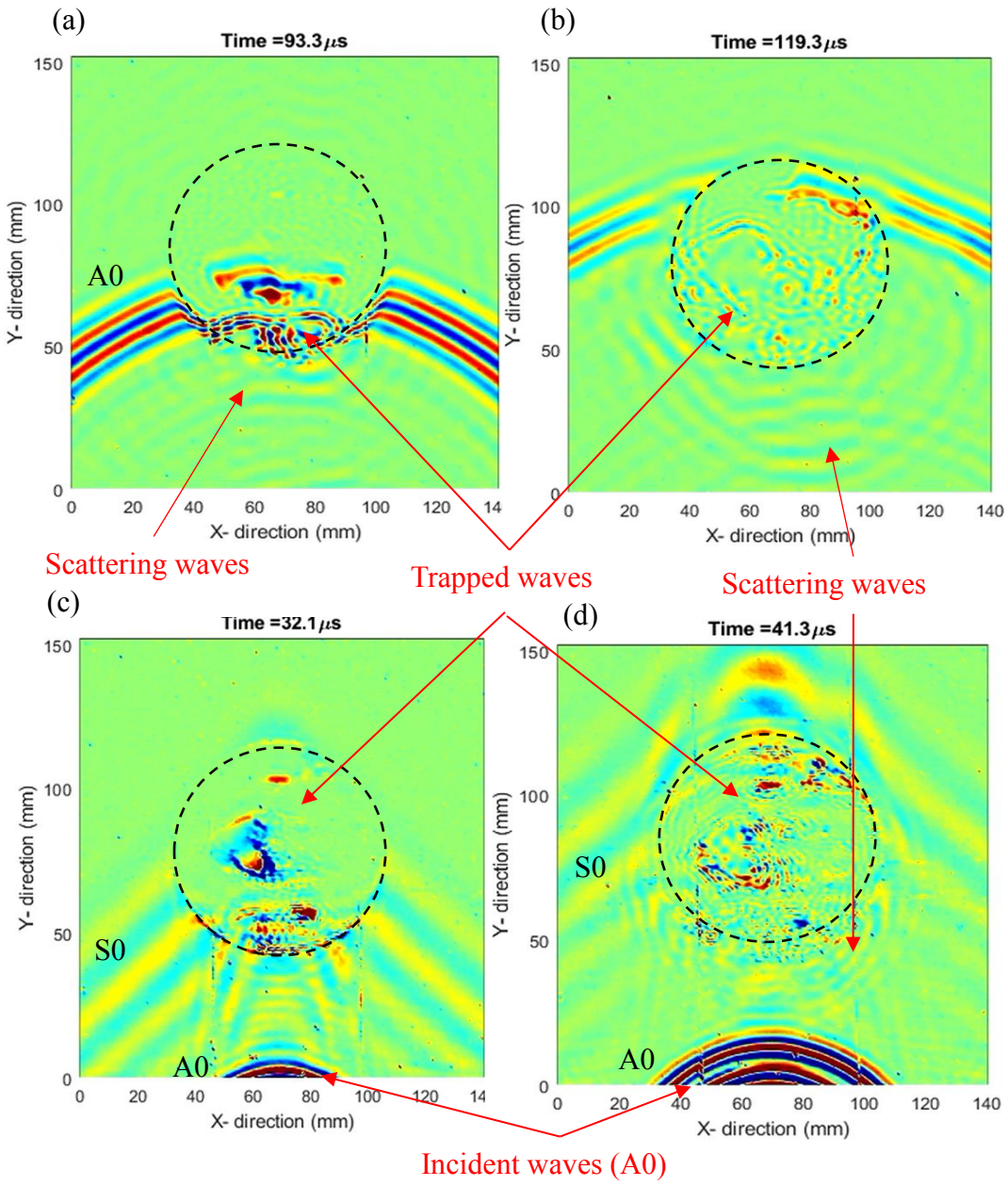

Figure 7.50: Snapshots of measured time-space wavefields for the 2-D scanning of 75-mm delamination; (a) wavefield image at 93.3 μs and 120 kHz; (b) wavefield image at 119.3 μs and 120 kHz; (c) wavefield image at 32.1 μs and 240 kHz; (d) wavefield image at 41.3 μs and 240 kHz.

7.6.2 SLDV Technique for Inspection Specimen 2

The experimental setup of scanning Laser Doppler vibrometer for inspection four interested areas of unidirectional composite laminates (specimen 2) is like the experimental

setup of specimen 1 which is shown in Figure 7.39. Four areas were scanned in this experiment. The first area is pristine area. The other three areas are the damaged areas which have three same sizes of simulated delamination inserted at different depths as shown in the Figure 7.52. The scanned areas were covered with special tap to improve the surface condition. The excitation signal is 3-count tone burst signal at frequency 120 kHz. The guided waves were propagated in transverse direction.

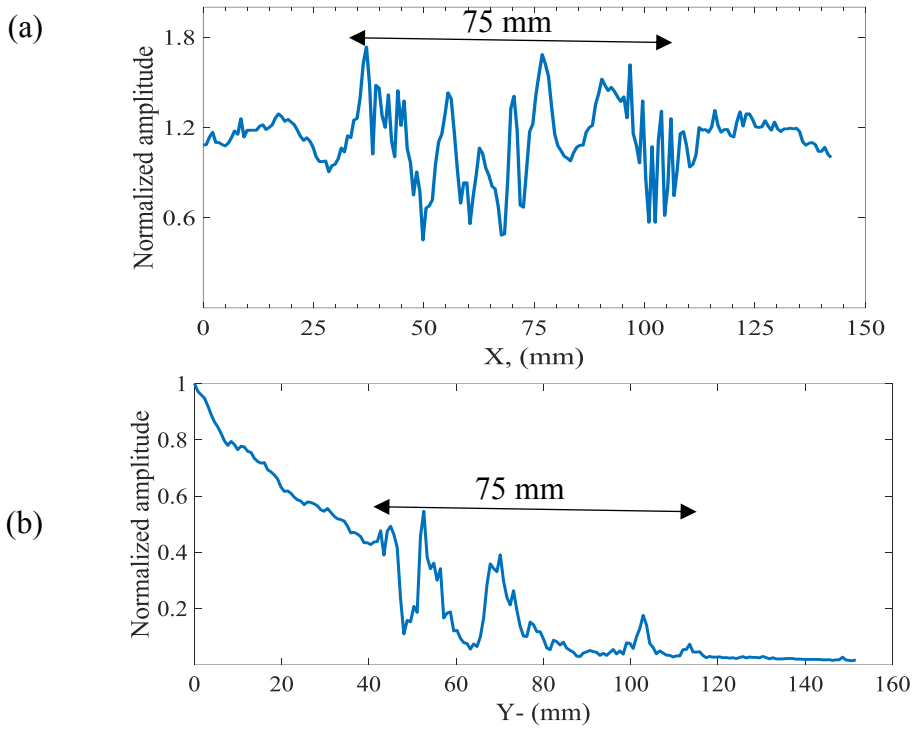

Figure 7.51: Maximum signals amplitude profiles along the center lines of 75-mm delamination area in; (a) X-direction; (b) Y-direction.

The hybrid PZT-SLDV experiments were implemented to study the propagation and interaction of guided waves with delamination. The delamination were simulated by inserted three pieces of Teflon at different depths across the 5-mm unidirectional composite laminates. Figure 7.53 shows the time-space wavefield and frequency-wavenumber spectrum of scanning points along the center line of pristine area at frequencies 120 kHz.

From Figure 7.53 (b), we can observe three Lamb modes which are A0, SH0 and S0. The SH0 mode is not clear in time-space domain because it is overlapped with A0 and S0 modes. Figure 7.54 shows the time-space domains and frequency-wavenumber spectrums of scanning points along the center lines of scanning areas at frequencies 120 kHz. Figure 7.54 (a), (c), (e) show the time-space domains of wavefields along the line-points of area C, area B and area A. It can be clearly seen the trapped waves, reflected waves due to Lamb waves interaction with delamination. The area C has fine trapped waves over the delamination because it is near the surface.

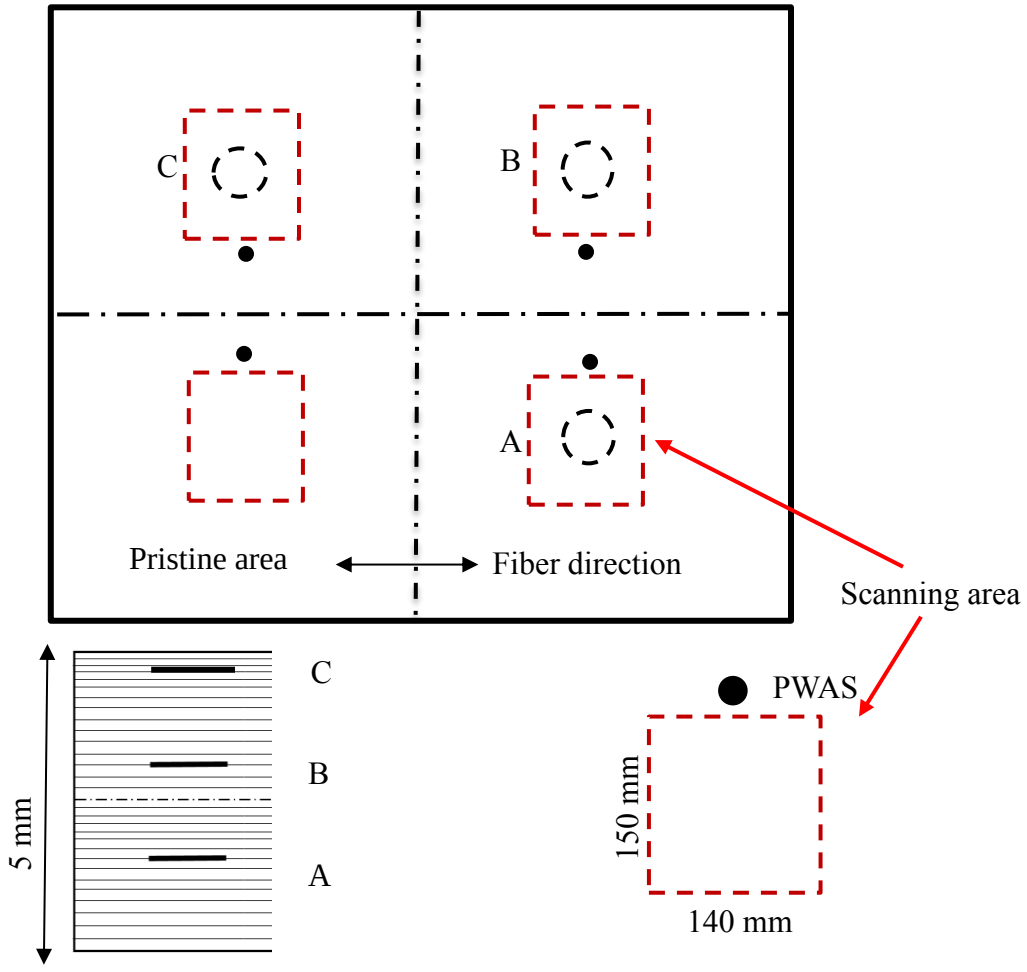

Figure 7.52: The configuration of scanning areas of unidirectional composite laminates (specimen 2).

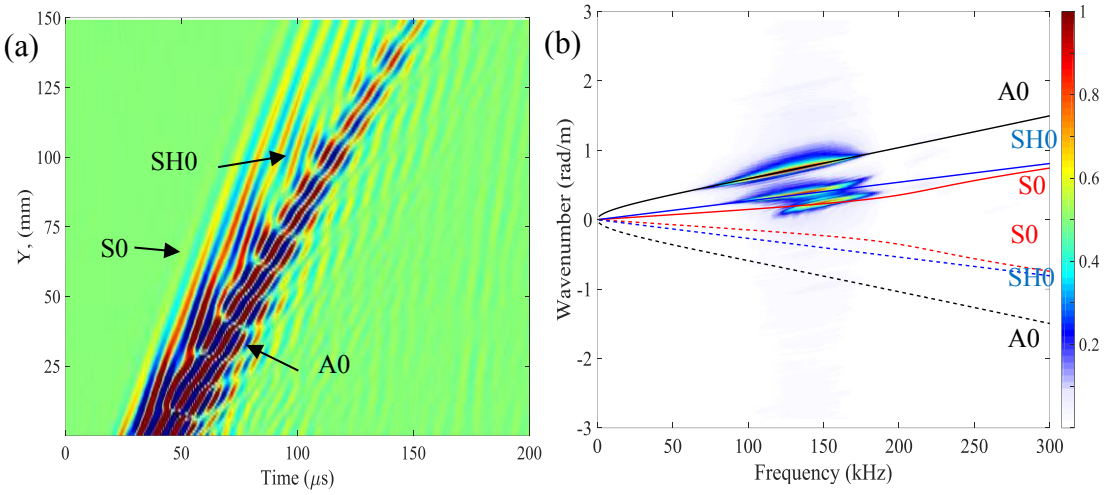

Figure 7.53: 1-D scanning of pristine area using SLDV at certain frequency 120 kHz; (a) time-space wavefield; (b) wavenumber-frequency spectrum.

Figure 7.54(b), (d), (f) show the wavenumber-frequency spectrums of wavefields along the line-points of area C, area B and area A. We can observe new components comparing with the pristine case which shown in the Figure 7.53 (b). These new components are created due to the trapped and scattering waves. The area C has strongest new components among other areas.

The snapshots at certain time of Lamb wave propagation and interaction with delamination in scanning areas at frequency 120 kHz are shown in the Figure 7.55. We can see the trapped waves over delamination and scattering waves emanated from delamination. These trapped waves can be used to quantify the size, shape of delamination area. Figure 7.55 (a) shows the snapshot image of delamination area C. We can see intensive and smooth trapped waves over the delamination area. Figure 7.55 (b) shows the snapshot image of delamination area B. we can observe coarse trapped waves over the delamination area. The snapshot image of area A which is shown the Figure 7.55 (c) has coarser trapped waves. We can conclude that the damage depth affects the amount and the length of trapped

waves over the delamination areas. Based on these results we can predict the delamination depth across the plate thickness.

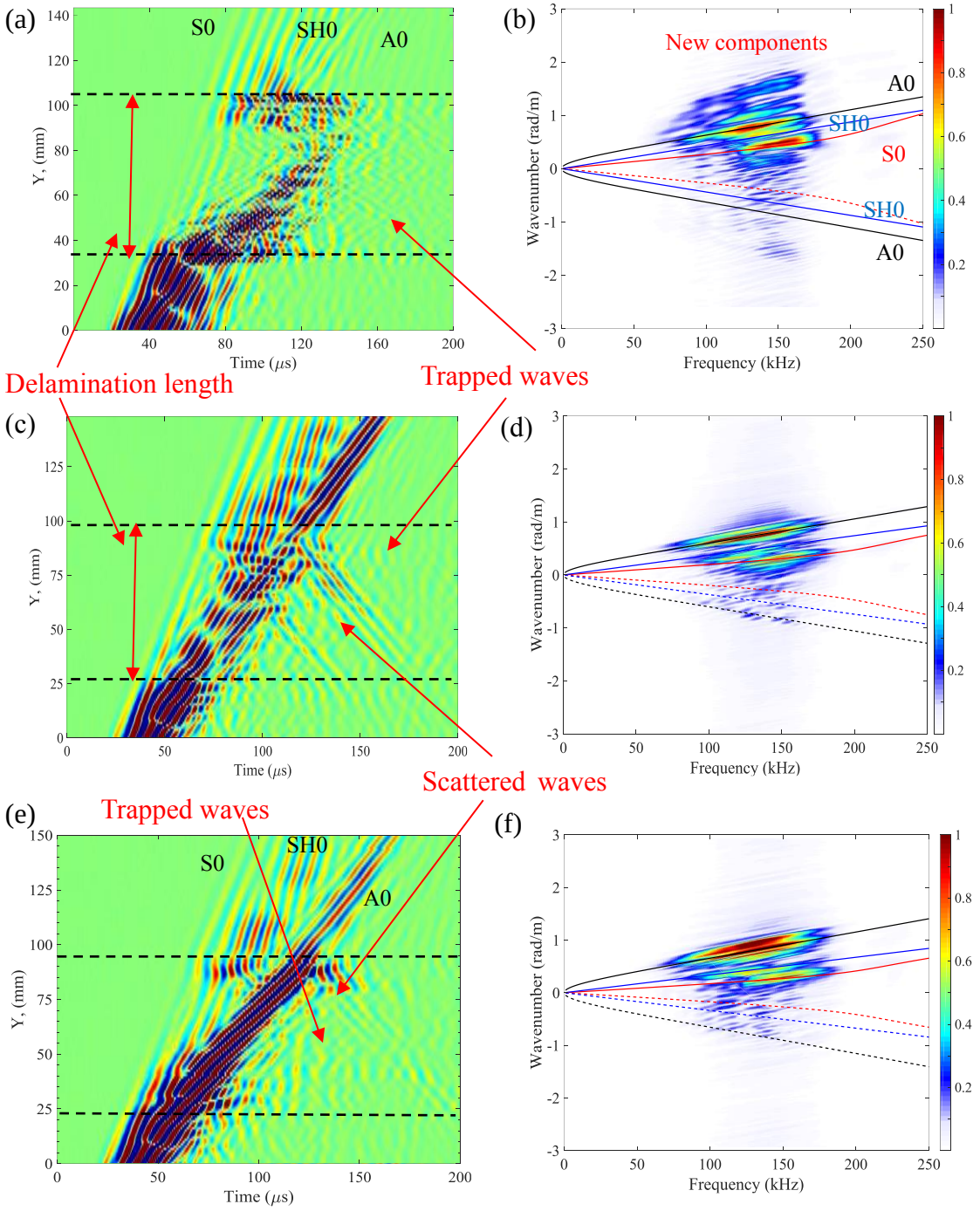

Figure 7.54: Time-space wavefields and wavenumber-frequency spectrums of 1-D scanning at frequency 120 kHz; (a) and (b) area C; (c) and (d) area B; (e) and (f) area A.

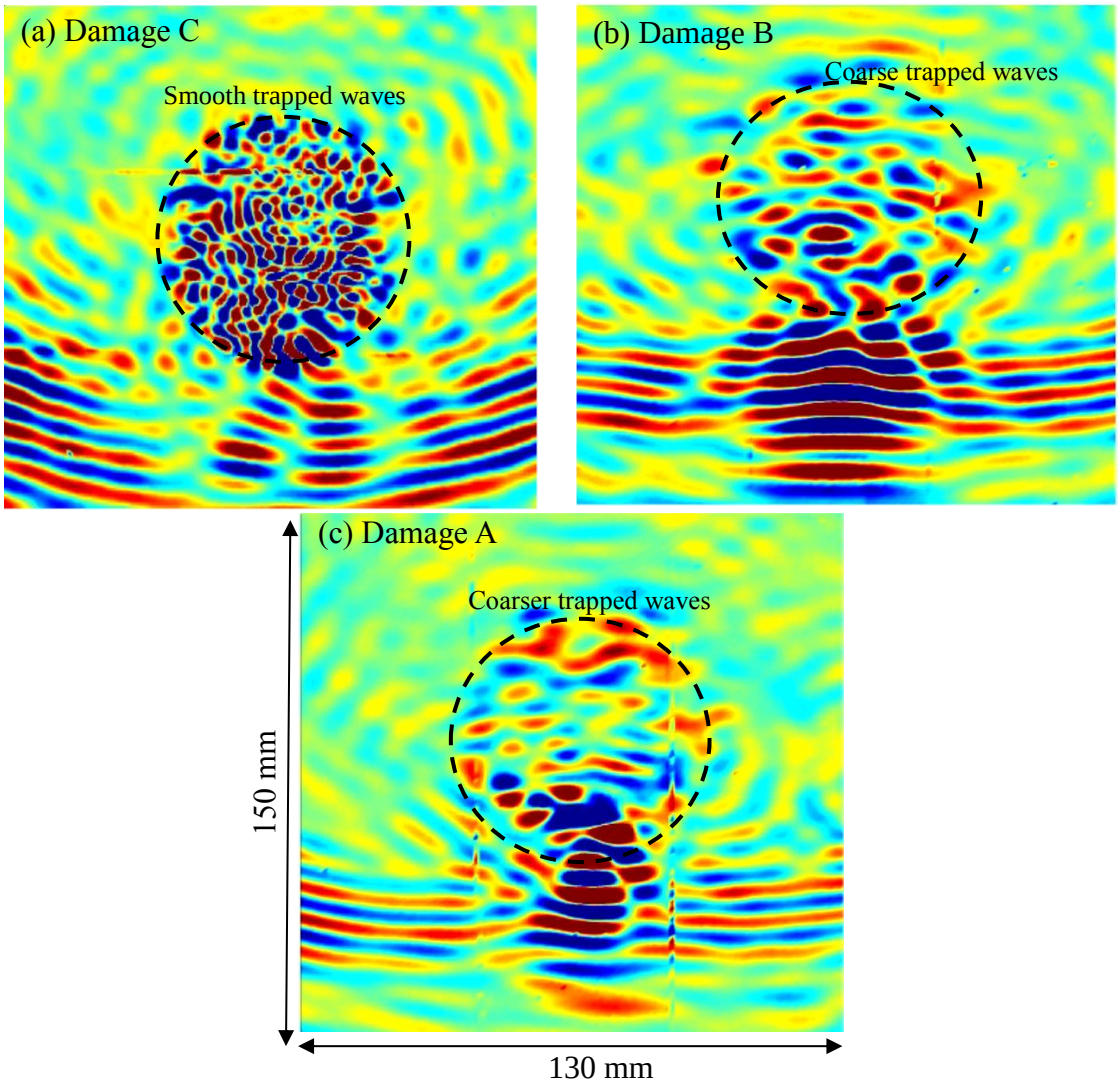

Figure 7.55: Snapshots of measured wavefields at certain time of three scanning areas at frequency 120 kHz; (a) scanning area C; (b) scanning area B; (c) scanning area A.

7.7 LOCAL VIBRATION-BASED DELAMINATION DETECTION

In recent years, many non-destructive techniques have been developed to investigate several of structures and detect different kind of damages. One of these NDT techniques is local vibration. The idea behind this technique is to measure the change in frequency response of structure due to decrease the stiffness of damaged structure. Many techniques were presented to detect delamination of composite plates. The chosen of

appropriate technique depends on the defect size which must be found, the size of the structure to be inspected, and the environment in which the tests are to be carded out [94]. The structural damages in metallic and composite materials were localized using vibration analysis of inspected structure [95]. The mechanical impedance technique was investigated to detect delamination and disband in composite structure. The result showed that this technique is sensitive when the defect is closed to the surface [96]. The torsional vibration of bars was measured to detect the damages [94]. Many researches have been implemented to detect structural damages using electromechanical impedance spectroscopy (EMIS) along with PWAS. The PWAS excite the interested structure with harmonic excitation. After that, the electrical impedance of the PWAS is measured with EMIS method respect to the frequency of excitation. Most of the studies classify the NDT of damage detection in two categorizes which are local and global damage detection methods. The local damage detection methods need the damage area to be known before doing the inspection. For large structure in civil and aerospace application, it is difficult to predetermine the inspection area. To overcome this problem, the global damage identification techniques, such as vibration-based methods are used to inspect the interesting area [97].

The vibration-based structural health monitoring techniques have potential for identifying structural damage in civil and mechanical application. One of the vibration-based methods is modal analysis. This method has been used to investigate the structural integrity based on the natural frequencies and mode shapes of investigated structure [98]. A comprehensive literature review on the dynamic response-based structural damages detection methods was implemented. The principle, development and application of various vibration-based structural health monitoring techniques were presented [98] [99].

The modal analysis techniques have been used for structural damage detection. When the damage initiate in a structure, it will cause changes in the mechanical properties of a structure. The structural modal parameters are function of these properties. So, we can find certain modes to define the structural damage. Finite element analysis and experimental techniques were developed based on Vibration-based model-dependent methods to detect damages. The structural responses such as time, frequency and impedance responses were determined [100].

A numerical and experimental studies were implemented based on vibration analysis method to detect a damage in composite beam. For experimental work, the SLDV was used to measure the dynamic response of the beam. Both studies detected and localized the damage [98]. Vibration-based methods were investigated to detect damages in composite laminate plate due to low-velocity impacts. In this study, the structural vibration response was measured to quantify the structural damage [101]. A modal frequency surface (MFS)-base damage detection approach was investigated to identify near and far surface delamination in composite plate. The modal frequency data was determine numerically using FEM method.

The result shows that the MFS wavelet coefficient are able to identify the location and shape of delamination [102]. The delamination in composite beam was detected experimentally and numerically by investigating the modal frequency variations. A concentrated load was put closed to delamination area to observe delamination-induced modal frequency deviation. The delamination is detected and localized through the numerical and experimental modal frequency curves [103]. A strain energy-based numerical study was implemented to detect damages in composite structure. The results

show the ability of strain energy-based approach for detecting damages in composite material [104]. The electromechanical impedance technique is a local vibration technique for detecting damage in a structure. It is one of NDT techniques. This technique needs a PWAS to be a part of investigated structure through a permanent bonding. The frequency spectrum of a structure can be measured using E/M method. In this method the PWAS transducer can be used directly to investigate the structure under direct electrical excitation. The E/M impedance method measures the mechanical impedance of the structure in the form of the real part of the E/M impedance measured at PWAS terminals. Many researches were implemented for using E/M impedance method as an effective tool for structural health monitoring, the admittance or impedance frequency spectra of pristine and damaged structures were compared [104].

7.7.1 VIBRATION-BASED OF IDENTIFYING DELAMINATION IN SPECIMEN 1

We know, the damage can affect the stiffness and mass of a structure. The dynamic response of the structure will be changed when it has a damage. Many analytical and experimental vibration tests have been approved that the structural dynamic response at lower frequency may not be affected by a local structural damage. The first step of vibration-based delamination detection is to perform modal analysis of the whole composite plate using FEA commercial ANSYS code. At lower frequency range of modal analysis, we will determine the natural frequencies and their associated mode shapes for pristine and damaged cases. From the Figure 7.56, it can be clearly observed that mode shapes are the same in both cases. The scanning laser Doppler vibrometer (SLDV) experiment was implemented to study the local vibration four areas (three damaged and one pristine areas) as shown in Figure 7.57.

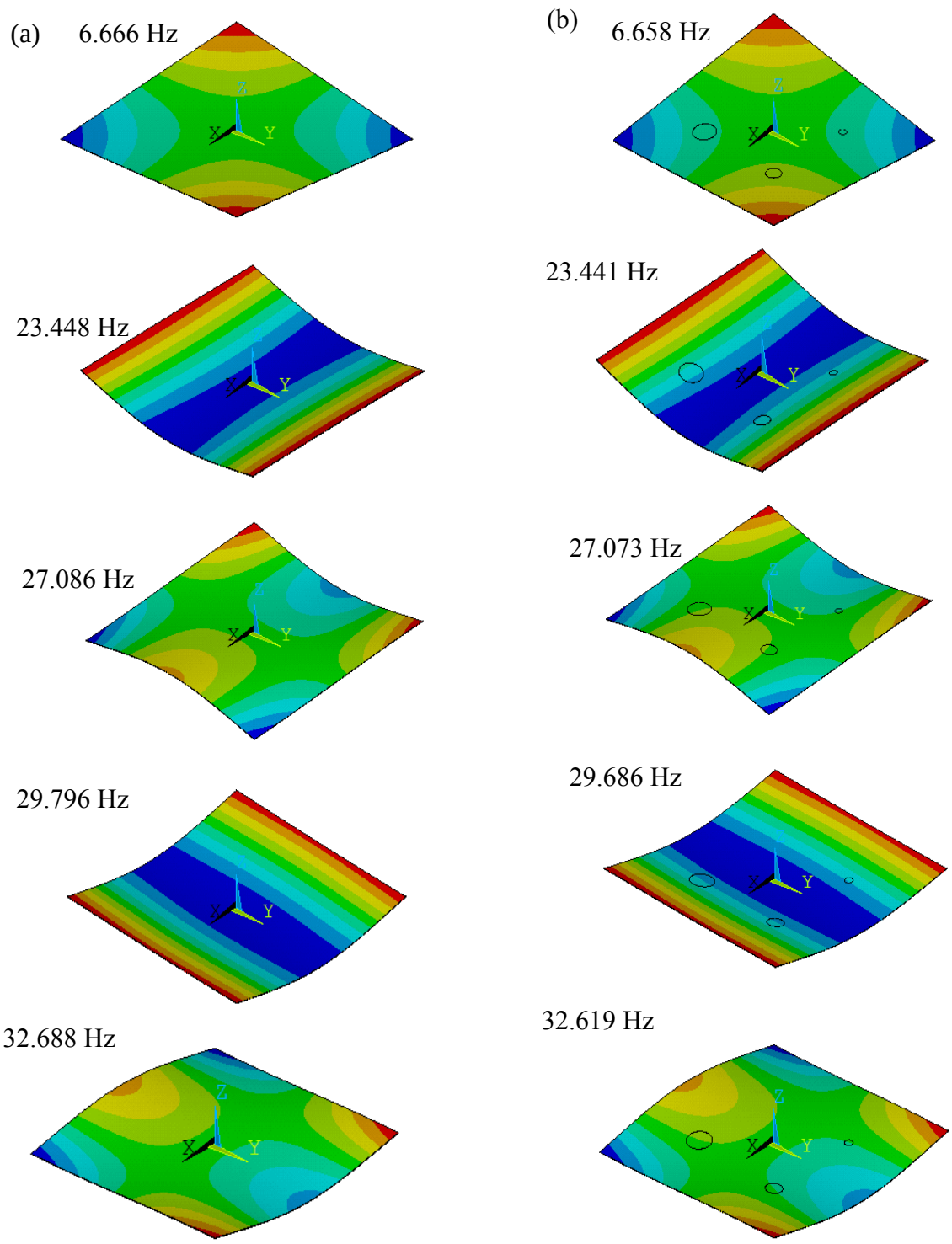

Figure 7.56: The first five mode shapes and their natural frequencies of pristine and damaged cases of specimen 1 calculated with ANSYS FEM analysis: (a) pristine plate; (b) multiple delamination plate.

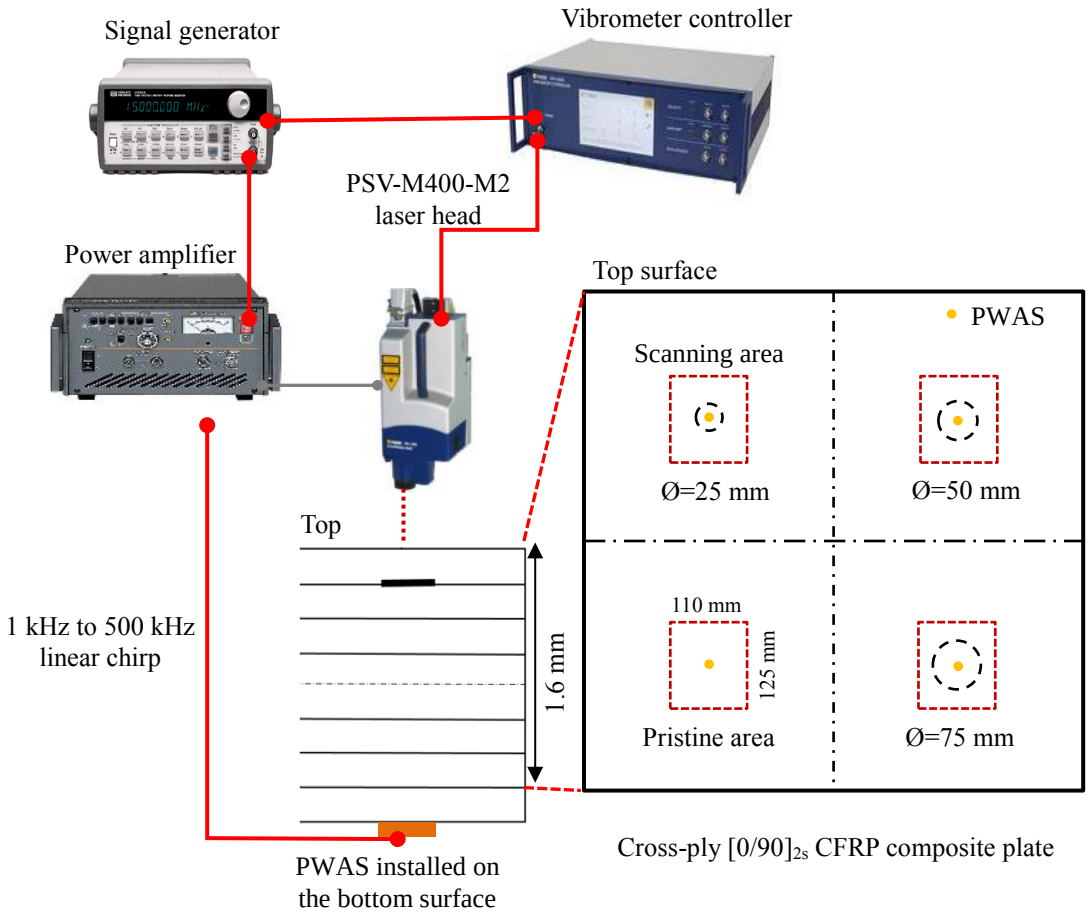

Figure 7.57: Experimental setup of vibration-based inspection using scanning laser Doppler vibrometer.

The interested areas were covered with tab material to decrease the generated noise. Four PWAS transducers were installed at centers of interested areas from bottom surfaces. A function generator was used to generate a 1–500 kHz, 1000 μs linear chirp. Before the excitation signal is applied to the PWAS transducers, the excitation is amplified to 140V by a power amplifier. The scanning laser Doppler vibrometer is used to acquire the time space of harmonic waves over the scan area. The laser head generate laser beam which is perpendicular to scanning area to measure out of plan motion. The scanning areas were divided to coarse points to measure their responses by SLDV. At each point, the 1-500 kHz,

1000 μs linear chirp was excited. The Laser head acquires the whole chirp signal response at a point before moving to other point.

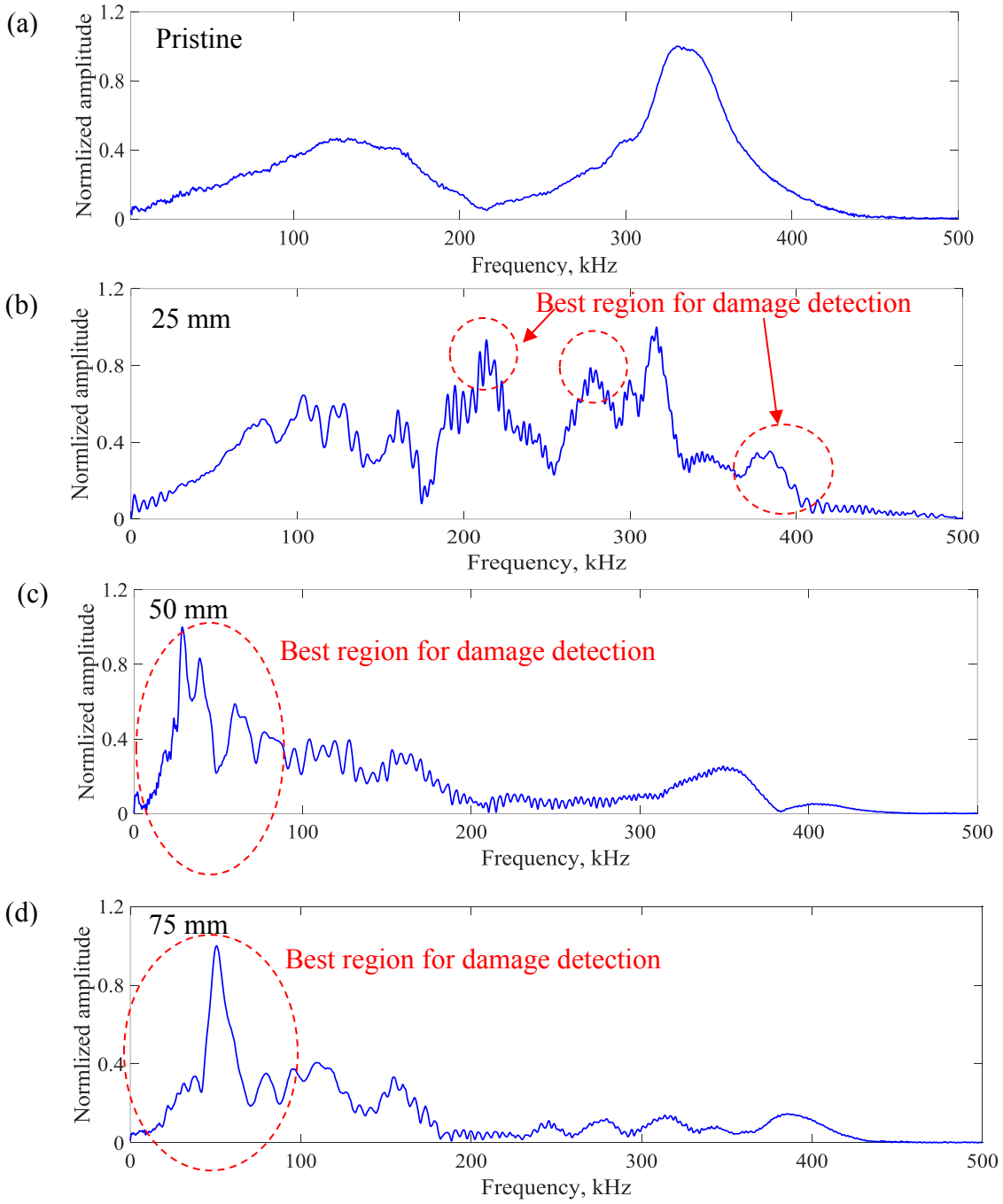

Figure 7.58: Frequency spectrum of the signals at the center point of different scanning areas: (a) pristine; (b) 25 mm delamination; (c) 50 mm delamination; (d) 75 mm delamination.

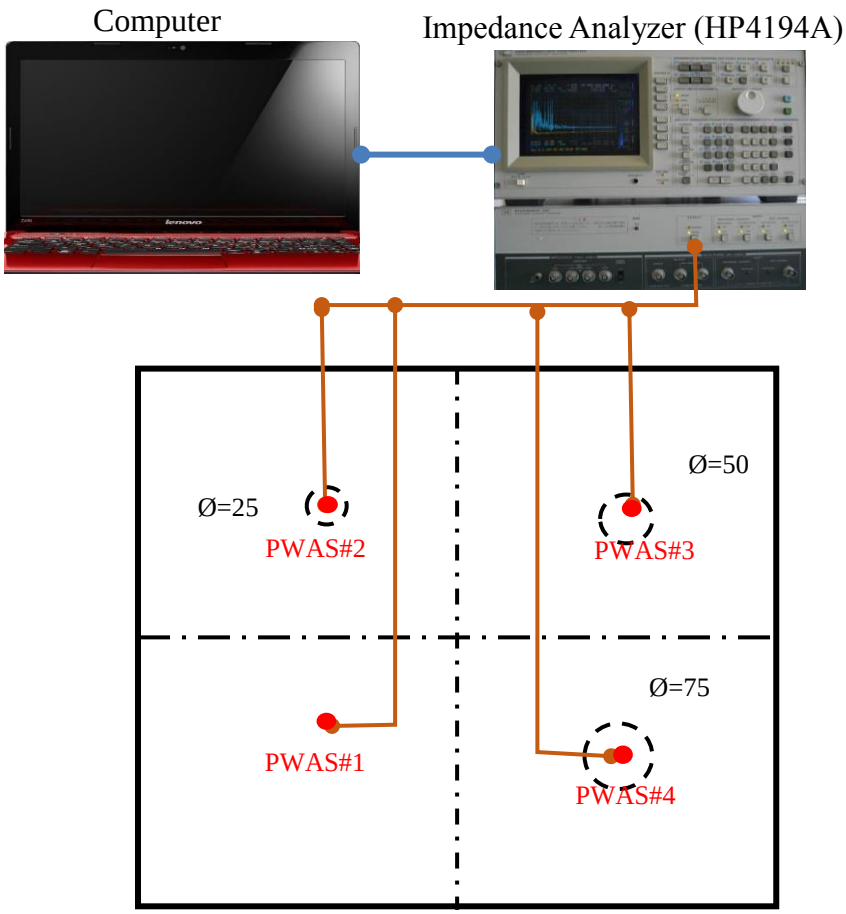

Figure 7.59: Experimental Setup for measuring the impedance of the PWAS transducers.

The fast Fourier transform (FFT) of the response signals was performed to determine the local damage resonance frequencies. Figure 7.58 shows the frequency spectrum of measured response signals at the center point of the four scanning areas. Figure 7.58 (a) shows the FFT result of the pristine area. Figure 7.58 (b), (c), and (d) show the FFT results of the response signals at the center point of the 25-mm, 50-mm, and 75-mm delamination, respectively. It can be found that the delamination modifies significantly the frequency response compared to the pristine area. The local damage resonance frequencies can be obtained by peak picking from the FFT results of the delamination. More specifically, some resonance peaks in the frequency range from 80 kHz to 350 kHz can be

found for the 25-mm delamination. However, the resonance peaks of the 50-mm and 75-mm delamination are below 100 kHz. It can be found that the delamination size has a significant effect on the local defect resonance frequency. An experiment of using Electromechanical Impedance Spectroscopy (EMIS) was implemented to study the resonance frequencies of damaged areas. In this experiment, Four PWAS transducers were bonded permanently on the interested subareas of composite specimen.

The first sensor was installed over the pristine area and the other three sensors were installed over three damaged sub-areas as shown the Figure 7.59. An HP 4194A impedance analyzer was used to measure the impedance of the four PWAS on each sub-area. The results were saved through a LabVIEW. The results were compared between pristine case and delamination case for each size of delamination as shown in the Figure 7.60. Figure 7.60 (a) shows the results of real impedance for PWAS#2 of 25 mm-delamination area which is compared with pristine case.

We can observe new resonance peaks at frequencies 215 kHz and 352 kHz due to 25 mm- delamination. Figure 7.60 (b) shows the result of real impedance of PWAS#3 of 50-mm delamination which is compared with pristine case. This result was measured between frequencies 10 kHz and 100 kHz because there are significant resonance peaks can be observed in this frequency range. Figure 7.60 (c) shows the results of real impedance of PWAS#4of 75-mm delamination area which are compared with pristine case. We can also observe remarkable resonance peaks in the frequency range between 10 kHz and 100 kHz. From Table 7.2, we can observe a good matching of predicting resonance peaks between SLDV method and EMIS method. These resonance frequencies due to delaminations cause significant local vibrations over delamination areas.

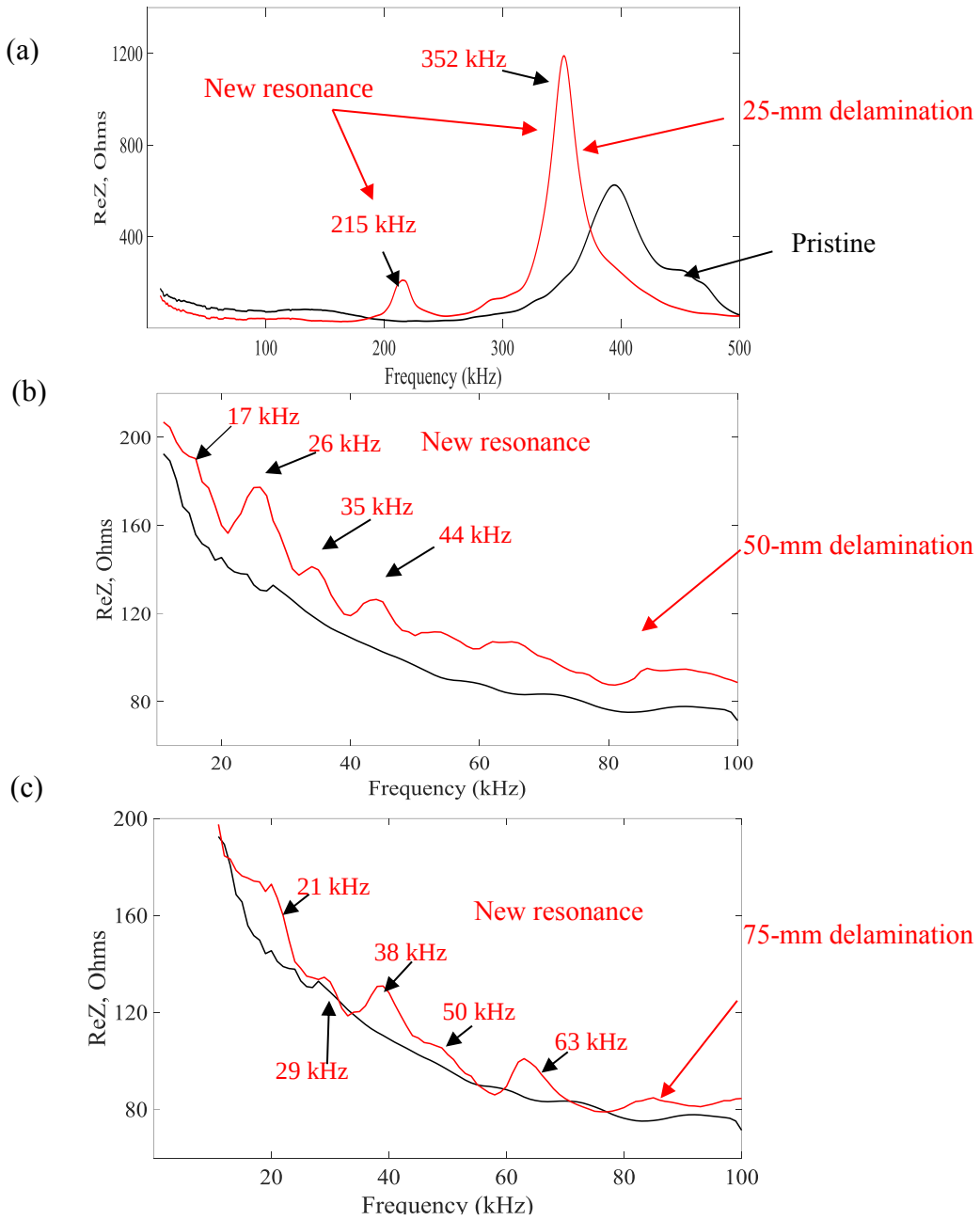

Figure 7.60: Real impedance for the pristine and damaged areas (new resonance peaks due to delamination); (a) 25-mm delamination; (b) 50-mm delamination; (c) 75-mm delamination.

The delamination can be quantified by analyzing the mode shape of the local vibration. The operational vibration shapes can be extracted at the resonance frequencies from the SLDV scanning data.

Table 7.2: The similarities in resonance frequencies between EMIS and SLDV methods for specimen 1

Expermental methods	25-mm delamination (Resonance peaks) (kHz)	50-mm delamination (Resonance peaks) (kHz)	75-mm delamination (Resonance peaks) (kHz)
EMIS	214, 351	17, 26, 35	21, 29, 38
SLDV	215, 352	18, 28, 38	22, 27.8, 37

The Fourier transform of all the response signals was implemented and the operational vibration shapes is extracted using the FFT amplitudes of a certain frequency at all measurement points. Figure 7.61 shows the operational vibration shapes of pristine area at certain resonance frequencies. It can be found that no significant local vibration on the pristine area. Figure 7.62 shows the operational vibration shapes of 25-mm delamination area at resonance frequencies 214 kHz, 352 kHz and 384 kHz. We can observe a significant local vibration over the delamination. The location and the size of delamination can be quantified. Figure 7.63 shows the operational vibration shapes of 50-mm delamination at resonance frequencies 18 kHz, 28 kHz and 38 kHz. We can clearly see the local vibration over the delamination. Figure 7.64 shows the operational vibration shapes of 75-mm delamination area at resonance frequencies 22 kHz, 27.8 kHz and 37 kHz. These mode shapes are clearly quantified the shape and size of 75-mm delamination. Based on these results, we can say that local vibration techniques can be used to localize and size the structural damages.

7.7.2 Vibration-Based of Identifying Delamination in Specimen 2

The modal analysis was performed using FEM commercial ANSYS code for the second plate (specimen 2) to study its global dynamic response at lower frequency test.

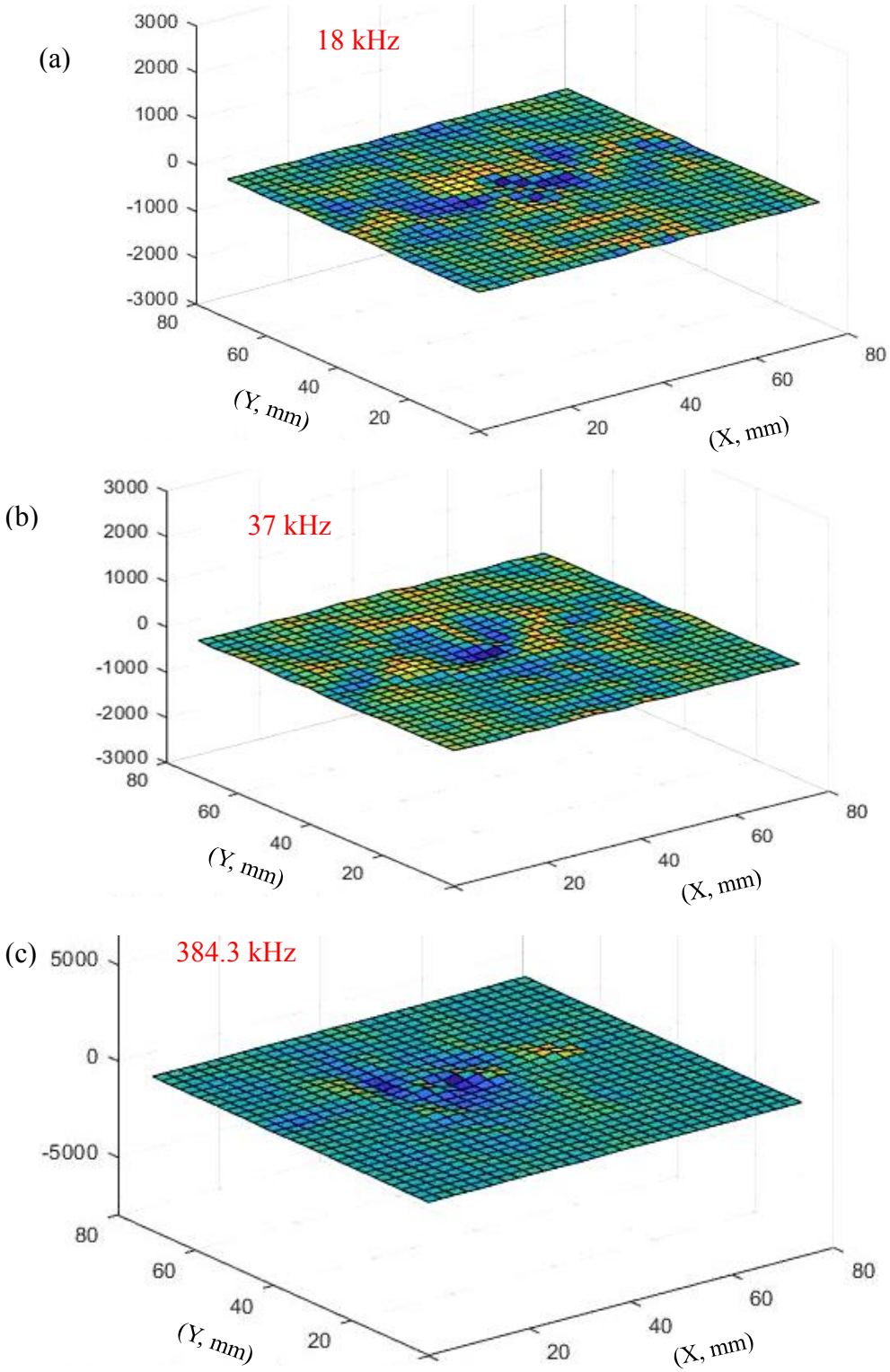

Figure 7.61: Measured operational vibration shapes for pristine area at different frequencies; (a) 18 kHz; (b) 37 kHz; (c) 384.3 kHz.

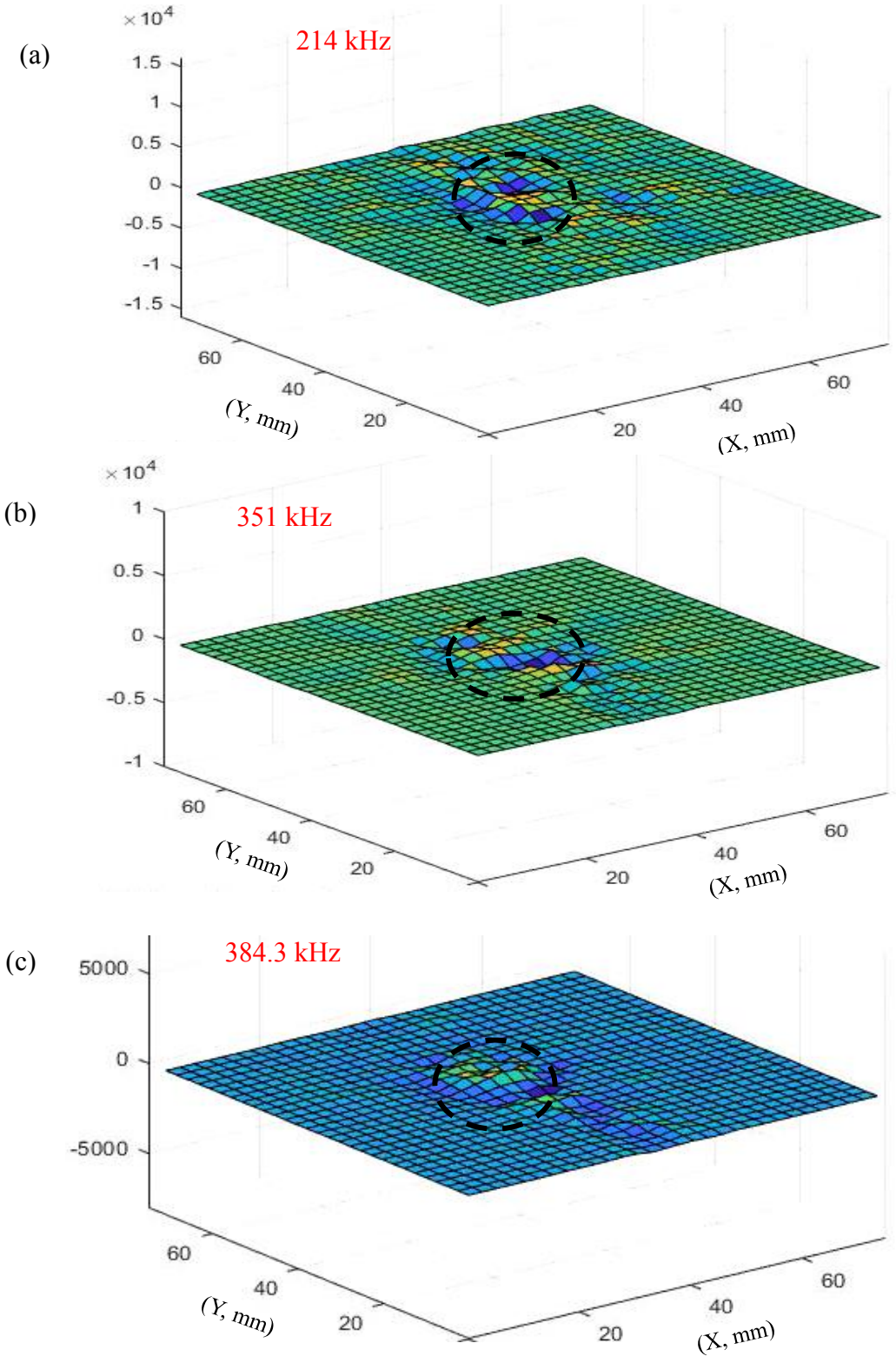

Figure 7.62: Measured operational vibration shapes for 25-mm delamination at resonance peaks; (a) 214 kHz; (b) 351 kHz; (c) 384.3 kHz.

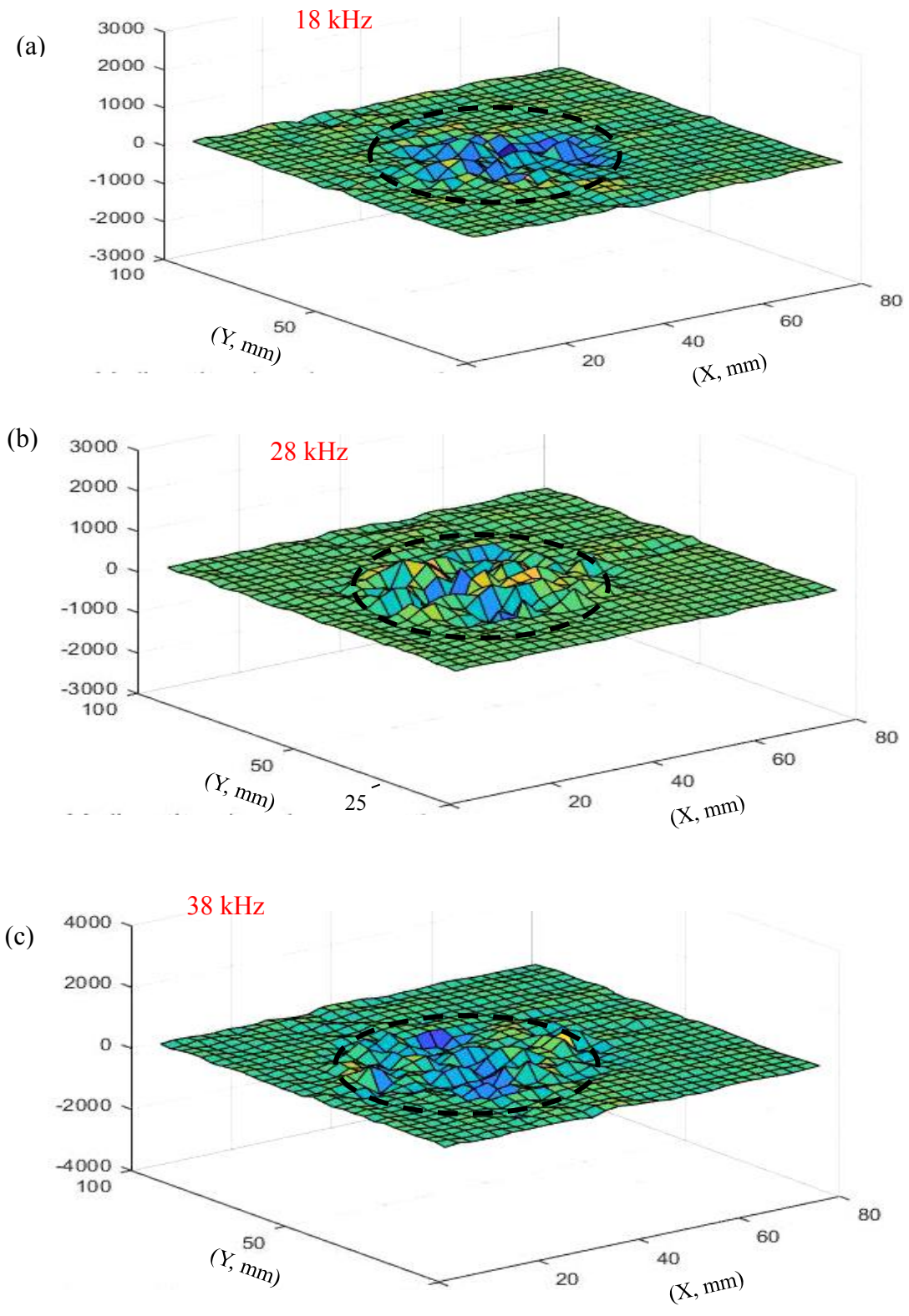

Figure 7.63: Measured operational vibration shapes for 50-mm delamination at resonance peaks; (a) 18 kHz; (b) 28 kHz; (c) 38 kHz.

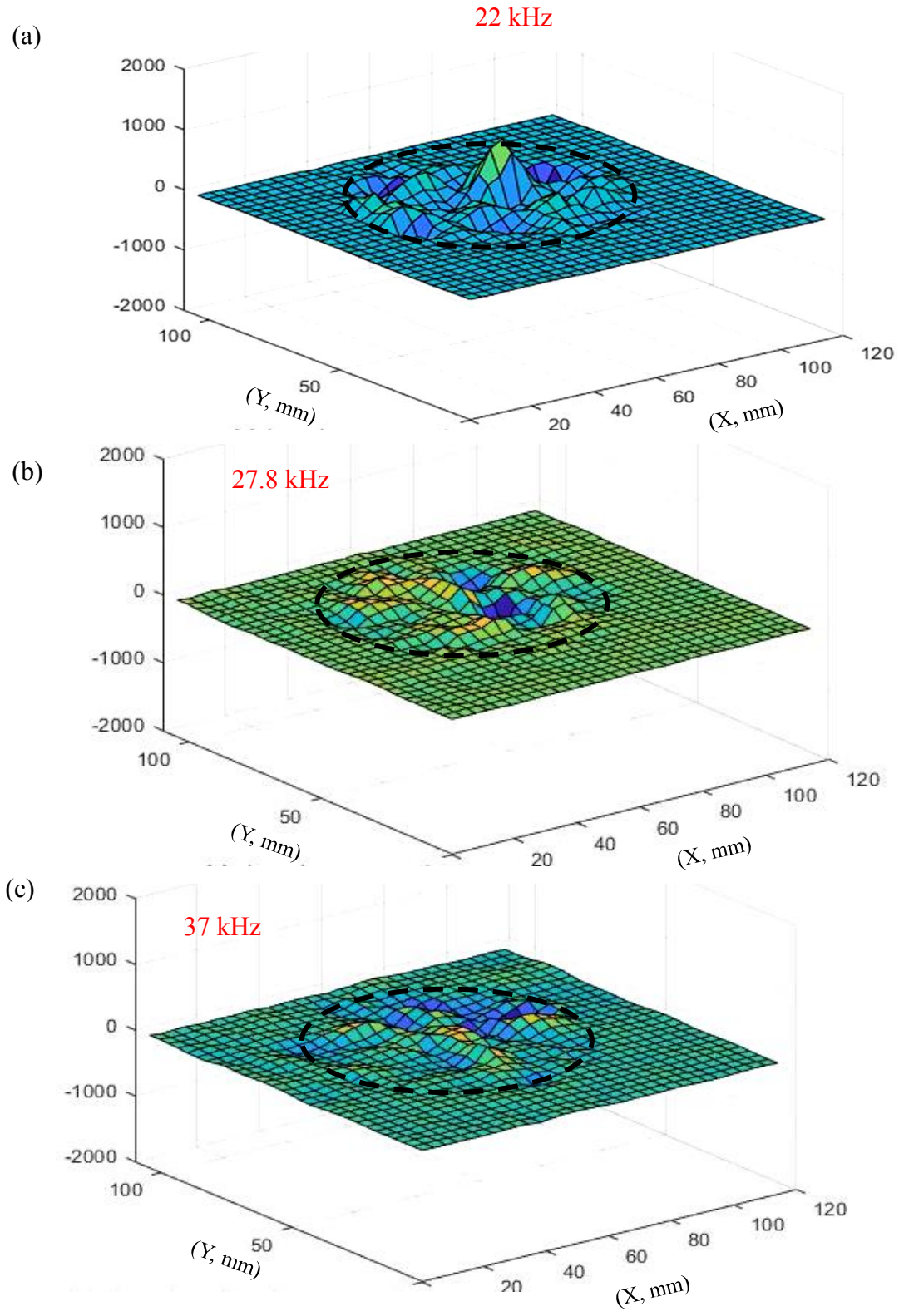

Figure 7.64: Measured operational vibration shapes for 75-mm delamination area at resonance peaks; (a) 22 kHz; (b) 27.8 kHz; (c) 37 kHz.

Figure 7.65 (a), (b) show the first five mode shapes and their natural frequencies of pristine and damaged plates. The mode shapes for both cases are the same. The natural frequencies values of damaged case are decreased with insignificant values. Based on this study, we will use higher frequency test to detect and quantify the delamination areas of specimen 2

The experimental setup of the SLDV measurements on the unidirectional $[0]_{30}$ CFRP composite plate is like the first specimen in Figure 7.57. Four areas (one pristine and three damaged areas) were inspected to investigate the local vibration, as shown in Figure 7.66. The size of each scanning area is 110 mm × 125 mm. In this experiment, at the center of each inspection area, a circular PWAS (APC 850, 7-mm diameter and 0.2-mm thick) transducer was bonded on the top surface as the excitation source. The same linear sine wave chirp from 1 kHz to 500 kHz was applied to the PWAS transducers for the high-frequency excitation. The wavefield data were recorded by the SLDV on the bottom surface of the plate. The fast Fourier transform (FFT) of the response signals was performed to find the local defect resonance frequencies of the delamination at different depths. Figure 7.67 shows the frequency spectrum of measured response signals at the center point of the four scanning areas. Figure 7.67 (a) shows the FFT of the response signal for the pristine area. Figure 7.67 (b), (c), and (d) show the FFT results of the response signals at the center point of the top, middle, and bottom 75-mm delamination, respectively. It can be noted that the delamination at various depths change the frequency response compared to the pristine area. The local defect resonance frequencies can be obtained by peak picking from the FFT results. It can be found that the resonance peaks are mainly in the frequency range below 100 kHz.

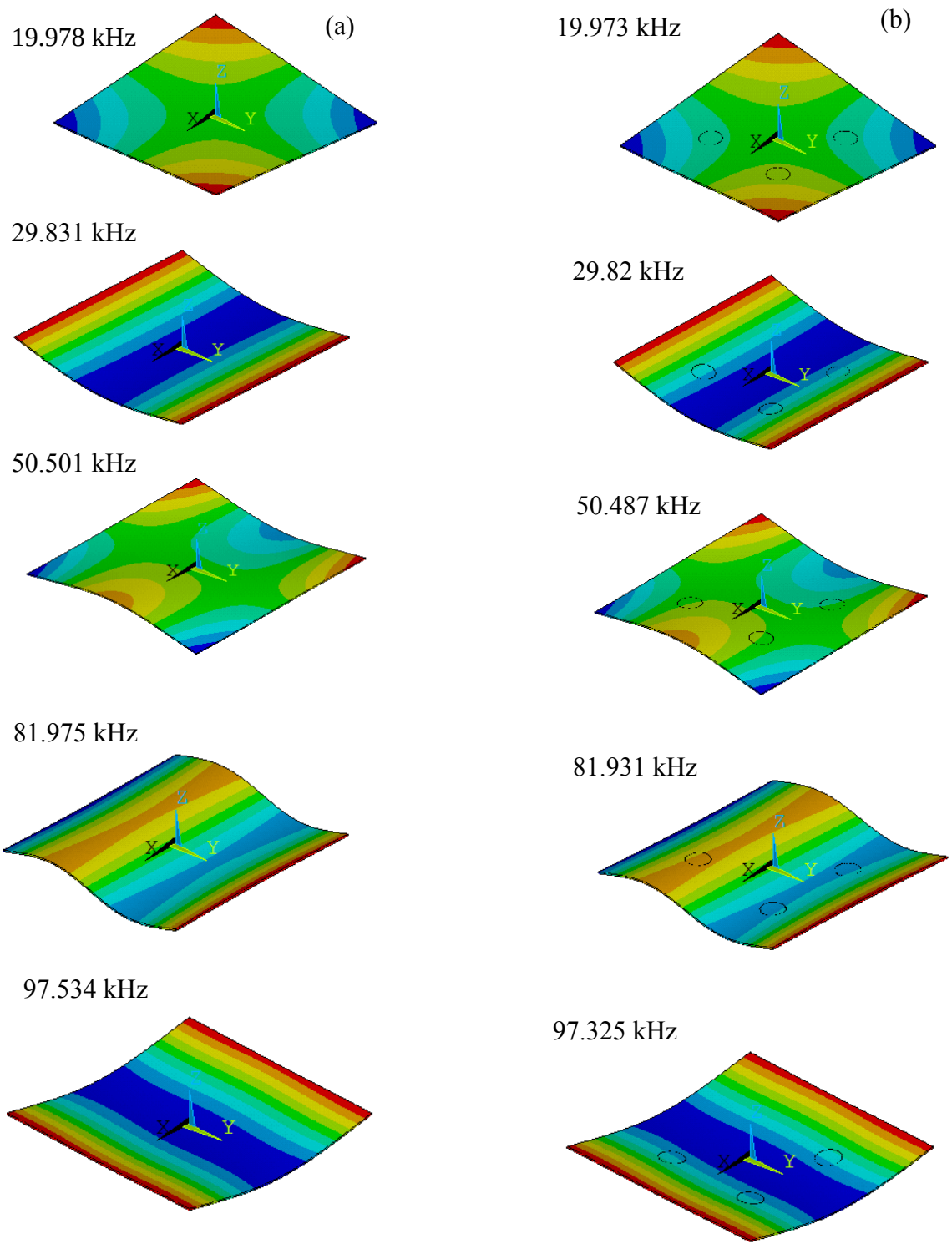

Figure 7.65: The first five mode shapes and their natural frequencies of pristine and damaged cases of specimen 2 calculated with ANSYS FEM analysis: (a) pristine plate; (b) multiple delamination plate.

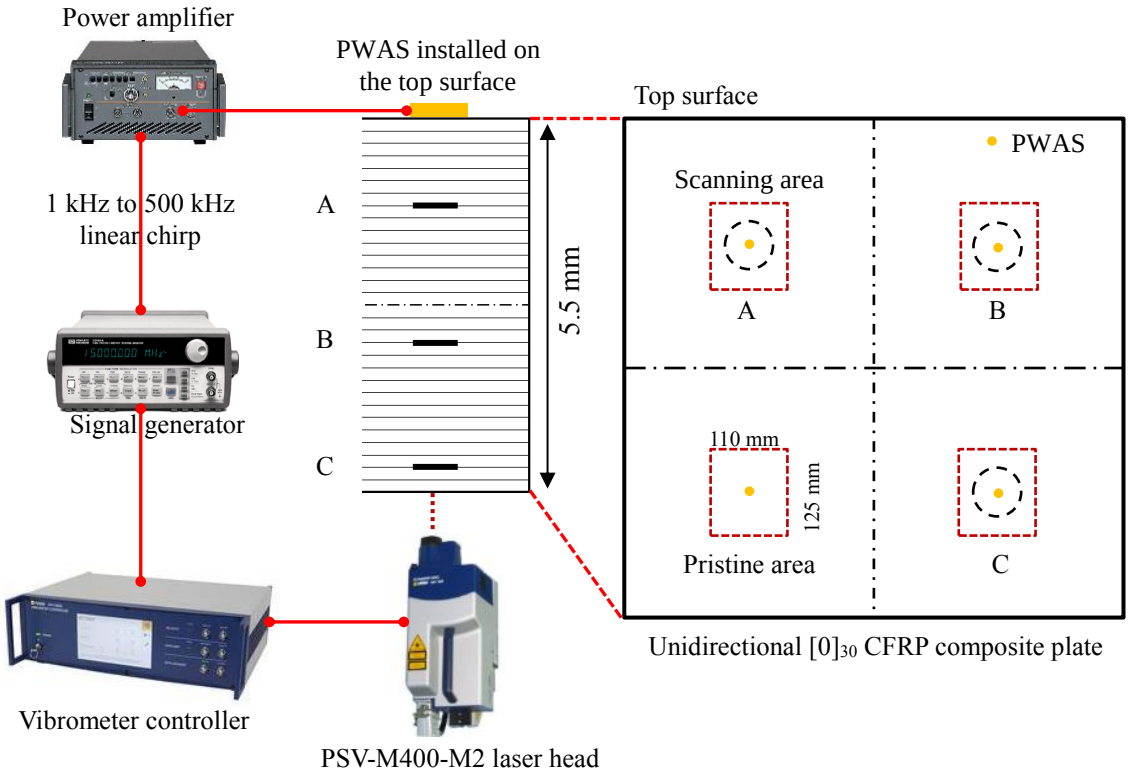

Figure 7.66: Experimental setup on the unidirectional $[0]_{30}$ CFRP composite plate using the SLDV measurement.

The corresponding mode shapes at these local defect resonance frequencies will be extracted from the SLDV area measurement for quantification of the delamination at different depths. The experimental setup of electromechanical impedance spectroscopy (EMIS) of specimen 2 is like the pervious experiment of specimen 1 which is seen in the Figure 7.59. The results were compared between the intact and damaged areas. Figure 7.68 (a) shows the locations of PWAS and delamination depths. Figure 7.68 (b) shows the real impedance-frequency plots for the PWAS transducers, which installed over the delamination (C, B, and A) and pristine areas. We can observe new resonance peaks for all damaged areas with frequency range between 10-110 kHz. The PWAS of area C has more and higher resonances frequency peaks than other areas because its delamination area near the surface.

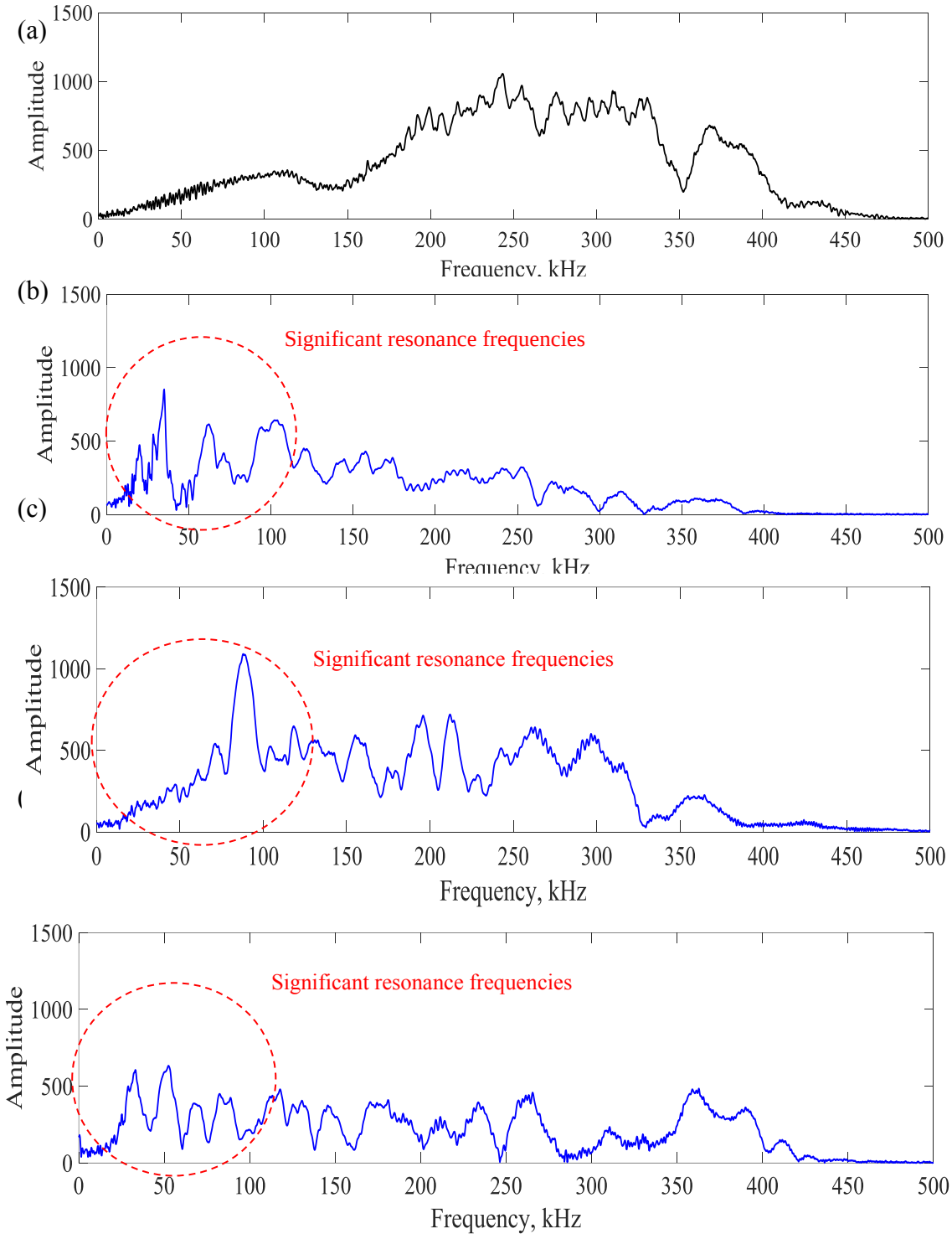

Figure 7.67: Frequency spectrum of the signals at the center point of different scanning areas: (a) pristine; (b) top 75-mm delamination A; (c) middle 75-mm delamination B; (d) bottom 75-mm delamination C.

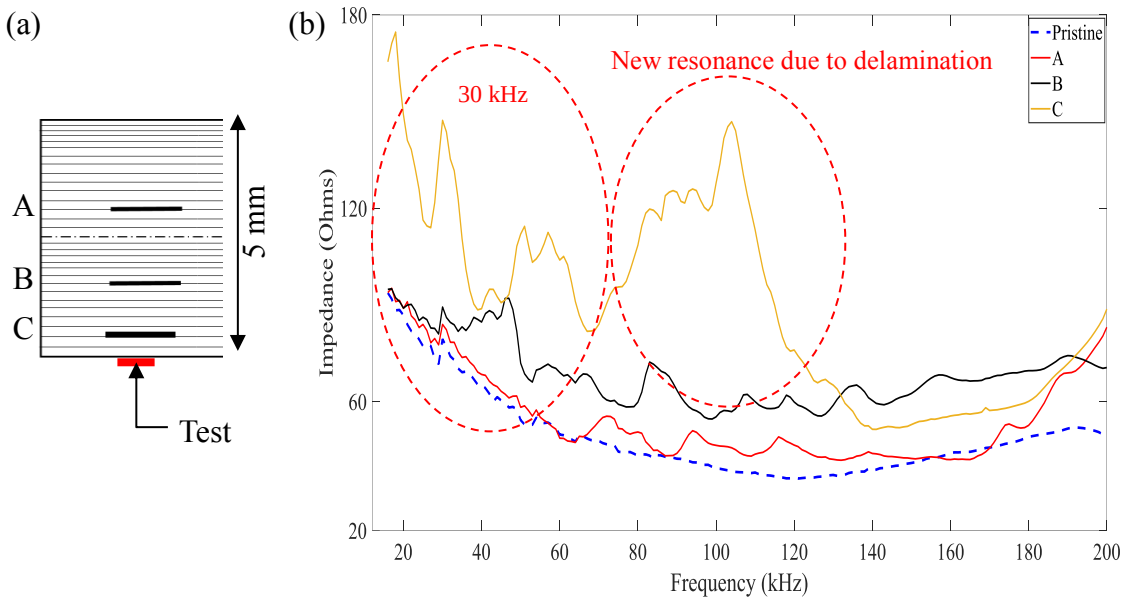

Figure 7.68: Real impedance-frequency plots for the pristine and damaged areas of specimen 2.

From the results of SLDV and EMIS experiments, we can observe a good matching of predicting resonance peaks between SLDV and EMIS methods.

Table 7.3 shows a good matching of the resonance frequencies for damaged areas predicted by SLDV and EMIS methods. These resonance frequencies are sufficient to predict and size the deamination areas by plotting the mode shapes at certain resonance frequencies. The operational vibration shapes can be extracted at some resonance peaks using SLDV scanning data. To plot the operational vibration shapes of scanning area, The FFT is determined for each signal of scanning points. These operational vibration shapes can be used to detect and quantify the structural damage. Figure 7.69 shows the operational vibration shapes of damaged area C at resonance frequencies 62 and 94 kHz. We can observe a significant local vibration over the delamination region. The location and the size of delamination area can be remarked in these plots. The scanning points over the delamination area have higher vibrational amplitudes than other points. Figure 7.70 shows

the operational vibration shapes of damaged area B at resonance frequencies 88 and 118 kHz.

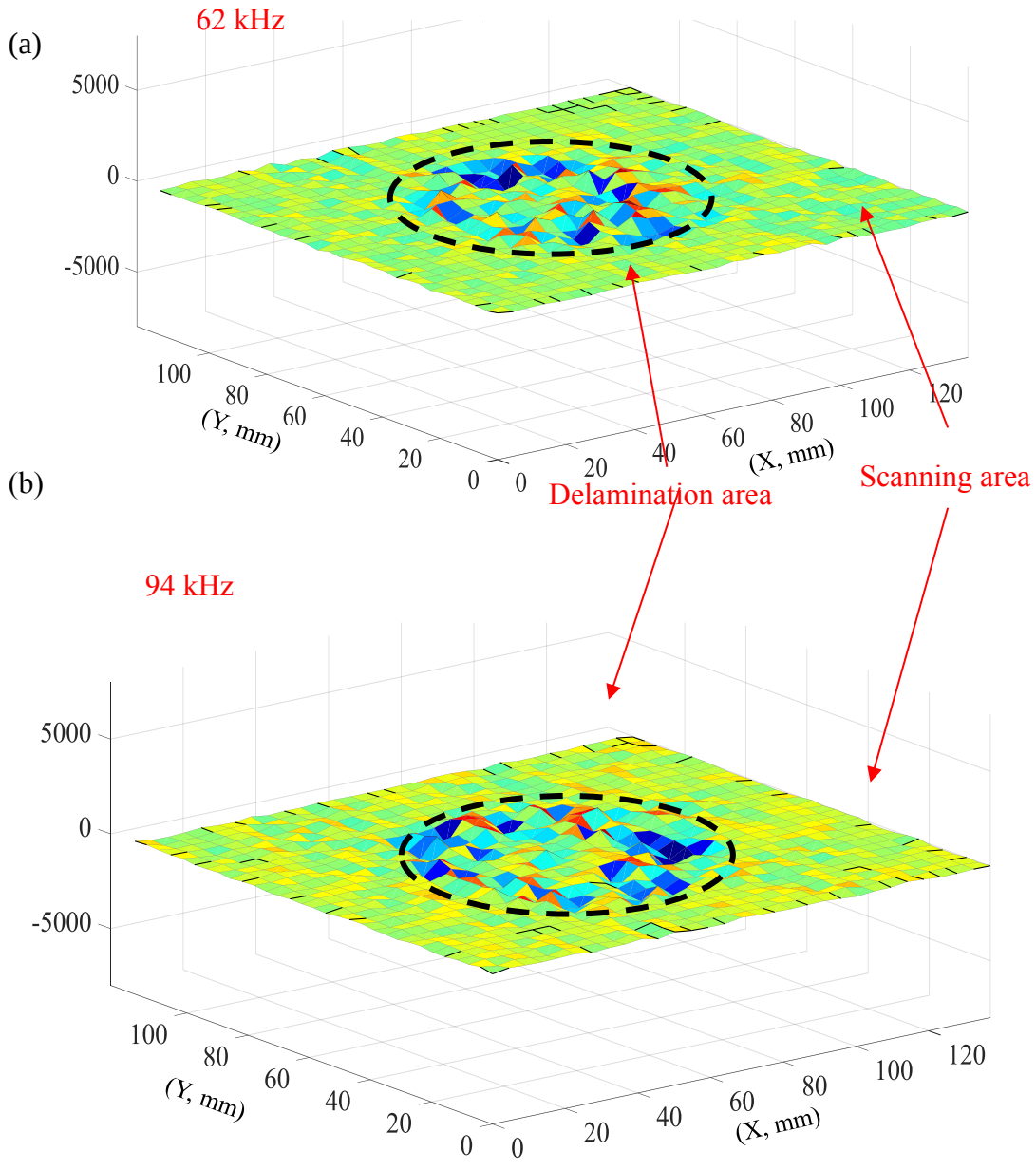

Figure 7.69: Measured operational vibration shapes for delamination C at resonance frequencies; (a) 62 kHz; (b) 94 kHz.

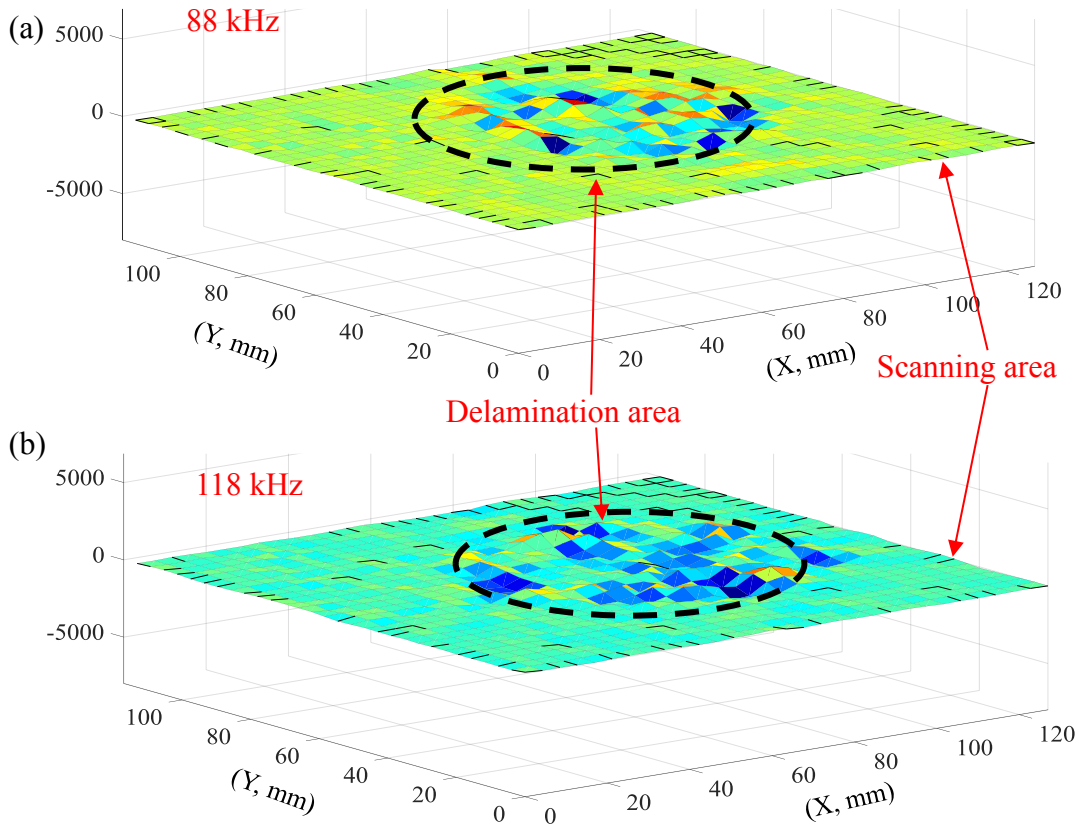

Figure 7.70: Measured operational vibration shapes for delamination B at resonance frequencies; (a) 88 kHz; (b) 118 kHz.

Table 7.3: The similarities in resonance frequencies between EMIS and SLDV methods for specimen 2.

Expermental methods	Area C (Resonance frequency (kHz))	Area B (Resonance frequency (kHz))	Area A (Resonance frequency (kHz))
EMIS	30, 58, 94, 104	47, 67, 87,118	50, 72, 80, 94, 116
SLDV	28, 62, 94, 103	47, 65, 88,118	52, 71 ,82, 90, 117

We can clearly see the higher amplitudes of local vibration over the delamination. Figure 7.71 shows the operational vibration shapes of damaged area A at resonance frequencies 52 and 71 kHz. It can be observed large motion over the delamination area. The damaged

area C has the largest motion among others damaged areas because the delamination is near to the surface. The operational vibration shapes of scanning area C are the best among the operational vibration shapes of other delamination for quantifying the size and shape of delamination.

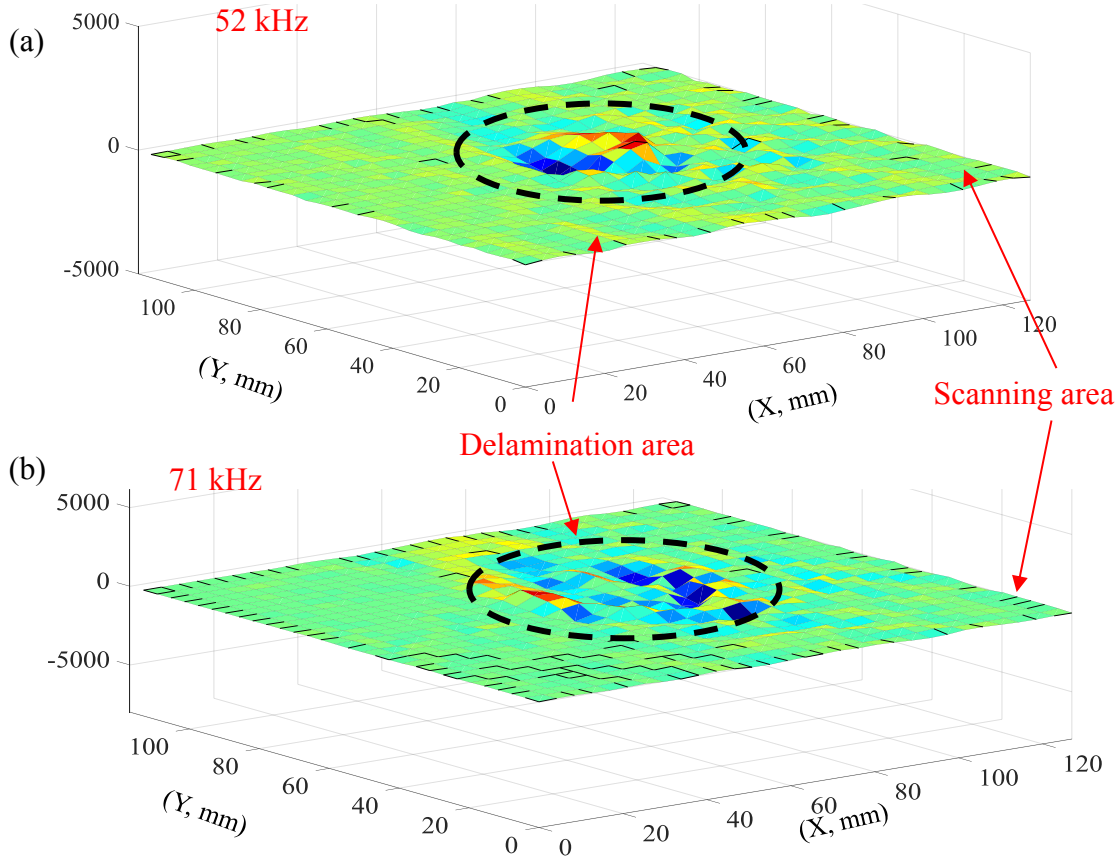

Figure 7.71: Measured operational vibration shapes for delamination A at resonance frequencies; (a) 52 kHz; (b) 71 kHz

7.8 SUMMARY AND CONCLUSION

In this chapter, I have presented four different experimental techniques to detect and quantify the delaminations of two different specimens. The first specimen (specimen 1) has three different sizes of delamination areas at the same level across the plate thickness. The second specimen (specimen 2) has three same size of delamination inserted at different

depths. First, The NDT technique was used to inspect these specimens using Rollerform and Omniscan. The results show quantitative information for identifying delamination areas in both specimens. The A-scan, C-scan and S-scan results accurately localize and size the delamination areas. Second, the SHM technique was used to inspect both specimens using a network of PWAS sensors, Lamb wave and imaging methods. The experimental dispersion and tuning curves of propagating Lamb waves were determined to deep understand the behavior of Lamb modes. The measured signals show that the delamination area has multiple scattering waves. The results show that scattering waves are dependent on the dominant incident modes, which hit the delamination, and the scattering direction. We have developed a methodology of detection and localization a damage point before using the imaging methods to accurately determine the directions and group velocities of incident and scattering waves. The imaging methods were used in conjunction with scattering waves of sensing paths to localize and size the delamination. These imaging results show the ability of SHM technique for quantifying the delamination in both specimens. The SLDV technique were used to study the guided wave propagation and interaction with delamination areas for both specimens. The time-space domain, frequency-wavenumber spectrum and wavefields images obviously detect the delamination areas. Fourth, the local vibration technique was used to detect and quantify the delamination. In this technique, we used the SLDV to acquire the data of linear chirp signals at each scanning point. The structural operational vibration shapes at resonance frequencies clearly predict and quantify the delamination. It can be found that the strong local vibrations only occur in the delamination region.

CHAPTER 8
CONCLUSIONS AND FUTURE WORK

This dissertation has presented the experimental methods of impact sources localization and damages identification in metallic and composite plates using structural health monitoring (SHM) and non-destructive inspection (NDI) methods. The experimental works in this dissertation focus on developed methodologies that help for imaging and identifying the location of impact sources and structural damages in isotropic and composite plates.

The dissertation started with a state of the art of identifying damages and acoustic emission sources localization in metallic and composite plates using passive and active SHM. Most of the imaging methods for localization and sizing structural defects in conjunction with Lamb waves were presented. The impact sources on isotropic plate were localized experimentally using sparse array of PWAS transducers, numerical methods and developed imaging methods. Then, the impact sources on composite plate due to pencil lead breaks were localized with two assumptions of unknown and known its material properties using numerical and imaging methods. The damages in aluminum plates were identified experimentally using sparse array of PWAS sensors, Lamb waves, pitch-catch mode, pulse-echo mode and imagining methods to localize, size and map the crack damage in the first experiment and the hole-plate in the second experiment. The dissertation continued with an introduction to FEM simulation of Lamb wave propagation and interaction with structural damages. The multi-physics finite element method (MP-FEM)

were used for 2-D simulation of Lamb wave propagation in cracked plate and interaction with horizontal crack at various incident wave directions. The hybrid global-local (HGL) approach was used for simulation Lamb wave propagation and interaction with horizontal crack. From this simulation, the scattered waves of different sensing paths were determined. These scattered waves were used to image the crack damage. Two composite plates with different layers orientation and thicknesses were manufactured with simulated delamination. The first plate has three different sizes of delamination inserted at the same depth. The second plate has three same sizes of delamination areas inserted at different thickness depths. The NDT technique was used to identify the delamination in both plates using Rollerform and Omniscan equipment. The SHM technique was used to quantify the delamination of the composite plates using sparse array of sensors and imaging methods. The SLDV technique was used to visualize the interaction of Lamb waves with delamination for both composite plates. The vibration-based technique was used to identify the delamination in both composite plates. In this technique, the operational vibration shapes were obtained at resonance frequencies.

8.1 RESEARCH CONCLUSIONS

8.1.1 PART I: IMPACT SOURCE LOCALIZATION ON METALLIC AND COMPOSITE PLATES

The impact sources on metallic plate were successfully localized using sparse array of sensors which were distributed across the area of interested. Two different methods were used to localize the impact points which are numerical method (triangulation algorithm) and image method. The numerical results showed that the percentage errors of localization the impact points are decreased with increasing the number of used sensors. The numerical method detected the impact points without knowing the group velocity of propagating

Lamb wave using at least four passive sensors. However, this method needs to predict the initial values of the unknowns to determine the coordinates of an impact point. The idea behind the imaging method is to predict the impact point on the interested area by finding the intersection point of some hyperbolae paths (at least two paths). This imaging method needs at least three sensors with known group velocity value of propagating Lamb wave to localize the impact source point. The imaging method can be used to localize the acoustic emission sources inside or outside the area of a network sensors.

The impact sources on a composite plate, which are generated by pencil lead breaks, were localized with two cases. In first case, the material properties of the composite plate is assumed to be unknown (the group velocity profiles of propagated Lamb wave are unknown). In second case, the material properties of the composite plate is assumed to be known. In the first case of localization, six PWAS transducers in conjunction with numerical and imaging methods were used to indicate the impact points. For first numerical method (method 1), which is based on the Kundu's approach, we used two linear equations (independent with group velocity profile of interested Lamb wave). For second numerical method (method 2), which is developed triangulation algorithm, we used a set of nonlinear equations. The developed visual methods are based on Kundu's approach, synthetic signals and imaging methods. The first visual method (method v1) has two smooth synthetic signals (one synthetic signal for each slope path). These synthetic signals have maximum amplitude at the experimental slope values. The synthetic signals of second imaging method (method v2) have square packets. The square synthetic signal has two values (one at experimental slope value and zero at different values). The idea behind these developed imaging method is to create two straight paths for each clusters using imaging methods.

The intersection point of these two paths represents the impact point. The developed imaging method predicted the impact points on the interested area with best results. In the second case (the material properties is available), the second developed imaging method was used to localize the impact points by indicating the intersection point of two hyperbolae paths. In this method, we need four PWAS transduces to create two hyperbolae paths (every two sensors have one hyperbola). This developed hyperbola path-based image methods has interested results.

8.1.2 PART II: DAMAGES DETECTION IN METALLIC STRUCTURES

This part of work briefly explained the principles of two imaging methods by presenting two flowcharts. Method A involves synthetic time reversal concept and method B involves Gaussian distribution function. The first experiment involved a sparse array of eight PWAS transducers to quantify the crack size by using the imaging methods. Pitch-catch and pulse-echo experimental modes were considered for each imaging method. The scattering waveform and imaging results were presented for both methods in each experimental mode. The directionality effect of various Lamb wave incidences (0°, 45°, 90° to the crack) and imaging results were studied. Both incident and sensing direction of Lamb wave affect the scattering wave signals which eventually affect the quality of imaging results. The experiments show that both imaging methods successfully quantify the crack size, shape, and orientation within an acceptable level of accuracy. The experiment involved confounding factors which affect the measurement of scattering wave signals. These scattering signals play an important role in crack quantification. Stronger scattering waves result in better imaging results. The optimum sensor configuration results in better scattering signals which eventually give better damage quantification. For pitch-

catch mode, the sensing paths of two transmitters in optimum locations may be enough to quantify the crack size. The synthetic time reversal-based imaging method (method A) can be used with threshold setting and without threshold setting. The use of combined summation and multiplication algorithm may eliminate the need of thresholding for better crack imaging. Both pitch-catch and pulse-echo modes show that the scattering waves are stronger when incident waves are perpendicular to the crack. In both experimental modes, the Gaussian distribution-based imaging method (method B) seems to overestimate the crack size.

The second experiment involved a network of sparse array of six PWAS transducers to quantify hole size by using the same imaging methods. The pitch-catch experimental mode was used to obtain the scattering signals. The relation between the hole size and the scattering signals was studied. In an attempt of smaller (1-mm to 3-mm) through thickness-hole size estimation, it was found that smaller hole produces relatively weaker scattering waves. These scattering waves can be used for hole detection and localization but may not be sufficient to quantify the hole size.

The multi-physics finite element method (MP-FEM) was used to simulate the Lamb wave propagation and interaction with horizontal crack damage on an aluminum plate. Several local FEM simulations were performed for various Lamb wave incidences (0°, 45°, 90° to the crack). The directionality effect on scattering waves were studied. The snapshot images of these three cases shows the Lamb wave propagation and interaction with the crack damage. It can also be noticed that maximum scattering amplitude occurs when the Lamb waves were incident perpendicular (90°) to the crack. For 0° Lamb wave incident, weak scattering amplitude occurred. The hybrid global-local (HGL) approach with imaging

methods provided fast and efficient simulation of crack size estimation. The polar plot of simulated WDICs revealed the directionality effect of the scattering wave signals emanated from the crack. Both incident and sensing direction of Lamb waves affect the scattering wave signals. The simulations and experiments show that both imaging methods successfully quantify the crack size, shape, and orientation within an acceptable level of accuracy

8.1.3 PART III: DAMAGE DETECTION IN COMPOSITE STRUCTURES

Two composite specimens were manufactured with simulated circular delamination areas. The first specimen (specimen 1) has three different sizes of circular delamination areas inserted at the same thickness depth. The second specimen (specimen 2) has three equal sizes of delamination areas inserted at different thickness depth. The NDT, SHM, SLDV and vibration-based techniques were used to identify all these delamination. First, the NDT technique was used to inspect these specimens using Rollerform and Omniscan device. The results showed quantitative information of delamination areas in both specimens. The A-scan, C-scan and S-scan results accurately localize and size the delamination. Second, the SHM technique was used to inspect the specimen 1 using a network of twenty-two sensors and imaging methods. The group velocity dispersion curves and tuning curves were determined experimentally at the directions of 45^0 and 0^0. A new methodology has been adopted to predict the location of damage point on the interested area before using imaging methods. After prediction the damage location, the group velocities of incident and scattering waves can be determined. For the second specimen (specimen 2), A new methodology of using higher order Lamb modes has been developed to study the interaction of Lamb waves with delamination in thick unidirectional composite

plate. The summation and multiplication imaging methods were combined to fuse all the constructed images of different sensing paths. The image results showed the ability of SHM technique for identifying delamination in composite plates. Third, SLDV technique was used to scan four sub-areas of specimen 1. The interaction of Lamb waves with three delamination were visualized. The time-space and frequency-wavenumber analysis were determined for these four scanning areas. The results of wavefield images, time-space domain and frequency-wavenumber domain are clearly identified the three different sizes of delamination. For specimen 2, the trapped waves over delamination areas have been studied as a function of delamination depth. The results show that the delamination near the surface has smooth and short length of trapped waves. The other delamination which are far away from the surface have a coarse and long length of trapped waves.

Fourth, a new method of vibration-based technique has been used to detect and identify the delamination areas of both specimens. The hybrid of PZT- laser Doppler vibrometer experiments were implemented to excite a chirp signal and acquire the response signals of scanning area. The EMIS experiments were implemented to determine the resonance frequencies of damaged areas. Based on the resonance frequencies, the mode shapes of delamination areas were obtained. These operational vibration shapes observe the shape and size of delamination.

8.2 MAJOR CONTRIBUTIONS

This dissertation research implements the following contributions to the state of the art:

1. A new imaging method to successfully detect the impact location on isotropic metallic plates.

2. Two new imaging methods to successfully detect the impact location on anisotropic composite plates.
3. A new methodology to successfully identify crack damage in metallic plates using pitch-catch and pulse-echo Lamb imaging waves.
4. A new methodology to successfully identify delamination in composite plates using pitch-catch and pulse-echo Lamb imaging waves.
5. A new methodology for damage imaging in thick composite plates using higher-order Lamb wave modes.
6. A new high-frequency vibration-based method to identify delamination in composite plates using SLDV instrumentation.
7. A methodology for in-situ delamination detection in composite plates using electromechanical impedance spectroscopy (EMIS).

8.3 RECOMMENDATION FOR FUTURE WORK

1. Use newly imaging methods to localize the source of acoustic emission during a fatigue crack experiment.
2. It would be interesting to study how small fatigue crack can be sized using developed imaging methods.
3. The experiment involving various hole-diameters can be extended further. The diameter of the hole may be increased gradually to a size where one can use these imaging methods to quantify the hole-size. These methods may be used for sizing of actual.
4. Use the new vibration-based method to identify a crack damage on isotropic plate.

5. Quantifying delamination areas in composite plates by extracting the special wavenumber images.

REFERENCES

[1] Zhou, C.; Su, Z. and Cheng, L. (2011) "Probability-based diagnostic imaging using hybrid features extracted from ultrasonic Lamb wave signals," *Smart Materials and Structures*, vol. 20, no. 12, 2011.

[2] Lin, B. and Giurgiutiu, V. (2010) "Modeling of Power and Energy Transduction of Embedded Piezoelectric Wafer Active Sensors for Structural Health Monitoring," University of South Carolina, 2010.

[3] Giurgiutiu, V. (2014) *Structural Health Monitoring with Piezoelectric Waver Active Sensors*, Second Edi. Elsevier Academic Press, 2014.

[4] Cuc, A.; Giurgiutiu, V.; Joshi, S. and Tidwell, Z. (2007) *Structural Health Monitoring with Piezoelectric Wafer Active Sensors for Space Applications*, vol. 45, no. 12. Oxford,UK: Elsevier Academic Press, 2007.

[5] Rizzo, P. and di Scalea, F. L. (2006) "Feature extraction for defect detection in strands by guided ultrasonic waves," *Structural Health Monitoring*, vol. 5, no. 3, pp. 297–308, 2006.

[6] Ihn, J. and Chang, F. (2004) "Jeong-Beom Ihn and Fu-Kuo Chang," vol. 13, no. April 2016, pp. 621–630, 2004.

[7] Souza, P. R. and Nobrega, E. G. O. (2015) "Lamb wave based damage detection and localization using two ring-shaped arrangement of piezo transducers," *IFAC-PapersOnLine*, vol. 28, no. 21, pp. 646–651, 2015.

[8] Ihn, J.-B. and Chang, F.-K. (2008) "Pitch-catch Active Sensing Methods in Structural Health Monitoring for Aircraft Structures," *Structural Health Monitoring: An International Journal*, vol. 7, no. 1, pp. 5–19, 2008.

[9] Su, Z. and Ye, L. (2009) *Identification of Damage using Lamb waves*. Verlag Berlin Heidelberg: Springer, 2009.

[10] Yu, L. and Giurgiutiu, V. (2010) "Piezoelectric Wafer Active Sensor Guided Wave Imaging," *Proc of 2010 SPIE*, vol. 7648, pp. 1–11, 2010.

[11] Wang, C. H.; Rose, J. T. and Chang, F.-K. (2004) "A synthetic time-reversal imaging method for structural health monitoring," *Smart Materials and Structures*, vol. 13, no. 2, pp. 415–423, 2004.

[12] Michaels, J. E. and Michaels, T. E. (2007) "Guided wave signal processing and image fusion for in situ damage localization in plates," *Wave Motion*, vol. 44, no. 6,

pp. 482–492, 2007.

[13] Zhou, C.; Su, Z. and Cheng, L. (2011) "Quantitative evaluation of orientation-specific damage using elastic waves and probability-based diagnostic imaging," *Mechanical Systems and Signal Processing*, vol. 25, no. 6, pp. 2135–2156, 2011.

[14] Yu, L. and Leckey, C. A. C. (2013) "Lamb wave-based quantitative crack detection using a focusing array algorithm," *Journal of Intelligent Material Systems and Structures*, vol. 24, no. 9, pp. 1138–1152, 2013.

[15] Michaels, J. E. (2008) "Detection, localization and characterization of damage in plates with an in situ array of spatially distributed ultrasonic sensors," *Smart Materials and Structures*, vol. 17, no. 3, 2008.

[16] Chang, F.-K.; Markmiller, J. F. C.; Ihn, J.-B. and Cheng, K. Y. (2007) "A potential link from damage diagnostics to health prognostics of composites through built-in sensors," *Journal of Vibration and Acoustics-Transactions of the ASME*, vol. 129, no. 6, pp. 718–729, 2007.

[17] Michaels, J. E. (2006) "Enhanced Differential Methods for Guided Wave Phased Array Imaging Using Spatially Distributed Piezoelectric Transducers," *32nd Annual Review of Progress in Quantitative Nondestructive Evaluation (AIP Conf. Proc. 820)*, vol. 25, pp. 837–844, 2006.

[18] Zhao, X.; Qian, T.; Mei, G.; Kwan, C.; Zane, R.; Walsh, C.; Paing, T. and Popovic, Z. (2007) "Active health monitoring of an aircraft wing with an embedded piezoelectric sensor/actuator network: II. Wireless approaches," *Smart Materials and Structures*, vol. 16, no. 4, pp. 1218–1225, 2007.

[19] Wandowski, T. (2016) "Damage Detection in Composite Materials," pp. 1–10, 2016.

[20] Peng, T.; Saxena, A.; Goebel, K.; Sankararaman, S.; Xiang, Y. and Liu, Y. (2013) "Probabilistic delamination diagnosis of composite materials using a novel Bayesian Imaging Method," *Annual Conference of the Prognostic and Health Managment society*, pp. 1–9, 2013.

[21] Tian, Z.; Leckey, C. A. C.; Yu, L. and Seebo, J. P. (2015) "Impact induced delamination detection and quantification with guided wavefield analysis," *SPIE Smart Structures and Materials + Nondestructive Evaluation and Health Monitoring*, vol. 9435, p. 94351P, 2015.

[22] Staszewski, W. J.; Mahzan, S. and Traynor, R. (2009) "Health monitoring of aerospace composite structures - Active and passive approach," *Composites Science and Technology*, vol. 69, no. 11–12, pp. 1678–1685, 2009.

[23] Katunin, A.; Dragan, K. and Dziendzikowski, M. (2015) "Damage identification in aircraft composite structures: A case study using various non-destructive testing techniques," *Composite Structures*, vol. 127, pp. 1–9, 2015.

[24] Tan, K. S.; Guo, N.; Wong, B. S. and Tui, C. G. (1995) "Experimental evaluation of delaminations in composite plates by the use of Lamb waves," *Composites Science and Technology*, vol. 53, no. 1, pp. 77–84, 1995.

[25] Su, Z.; Ye, L. and Lu, Y. (2006) "Guided Lamb waves for identification of damage in composite structures: A review," *Journal of Sound and Vibration*, vol. 295, no. 3–5, pp. 753–780, 2006.

[26] Diamanti, K.; Soutis, C. and Hodgkinson, J. M. (2007) "Piezoelectric transducer arrangement for the inspection of large composite structures," *Composites Part A: Applied Science and Manufacturing*, vol. 38, no. 4, pp. 1121–1130, 2007.

[27] Su, Z.; Cheng, L.; Wang, X.; Yu, L. and Zhou, C. (2009) "Predicting delamination of composite laminates using an imaging approach," *Smart Materials and Structures*, vol. 18, no. 7, 2009.

[28] Wang, D.; Ye, L.; Lu, Y. and Su, Z. (2009) "Probability of the presence of damage estimated from an active sensor network in a composite panel of multiple stiffeners," *Composites Science and Technology*, vol. 69, no. 13, pp. 2054–2063, 2009.

[29] Sengupta, S.; Datta, A. K. and Topdar, P. (2015) "Structural damage localisation by acoustic emission technique: A state of the art review," *Latin American Journal of Solids and Structures*, vol. 12, no. 8, pp. 1565–1582, 2015.

[30] Acoustic, D.; Technology, E.; Safety, I. I. and Saving, E. M. "www.idinspections.com."

[31] Ciampa, F. and Meo, M. (2010) "A new algorithm for acoustic emission localization and flexural group velocity determination in anisotropic structures," *Composites Part A: Applied Science and Manufacturing*, vol. 41, no. 12, pp. 1777–1786, 2010.

[32] Shrestha, P.; Kim, J. H.; Park, Y. and Kim, C. G. (2015) "Impact localization on composite wing using 1D array FBG sensor and RMS/correlation based reference database algorithm," *Composite Structures*, vol. 125, pp. 159–169, 2015.

[33] Mostafapour, A.; Davoodi, S. and Ghareaghaji, M. (2014) "Acoustic emission source location in plates using wavelet analysis and cross time frequency spectrum," *Ultrasonics*, vol. 54, no. 8, pp. 2055–2062, 2014.

[34] Yamada, H.; Mizutani, Y.; Nishino, H.; Takemoto, M. and Ono, K. (2000) "Lamb wave source location of impact on anisotropic plates," *Journal of Acoustic Emission(USA)*, vol. 18, p. 51, 2000.

[35] Coelho, C. K.; Hiche, C. and Chattopadhyay, A. (2010) "Impact Localization and Force Estimation on a Composite Wing using Fiber Bragg Gratings Sensors," no. April, p. 85287, 2010.

[36] Park, W. H.; Packo, P. and Kundu, T. (2016) "Acoustic source localization in an anisotropic plate without knowing its material properties: a new approach," p. 98050J, 2016.

[37] Salinas, V.; Vargas, Y.; Ruzzante, J. and Gaete, L. (2010) "Localization algorithm for acoustic emission," *Physics Procedia*, vol. 3, no. 1, pp. 863–871, 2010.

[38] Kundu, T. (2014) "Acoustic source localization," *Ultrasonics*, vol. 54, no. 1, pp. 25–38, 2014.

[39] Al-jumaili, S.; Pearson, M.; Holford, K.; Eaton, M. and Pullin, R. (2016) "Fast and Reliable Acoustic Emission Source Location Technique in Complex Structures," no. April, pp. 81–84, 2016.

[40] Kundu, T.; Nakatani, H. and Takeda, N. (2012) "Acoustic source localization in anisotropic plates," *Ultrasonics*, vol. 52, no. 6, pp. 740–746, 2012.

[41] Zhao, X.; Yuan, S.; Zhou, H.; Sun, H. and Qiu, L. (2009) "An evaluation on the multi-agent system based structural health monitoring for large scale structures," *Expert Systems with Applications*, vol. 36, no. 3 PART 1, pp. 4900–4914, 2009.

[42] (2005) "Title: Structural Health Monitoring with Piezoelectric Wafer Active Sensors Author: Victor Giurgiutiu Paper presented at: 16," no. October, pp. 10–12, 2005.

[43] Chassignole, B.; Guerjouma, R. El; Ploix, M. and Fouquet, T. (2010) "ARTICLE IN PRESS NDT & E International Ultrasonic and structural characterization of anisotropic austenitic stainless steel welds : Towards a higher reliability in ultrasonic non-destructive testing," *NDT and E International*, vol. 43, no. 4, pp. 273–282, 2010.

[44] Nath, S. K.; Krishnamurthy, C. V and Narayana, B. H. (2019) "Detection and Sizing of Defects in Complex Geometry Weld by Manual Ultrasonic Time of Flight," vol. 131, no. October 2009, pp. 1–9, 2019.

[45] Giurgiutiu, V.; Zagrai, A. and Bao, J. (2002) "Piezoelectric Wafer Embedded Active Sensors for Aging Aircraft Structural Health Monitoring," *Structural Health Monitoring*, vol. 1, no. 1, pp. 41–61, 2002.

[46] Rose, J. L. (2014) *No Title Ultrasonic Guided Waves in Solid Media*. Cambridge: Cambridge University Press., 2014.

[47] Farrar, C. R. and Worden, K. (2007) "An introduction to structural health monitoring," *Philosophical Transactions of the Royal Society A: Mathematical, Physical and Engineering Sciences*, vol. 365, no. 1851, pp. 303–315, 2007.

[48] Bhuiyan, M. Y.; Bao, J.; Poddar, B. and Giurgiutiu, V. (2017) "Toward identifying crack-length-related resonances in acoustic emission waveforms for structural health monitoring applications," *Structural Health Monitoring*, 2017.

[49] Tobias, A. (1976) "Acoustic-emission source location in two dimensions by an array of three sensors," *Non-Destructive Testing*, vol. 9, no. 1, pp. 9–12, 1976.

[50] Vallen "Vallen-system." Munich, Germany.

[51] Hajzargerbashi, T.; Kundu, T. and Bland, S. (2011) "An improved algorithm for detecting point of impact in anisotropic inhomogeneous plates," *Ultrasonics*, vol. 51, no. 3, pp. 317–324, 2011.

[52] Shen, Y. and Giurgiutiu, V. (2012) "Simulation of Interaction Between Lamb Waves and Cracks for Structural Health Monitoring With Piezoelectric Wafer Active Sensors," *Volume 1: Development and Characterization of Multifunctional Materials; Modeling, Simulation and Control of Adaptive Systems; Structural Health Monitoring*, p. 615, 2012.

[53] Alleyne, D. N. and Cawley, P. (1992) "The Interaction of Lamb Waves with Defects," *IEEE Transactions on Ultrasonics, Ferroelectrics, and Frequency Control*, vol. 39, no. 3, pp. 381–397, 1992.

[54] Ghosh, T.; Kundu, T. and Karpur, P. (1998) "Efficient use of Lamb modes for detecting defects in large plates," *Ultrasonics*, vol. 36, no. 7, pp. 791–801, 1998.

[55] Fromme, P. and Sayir, M. B. (2002) "Detection of cracks at rivet holes using guided waves," *Ultrasonics*, vol. 40, no. 1–8, pp. 199–203, 2002.

[56] Wilcox, P.; Lowe, M. and Cawley, P. (2005) "Omnidirectional guided wave inspection of large metallic plate structures using an EMAT array," *IEEE Transactions on Ultrasonics, Ferroelectrics, and Frequency Control*, vol. 52, no. 4, pp. 653–665, 2005.

[57] Purekar, A. S.; Pines, D. J.; Sundararaman, S. and Adams, D. E. (2004) "Directional piezoelectric phased array filters for detecting damage in isotropic plates," *Smart Materials and Structures*, vol. 13, no. 4, pp. 838–850, 2004.

[58] Wang, C,; Rose , J,; and Chang, F. (2004) "A Synthetic Time-Reversal Imaging Method for Structural Health Monitoring," *Smart Material and Structures*, pp. 415–423, 2004.

[59] Leckey, C. A. C.; Rogge, M. D.; Miller, C. A. and Hinders, M. K. (2012) "Multiple-mode Lamb wave scattering simulations using 3D elastodynamic finite integration technique," *Ultrasonics*, vol. 52, no. 2, pp. 193–207, 2012.

[60] Gresil, M.; Yu, L. and Giurgiutiu, V. (2011) "Fatigue crack detection in thick steel structures with piezoelectric wafer active sensors," vol. 12, no. 2, p. 79832Y, 2011.

[61] Golato, A.; Demirli, R. and Santhanam, S. (2014) "Lamb wave scattering by a symmetric pair of surface-breaking cracks in a plate," *Wave Motion*, vol. 51, no. 8, pp. 1349–1363, 2014.

[62] Shen, Y. and Giurgiutiu, V. (2016) "Combined analytical/FEM approach for efficient simulation of lamb wave damage detection," *Ultrasonics*, vol. 69, no. 3, pp. 116–128, 2016.

[63] Yeasin Bhuiyan, M.; Shen, Y. and Giurgiutiu, V. (2017) "Interaction of Lamb waves with rivet hole cracks from multiple directions," *Proceedings of the Institution of*

Mechanical Engineers, Part C: Journal of Mechanical Engineering Science, vol. 231, no. 16, pp. 2974–2987, 2017.

[64] Shen, Y. and Giurgiutiu, V. (2015) "Effective non-reflective boundary for Lamb waves: Theory, finite element implementation, and applications," *Wave Motion*, vol. 58, pp. 22–41, 2015.

[65] Moreau, L.; Caleap, M.; Velichko, A. and Wilcox, P. D. (2012) "Scattering of guided waves by flat-bottomed cavities with irregular shapes," *Wave Motion*, vol. 49, no. 2, pp. 375–387, 2012.

[66] Wang, C. H. and Chang, F. K. (2005) "Scattering of plate waves by a cylindrical inhomogeneity," *Journal of Sound and Vibration*, vol. 282, no. 1–2, pp. 429–451, 2005.

[67] Hadi Hafezi, M. and Kundu, T. (2017) "Peri-Ultrasound Modeling of Dynamic Response of an Interface Crack Showing Wave Scattering and Crack Propagation," *Journal of Nondestructive Evaluation, Diagnostics and Prognostics of Engineering Systems*, vol. 1, no. 1, p. 11003, 2017.

[68] Shen, Y. and Cesnik, C. E. S. (2017) "Modeling of nonlinear interactions between guided waves and fatigue cracks using local interaction simulation approach," *Ultrasonics*, vol. 74, pp. 106–123, 2017.

[69] Shen, Y.; Wang, J. and Xu, W. (2018) "fatigue cracks considering the rough contact surface condition Nonlinear features of guided wave scattering from rivet hole nucleated fatigue cracks considering the rough contact surface condition," 2018.

[70] Shen, Y. and Giurgiutiu, V. (2016) "Combined analytical FEM approach for efficient simulation of Lamb wave damage detection," *Ultrasonics*, vol. 69, pp. 116–128, 2016.

[71] Shen, Y. and Giurgiutiu, V. (2014) "WaveFormRevealer: An analytical framework and predictive tool for the simulation of multi-modal guided wave propagation and interaction with damage," *Structural Health Monitoring*, vol. 13, no. 5, pp. 491–511, 2014.

[72] Bhuiyan, Y.; Lin, B. and Giurgiutiu, V. (2018) "Acoustic emission sensor effect and waveform evolution during fatigue crack growth in thin metallic plate," vol. 29, no. 7, pp. 1275–1284, 2018.

[73] Yelve, N. P.; Mitra, M.; Mujumdar, P. M. and Ramadas, C. (2016) "A hybrid method based upon nonlinear Lamb wave response for locating a delamination in composite laminates," *Ultrasonics*, vol. 70, pp. 12–17, 2016.

[74] Feng, B.; Ribeiro, A. L. and Ramos, H. G. (2018) "Interaction of Lamb waves with the edges of a delamination in CFRP composites and a reference-free localization method for delamination," *Measurement*, vol. 122, no. September 2017, pp. 424–431, 2018.

[75] He, M Y; Hutchinson, J. W. (1989) “Damage detection in composite materials using frequency response methods,” *Journal of Applied Mechanics*, vol. 111, no. 1, pp. 270–78, 1989.

[76] Giurgiutiu, V. and Soutis, C. (2012) “Enhanced composites integrity through structural health monitoring,” *Applied Composite Materials*, vol. 19, no. 5, pp. 813–829, 2012.

[77] Hayashi, T. and Kawashima, K. (2002) “Multiple reflections of Lamb waves at a delamination,” *Ultrasonics*, vol. 40, no. 1–8, pp. 193–197, 2002.

[78] Azuara, G.; Barrera, E. and Ruiz, M. (2018) “Integration of algorithms for damage detection in thermoplastic materials inside electronic embedded devices,” *European Workshop on Structural Health Monitoring Series (EWSHM)*, 2018, pp. 1–12.

[79] He, J.; Ran, Y.; Liu, B.; Yang, J. and Guan, X. (Sep. 2017) “A Fatigue Crack Size Evaluation Method Based on Lamb Wave Simulation and Limited Experimental Data,” *Sensors (Basel, Switzerland)*, vol. 17, no. 9, p. 2097, Sep. 2017.

[80] Salas, K. I. and Cesnik, C. E. S. (2010) “Guided wave structural health monitoring using CLoVER transducers in composite,” vol. 19, 2010.

[81] Maio, L.; Memmolo, V.; Ricci, F.; Boffa, N. D.; Monaco, E. and Pecora, R. (2015) “Ultrasonic wave propagation in composite laminates by numerical simulation,” *Composite Structures*, vol. 121, pp. 64–74, 2015.

[82] Guo, N. and Cawley, P. (1993) “The interaction of Lamb waves with delaminations in composite laminates,” *The Journal of the Acoustical Society of America*, 1993.

[83] Lemistre, M. and Balageas, D. (2001) “Structural health monitoring system based on diffracted Lamb wave analysis by multiresolution processing,” vol. 10, pp. 504–511, 2001.

[84] Magruder, C. “RollerFORM Inspection of CFRP using OmniScan SX \ MX2 Part 1 – OmniScan Setup and Configuration.”

[85] LAMSS (2017) “LAMSS_COMPOSITES_V1.0.” 2017.

[86] Ip, K. and Mai, Y. (2004) “Delamination detection in smart composite beams using Lamb waves,” 2004.

[87] Jothi Saravanan, T.; Gopalakrishnan, N. and Prasad Rao, N. (2015) “Damage detection in structural element through propagating waves using radially weighted and factored RMS,” *Measurement*, vol. 73, pp. 520–538, 2015.

[88] Masserey, B. and Fromme, P. (Apr. 2015) “In-situ monitoring of fatigue crack growth using high frequency guided waves,” *NDT & E International*, vol. 71, Apr. 2015.

[89] Michaels, T. E.; Michaels, J. E. and Ruzzene, M. (2011) “Frequency-wavenumber

domain analysis of guided wavefields," *Ultrasonics*, vol. 51, no. 4, pp. 452–466, 2011.

[90] Rogge, M. D. and Leckey, C. A. C. (2013) "Characterization of impact damage in composite laminates using guided wavefield imaging and local wavenumber domain analysis," *Ultrasonics*, vol. 53, no. 7, pp. 1217–1226, 2013.

[91] Tian, Z.; Leckey, C. A. C.; Yu, L. and Seebo, J. P. (2015) "Impact induced delamination detection and quantification with guided wavefield analysis," p. 94351P, 2015.

[92] Sohn, H.; Dutta, D.; Yang, J. Y.; Park, H. J.; DeSimio, M.; Olson, S. and Swenson, E. (2011) "Delamination detection in composites through guided wave field image processing," *Composites Science and Technology*, vol. 71, no. 9, pp. 1250–1256, 2011.

[93] Sohn, H.; Dutta, D.; Yang, J. Y.; Desimio, M.; Olson, S. and Swenson, E. (2011) "Automated detection of delamination and disbond from wavefield images obtained using a scanning laser vibrometer," *Smart Materials and Structures*, vol. 20, no. 4, 2011.

[94] Cawley, P. and Adams, R. D. (1979) "Vibration Technique For Nondestructive Testing Of Fiber Composite Structures," *Journal Of Composite Materials*, vol. 13, pp. 161–175, 1979.

[95] Cawley, P. and Adams, R. D. (1986) "Fokker Bond Tester probe ! Hooked," vol. 24, pp. 318–324, 1986.

[96] Cawley, P. (1984) "The sensitivity of the mechanical impedance method of nondestructive testing," *NDT International*, vol. 17, no. 2, pp. 59–66, 1984.

[97] Fan, W. and Qiao, P. (2011) "Vibration-based damage identification methods: A review and comparative study," *Structural Health Monitoring*, vol. 10, no. 1, pp. 83–111, 2011.

[98] Manoach, E.; Warminski, J.; Kloda, L. and Teter, A. (2017) "Numerical and experimental studies on vibration based methods for detection of damage in composite beams," *Composite Structures*, vol. 170, pp. 26–39, 2017.

[99] Montalvao, D. (2006) "A Review of Vibration_based Structural Health Monitoring with Special Emphasis on Composite Materials," *The Shock and Vibration Digest*, vol. 38, no. 4, pp. 295–324, 2006.

[100] Zou, Y.; Tong, L. and Steven, G. P. (2000) "Vibration-based model-dependent damage (delamination) identification and health monitoring for composite structures - a review," *Journal of Sound and Vibration*, vol. 230, no. 2, pp. 357–378, 2000.

[101] Pérez, M. A.; Gil, L. and Oller, S. (2014) "Impact damage identification in composite laminates using vibration testing," *Composite Structures*, vol. 108, no. 1, pp. 267–276, 2014.

[102] Yang, C. and Oyadiji, S. O. (2017) “Damage detection using modal frequency curve and squared residual wavelet coefficients-based damage indicator,” *Mechanical Systems and Signal Processing*, vol. 83, pp. 385–405, 2017.

[103] Vo-Duy, T.; Ho-Huu, V.; Dang-Trung, H.; Dinh-Cong, D. and Nguyen-Thoi, T. (2016) “Damage detection in laminated composite plates using modal strain energy and improved differential evolution algorithm,” *Procedia Engineering*, vol. 142, pp. 181–188, 2016.

[104] Giurgiutiu, V. and Zagrai, A. N. (2001) “Characterization of piezoelectric wafer active sensors,” *Journal of Intelligent Material Systems and Structures*, vol. 11, no. 12, pp. 959–976, 2001.

APPENDIX A: DATA STORAGE AND RETRIEVAL INFORMATION

The experimental data and all other files of the dissertation work are organized on the following five chapters

1. CHAPTER 3

In this chapter, the impact experiment on an aluminum plate was implemented. The data of received signals and MATLAB files have been saved within the Asaad share drive under the following folder.

Dissertation\Appendix A\CHAPTER_3

2. CHAPTER 4

In this chapter, the impact experiment on a composite plate was implemented. The data of received signals and MATLAB files have been saved within the Asaad share drive under the following folder.

Dissertation\Appendix A\CHAPTER_4

3. CHAPTER 5

In this chapter, two works were implemented in this chapter. The first work is crack damage identification on an aluminum plate using guided wave and imaging methods. The second work is through thickness hole damage detection on an aluminum plate using guided wave and imaging methods. The data of received signals and MATLAB files have been saved within the Asaad share drive under the following folder.

Dissertation\Appendix A\CHAPTER_5

4. CHAPTER 6

In this chapter, the interaction of Lamb waves with crack damage are studied numerically using multi-physics finite element method (MP-FEM) and A hybrid global-local (HGL) The DATA and ANSYS and MATLAB files have been saved within the Asaad share drive under the following folder.

Dissertation\Appendix A\CHAPTER_6

5. CHAPTER 7

In this chapter, we investigated two damaged composite plates using NDT, SHM, SLDV and vibration based techniques.

The setting up files of NDT method can be found within the Asaad share drive under the following folder.

Dissertation\Appendix A\CHAPTER_7\NDT

For SHM technique, we have two specimens (specimen1 and specimen 2).The data of received signals and MATLAB files have been saved within the Asaad share drive under the following folder.

Dissertation\Appendix A\CHAPTER_7\SHM

For SLDV technique, we investigated specimen1 and specimen 2.The wavefield data and MATLAB files have been saved within the Asaad share drive under the following folder: Dissertation\Appendix A\CHAPTER_7\SLDV

For vibration based technique, we investigated specimen1 and specimen 2.The wavefield data and MATLAB files have been saved within the Asaad share drive under the following folder.

Dissertation\Appendix A\CHAPTER_7\Vibration-based method